Development of Multi-Alkali Antimonide Photocathodes for High-Brightness RF Photoinjectors

Dissertation
zur Erlangung des Doktorgrades
an der Fakultät für Mathematik, Informatik und Naturwissenschaften
Fachbereichs Physik
der Universität Hamburg

vorgelegt von

Sandeep Kumar Mohanty

Hamburg
2024

Gutachter/innen der Dissertation:	Prof. Dr. Wolfgang Hillert
	Dr. Anne Oppelt
Zusammensetzung der Prüfungskommission:	Prof. Dr. Wolfgang Hillert
	Dr. Anne Oppelt
	Dr. Daniele Sertore
	Prof. Dr. Daniela Pfannkuche
	Prof. Dr. Florian Grüner
Vorsitzende/r der Prüfungskommission:	Prof. Dr. Daniela Pfannkuche
Datum der Disputation:	15.10.2024
Vorsitzender des Fach-Promotionsausschusses PHYSIK:	Prof. Dr. Markus Drescher
Leiter des Fachbereichs PHYSIK:	Prof. Dr. Wolfgang J. Parak
Dekan der Fakultät MIN:	Prof. Dr.-Ing. Norbert Ritter

एकम् सत् विप्राः बहुधा वदन्ति

~ Rigveda

Abstract

Multi-alkali antimonide photocathodes can have high quantum efficiency similar to UV-sensitive Cs_2Te photocathodes, but with the advantages of photoemission sensitivity in the green wavelength and a significant reduction in the mean transverse energy of the photoelectrons. To explore their feasibility for use in a high-gradient RF gun, DESY collaborated with INFN LASA to develop multi-alkali photocathode materials. This dissertation provides detailed insights into the fabrication recipes of various alkali antimonide photocathodes, including K-Cs-Sb, Na-K-Sb, and Na-K-Sb-Cs photocathodes, all of which were grown on a Mo substrate. This thesis also provides information regarding film thickness, substrate temperature, deposition rate, and their possible effects on the photocathode's properties. In addition, the influence of temperature on the cathode degradation is also summarized. Moreover, this report presents a summary of the test results obtained from the K-Cs-Sb cathodes inside the high-gradient RF gun at PITZ.

Furthermore, within the framework of density functional theory (DFT), the dissertation explores the electronic and optical properties of materials like K_3Sb, K_2CsSb, and Na_2KSb. The optical properties, including the dielectric function, reflectivity, refractive index, and extinction coefficient, were evaluated. The correlation between the simulated and measured optical properties, such as reflectivity, provides a more efficient strategy for rationalizing and understanding the properties of photoemissive materials. This further helps to improve the cathode recipe. This dissertation also outlines such correlations between experimental and simulation results for the aforementioned photoemissive films. This study represents a step forward in the development of multi-alkali photocathodes for high-charge RF photoinjector applications, providing a valuable characterization of K-Cs-Sb photocathode performance.

Zusammenfassung

Multi-Alkali-Antimonid-Photokathoden können eine hohe Quanteneffizienz ähnlich wie UV-empfindliche Cs_2Te-Photokathoden haben, jedoch mit den Vorteilen einer Photoemissionsempfindlichkeit im grünen Wellenlängenbereich und einer signifikanten Reduktion der mittleren transversalen Energie der Photoelektronen. Um ihre Machbarkeit für den Einsatz in einer Hochgradienten-RF-Kanone zu untersuchen, arbeitete DESY zusammen mit INFN LASA bewertet, um Multialkali-Photokathodenmaterialien zu entwickeln. Diese Dissertation bietet detaillierte Einblicke in die Herstellungsrezepte verschiedener Alkali-Antimonid-Photokathoden, einschließlich K-Cs-Sb, Na-K-Sb und Na-K-Sb-Cs Photokathoden, die alle auf einem Mo-Substrat gewachsen sind. Diese Arbeit liefert auch Informationen über die Filmdicke, die Substrattemperatur, die Abscheiderate und deren mögliche Auswirkungen auf die Eigenschaften der Photokathode. Darüber hinaus wird auch der Einfluss der Temperatur auf die Verschlechterung der Kathodeneigenschaften zusammengefasst. Ferner präsentiert dieser Bericht eine Zusammenfassung der Testergebnisse, die mit den KCsSb-Kathoden in der Hochgradienten-RF-Kanone bei PITZ erhalten wurden.

Darüber hinaus untersucht die Dissertation im Rahmen der Dichtefunktionaltheorie (DFT) die elektronischen und optischen Eigenschaften von Materialien wie K_3Sb, K_2CsSb und Na_2KSb. Die optischen Eigenschaften, einschließlich der dielektrischen Funktion, Reflexivität, Brechungsindex und Extinktionskoeffizient, wurden bewertet. Die Korrelation zwischen den simulierten und gemessenen optischen Eigenschaften, wie der Reflexivität, bietet eine effizientere Strategie zur Bewertung und zum Verständnis der Eigenschaften von photoemissiven Materialien. Dies trägt weiterhin zur Verbesserung der Ablauf bei der Herstellung von Methoden bei. Diese Dissertation skizziert auch Korrela-

tionen zwischen experimentellen und Simulationsergebnissen für die genannten photoemissiven Filme. Diese Studie stellt einen Fortschritt in der Entwicklung von Multialkali-Photokathoden für Hochladungs-RF-Photoinjektoranwendungen dar und liefert eine wertvolle Charakterisierung der Leistung von K-Cs-Sb-Photokathoden.

Contents

Chapter 1

Introduction

Since the dawn of human civilization, there has been an unending quest for powerful and dependable light sources. These sources have played a vital role in enhancing our comfort, ensuring safety, facilitating hunting, enabling learning, and serving numerous other purposes. As technology progressed, a multitude of light sources were developed, each with its unique properties and applications. These sources have empowered us to illuminate objects, revealing intricate details that were once unobservable. In its most fundamental sense, a light source can be defined as an emitter of electromagnetic radiation possessing specific properties. This radiation, in the form of photons, carries energy and enables us to perceive and explore our surroundings. One way to characterize a photon beam is through its brilliance, which encapsulates the intensity and quality of the emitted light. Brilliant beams hold immense potential for scientific research, technological advancements, and various practical applications. In the realm of light sources, the broadest spectrum of photon beam properties is covered by accelerator-based facilities such as synchrotron light sources and free electron lasers (FELs) [1]. In accelerator-driven light sources, electron beams moving with relativistic speed produce photon beams under the influence of external magnetic fields. The quality of these photon beams is directly influenced by the properties of the electron beams, with brightness being a key factor in determining their characteristics. Within this context, the properties of the photocathode hold significant importance as they directly impact the initial brightness of the electron beam. Photocathodes are surfaces specifically designed to convert incoming photons into

streams of electrons using the phenomenon known as the photoelectric effect. These photocathodes serve as the primary source of electrons for generating high-brightness electron beams. Their properties such as quantum efficiency, material composition, and electron emission characteristics have a direct influence on the brightness and quality of the electron beam, which, in turn, affects the quality of the final photon beam. Therefore, photocathodes serve as essential components for electron sources in free electron lasers.

Free electron lasers such as the European XFEL generate intense and ultrashort pulses of photon radiation with a dedicated pulse structure [2]. In order to achieve the desired beam quality, developing a sophisticated photocathode laser system and optimizing the photocathode setup play a significant role. Furthermore, the selection of an appropriate cathode type is a key issue to further progress in photoinjector improvement since it defines the complexity of the photocathode laser system and sets a limit in the achievable beam quality.

In the initial development days of linear accelerators, several metal cathodes, such as Cu, Ag, Mg, etc., were used. However, due to the high reflectivity and shallow escape depth, these metal photocathodes usually give a poor quantum efficiency (QE) (<1%) [3]. Moreover, to achieve the desired short radiation pulses and extract the required charge from these low QE photocathodes, photocathode laser systems typically operate in the ultraviolet (UV) wavelengths. Typically, the required UV laser light is generated by converting the third or fourth harmonic of the fundamental laser light (IR). The conversion efficiency across multiple stages is inherently low, requiring high initial laser powers. Additionally, the complexity of this laser system typically leads to increased operational costs [4, 5]. In contrast, semiconductor-based photocathodes generally offer a high QE (>1%) [3] and the capability to produce high-charge electron beams. Furthermore, some semiconductor photocathodes can operate in the visible wavelengths, eliminating the need for complex UV laser systems. These advantages in terms of efficiency, flexibility, and reduced operational complexity have made semiconductor-based photocathodes the preferred choice for generating high-brightness electron beams in modern FEL accelerators.

The Photo Injector Test facility located at the DESY Zeuthen site, known as PITZ, focuses specifically on the development and optimization of high-brightness electron

sources used for free-electron lasers (FELs), such as FLASH and European XFEL [6]. The UV-sensitive Cs_2Te photocathode is currently employed in the operation of the PITZ photoinjector system. The primary objective of this Ph.D. thesis is to explore and evaluate a novel photocathode material capable of withstanding continuous-wave (CW) operation. The objective is to address the future upgrade of the European XFEL facility, specifically aiming to achieve highest possible beam quality in order to allow lasing at shortest wavelength and continuous MHz extraction of electron bunches in the photoinjector system. These requirements pose a challenge to the laser operation in terms of average power that can hardly be realized with the current UV laser system in combination with the currently used, UV-sensitive Cs_2Te photocathodes. Multi-alkali antimonide photocathodes provide a similar high quantum efficiency to UV-sensitive Cs_2Te photocathodes while offering the benefits of photoemission sensitivity in the green wavelength and a notable reduction in the mean transverse energy of photoelectrons. Operating with cathodes in the green wavelengths eases the burden on the laser drive system, eliminating the need for a fourth harmonic of the initial infrared (IR) wavelength. Nevertheless, these alkali antimonide compounds require a better vacuum quality (i.e., 10^{-11} mbar) range than Cs_2Te (i.e., 10^{-10} mbar) to limit QE degradation [7].

These multi-alkali photocathodes have been successfully demonstrated in various DC and CW guns operating at a lower gradient (below 20 MV/m) [8,9]. The parameters, such as quantum efficiency and thermal emittance, have shown great promise. However, in order to enhance the brightness of the electron beam in next-generation CW guns for various applications, higher accelerating gradients at the cathode (30-40 MV/m) are required. As a result, our ongoing research primarily focuses on the development of multi-alkali photocathode materials and their feasibility assessment for high-gradient operation in the PITZ radio frequency (RF) gun.

The proposed study is based upon the development of multi-alkali photocathode materials such as K_2CsSb, $Na_2KSb(Cs)$, etc., which are particularly sensitive to the green wavelength of light [3]. The primary development of this photocathode material takes place in collaboration with the partner institute, Istituto Nazionale di Fisica Nucleare - Laboratorio Acceleratori e Superconduttività Applicata (INFN LASA), which is situated

in Milan. INFN LASA has a long-standing experience with the study and growth of photo emissive materials since the 90s [10], and Cs_2Te photocathodes produced at INFN LASA are regularly used at different facilities such as FLASH, European XFEL, and PITZ for years.

The objective of the research plan is to develop multi-alkali photocathodes using the sequential vapor deposition method on a molybdenum substrate. The main aim is to achieve an optimized and reproducible recipe. Subsequently, the photocathodes are tested in the PITZ RF gun, and the results in terms of QE, lifetime, and produced electron beam quality are compared to the parameters of the currently used Cs_2Te photocathodes.

Chapter 2 of this thesis provides an in-depth exploration of photocathode materials, covering their fundamental characteristics and key features and a comprehensive overview of the range of photocathode materials available. Chapter 3 provides a detailed overview of two facilities, namely PITZ and INFN-LASA, offering insights into their operations and functionalities. In Chapter 4, a detailed examination of different cathode growth recipes is presented, which were derived from both the “R&D" and “Production" systems. Additionally, this chapter includes an analysis of the experimental outcomes associated with these recipes, including the test results obtained at the PITZ RF gun. Chapter 5 presents detailed simulation results obtained through the application of Density Function Theory (DFT) to analyze the properties of alkali antimonide compounds. Chapter 6 encompasses the interpretation of experimental results through the comparison of simulation and experimental outcomes. Chapter 7 contains the conclusion and outlook for future research directions. Appendices A-H, the list of references, and the acknowledgments conclude this thesis.

Chapter 2

Overview of Photocathode Material

2.1 Electron Source

For accelerator applications, it normally needs a source of free electrons, which are usually generated by being loosened from their binding affinity with atoms. Fundamentally, there are various ways to produce electrons, but among them, thermionic emission and photoemission are considered to be effective processes for this application. Both of these processes are briefly described in the section below.

2.1.1 Thermionic Emission

The term 'thermionic' is derived from 'thermal' and 'ion'. As the name suggests, in thermionic emission, cathodes are heated to a temperature that provides electrons with sufficient energy to escape from the atoms. The liberation of electrons depends primarily not only on the external thermal energy but also on the Fermi energy level of the cathode material. The emission of current from the cathode material is usually understood by Richardson-Dushman equation [11],

$$J_0 = A_0 T^2 e^{\frac{-e\phi}{kT}} \tag{2.1}$$

Where J_0 is the emission current density(A/mm^2), A_0 is the Richardson-Dusman con-

stant, the theoretical value is 1.20173×10^6 A/m^2K^2, k is Boltzmann constant (8.6 × 10^5 eV/ K), T is the temperature of metal (K), e is the charge of the electron (1.602×10^{-19} C), and ϕ is the work function of the material (eV). From the above equation, it is articulated that to achieve higher emission, it is mainly relative to the temperature, work function of the material, and cathode surface area. For accelerator applications, the cathode must meet these requirements and also exhibit low volatility at high temperatures. Generally, Lanthanum hexaboride (LaB_6) is used as a thermionic source for these applications, with a work function ranging from 2.66 eV to 2.87 eV and an operating temperature of 1700K [12]. Additionally, Cerium hexaboride (CeB_6) is also used as a cathode material for these high-temperature applications [13].

The main advantage of this type of source is that it does not require a sophisticated and complex laser drive system for the emission process. However, there are several drawbacks, such as in the presence of back bombardment electrons, the cathode temperature and current density primarily increase, which causes an adverse effect on the cathode's lifetime. The phenomenon of back bombardment is defined as the process where the residual gas inside the RF gun is usually ionized by the extracted electron beam and typically moves backward towards the cathode, which could affect the lifetime and QE of the photocathode [14]. Also, in this process, it is hard to produce the short bunch length with an adjustable bunch structure, which is demanded from the various accelerators.

2.1.2 Photoemission

The phenomenon of the photoelectric effect was first observed by physicist Heinrich Hertz in 1887 [15, 16]. He used a spark gap to detect the presence of electromagnetic waves; later, he modified this experiment by enclosing the apparatus in a box made of different materials and found that the change in spark length varied with the materials used. Afterward, these experiments were developed into the visible spectrum by Elster and Geitel in 1889 with the use of alkali metals [17]. In 1902 Lenard observed that the kinetic energy of emitted electrons increases with respect to the frequency of radiation used [18, 19]. A few years later, in 1905, Einstein came up with a resolution, where he explained the quantum mechanical aspect of the photoelectric effect [20], for which he

got the Nobel Prize in 1921 [21]. The photoelectric effect is attributed to the photoelectrons being emitted into the vacuum level from a material when electromagnetic radiation hits the material and causes the excitation of the electrons to the conduction band. It is defined by Equation 2.2 [20],

$$E_k = h\nu - \phi \tag{2.2}$$

Where E_k is the maximum kinetic energy released by the emitted electron, h is the Planck constant (6.626×10^{-34} J.s), ν is the frequency of the light, ϕ is the work function of the material. From the equation, it is articulated that the number of emitted electrons depends on the frequency of the absorbed photons, which must be sufficient to overcome the material's work function, and on the number of photons absorbed.

A similar principle is used in the photocathode RF gun. Photocathodes are used as electron sources, which are usually unified with an RF gun. A pulsed laser light which is synchronized with the phase of the RF system, primarily hits the cathode surface and emits the photo electrons. Immediately following their emission, in order to control the charge distribution and bunch length, these photoelectrons are accelerated by a high gradient electromagnetic field within the RF gun.

Photoemission provides an efficient alternative source in terms of beam quality and emittance compared to thermionic emission [22]. There are various types of photocathodes available, but among them, K_2CsSb, Cs_2Te, Cs_3Sb, and GaAs are quite popular due to their acceptable lifetime and intrinsic emittance. However, there is a window available for further development, particularly a better understanding of the physical properties of these photocathodes is required in order to improve the electron emission for high average flux FEL and high current collider applications.

2.2 Photocathode Properties

The inherent properties of photocathodes usually play a vital role relating to the performance of photoinjectors [23]. Some of the crucial properties, such as quantum efficiency and its spectral response, intrinsic emittance, response time, mean transverse energy, and lifetime, are considered to be most relevant in order to improve the beam quality and

function of the photoinjector system. The selection of the photocathode usually depends upon the specific requirement and application of the electron beam. Some of the above-described properties are abbreviated in this section.

2.2.1 Quantum Efficiency

The Quantum efficiency (QE) of a photocathode can be defined as the ratio of the number of emitted electrons to the number of incident photons as defined in Equation 2.3,

$$QE = \frac{\text{number of emitted electrons}}{\text{number of incident photons}} \tag{2.3}$$

In general, the quantum efficiency is a very significant parameter due to it includes many characteristics of photocathode material in one number, such as optical characteristics (reflectance and absorption), electron transport characteristics (scattering effect and mean free path), and surface energy barrier characteristics (work function, etc.). In practice, the actual QE is defined as shown in Equation 2.4,

$$QE = \frac{I_{\text{net}} hc}{\lambda e P_{\text{net}}} \tag{2.4}$$

Where I_{net} is the net incident photocurrent (A) (I_{net} = $I_{\text{totalincident}}$ - I_{dark}), h is the Plank's constant (6.626×10^{-34} J.s), c is the speed of light (2.998×10^{8} m/s), λ is the wavelength of incident light (nm), e is the electron charge (1.6×10^{-19} C), and P_{net} represents the net incident power applied on the surface (W) (P_{net} = $P_{\text{totalincident}}$ - $P_{\text{background}}$). By incorporating the values of h, c, and e, Equation 2.4 can be simplified as follows:

$$QE = \frac{1240 \times I_{\text{net}}}{\lambda P_{\text{net}}} \tag{2.5}$$

The QE usually depends on the photocathode material. The QE of metal photocathodes typically remains lower in comparison to that of semiconductor-based photocathodes. This is due to the better electron transport mechanism in the semiconductor material, as will be discussed later in this section (Section 2.3.1.1).

2.2.2 Spectral Response

The spectral response of photocathode material is defined as the sensitivity of the photocathode material at a different wavelength. In other words, it can be described as the measured QE of the photocathode material as a function of the incident photon's wavelength. The spectral response curve of photocathode material usually plays a very significant role since it provides much vital information about the material, such as work function, quantum efficiency, band structure, etc. Additionally, the spectral response can reveal important information about the aging behavior of a sample, including surface contamination, segregation, or oxidation.

The threshold of the spectral response curve at the short wavelength side is generally called the short wavelength limit, and it is usually determined by the optical properties of the viewport material used in the deposition system. Materials such as sapphire, N-BK7, quartz, etc. are commonly employed as viewports and can impose this limit due to their inherent optical characteristics. Likewise, the threshold of the spectral response curve at the longer wavelength side is called cut-off. This cut-off is specific to the photocathode material and can provide an estimate of the material's work function. By analyzing the position of the cut-off, one can gain insights into the energy required to liberate electrons from the material's surface, which is directly related to the work function of the photocathode material. The wide range between short and longer wavelengths is called the spectral response range.

2.2.3 Spectral Reflectivity

Reflectivity is a quantitative measure of how much light or other electromagnetic radiation is reflected by a surface. It is defined as the ratio of the reflected power to the incident power on a surface, as shown in Equation 2.6 [24],

$$R(\%) = \frac{R_{\text{net}}}{P_{\text{net}}} \times 100 \tag{2.6}$$

where R_{net} represents net reflected power by the surface ($R_{\text{net}} = R_{\text{total reflected}} - R_{\text{background}}$) and P_{net} represents net incident power applied on the surface ($P_{\text{net}} = P_{\text{total incident}} - P_{\text{background}}$).

Spectral reflectivity is defined as the reflectivity of the photocathode surface across different wavelengths. In essence, it explains how the reflectivity of the photocathode material varies as a function of the wavelength of the incident photons. Spectral reflectivity provides critical insights into the electronic and optical characteristics of photocathode materials. It offers crucial insights into how light interacts with the material, revealing valuable details about its energy band structure, electronic transitions, and optical characteristics.

2.2.4 Intrinsic Emittance

Emittance is the property of a particle beam that characterizes its phase space volume and, consequently, its beam quality; it is the area or volume in the phase space of the particles [25]. An electron beam is defined as a collection of emitted electrons that are traveling together with similar energy and direction, and its motion can be defined by six degrees of freedom in space, namely the position (x,y,z) and momentum (p_x, p_y, p_z) in cartesian coordinate. As the magnitude of emittance could be reduced, the overall beam quality will also be improved since it follows the relationship between the beam's brightness and emittance, as shown in Equation 2.7 [26].

$$B = \frac{N_e}{\varepsilon_{n_x}\varepsilon_{n_y}\varepsilon_{n_z}} \tag{2.7}$$

Where B is the brightness of the beam, N_e is the number of electrons per bunch, ε_{n_x},ε_{n_y},ε_{n_z} is the normalized emittance in the x, y, and z planes. Normalized emittance is an important measure as it quantifies the spread of electron beam momenta and positions in phase space, factoring in relativistic adjustments [3].

Low emittance refers to a reduced beam size in phase space in which all the particles have the same momentum and position, which is essential for an efficient accelerator operation. In practice, the total emittance is determined by a combination of components of RF-induced emittance (ε_{rf}), space charge emittance (ε_{sc}), and thermal emittance (ε_{th}) as shown in Equation 2.8 [27].

$$\varepsilon_{total} = \sqrt{{\varepsilon_{rf}}^2 + {\varepsilon_{sc}}^2 + {\varepsilon_{th}}^2} \tag{2.8}$$

The RF-induced emittance (ε_{rf}) predominantly originates from the radio frequency fields within the RF gun, whereas space-charge-induced emittance (ε_{sc}) arises from the repulsive interactions among electrons in the beam [28]. Thermal emittance (ε_{th}) arises from the intrinsic motion of excited electrons within the cathode material, contributing to the spread of the initial electron velocities as they leave the cathode and influencing the overall beam quality and emittance [28]. Thermal emittance is commonly attributed to intrinsic emittance and usually determines the lower limit of normalized emittance of the electron beam in the accelerator system [6]. The thermal emittance can be determined by Equation 2.9 [29].

$$\varepsilon_{th} = \sigma_x \sqrt{\frac{h\nu - \phi}{3mc^2}} \tag{2.9}$$

Where σ_x represents the laser spot size, $h\nu$ the photon energy, ϕ the work function of the material, and mc^2 the electron rest mass. A thorough discussion regarding thermal emittance can be found in the upcoming section (2.3.1.4) of this chapter.

2.2.5 Response Time

Response time is the time taken between absorption of the light pulse and photoemission. The response time of a photocathode material mainly depends on both photon absorption length and the mean free path of the excited electrons [23]. Therefore, the response time may vary with respect to photon energy for a particular material. Usually, metal-based photocathodes have a very short response time (order of sub-picosecond/femtosecond) because the mean free path of excited electrons is relatively short compared to that in semiconductor materials [3]. In metals, the generation of electrons primarily occurs near the surface of the cathode. As a result, the excited electrons do not have to travel far before being emitted. This short distance allows for rapid electron emission, contributing to the short response time of metal-based photocathodes.

On the other hand, in semiconductor photocathodes, the transport of excited electrons

to the surface involves electron-phonon scattering. This scattering process introduces additional interactions with lattice vibrations (phonons), leading to a longer response time compared to metals. The electron-phonon scattering delays the emission process, resulting in response times typically on the order of picoseconds for semiconductor photocathodes [30].

The response time is a significant parameter in order to produce a very short electron pulse and for the temporal shaping of laser pulses to achieve a high-brightness electron beams.

2.2.6 Lifetime

Lifetime can be defined as the time taken for the QE of a photocathode to reach $\frac{1}{e}$ of its initial value [31]. In other words, it can be defined as how long the QE of a photocathode outstays. It can be attributed to a mathematical term, as shown in Equation 2.10 [32].

$$QE(t) = QE(t_0)\exp\left(-\frac{t}{\tau}\right) \tag{2.10}$$

Where $QE(t_0)$ represents the initial quantum efficiency at time t_0. The term $exp(\frac{-t}{\tau})$ represents the decay factor, where τ is the characteristic decay time.

Several factors, such as vacuum conditions, partial pressure of contaminating gases (i.e., oxidizers), cathode heating, possible surface coating evaporation, etc., affect the lifetime of photocathodes. Usually, if the vacuum condition in the electron gun is poor, then the photocathode surface may be contaminated by the residual gas inside the gun, which can alleviate the emissivity of the cathode. Apart from that, during operation, a subsequent back bombardment in the electron gun can also do surface damage to the photocathode. However, the necessary lifetime will certainly depend on applications, and a longer period will be better in any case.

2.2.7 Dark Current

Dark current is another important parameter for a photocathode. The field-emitted electrons are the significant source of the dark current in RF guns [33,34], which parasitically

absorb radio frequency energy (in RF cavities) and cause noise in the instrument, radiation issue, etc. The origin of the dark current basically derived from mainly two sources, such as gun body or gun cavity, and from the photocathode itself [35]. The primary part of the source of dark current from the cathode could vary from photocathode to photocathode. This effect can be reduced by applying surface cleaning and polishing techniques to the photocathode to reduce surface roughness and improve cleanliness [36, 37].

2.3 Photocathode Theory

When studying solids, it is often useful to classify them into different groups based on their electrical conductivity, which leads to the categorization of conductors, insulators, and semiconductors. Band theory is a framework in solid-state physics that helps to understand and explain the differences between metals, semiconductors, and insulators. Therefore it is briefly summarized in this section.

In a metallic crystal, the outermost electrons of each atom are able to move freely throughout the entire crystal. This creates a "sea" of delocalized electrons that surround the positively charged atomic nuclei in a lattice structure [38]. The free electron model is a simplified theoretical model that assumes that the electrons in a metal are completely free to move around in the presence of an external electric field without any interactions with the ionic lattice of the metal. However, the nearly free electron model considers this interaction between the electrons and the lattice. In this theory, the energy levels of the electrons in a metal are described by energy bands, which result from the periodic potential created by the regular arrangement of metal ions in the crystal lattice. Within each energy band, the electrons are delocalized and can move freely throughout the crystal. The dispersion relation for a free electron relates the energy E of an electron to its momentum k can be defined as [38],

$$E(k) = \frac{\hbar^2 k^2}{2m} = \frac{p^2}{2m} \tag{2.11}$$

Where $\hbar$ is the reduced plank's constant, k is the wave vector which equals to $\frac{2\pi}{\lambda}$, and m is the mass of the electron. The form of relationship between E and k, as mentioned in

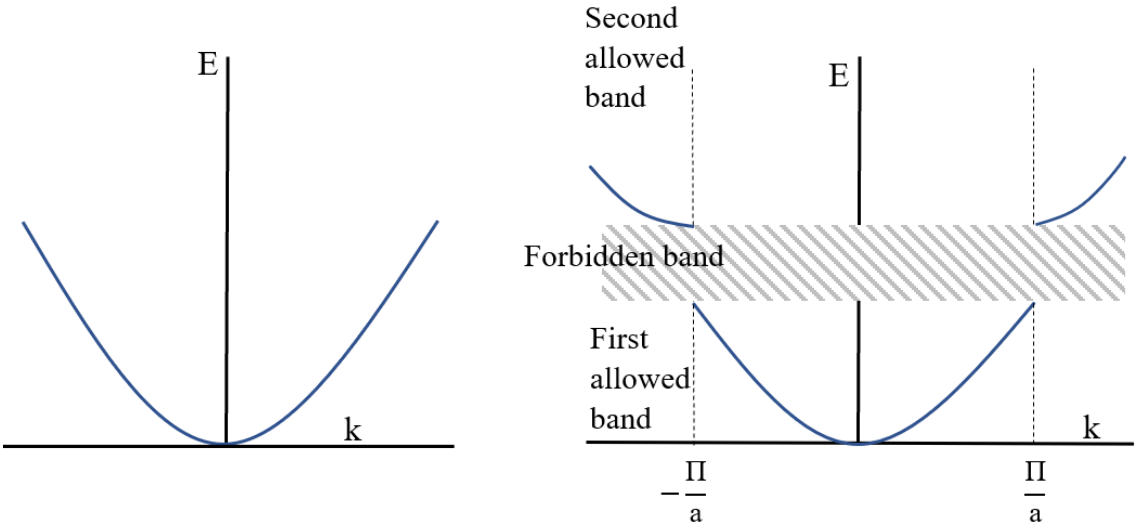

Figure 2.1: (a) Illustrates Energy (E) Vs. Wave vector (k) for a free electron, (b) illustrates a plot of Energy (E) Vs. Wave vector (k) for an electron in a monoatomic linear lattice of lattice constant a [39].

Equation 2.11, is parabolic. The parabolic form arises due to the quadratic dependence of energy on momentum, as it is shown in Fig. 2.1.

For a free electron in a perfectly periodic crystal lattice, there are no restrictions on the allowed values of the electron's momentum, k. Therefore, the energy of the electron, E(k), is continuous over all values of k, as illustrated in Fig. 2.1a [39]. However, if an electron is confined within a potential well, the electron's allowed momentum values, k, are restricted by the boundary conditions of the well. Specifically, the electron's wave function must go to zero at the edges of the well (shown in Fig. 2.1b), which leads to the condition that k must be equal to an integer multiple of π divided by the length of the well, L. That is, $k = n\pi/L$, where n is an integer.

The shaded line in Fig. 2.1b shows that there are energy values that electrons in the solid can not occupy, usually called forbidden bands or popularly known as "energy gap". The region representing allowed states in Fig. 2.1b is generally known as energy bands.

Although the free electron model leads us to understand the solid in terms of energy bands, it does not much enlighten the wavefunction of the electrons. The tight-binding

model is a theoretical framework that provides insight into what happens when a large number of atoms (initially at an infinite distance apart) come closer together to form a solid. This can be further understood, for example, in the physical vapor deposition method (described in the following chapters), as the vaporized gas starts to condense onto a substrate to form a thin layer of solid material. In the condensation process, as the atoms get closer to each other, the wavefunction of their electrons starts to overlap. Consequently, the discrete levels of each isolated atom split into a vast number of energy levels forming a band of levels [40]. Usually, these energy bands are more closely spaced and considered a continuum of energy levels, as shown in Fig. 2.2. The size of these bands may differ, and the number of states within each band is generally equal to the number of atoms forming the solid multiplied by the number of energy levels in the corresponding original subshell of an isolated atom [40].

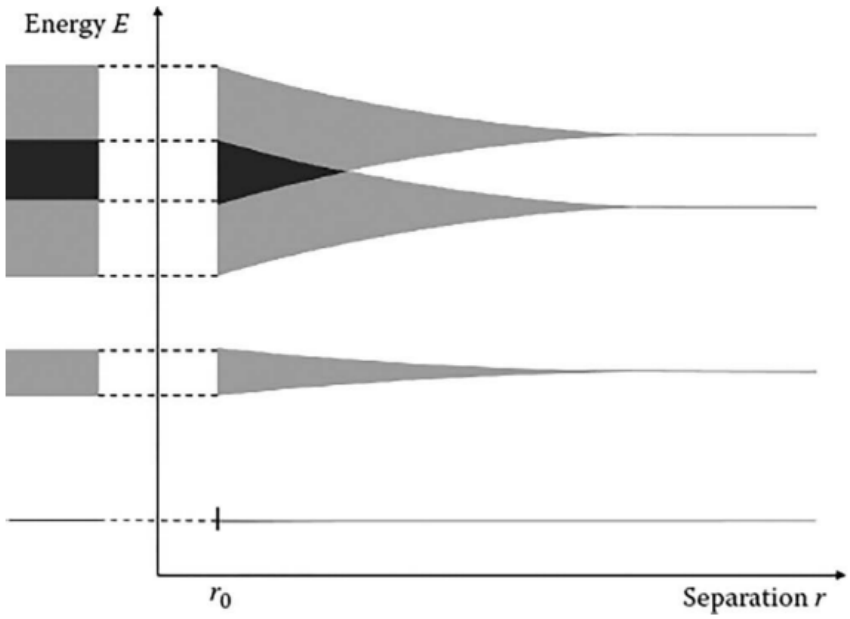

Figure 2.2: The right part of the diagram shows that the electron's energy is separate when the atoms are a long distance apart. A solid forms when the atoms are a distance r_0 apart and the band structure of the solid is shown on the left side of the plot [40].

The wave functions of electrons in the outermost electron shells (also known as valance shells) usually can overlap more with neighboring atoms than the electrons closer

to the nucleus. This is because the wave functions of electrons closer to the nucleus are more localized and tightly bound to their respective atoms. The electrons in the outermost shell, called the valence shell, have higher energy levels and are more loosely tied to the nucleus. This results in the density of states being broader for the outer bands compared to those closer to the nucleus. In the case of metal, any electrons within this valence shell are usually no longer bound to their atoms but are relatively free to move throughout the solid and can participate in conduction. As a result, the outermost energy bands of the individual atoms merge into a continuous band called the valence band, as shown in Fig. 2.3. The valence electrons from each atom in a metal contribute to the formation of the conduction band. The conduction band is a range of energy levels that corresponds to the available energy states for the valence electrons to occupy when they gain sufficient energy to move away from their parent atoms. In metals, the valence band is either not fully occupied with electrons or the filled valence band overlaps with the empty conduction band. In general, both states can occur simultaneously, and the electrons can therefore move inside the partially filled valence band or inside the two overlapping bands. Which enables metals to conduct electricity efficiently. In metal, there is no gap between the valance and conduction bands.

Whereas in semiconductors, the valence and conduction bands are separated by a relatively small energy gap called the “band gap". At low temperatures, the valence band is usually fully occupied, and the conduction band is empty. However, with increased temperature or other external influences, electrons can acquire enough energy to jump across the band gap and move into the conduction band. This process, called excitation, allows semiconductors to conduct electricity.

In the insulator case, the band gap is usually very large compared to the semiconductors. The valence band is fully occupied, and the conduction band is significantly higher in energy, making it difficult for electrons to bridge the gap and enter the conduction band. As a result, insulators have very limited electrical conductivity. Fig. 2.4 shows the simplified version of the energy band structure of metal, semiconductor, and insulator.

Photocathode materials usually fall into two categories, including metals and semiconductors photocathode. Spicer’s three-step model of photoemission is generally used

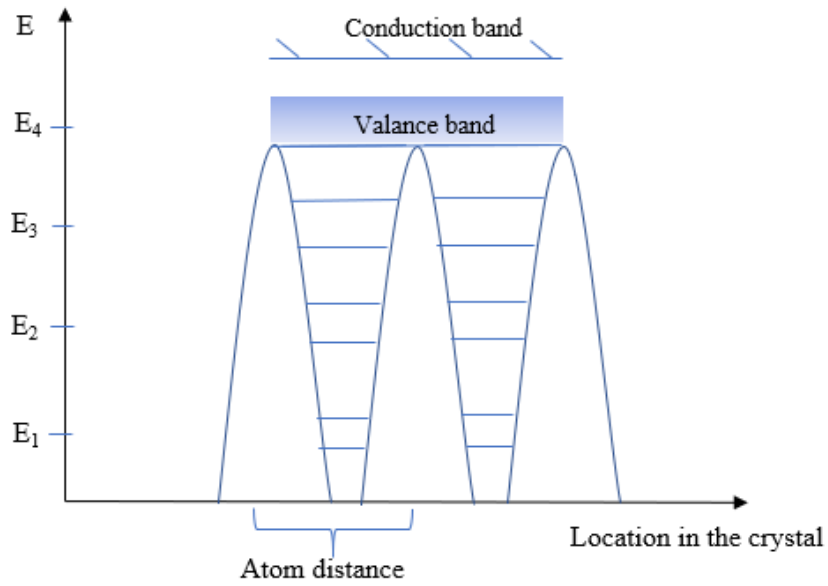

Figure 2.3: Energy band diagram of the atoms which are interdependent with other atoms.

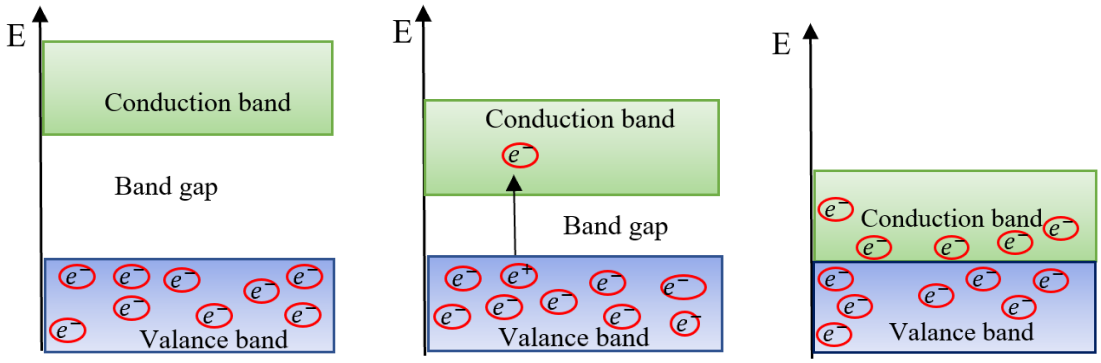

Figure 2.4: Illustrates energy band diagram for (a) Insulator, (b) Semiconductor, and (c) Metal

to understand the photo emission mechanism of metal and semiconductor-based photocathodes [41]. The model was developed in 1950, and it describes the photo-emission process by relying on material work function, electron scattering lengths, and dielectric function variables for fitting experimental data. The following part of this section presents

a detailed explanation of the photoemission mechanism using the three-step photoemission model.

2.3.1 Photoemission Model

2.3.1.1 Three-step Photoemission

A simple three-step photoemission model was first proposed by William Spicer to describe the photoemission process in both metal and semiconductor materials [41]. The central assumption of this model is that the photoemission process consists of three main independent steps: (i) excitation of an electron after photon absorption, (ii) transport of the excited electrons to the surface, and (iii) the emission of the electron to vacuum. The probability for each step is considered in this section below, as described by D.Dowell [3]. Figure 2.5 illustrates the three steps involved in the photoemission process of semiconductor photocathode materials.

(i) Absorption and Excitation

The first step of this model accounts for two processes. Firstly, the probability of incident light that is transmitted through the material is taken into account. The probability transmission $T(\nu)$ depends upon the material's reflectivity $R(\nu)$ and can be determined by using Equation 2.12.

$$T(\nu) = 1 - R(\nu) \tag{2.12}$$

Once the photon is absorbed, then in the second process, the probability of exciting an electron from the initial state energy, E_0, to an excited state with energy, $E = E_0 + h\nu$, is considered. Step one is primarily the same for both metallic and semiconductor photocathodes.

(ii) Transport

Step 2 of this model calculates the probability of the photoexcited electron that is transported to the material's surface while retaining sufficient energy to escape into the vacuum. During transportation, the electron encounters different scattering processes.

Here the photon absorption length, λ_{ph}, is compared to the electron scattering length, λ_e, to determine the fraction of electrons lost that is due to the scattering events. The electron scattering length is a measure of electron travel through the material before it collides with another electron. Whereas the photon absorption length is a measure of how far a photon can travel through the material before it is absorbed by an electron.

In the case of metal, the transportation process is mainly dictated by the electron-electron (e-e) scattering events, and a single scattering phenomenon is considered to be a loss mechanism. The electron-phonon (e-p) scattering does not play a significant role in changing an electron's energy distribution in the case of metal. Whereas for semiconductor cases, electron-electron (e-e) scattering is commonly forbidden, and mostly electron-phonon (e-p) scattering dominates in this step.

In semiconductors, band gaps are crucial as they prevent unproductive absorption of light by not allowing any electrons to be excited into the bandgap, which is caused by the absence of available states for the electron to occupy. Only photons with energies greater than bandgap can be absorbed and create free charge carriers. The lack of available electronic states in the bandgap can significantly impact electron-electron scattering processes. If the final energy state of the electron falls into the bandgap, then there are no available states for the electron to occupy, and the scattering process is forbidden. This leads to a suppression of electron-electron scattering in the bandgap region, which can have significant consequences for the transport properties of the semiconductor material. As a consequence, the electron scattering length (λ_e) could be larger than the photon absorption length (λ_{ph}) and all the photo-excited electrons could reach the material's surface without experiencing significant energy loss. This makes the QE of the semiconductor larger than the metal.

(iii) Electron Escape

In step 3, the objective is to calculate the probability that the photoexcited electron will move in the correct direction to have enough energy to overcome the potential barrier and escape from the material's surface. In order to escape, the direction of motion of a photoexcited electron must exist within a cone, which is derived from the conservation of energy and momentum in the photoemission process and can be defined as [29],

$$\cos\theta_{max} = \sqrt{\frac{E_f + \phi}{E + h\nu}} \tag{2.13}$$

Equation 2.13 elucidates the opening angle of the escape cone, where θ_{max} represents the maximum angle of the escape cone containing the trajectories of all the electrons, E_f is the fermi energy level, ϕ represents the work function, and E represents the electron's energy. In Equation 2.13, the term, $E + h\nu$, represents the total energy of the electrons (after absorbing a photon), and the term, $E_f + \phi$, represents the energy of the vacuum state [29]. In order to escape, the photo-excited electron that approaches the material's surface should have enough momentum normal to the barrier, and this leads to the maximum escape angle by which the photo-excited electrons (with energy E) can escape from the surface, as defined in Equation 2.13. In general, if the electron's energy is very high, it will have a wider emission cone, while if the energy is low, then a narrow escape cone is expected. Similarly, if the material's work function is high, then the escape cone will be narrower; while the work function is low, the emission cone will be wider. Usually, only a small fraction of the photoexcited electrons whose trajectory falls within the cone will actually escape from the material's surface.

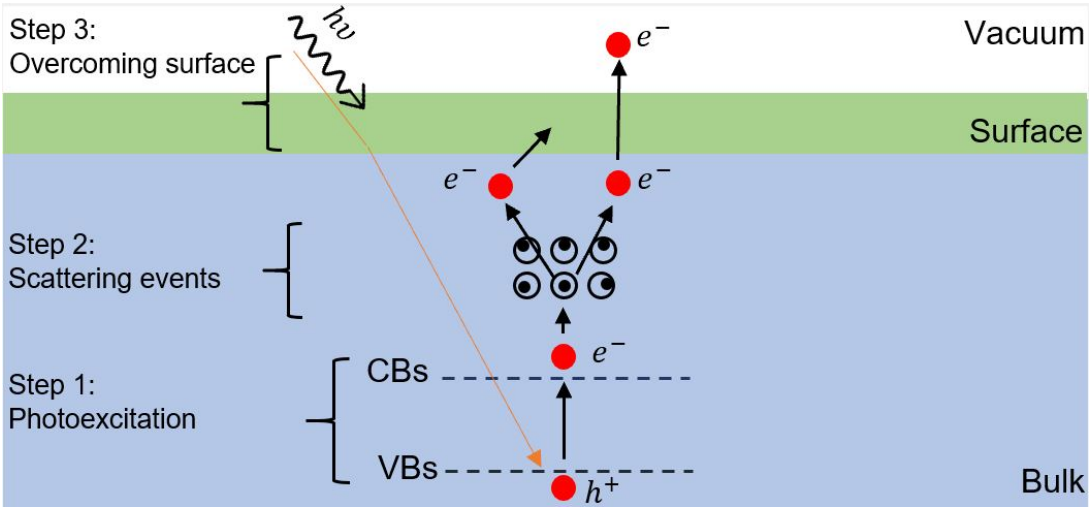

Figure 2.5: Schematic overview of the photoemission process of semiconductor photocathodes. The main physical mechanism that happened in bulk (bottom, blue), on the surface (middle, green), and in the vacuum (top, white) are sketched in the boxes. The three steps of photoemission are also illustrated.

2.3.1.2 Yield and Quantum Efficiency in the Three-step Model

In the first step of the three-step model, it is considered that the photo-excitation process is usually governed by the absorption coefficient, $\alpha(h\nu)$, of the material. The intensity of light, $I(x,h\nu)$, inside the material at a distance x from the surface is given by [41],

$$I(x,h\nu) = I_0(h\nu)[1-R(h\nu)]e^{-\alpha(h\nu)x} \tag{2.14}$$

Where $I_0(h\nu)$, represents the intensity of incident light of photon energy $h\nu$, $R(h\nu)$ is the reflectivity of light from the solid surface, and $\alpha(h\nu)$ represents the absorption coefficient of the material. The amount of absorbed intensity of light within a thin slab of a thickness of dx (as shown in Fig. 2.6a) can be expressed as follows,

$$dI(x) = (1-R)I_0 e^{-\alpha(h\nu)x}\alpha dx \tag{2.15}$$

Once the electron gets excited by absorbing the photon, then in the second and third steps, some of the photoexcited electrons will travel to the material's surface and escape to the vacuum. The contribution of $dI(x)$ to the photoemission yield from excitation is given by,

$$dI(x) = P_{O\alpha}(h\nu,x,dx)P_T(h\nu,x)P_E(h\nu) \tag{2.16}$$

Where $P_{O\alpha}(h\nu,x,dx)$, represents the probability of exciting electrons in the slab between x and $x+dx$ above vacuum level, is given by

$$P_{O\alpha}(h\nu,x,dx) = \alpha_{PE}(h\nu)I(x)dx = \alpha_{PE}(h\nu)I_0(1-R)e^{-\alpha x}dx \tag{2.17}$$

For this model, it uses the two components of the absorption coefficient, i.e., $\alpha_T = \alpha_{PE} + \alpha_n$, where α_T is the total absorption coefficient, α_{PE} refers to the part of absorption where the electrons are excited above the vacuum level, and α_n refers to the part of absorption that doesn't contribute to the yield (see [41]). Since α_{PE} accounts for the absorption where electrons are excited above the vacuum level, it is used in Equation 2.17.

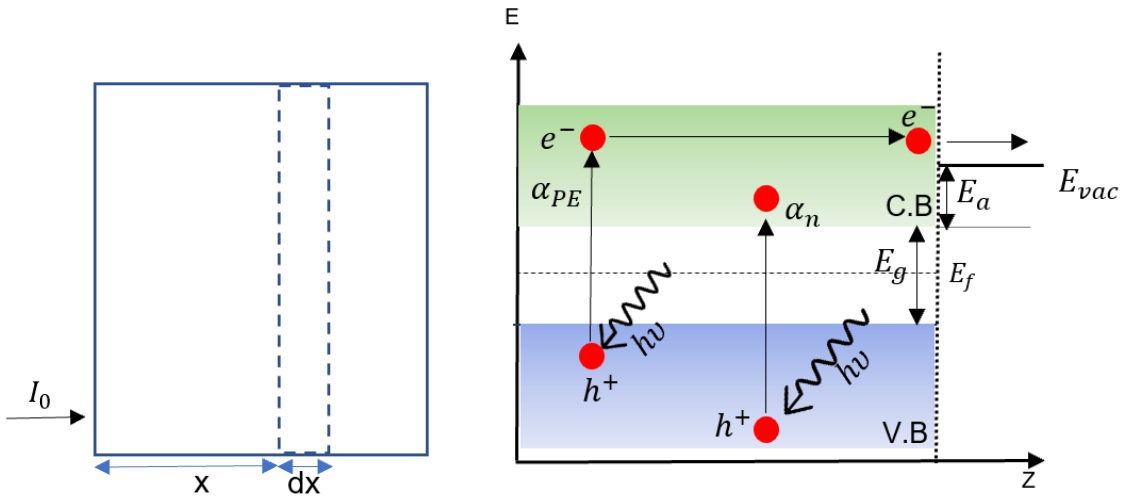

(a) (b)

Figure 2.6: (a) illustrates the slab of a thickness of dx that contributes to the photoemission yield from the excitation of electrons, and (b) illustrates the energy levels assumed in Spicer's three-step model. α_{PE} represents the part of absorption where the electrons are excited above the vacuum level and have a possibility to escape. α_n represents the part of absorption that doesn't contribute to the yield. E_g represents the band gap of the material, and E_a represents the electron affinity of the material. The figure in plot b represents an idealized case that ignores the shape of energy bands as determined by the density of states. Both figures are adapted from reference [41].

In Equation 2.16, $P_T(h\nu,x)$ refers to the probability that electrons travel to the material's surface (travel distance x, as shown in Fig. 2.6a) without undergoing electron-electron scattering that would reduce their energy below the vacuum level. $P_E(h\nu)$ represents the probability that the electron's momentum vector points in the right direction, specifically having a component normal to the surface that is large enough to overcome the surface barrier.

Because the probability of scattering is proportional to the electron's traveled distance, so P_T can be expressed as follows,

$$P_T(x,h\nu) = e^{-\frac{x}{L(h\nu)}} \tag{2.18}$$

Where $L(h\nu)$ is the average electron-electron scattering length. Then by putting the value of $P_{O\alpha}(h\nu,x,dx)$ and $P_T(x,h\nu)$, Equation 2.16 can be written as,

$$dI(x) = I_0(1-R)\alpha_{PE}e^{-\alpha x}e^{-\frac{x}{L}}P_E(h\nu)dx \tag{2.19}$$

Then the total electron yield $I(h\nu)$ is given by,

$$I(h\nu) = \int_0^\infty dI(x) \tag{2.20}$$

$$I(h\nu) = I_0(1-R)\frac{\alpha_{PE}}{\alpha+\frac{1}{L}}P_E(h\nu) \tag{2.21}$$

The Quantum efficiency (QE) can be defined as the number of electrons released per absorbed photon and can be expressed as follows [41],

$$QE(h\nu) = \frac{I(h\nu)}{I_0} = (1-R)\frac{\frac{\alpha_{PE}}{\alpha}P_E}{1+\frac{L_a}{L}} \tag{2.22}$$

where L_a is the absorption length and is defined as $L_a(h\nu) = \frac{1}{\alpha(h\nu)}$, $\frac{L_a}{L}$ is the ratio of the absorption length to the electron scattering length, $\frac{\alpha_{PE}}{\alpha}$ is the ratio of electrons that get excited above the vacuum level. From Equation 2.22, it can be observed that two terms, i.e., $\frac{L_a}{L}$ and $\frac{\alpha_{PE}}{\alpha}$, can influence the QE of a material. The ratio $\frac{\alpha_{PE}}{\alpha}$ increases monotonically as the excitation energy $h\nu$ increases and can be maximized by lowering the vacuum level towards the conduction band minimum (i.e., reducing the electron affinity E_a, see Fig. 2.6b). Material that exhibits a higher QE often the $\frac{\alpha_{PE}}{\alpha}$ value lies between 0.1 and 1, and for negative electron affinity photocathodes, this value could be close to 1.

In the denominator of Equation 2.22, the $\frac{L_a}{L}$ ratio defines the spatial region where photoexcited electrons may contribute to the photoemission yield. If L_a is larger compared to the escape distance, then few electrons will escape from the material's surface, and as a consequence, the QE of the photocathode will be low. The electron scattering length can be as low as 0.1 nm for metal due to pronounced electron-electron scattering. Whereas in semiconductors, the $\frac{L_a}{L}$ ratio could be close to unity in the visible or infrared spectrum. This makes the QE of the semiconductor larger compared to the metal. The value P_E usually depends upon the incident photon energy $(h\nu)$ and increases monotonically with $h\nu$. Typically, the value of P_E in semiconductors is around 0.5 while metals tend to have

0.1 [41].

When electron-electron scattering is pronounced, the direction of the momentum vector of the excited electron is crucial. When an excited electron interacts with other electrons through electron-electron scattering, its energy may be reduced to below the vacuum level. However, only those electrons that reach the surface without scattering can be emitted. As discussed in the Section 2.3.1.1, to escape, a photoexcited electron's direction of motion should exist within a cone, and in the electron-electron scattering-dominated scenarios, a narrow escape cone is expected. By considering the dependency of opening angle (θ) and α_{PE} on the electron's energy before emission, we can get a more quantitative expression for QE. The term $\frac{\alpha_{PE}}{\alpha}$ in Equation 2.22 can be determined by integrating over the energy range in the valance band, which contributes to the photoemission yield. Then the term $\frac{\alpha_{PE}}{\alpha}P_E$ in Equation 2.22 can be determined (for metal) as [29],

$$\frac{\alpha_{PE}}{\alpha}P_E = \frac{\int_{E_f+\phi-h\nu}^{E_f}\int_0^{\theta_{max}} d\theta dE}{\int_{E_f-h\nu}^{E}\int_0^{\pi} d\theta dE} \tag{2.23}$$

$$\frac{\alpha_{PE}}{\alpha}P_E = \frac{\int_{E_f+\phi-h\nu}^{E_f} dE \int_{\sqrt{\frac{(E_f+\phi)}{(E+h\nu)}}}^{1} d(\cos\theta)}{\int_{E_f-h\nu}^{E_f} dE \int_{-1}^{1} d(\cos\theta)} \tag{2.24}$$

$$\frac{\alpha_{PE}}{\alpha}P_E = \frac{E_f+h\nu}{2h\nu}\left[1+\frac{E_f+\phi}{E_f+h\nu}-2\sqrt{\frac{E_f+\phi}{E_f+h\nu}}\right] \tag{2.25}$$

$$\frac{\alpha_{PE}}{\alpha}P_E = \frac{E_f+h\nu}{2h\nu}\left[1-\sqrt{\frac{E_f+\phi}{E_f+h\nu}}\right]^2 \tag{2.26}$$

By putting the value $\frac{\alpha_{PE}}{\alpha}$ in Equation 2.22, The expression for QE for metal can be written as [29],

$$QE_{metal} = \frac{(1-R)}{1+\frac{L_a}{L}}\frac{E_f+h\nu}{2h\nu}\left[1-\sqrt{\frac{E_f+\phi}{E_f+h\nu}}\right]^2 \tag{2.27}$$

In the semiconductor case, the electron-electron scattering process is suppressed mainly in the "magic window energy" level (discussed in the following section); therefore, dur-

ing the emission process, the electron-phonon scattering primarily dominated. The energy loss due to electron-phonon scattering is less compared to the electron-electron scattering process, resulting in a higher probability of electron emission. Therefore, the probability of emission,i.e., P_E, may be approximated by a step function for efficient semiconductor photocathodes [41]. In that case, Equation 2.27 can be written as,

$$QE_{semiconductor} = \frac{1-R}{1+\frac{L_a}{L}} \frac{(h\nu - E_g - E_a)}{h\nu} \tag{2.28}$$

The term $(h\nu - E_g - E_a)$ in Equation 2.28 represents the excess energy available for the emitted electron, and the QE is proportional to this term.

2.3.1.3 Electron Scattering Mechanism and its Effect on Photoemission Efficiency

In general, as described above, there are two types of inelastic scattering mechanisms, i.e., (1) electron-electron and (2) electron-phonon (lattice) scattering, that can affect the photoemission efficiency. As noted in the previous section, the energy loss per collision is generally significantly lower in electron-phonon scattering compared to electron-electron scattering. These scattering events can alter the direction of electrons during photoemission. In the electron-phonon scattering case, it redirects the disoriented electrons in such a way (i.e., perpendicular to the surface) that they can escape from the material's surface [41]. This effect will only be helpful in increasing the photoemission efficiency if the electron-electron scattering can be neglected.

As shown in Fig. 2.7, primary electrons can lose significant energy in a metal through single electron-electron scattering events. During these events, a primary electron may transfer some of its energy to other electrons, thereby creating secondary electrons. Near the threshold, these secondary electrons are subject to strong Coulombic interactions with other electrons in the material. This interaction can cause the secondary electrons to lose energy rapidly, preventing them from escaping the material's surface. Consequently, neither the primary nor the secondary electrons are likely to escape from the material's surface, resulting in a typically short escape depth in metals.

In the semiconductor case, the electron-electron scattering process is suppressed mainly

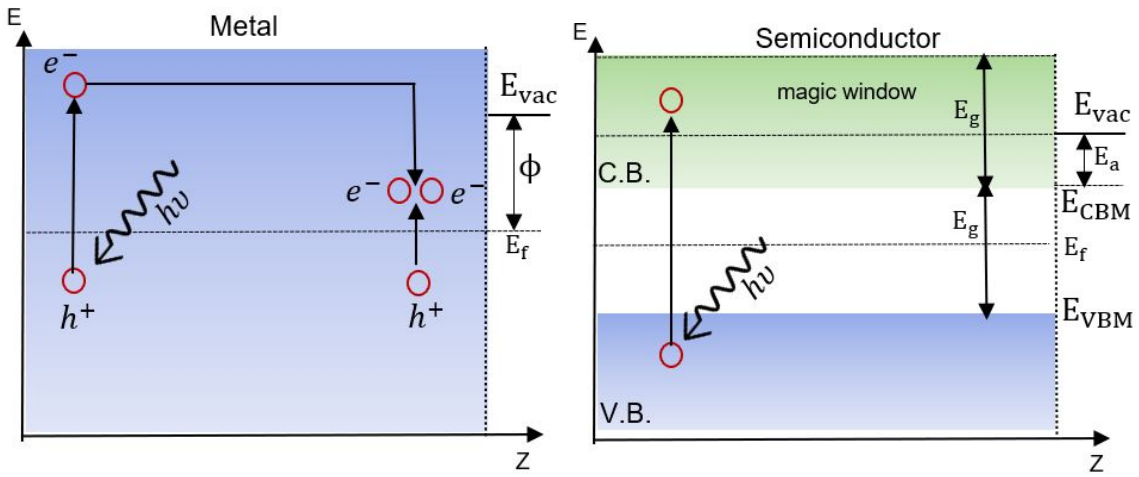

Figure 2.7: illustrates the comparison of the electron-electron scattering mechanism between (a) metal and (b) semiconductor. V.B. and C.B. refer to the valance band and conduction band, respectively. Adapted from reference [41].

in the “magic window energy" level (E_{MW}), where $E_{vac} < E_{MW} < E_{VBM} + 2E_g$ [41]. In the “magic window" energy range of a semiconductor, the energy of the excited electron is typically too low to excite an electron from the valence band to the conduction band through electron-electron scattering. This is because the energy of the excited electron in the “magic window" is close to the bandgap energy, and the energy required to excite an electron from the valence band to the conduction band is typically greater than the bandgap energy. As a consequence, in the “magic window" energy range, there are typically no available states for scattering to occur, and the energy of the excited electron is too low to raise a scattering partner from the valence band to the conduction band. This contributes to the suppression of electron-electron scattering in this energy range and allows the excited electron to travel further in the conduction band without losing energy through scattering events.

From the above discussion, we understand that the requirement for an efficient photocathode, the P_E and $\frac{\alpha_{PE}}{\alpha}$ should be large, whereas the value of $\frac{L_a}{L}$ should be small. In semiconductors, this can be achieved if the electron affinity (E_a) is smaller than the band gap (E_g). This is because if electron affinity is smaller than the band gap, then in that case,

the electron has a higher probability of escaping into the vacuum. On the other hand, if the electron affinity is greater than the bandgap, then the electron raised to the conduction band either has sufficient energy to escape to the vacuum or will raise a second electron from the valance band to the conduction band. In the second case, as we know, neither of the electrons has sufficient energy to escape into the vacuum. Therefore, semiconductors having E_g:E_a ratio greater than unity tend to have a higher quantum yield compared to those semiconductor photocathodes having E_g<E_a.

2.3.1.4 Transverse Emittance in the Three-step Model

The rms transverse emittance (ε_x) of a beam of charged particles can be expressed in terms of the transverse momentum (p_x) and position (x) distributions of the particles as [3],

$$\varepsilon_x = \sqrt{\langle x^2 \rangle \langle x'^2 \rangle - \langle xx' \rangle^2}, \quad \text{where } x' = \frac{dx}{dz} = \frac{p_x}{p_z} \tag{2.29}$$

The term $\langle x'^2 \rangle$ and $\langle x^2 \rangle$ represent the mean square of the momentum and position distribution, respectively, and $\langle xx' \rangle^2$ represents the correlation between the momentum and position distribution. The first term in Equation 2.29, i.e., $\langle x^2 \rangle \langle x'^2 \rangle$, generally gives information regarding the geometric size of the beam, and the second term, i.e., $\langle xx' \rangle^2$, represents the shape of the beam. In Equation 2.29, p_x and p_z are the components of the particle's momentum in the transverse and longitudinal directions, respectively.

If electrons are rapidly accelerated from rest, their longitudinal momentum (p_z) can quickly reach relativistic values, where $p_z = \beta\gamma mc$. Here, m represents the rest mass of the electron, c is the speed of light in a vacuum, β is the ratio of the electron's velocity to the speed of light, and γ is the Lorentz factor, defined as $\gamma = \frac{1}{\sqrt{1-\beta^2}}$. Accordingly, Equation 2.29 can be rewritten as follows [3]:

$$\varepsilon_x \equiv \frac{1}{\beta\gamma mc} \sqrt{\langle x^2 \rangle \langle {p_x}^2 \rangle - \langle x {p_x}^2 \rangle} \tag{2.30}$$

If there is no cross-correlation between the transverse momentum and the position (location of emission), then the normalized emittance can be expressed as:

$$\varepsilon_n \equiv \beta\gamma\varepsilon_x = \frac{1}{mc}\cdot\sqrt{\langle x^2\rangle}\sqrt{\langle {p_x}^2\rangle} = \sigma_x\sigma_{p_x} \tag{2.31}$$

Where σ_x represents the rms spot size and σ_{p_x} represents the dimensionless rms transverse momentum.

Then the variance of transverse momentum can be calculated from the three-step photoemission method and can be expressed as [29],

$$(\sigma_{p_x})^2 = \frac{\int_{E_f+\phi-h\nu}^{\infty} dE\,[1-f_{\mathrm{FD}}(E+h\nu)]\,f_{\mathrm{FD}}(E)\int_{\cos\theta_{\max}(E)}^{1} d(\cos\theta)\int_0^{2\pi} d\Phi\,(p_x)^2}{(mc)^2\int_{E_f+\phi-h\nu}^{\infty} dE\,[1-f_{\mathrm{FD}}(E+h\nu)]\,f_{\mathrm{FD}}(E)\int_{\cos\theta_{\max}(E)}^{1} d(\cos\theta)\int_0^{2\pi} d\Phi} \tag{2.32}$$

Here in Equation 2.32, the Fermi-Dirac function, $f_{FD}(E)$, represents the density of initial states, and the term $[1-f_{FD}(E+h\nu)]$ represents the density of the excited states. As described earlier in this section, 2.3.1.1, to escape from the material's surface, the photo-excited electrons must have sufficient momentum normal to the surface to overcome the potential barrier. The maximum angle at which a photoelectron can escape is already described in Equation 2.13. The x component of the momentum can be defined as [29],

$$p_x = \sqrt{2m(E+h\nu)}\sin\theta\cos\Phi \tag{2.33}$$

By putting the value p_x, and replacing the Fermi-Dirac distributions with Heaviside step functions, Equation 2.32 can be written as [29],

$$(\sigma_{p_x})^2 = \frac{2}{(mc)^2}\frac{\int_{E_f+\phi-h\nu}^{E_f} dE\int_{\cos\theta_{\max}}^{1} d(\cos\theta)\int_0^{2\pi} d\Phi(E+h\nu)\sin^2\theta\cos^2\Phi}{\int_{E_f+\phi-h\nu}^{E_f} dE\int_{\cos\theta_{\max}}^{1} d(\cos\theta)\int_0^{2\pi} d\Phi} \tag{2.34}$$

Equation 2.34 can be further simplified and can be expressed for the rms of the transverse momentum given by [29],

$$\sigma_{p_x} = \sqrt{\frac{h\nu - \phi}{3mc^2}} \tag{2.35}$$

Then the expression for the normalized emittance for metal is given by

$$\varepsilon_{n_{\text{metal}}} = \sigma_x \sigma_{p_x} = \sigma_x \sqrt{\frac{h\nu - \phi}{3mc^2}} \tag{2.36}$$

The term $h\nu - \phi$ in Equation 2.36 is generally called the excess energy of the electron in the vacuum.

Several assumptions are considered when the expression is made for the normalized emittance in Equation 2.36. Such as in this case, the initial state electrons are assumed to be in an s-wave state (has zero orbital angular momentum) with an energy distribution given by the Fermi-Dirac function. This s-wave assumption leads to a simple isotropic angular distribution of the electron. However, in general, the electron density of states is more complicated; higher angular momentum states such as d- and p-wave are associated with the density of states. The d- and p-wave states have directional dependence and are not spherically symmetric, leading to anisotropic angular distributions.

In the semiconductor case, one must consider two emission types separately, i.e., prompt and delayed emission. In prompt emission, the electron undergoes no scattering interactions, and the emittance is typically determined by the electron's excess energy in the vacuum. It can be expressed as [42],

$$E_{\text{excess, semiconductor}} = h\nu - (E_g + E_a) \tag{2.37}$$

Then Equation 2.36 (normalized emittance) can be written for the semiconductor as,

$$\varepsilon_{n_{\text{semiconductor}}} = \sigma_x \sigma_{p_x} = \sigma_x \sqrt{\frac{h\nu - (E_g + E_a)}{3mc^2}} \tag{2.38}$$

Equation 2.38 can also be written as,

$$\varepsilon_{n_{\text{semiconductor}}} = \sigma_x \sigma_{p_x} = \sigma_x \sqrt{\frac{\text{MTE}}{mc^2}} \tag{2.39}$$

Where MTE represents the average transverse kinetic energy of the photo-emitted

electron. In the simplest model, where it is assumed that the photoelectrons are distributed uniformly with the kinetic energy between $h\nu - (E_g + E_a)$ and 0, then MTE can be defined as,

$$\text{MTE} = \frac{h\nu - (E_g + E_a)}{3} \tag{2.40}$$

In delayed photoemission, the excited electrons have sufficient time to equilibrate with the lattice before they are emitted into the vacuum. In this case, the excited electrons have sufficient time to scatter with the lattice phonons and reach thermal equilibrium with the ambient temperature before they are emitted into the vacuum. This emission type usually happens in negative electron (NEA) cathodes; for example, Cs:GaAs photocathode. Since the electrons are thermally equilibrated, therefore the expression for the normalized emittance can be written as [42],

$$\varepsilon_{n_{\text{NEA-semiconductor}}} = \sigma_x \sqrt{\frac{k_B T}{mc^2}} \tag{2.41}$$

The following part of this chapter presents an overview of several photocathode materials (mainly metal and semiconductor) and their characteristics.

2.4 Different Photocathode Materials: A Review

2.4.1 Metal Photo Cathodes

Due to having a long operational lifetime and being easy to produce and handle, metal photocathodes are often a primary choice for low average current photoinjector applications. These kinds of cathodes are more robust against degradation compared to semiconductor photocathodes. Also, they can withstand higher electric surface fields as well as higher temperatures in RF accelerators. Other advantages include having a short response time (less than picoseconds) and minimum vacuum requirement during the operations [43]. However, the limiting factor that restricts its use primarily to applications involving intermediate average currents is the low quantum efficiency, which remains low even in the UV wavelengths. As described in the previous section, these types of cath-

odes typically exhibit high reflectivity in the visible range (including the near-infrared and near-ultraviolet spectra). As a consequence, the photon absorption process (i.e., the first step photoemission process) could not happen efficiently. Moreover, the motion of the photoexcited electrons will be encountered by electron-electron scattering events, which may cause a significant decrease in the final energy of the electron. Therefore, this may decrease the escape probability of an electron moving outside the surface barrier [41].

In metal, the surface barrier generally refers to the work function ϕ (minimum energy required to remove the electron from a solid to a point in the vacuum immediately outside the solid surface). In Table 2.1, the properties of several metallic photocathodes are listed.

Copper is an attractive choice as a photocathode, as it is more robust and insensitive to air. However, it has the lowest QE compared to other materials. From the QE point of view, Barium has a better spectral response (0.1% at 337 nm) [43], but it is less robust compared to other materials (it can not withstand a high electric field). Magnesium has a relatively high work function of 3.66 eV but still has a respectable QE (i.e., 0.06 % at 266 nm) making it a reliable photocathode material [43].

In order to increase the QE of metal photocathodes, several attempts, such as the deposition of a thin layer on top of the photocathode (to decrease the effective work function of the composite structure), have been carried out [44]. For example, in recent years, to improve the QE of the Copper photocathode, a thin layer of MgO has been deposited on the top [44], and as a consequence, a significant improvement in the photocathode's QE (an increase of more than an order of magnitude) has been noticed.

2.4.2 Semiconductor Photocathodes

Semiconductor photocathodes provide a great advantage for generating high average current due to their high quantum efficiency in the UV or visible spectral ranges. Due to low reflectivity, the possibility of the absorption of photon energy is quite high compared to metal photocathodes. As a result, the conversion of photon energy to electron energy is more efficient, provided the photon energy is higher than the band gap.

In the semiconductor case, the second step of the photoemission process is usually dominated by electron-phonon scattering compared to electron-electron scattering. As

Metals	Work function (eV)	QE (%)	λ (nm)	Operational lifetime	Vacuum (mbar)	Res. time	Ref.
Cu	4.3–4.7	0.014	266	Very long	10^{-7}	$<$ ps	[43]
Mg	3.66	0.06	266	$>$ 5000 h	10^{-7}	$<$ ps	[43]
Y	2.9	0.05	266	Long	$< 10^{-7}$	$<$ ps	[43]
Sm	2.7	0.07	266	Long	$< 10^{-7}$	$<$ ps	[43]
Ba	2.5	0.10	337	Short-long	$< 10^{-7}$	$<$ ps	[43]
Nb	4	0.01	266	–	–	–	[45]
Ca	2.9	0.05	248	–	–	–	[45]

Table 2.1: Overview of several metal photocathodes

described in the previous section (Section 2.3.1.3, page 25), the energy loss per electron-phonon scattering is much smaller than the electron-electron scattering. Therefore, the probability of an electron reaching the surface is much higher in semiconductor photocathodes than in metal photocathodes. However, the operational lifetime is comparatively shorter for semiconductor photocathodes than for metal ones. Another disadvantage is semiconductor photocathodes have high sensitivity to contamination by O_2, CO_2, and H_2O, etc [46]. Therefore, semiconductor photocathodes require more stringent vacuum conditions (i.e., $\leq 10^{-9}$ mbar), a UHV condition is usually required for these cathodes' fabrication, transportation, and operation.

Semiconductor photocathodes are mainly divided into two types, i.e., (1) Positive Electron Affinity cathodes (PEA) and (2) Negative Electron Affinity cathodes (NEA). The major difference between the two types is the position of the vacuum level (E_{vac}), as depicted in Fig. 2.8. For PEA cathodes, the vacuum level lies above the conduction band minimum (CBM), whereas for NEA cathodes, the vacuum level usually lies below the CBM.

Since the vacuum level lies below the conduction band minimum for NEA photocathodes, the escape probability of an electron into the vacuum level is usually higher. GaAs is a typical example of NEA photocathodes. The surface of NEA photocathodes is generally prepared by creating a surface dipole by adding a monolayer of electropositive

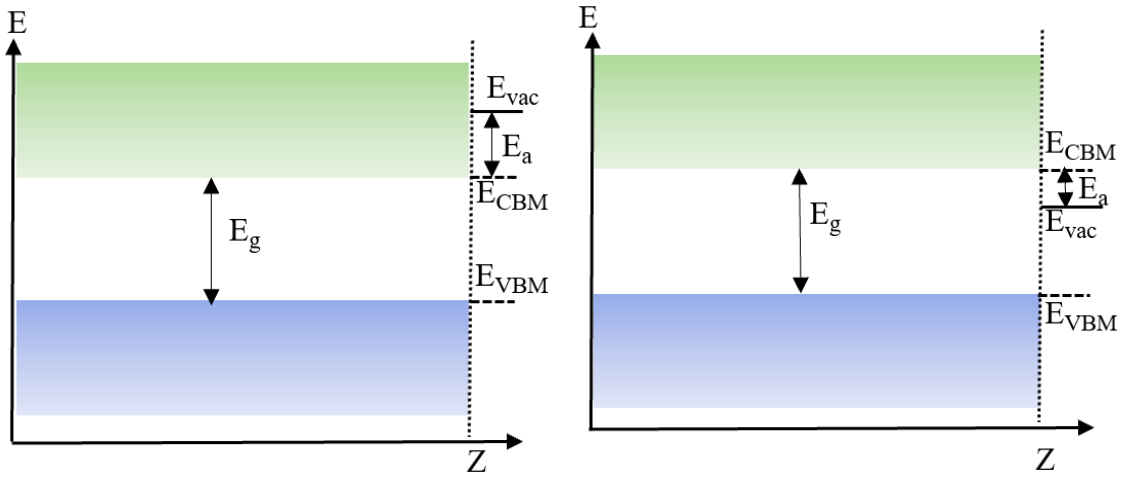

Figure 2.8: Comparative illustration of the energy band diagram of (a) PEA and (b) NEA photocathodes. Band gap (E_g) is defined as the energy difference between the conduction band minimum (E_{CBM}) and the valance band maximum (E_{VBM}), i.e., $E_g = E_{CBM} - E_{VBM}$. Electron affinity is defined as the difference between the energy of the vacuum level and the conduction band minimum.

elements on it, such as Cs or a combination of Cs and O. This monolayer creates a surface dipole, which functions as an electron donor to the underlying semiconductor material. As a result, the surface acquires a positive charge, effectively reducing the electron affinity to nearly zero. Therefore, the NEA photocathode's QE is usually higher ($> 20\%$ at UV wavelengths). However, these cathodes tend to have a longer response time (tens of ps) and high sensitivities under a radio frequency (RF) environment [47].

As it is named a positive electron affinity (PEA) semiconductor, the vacuum level typically lies above the conduction band minimum, as depicted in Figure 2.8a. Therefore, in order to escape into the vacuum, the electrons must have higher energy than the conduction band minimum energy. Additionally, in order to acquire sufficient momentum to escape, electrons typically exit through an escape cone (as described in Section 2.3.1.1, pages 19-20). Several types of PEA semiconductors commonly used as photocathodes include alkali tellurides (such as cesium telluride), alkali halides (such as cesium iodide), and alkali antimonides (such as cesium antimonide, cesium potassium antimonide, and sodium potassium antimonide, etc.).

In the alkali telluride family, cesium telluride (Cs_2Te) photocathodes are the most popular and widely used for the accelerator application due to their high QE (a typical QE of $> 10\%$ in UV wavelengths), relatively low emittance, longer operational lifetime, fast response time, and robustness in the high-gradient environment [48–52]. This photocathode is used as an electron source in many user facilities like FLASH (DESY), European XFEL (Germany), LCLS-II (SLAC, USA) and, in many accelerators around the world [53]. Since this cathode is sensitive to the UV range, photocathode laser systems are more demanding as it is necessary to go to the third or fourth harmonic from the fundamental infrared laser light (IR). As described in Chapter 1, the conversion efficiency over several stages is usually very small, which requires high initial laser powers [4]. Furthermore, this kind of laser system is generally very complex, which increases the operation cost [5].

Alkali halides photocathodes, such as cesium iodide, are relatively robust and have a reasonable QE in the deep UV wavelengths. However, the typical band gap of cesium iodide is around 6.3 eV, which means it requires vacuum ultraviolet (VUV) radiation with corresponding energy levels for efficient photoemission [54]. Furthermore, the high photoemission threshold forces the use of the fifth harmonic of an Nd: YLF laser. As discussed above, such laser systems are usually very complex and can increase operational costs. In addition, this photocathode experienced some kind of charge saturation effect while used inside the RF gun [55].

Compared to the above two cathode families, alkali antimonide photocathodes have an advantage for their high sensitivity in the visible range spectrum, which reduces the burden on the laser drive system by requiring only second harmonic conversion. Moreover, as described in Section 2.3.1.4, the mean transverse energy (MTE) of the photoemitted electrons from the cathode is typically proportional to one-third of the excess energy (Equation 2.40) [29]. Furthermore, the intrinsic emittance of semiconductor photocathodes is proportional to the square root of the MTE value (Equation 2.39). Given that alkali antimonide photocathodes primarily operate at visible wavelengths closer to their photoemission threshold, it is reasonable to expect a lower MTE and, consequently, reduced intrinsic emittance [42]. This expectation arises due to the lower amount of ex-

cess energy present at these wavelengths. In addition, these photocathodes exhibit a high QE (up to 10% in the visible wavelength range), prompt response time, and low thermal emittance, making them a promising candidate for generating a high-brightness beam for light source applications [8, 56–58]. However, due to the high sensitivity towards contamination, the usual operation lifetime of these cathodes is comparatively shorter [57]. There are several photocathodes from the alkali antimonide family, including K_2CsSb, Cs_3Sb, Na_2KSb, and $Na_2KSb(Cs)$, are extensively studied and investigated for accelerator applications. A brief description of these cathodes is discussed below in this section.

Cs_3Sb (cesium antimonide) is a well-known photocathode with a high quantum efficiency of up to approximately 10% in the visible spectrum. This cathode is easier to grow compared to K_2CsSb or Na_2KSb photocathodes. Typically, the sequential evaporation method or co-evaporation method can be employed for its production. In the sequential evaporation method, Cs and Sb layers are deposited sequentially onto the substrate. During the sequential deposition process, it is common to maintain the substrate temperature at a relatively high value, typically higher than 120°C [30]. Alternatively, in the co-evaporation method, Cs and Sb are simultaneously evaporated onto the substrate [59]. However, it is important to note that Cs_3Sb photocathodes are more sensitive to oxidation compared to K_2CsSb photocathodes [60]. The presence of atmospheric oxygen can readily react with Cs_3Sb, leading to surface oxidation and degradation of the photocathode's performance [58, 60].

The Na_2KSb and $Na_2KSb(Cs)$ compounds were initially discovered by Sommer [61]. These photocathodes can withstand a comparatively higher temperature than other photocathode materials in the alkali antimonide family [62–64]. This thermal stability is advantageous in applications where higher operating temperatures are required. These photocathodes also have a good QE (up to 6 % in the green wavelengths) and comparatively low emittance [63, 64]. However, the fabrication procedures are relatively complex compared to other photocathode materials. In addition, like other alkali antimonide photocathode materials, these photocathodes are also sensitive to oxidation. They can readily react with atmospheric oxygen, leading to surface oxidation and degradation of their performance. [65].

The K_2CsSb (potassium cesium antimonide) compound was first discovered by Sommer [66], and nowadays, it is commonly produced using both sequential and co-evaporation methods [67–69]. A sequential deposition involves depositing individual antimony, potassium, and cesium layers onto a substrate (such as molybdenum, copper, stainless steel, etc.). During the deposition process, it is common to maintain the substrate temperature at a relatively high value, typically higher than 80 °C [56, 67, 68]. On the other hand, co-evaporation involves either the simultaneous evaporation of potassium, cesium, and antimony from separate sources onto the substrate [69] or the simultaneous evaporation of potassium and cesium after an initial Sb deposition [70], forming the K_2CsSb compound. Nevertheless, alkali antimonide compounds need a better vacuum quality (i.e., 10^{-11}mbar) range than Cs_2Te (i.e.,10^{-10} mbar) to limit QE degradation [71].

The utilization of these alkali-antimonide photocathodes has so far successfully been demonstrated in various DC and continuous wave (CW) guns, particularly at low gradients (<20 MV/m) [8, 9, 30, 63, 72] and the parameters like QE and thermal emittance are found to be very promising. However, as described in Chapter 1, for next-generation CW guns and applications that demand even higher cathode gradients in the range of 30-40 MV/m, further advancements are necessary to enhance the brightness of the electron beam. Therefore, our current research domain is primarily centered around developing the multi-alkali photocathode materials and exploring their feasibility for high-gradient operation at the PITZ RF gun for a future upgrade of the European XFEL facility. In the alkali antimonide family, the K-Cs-Sb compound was selected, as it is more well-studied in terms of growth procedures, electronic structure, and behavior inside the photoinjector environments than the other photocathodes in this family. In addition, by considering the comparatively higher thermal stability properties, we also studied the Na-K-Sb-Cs photocathode compound as a potential alternative to the K-Cs-Sb photocathode. The primary goal is to produce a reliable and reproducible recipe for these selected photocathodes in our preparation system. This involves optimizing the growth procedures and deposition parameters to consistently produce high-quality photocathodes with desired properties. Once a reliable recipe is established, the next step is to test the feasibility of these photocathodes in the RF photoinjector environment at PITZ. Testing the feasibility includes

assessing important parameters such as quantum efficiency, thermal emittance, stability, and response time at various gun gradients.

In Table 2.2, an overview of the properties of several semiconductor photocathodes is presented.

Cathode type	**Material**	**E_g+E_a (eV)**	**QE (%)**	**λ (nm)**	**Operational lifetime**	**Vacuum (mbar)**	**Res. time**	**Ref.**
PEA	Cs_2Te	3.5	≥ 10	254	Long	$\leq 10^{-10}$	$\sim$ 200 fs	[51,52,73]
	CsI	6.4	≤ 5	209	Long	$\leq 10^{-4}$	-	[55,74]
	Cs_3Sb	1.9	≤ 10	532	Short	$\leq 10^{-11}$	$\sim$ ps	[30,58]
	Na_2KSb	2	~ 2	515	-	$\leq 10^{-11}$	$\sim$ ps	[63,75,76]
	Na_2KSb(Cs)	1.5	~ 4	515	-	$\leq 10^{-11}$	-	[77,78]
	K_2CsSb	1.9	5-10	515	Short-long	$\leq 10^{-11}$	$\sim$ 100 fs	[72,79,80]
NEA	GaAs(Cs,O)	1	5-10	532	Short	$\leq 10^{-11}$	$\sim$ ps	[47,81–83]

Table 2.2: Overview of several semiconductor photocathodes

Chapter 3

Facility Overview

3.1 Overview of the Photoinjector Test facility at DESY in Zeuthen (PITZ)

The Photo Injector Test facility at DESY, Zeuthen site (PITZ), is primarily dedicated to developing and optimizing high-brightness electron sources for free-electron lasers (FELs) such as FLASH and European XFEL [6]. The research activities at PITZ encompass experimental benchmarking of injector simulations, the development of laser pulse shaping methods, modeling of the photoemission process in high gradient RF guns [84], next-generation long-pulsed electron gun development [85], and various applications of high brightness electron photoinjectors. These applications include investigating plasma wakefield acceleration [86, 87], electron diffraction experiments [88], and accelerator-based generation of THz radiation [89, 90]. An R&D platform dedicated to electron radiation therapy and radiation biology is currently being established at PITZ [91].

An overall schematic layout of the facility is shown in Fig.3.1. The electron bunches are generated in a 1.6-cell photocathode radio frequency (RF) gun. This RF gun operates at a resonant frequency of 1.3 GHz with a high accelerator gradient at the cathode of up to 60 MV/m. The PITZ photoinjector system is being operated with a UV-sensitive Cs_2Te photocathode. The other main components illustrated in Fig.3.1 are the Low-Energy Dispersive Arm (LEDA), the Cut-Disk Structure (CDS) booster, Emittance Measurement

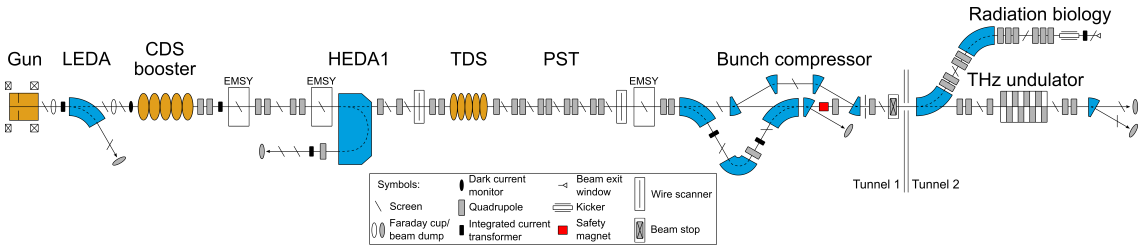

Figure 3.1: Schematic layout of the PITZ beamline. The beam is generated in the gun (top left) and travels from left to right.

System (EMSY) stations, the High-Energy Dispersive Arm (HEDA1), the transverse deflecting structure (TDS), and the phase space tomography (PST) module. Besides the main components, several additional instruments are installed for detailed control and diagnostics of the electron beam; Faraday cups are used for charge and dark current measurements, integrated current transformers are used for non-destructive charge measurements, and several magnets (steerers, dipoles, quadrupoles) and screen stations are used for steering, focusing, and imaging of the beam.

In the gun, UV laser pulses are directed onto the photocathode to generate electron bunches through the photoelectric effect. The RF pulses accelerate the electron bunches to a nominal momentum of 6.5 MeV/c in the RF gun and further boost them up to 25 MeV/c after passing through the booster cavity. Momentum distribution measurements of the electron bunches are obtained using the energy spectrometers LEDA and HEDA1. The TDS is employed to provide the electron bunch with a vertical, time dependant kick, allowing for temporal profile measurements. In addition, a phase space tomography (PST) module is installed with matching quadrupole magnets, a FODO section of quadrupole magnets, and screen stations. The main purpose of this section is to reconstruct the transverse phase space. A bunch compression chicane is added in the beamline to increase the beam current, enabling more powerful THz radiation output in the subsequent undulator. It also enables the investigation of seeding methods for the THz generation [92]. In tunnel 2, as illustrated in Fig.3.1, a dedicated beamline is used for both THz and radiation biology experiments, respectively [91, 92]. More details on the PITZ accelerator can be found in [6]. Some relevant components mentioned above related to the thesis topic are described in the section below.

3.1.1 Photocathode Laser System

At PITZ, two photocathode laser systems are available to produce electron beams by illuminating the photocathode surface. Both laser systems are located in the same laser room, and they utilize a common laser beam line that extends approximately 35 meters from the laser room to the photocathode system. This configuration enables seamless switching between the two lasers by introducing a mirror into the laser beamline. The Max-Born Institute, Berlin, designed, built, and developed the first photocathode laser system at PITZ [93, 94]. An overview of the MBI photocathode laser system is illustrated in Fig.3.2. The fundamental laser oscillator consists of an Yb:YAG infrared (IR) laser operating at a wavelength of 1030 nm with a 54 MHz oscillator frequency. The pulses produced by this oscillator have a duration of 1 ps. These pulses are then divided into to beam paths and can be utilized for cross-correlation purposes or directed to the pulse shaper for further manipulation. The laser pulse shaper allows for the manipulation of the temporal profile of the laser pulse. It comprises a collection of 13 birefringent crystals and is utilized to modify the initial short Gaussian-shaped pulses produced by the oscillator. The pulse shaper enables the transformation of the pulse shape into a comb-like or a flat-top profile of length up to $\sim$25 ps, offering versatility in pulse characteristics [95]. Alternatively, it is possible to bypass the pulse shaper to maintain the short Gaussian temporal distribution of the laser pulses, with a duration as low as 1.5 ps. After this stage, the laser pulse power undergoes amplification through two successive amplifier stages. Thereafter, the wavelength is converted using a Lithium triborate (LBO) crystal, resulting in a wavelength of 515 nm. Finally, a β-Barium Borate (BBO) crystal is used to further convert the wavelength to 257.5 nm.

The MBI laser system has the capability to generate UV laser pulses with energies of up to 2 μJ. These pulses are organized into trains containing a maximum of 800 pulses at a pulse repetition rate of 1 MHz and a train repetition rate of 10 Hz. The pulse energy can be reduced by employing an attenuator consisting of a half-wave plate mounted on a rotational stage and a birefringent crystal. Then, the laser is focused onto an adjustable iris known as the beam shaping aperture (BSA) [96, 97]. The laser at the BSA is imaged onto the cathode, enabling the remote adjustment of the laser size at the cathode. The

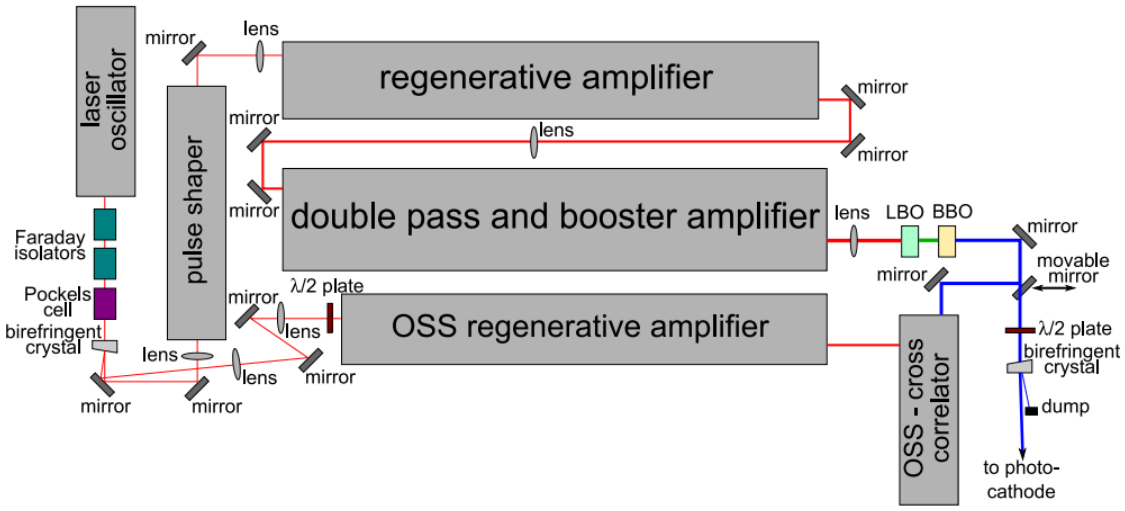

Figure 3.2: Layout of the MBI photocathode laser system. Adapted from [94]

magnification of the imaging optics between the MBI laser exit and the BSA is carefully selected to ensure that the laser beam size is larger than the BSA itself. Consequently, when the BSA is predominantly illuminated, only the central portion of the transverse laser pulse distribution is imaged onto the photocathode. This produces circular laser profiles characterized by a transverse flat-top distribution. However, the magnification of the laser beamline can be adjusted to allow for a greater portion of the transverse Gaussian laser profiles to pass through the BSA. This results in the profiles being selectively clipped at different radii, offering versatility in the spatial distribution of the laser pulses on the photocathode.

The laser system is also equipped with other various diagnostic devices. The optical sampling system (OSS) performs cross-correlation between the short infrared (IR) laser pulses from the oscillator and the shaped ultraviolet (UV) pulses, enabling precise measurements of the temporal laser profile. A UV energy meter is utilized to accurately gauge the laser pulse energy, while a photodiode serves to monitor the laser pulse energy throughout the train of laser profiles.

The PITZ facility has a second photocathode laser system powered by a commercially available front-end laser known as PHAROS, which has a power output of 20 W [98]. One noteworthy aspect of this system is its ability to shape laser pulses in three dimensions,

achieved through the utilization of spatial light modulators (SLMs) [99]. Here, the grating is used to disperse the chirped laser pulse onto the spatial light modulator (SLM). On the SLM, the laser pulse is represented by a mask that exhibits a relationship between its frequency and its position in the transverse direction. At the polarizing beam splitter, only components with a specific polarization are extracted, allowing the shape of the output pulse to be altered by adjusting the modulation on the SLM. Since the SLM is programmable, it becomes possible to achieve arbitrary pulse shapes within one of the space-frequency planes. The beam transport from the laser table to the photocathode follows the identical path as that of the MBI laser system.

3.1.2 RF Photoelectron Gun

To obtain a high-brightness electron beam, a significant emission of electrons is necessary from the cathode. The extracted electrons exhibit repulsive forces among themselves due to space charge, resulting in divergence and expansion of the extracted bunch in both transverse and longitudinal directions. In order to mitigate the deterioration of beam quality caused by intense space charge forces, the beam must undergo rapid acceleration to reach relativistic energies. As a result, the photocathode is positioned within an electron gun, which accelerates the electrons with an RF electric field. As the electrons rapidly attain relativistic energies (achieved by high accelerating fields at the cathode), the contribution of space charge to the bunch emittance decreases. Solenoid-focusing magnets are strategically positioned around the electron gun to focus the diverging bunches; see Fig. 3.3. This arrangement serves the purpose of focusing the bunches and compensating for the emittance growth caused by the varying rotation of longitudinal bunch slices in the transverse phase space during acceleration [100]. The primary solenoid magnet, known as the main solenoid magnet, plays a crucial role in beam focusing. On the other hand, the bucking solenoid serves the purpose of counteracting the magnetic field generated by the main solenoid on the cathode surface. This compensation is essential to prevent any magnetic field from adversely affecting the beam quality at the cathode.

The gun can operate at a frequency of 10 Hz, with an RF pulse length of up to 650 μs^* [101]. A maximum RF power of 6.5 MW is delivered to the cavity during each RF

pulse, resulting in an electric field strength of 60 MV/m. Some important parameters associated with the RF gun are summarized in Table 3.1.

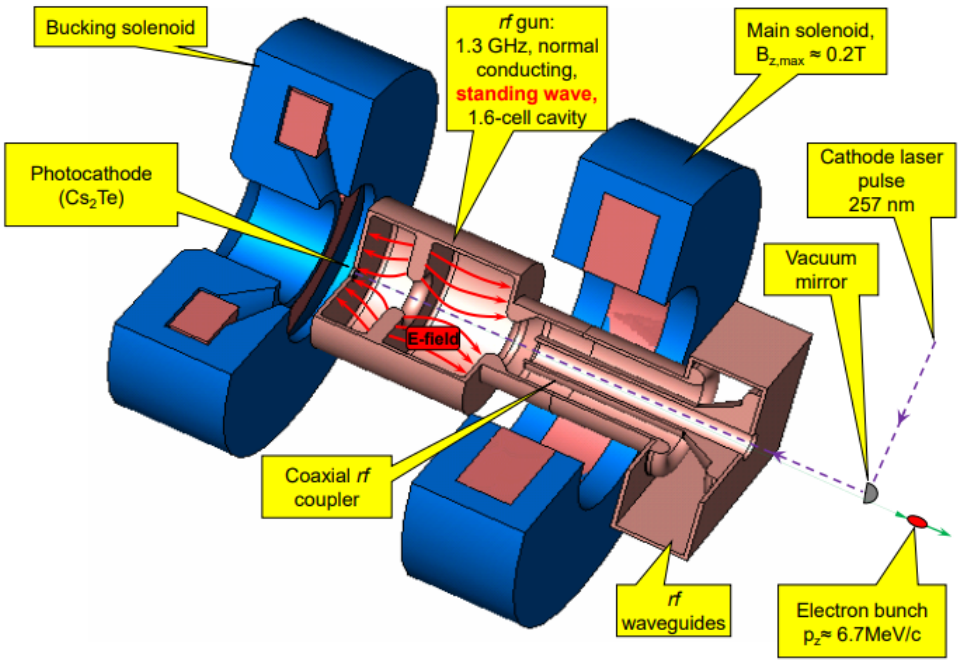

Figure 3.3: Schematic layout of the PITZ photoelectron gun. Adapted from [102].

Table 3.1: Some important parameters of the PITZ RF gun

Parameter	**Value**
Operating RF frequency	1.300 GHz
Peak power of RF pulse	6.5 MW
Maximum operating RF pulse length	650 µs*
RF pulse repetition rate	10 Hz
Maximum accelerating gradient	$\sim$ 60 MV/m
Maximum momentum gain	$\sim$ 7 MeV/c

*Additionally, further development of the RF gun has been realized, allowing an RF pulse length of up to 1 ms [103–105]. However, since these developments do not have a direct impact on the results of this thesis, they are not further elaborated in the dissertation.

3.1.3 Components of Electron Beam Diagnostics

3.1.3.1 Charge Measurement Devices

At PITZ, two different types of charge-measuring devices are used: Faraday cups (FCs) and integrating current transformers (ICTs).

A Faraday cup is a specially designed copper block that serves the purpose of collecting electrons upon impact. The collected electrons on the block generate a corresponding electric current. Within the PITZ beamline, two Faraday cups, namely LOW.FC1 and LOW.FC2, are positioned between the RF gun and the CDS booster. These Faraday cups are specifically suitable for measuring low charges.

An integrating current transformer (ICT) is a charge measurement device that operates based on the principle of electromagnetic induction. Within the PITZ beamline, ICTs (from Bergoz Instrumentation [106]) are installed in the straight section. LOW.ICT1 is employed to measure the bunch charge of the beam exiting from the RF gun, HIGH1.ICT1 measures the bunch charge of the beam exiting from the CDS booster, and HIGH2.ICT1 measures the bunch charge at the end of the beamline. The primary use of ICTs is to measure bunch charges exceeding 0.1 nC, offering a non-destructive measurement approach.

3.1.3.2 Screen Stations

Multiple screen stations are positioned along the beamline to assess the transverse distribution of the electron beam at various locations. The beam profile is converted into a light signal through the scintillation of the screen material. The emitted light is captured and focused onto a CCD camera chip for imaging. In the scintillator screens, the generation of light occurs through the following mechanism: as the particle beam passes through the scintillator, energy is lost due to inelastic scattering. This energy excites the scintillating molecules, which subsequently emit light during the relaxation process. The resulting intensity distribution of the emitted light reflects the local density of the bunch charge [107].

At PITZ, both inorganic powder screens containing cerium-doped ytterbium aluminum garnet (YAG) and cerium-doped lutetium yttrium orthosilicate (LYSO) are employed

[108]. For beam profile measurements with low charge density, such as low bunch charge, LYSO screens are favored over YAG screens. This preference stems from the fact that LYSO screens are composed of a 500 µm-thick LYSO crystal, exhibiting a light yield approximately 70 times higher than the YAG screen [108]. The screens are equipped with actuators that enable their movement into and out of the beamline. Most of the screen stations at PITZ are equipped with multiple movable lenses. However, only one lens is employed at a given time to capture the image of the screen and project it onto the CCD camera chip. A 12-bit CCD Prosilica GC 1350 camera (from Allied Vision Technologies GmbH) is used at all screen stations [109]. This camera is equipped with an array consisting of 1360 × 1024 pixels, with each pixel measuring 4.65 µm × 4.65 µm in size.

3.1.3.3 Emittance Measurement System (EMSYs)

There are three Emittance Measurement Systems (EMSYs) installed along the PITZ beamline. By utilizing the single-slit scan technique, these components enable the measurement of transverse emittance. The slit stations are equipped with vertical and horizontal actuators that are precisely controlled using stepper motors. These actuators hold tungsten slit masks with a thickness of 1 mm [110]. Although the thickness is inadequate to completely obstruct the electron beam, it effectively induces a pronounced scattering effect. Once the electron beam travels a short distance beyond the slit mask, the scattered electrons uniformly contribute to the beam images observed on the screen. The thickness of the slit mask was optimized, as a thinner slit mask would minimize scattering but increase the background on the observation screen. On the other hand, a thicker slit mask would decrease the angular acceptance of the slits, leading to a further reduction in the signal-to-noise ratio [110]. In order to maximize the number of electrons that pass through the slit mask, the yaw and pitch angles of the entire station can be adjusted within a milliradian range [110].

At PITZ, each EMSY station is equipped with two slit masks, one with a width of 10 µm and another with a width of 50 µm. The narrower slit enables the measurement of projected emittance with enhanced resolution and lower passed charge, effectively minimizing the passed beamlets and reducing systematic errors. Conversely, the wider slit

allows for greater transmission of electrons, resulting in a higher signal-to-noise ratio on the observation screen. This reduces systematic errors arising from low signal strength, particularly when dealing with beams of low charge [111]. Information regarding the principle and procedure used for emittance measurements can be found in references [112] and [113].

3.2 Overview of Photocathode Laboratory at INFN-LASA in Milan

Since the 1990s, LASA has been actively engaged in researching and advancing photoemissive materials, specifically antimony and tellurium compounds combined with alkali metals. These materials are used as high-brilliance electron sources in RF guns. In 1998, the first phase of production for Cs_2Te photocathodes was explicitly done for the TESLA Test Facility (TTF) RF gun situated at DESY-Hamburg. Since the year 2000, the production of Cs_2Te photocathodes has been carried out for the PITZ facility too [114]. So far, a total number of 150 photocathodes have been successfully manufactured and used in different facilities such as FLASH, PITZ, and LBNL, etc. As discussed in Chapter 1, DESY collaborated with INFN-LASA to facilitate the development of alkali antimonide photocathodes. The primary objective was to assess their viability in a high-gradient environment at the PITZ RF gun, with the intention of potentially incorporating them into a future upgrade of the European XFEL facility.

3.2.1 "R&D" Preparation System

In order to establish a reproducible recipe for the production of alkali antimonide photocathodes, the films are typically grown in the "R&D" preparation chamber at LASA. The "R&D" preparation system was originally constructed in the year 1990. A detailed layout of the "R&D" photocathode lab is illustrated in Fig. 3.4. The "R&D" preparation system comprises two interconnected chambers used for the cathode preparation and storage of samples (see Fig. 3.4a [115]). To transfer the cathode from the preparation chamber to a

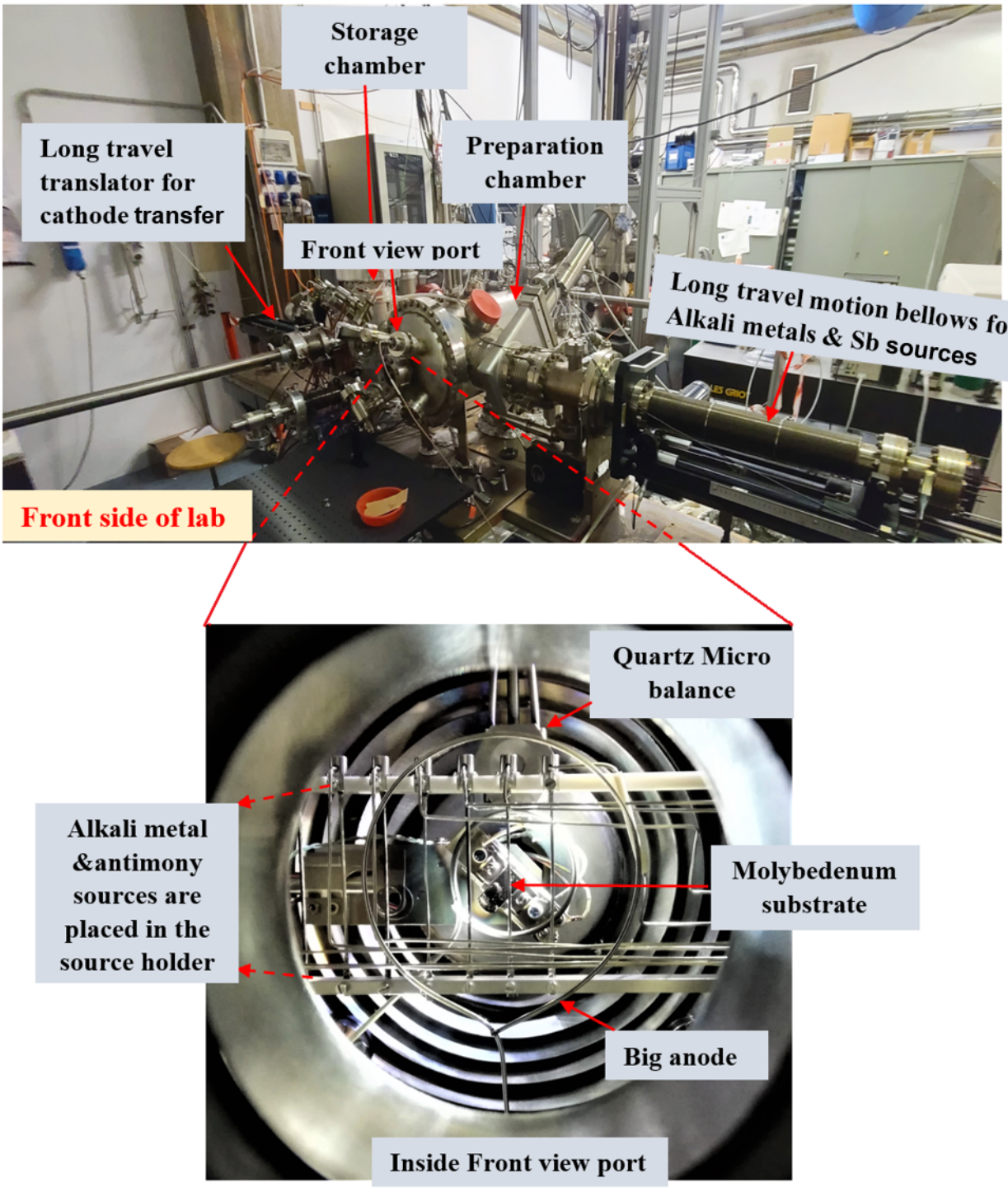
Storage chamber
Long travel translator for cathode transfer
Preparation chamber
Front view port
Long travel motion bellows for Alkali metals & Sb sources
Front side of lab
Quartz Micro balance
Alkali metal &antimony sources are placed in the source holder
Molybedenum substrate
Big anode
Inside Front view port

(a)

Figure 3.4

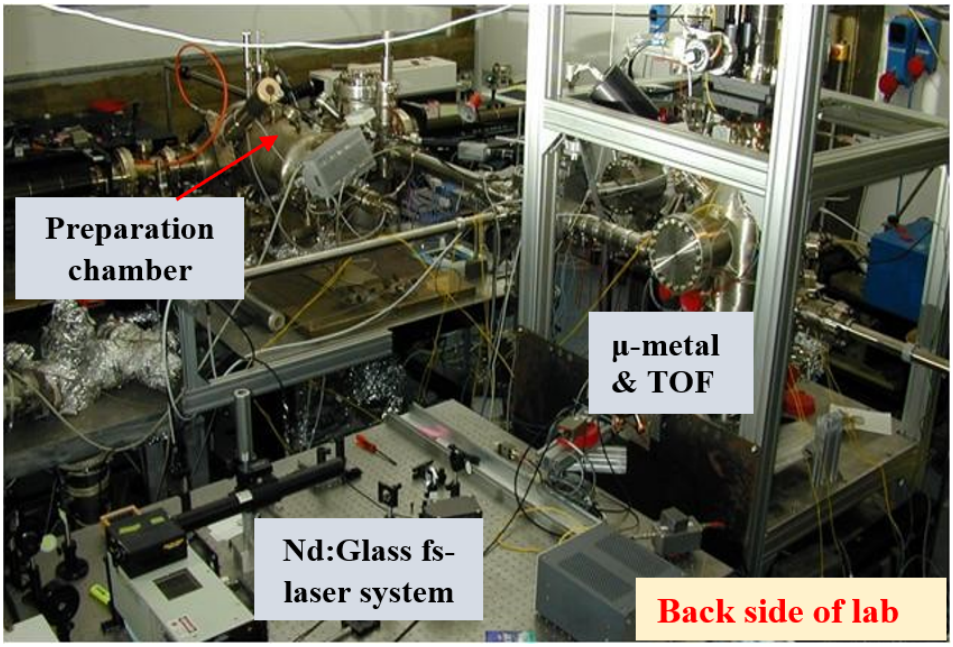

(b)

Figure 3.4: (a) Photograph of the front side of the R&D laboratory. In the picture (top one), the main preparation chamber and other components are highlighted. Additionally, a magnified version of the front viewport is included, offering a closer look at the interior of the preparation chamber. This detailed view reveals specific components such as the Mo substrate, alkali, and antimony sources, as well as other integral parts of the setup. (b) illustrates the back side of the R&D laboratory where the μ-metal and TOF chamber and other components are highlighted.

storage system, an all-metal bakeable load-lock is employed, equipped with a long linear translator featuring a 600 mm stroke. The cathode storage chamber is effectively pumped by using an ion pump and a getter cartridge [115]. The cathode preparation chamber is consistently maintained at a base pressure ranging around 10^{-11} mbar, achieved through the utilization of eight SAES Getters NEG St707® modules and a 400 l/s ion pump. Each NEG module (utilizing getter alloy ST707 [116]) exhibits a pumping speed of 560 l/s for hydrogen (at room temperature) and 220 l/s for carbon monoxide (at room temperature) [115]. The preparation chamber (based on a 304 LN stainless steel cylinder having a length of 750 mm and a diameter of 300 mm) was machined, welded, and cleaned following CERN specifications [117]. The alkali metal and antimony sources are inserted into the preparation system via a load lock mechanism. A schematic drawing of the "R&D"

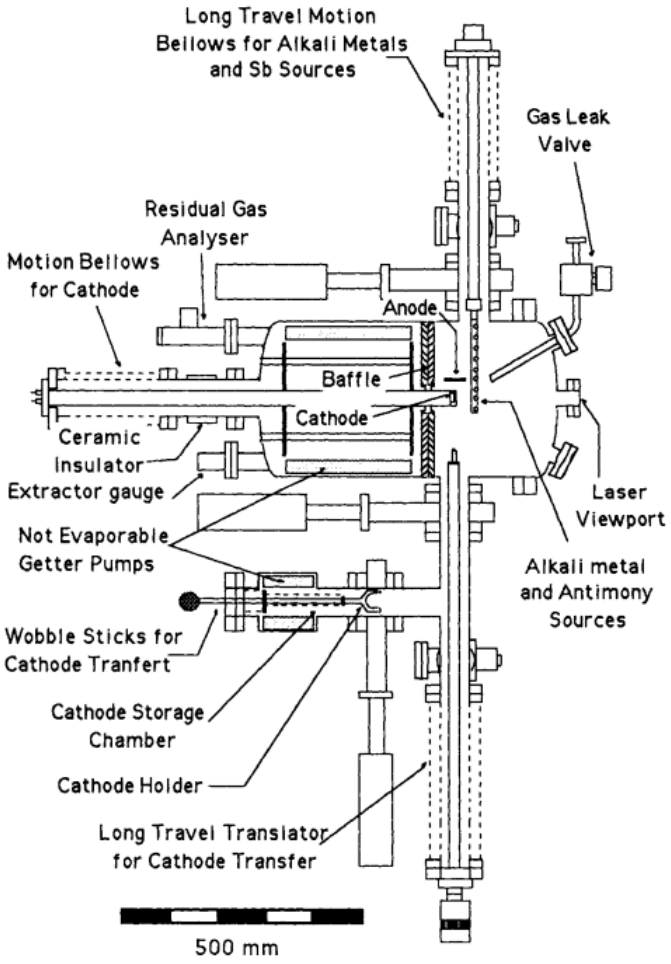

Figure 3.5: Schematic drawing of the "R&D" preparation system. Adapted from [115]

preparation system is s shown in Fig.3.5. A total of 9 sources (for multi-alkali preparation) are combined and installed on the source holder. Using a linear transfer mechanism, the sources can be positioned in front of either the cathode (for deposition) or the quartz microbalance (for calibration purposes). Additionally, this system is interconnected with a μ-metal shielded chamber that accommodates a Time-Of-Flight (TOF) spectrometer employed for conducting thermal emittance measurements [118]. After the cathode is placed within the storage chamber, it can be subsequently transferred to the TOF spectrometer. However, due to a technical problem, the TOF spectrometer is not used in this study. For further information on the geometric and other specifications of the "R&D" preparation system, refer to reference [115].

The Mo sample in the "R&D" preparation system is mounted on a commercially manufactured SH1 sample holder provided by Vacgen [119]. This sample holder is equipped with an HST module designed to heat the sample up to 950 °C [119], and a thermocouple is attached to the sample holder to measure the temperature. During the alkali antimonide deposition process, the Mo sample is subjected to controlled heating at a specific temperature while the alkali and antimonide compounds are sequentially evaporated using dispensers. The process parameters, such as deposition rates, thickness, cathode temperature, photocurrent, reflected power, etc., are precisely controlled by a LabVIEW program. The evaporation rate is monitored using a microbalance, while the real-time photocurrent and reflected power of the film are measured through the front viewport (which is made of sapphire material). To obtain an accurate photocurrent reading, it is necessary to subtract the dark current. This is achieved by utilizing a shutter to block the laser beam in a programmed manner during the photocathode deposition (detailed discussion will be provided in the following chapter). For measuring the spectral response of the photocathode, a Laser Drive Light Source (LDLS) system is employed, along with a collection of specialized optical filters spanning a range of 239 nm to 690 nm. Additionally, to facilitate measurements across an even broader spectrum, a monochromator is utilized. Furthermore, one Ar+ laser and three He-Ne lasers are employed to cover the wavelength range from 457 nm to 633 nm.

The deposition process utilizes a custom-made source for antimony (Sb) and commercially available dispensers for cesium (Cs), sodium (Na), and potassium (K) from SAES Getters ® [116]. The desorption of gases from the dispenser during evaporation has been minimized by the implementation of an appropriate conditioning procedure (details described in Chapter 4). Due to better handling, the photoemissive materials are produced on a simplified Mo substrate (see Fig. 3.4a) within the “R&D" preparation chamber (details described in Chapter 4).

3.2.2 “Production” Preparation System

A new dedicated preparation system has been recently constructed to facilitate the deposition of alkali antimonide films onto INFN Mo plugs for their testing in the PITZ RF

gun [64, 120]. While this new system is primarily designed as a “production" unit to supply cathodes to photoinjectors, it can also serve as a supportive system for R&D activities. It allows the production of cathodes using various recipes and techniques, including the co-evaporation of alkali metals. A detailed picture of the new production preparation system is illustrated in Fig. 3.6.

The new photocathode production system is a replica of the old production system that has been operational at LASA since the 1990s to produce Cs_2Te photocathodes [121]. More details on the old preparation & transfer (“suitcase”) system can be found in the reference [121]. However, this new preparation system incorporates an improved pumping system, plug temperature reading system, and source holder. In order to meet the required vacuum quality (base pressure 10^{-11} mbar) for the sensitive alkali antimonide compounds, two SAES Getters NEXTorr® D2000-10 pumps are equipped with this system. These pumps exhibit a pumping speed of 2000 l/s for hydrogen and 1100 l/s for carbon monoxide [122].

Typically, for deposition, the Mo plug is transferred to the deposition area using a Linear Transfer Mechanism (LTM). Afterward, a second LTM translator is utilized to move the cathode heater (i.e., a halogen lamp) along with a thermocouple to the rear hollow portion of the Mo plug. Further details can be found in the provided reference [123]. When comparing the thermocouple positioned in the "R&D" system, which provides a more accurate temperature reading (due to better contact with the sample holder) to the thermocouple positioned in the rear of the Mo plug in the "Production" system. Furthermore, to improve the accuracy of temperature reading in the "Production" system, a new plug temperature measuring system has been integrated into this setup. This system incorporates a thermocouple directly connected to the plug body, enabling direct temperature measurement from the plug body itself. Similar to the "R&D" system, during the alkali antimonide deposition process, the Mo plug undergoes controlled heating at a specific temperature, while the alkali and antimonide compounds are sequentially evaporated using dispensers. A circular masking system is positioned in front of the cathode to define the shape of the round active photoemissive layer and ensure its precise alignment with the plug’s center. The film’s diameter is determined through this circular mask, currently

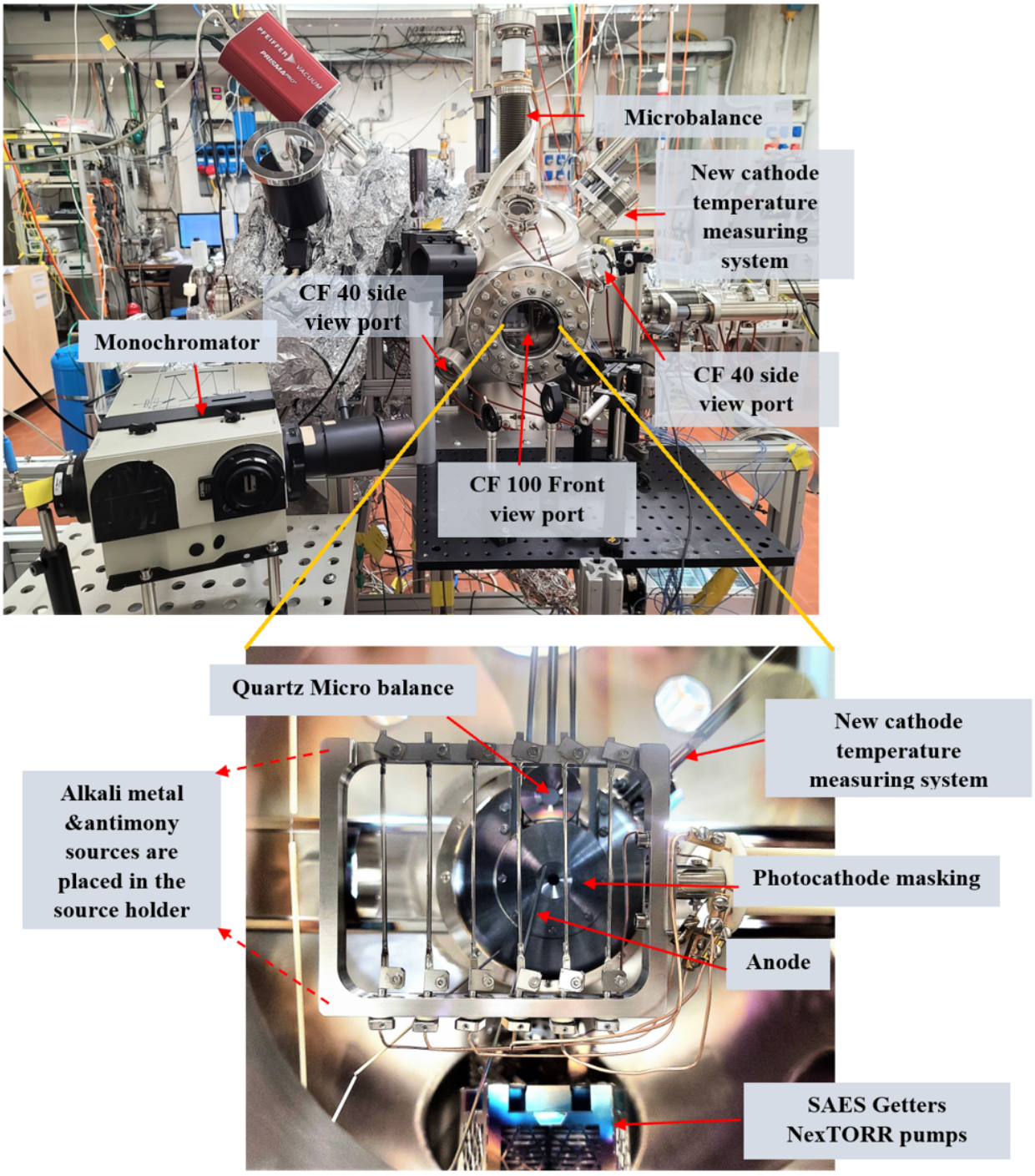

Figure 3.6: Photograph of the new alkali antimonide photocathode production system. A magnified version of the front viewport (bottom one) has been shown, where the components inside the preparation chamber, such as photocathode masking, alkali & antimony sources, and other parts are highlighted.

set at 5mm. In the area between the sources and the masking, an anode is positioned in front of the cathode (Fig. 3.6), allowing for the photocurrent measurement. This ultra-high vacuum (UHV) preparation system is equipped with a large CF 100 front viewport and two additional CF40 UV side viewports. These side viewports enable direct observation of the plug's front surface while in the masking position. This configuration facilitates optical measurements at a wider angle of 45°. The deposition of cathodes takes place on custom-made INFN-style Mo plugs, which are transported within the system using a carriage on a fixed rail. The transport boxes, commonly referred to as "suitcases", which were used in the preparation system for Cs_2Te can also be integrated into this system [121].

For spectral response and reflectivity measurements, a Laser Drive Light Source (LDLS) system, equipped with dedicated optical filters (239 nm to 690 nm) and a monochromator (170 nm to 1200 nm), is used. Additionally, He-Ne laser options are available within the 543 to 633 nm range for measurement. Furthermore, this preparation system is equipped with a multi-wavelength diagnostic system capable of measuring real-time photocurrent and reflectivity across a range of wavelengths from 254 nm to 690 nm (detailed discussion will be provided in the following chapter). The following chapter of this report offers an extensive overview of various cathode growth recipes developed in both the "R&D" and "Production" systems.

Chapter 4

Photocathode Preparation and Test Results of Multi-Alkali Photocathodes

4.1 Substrate Preparation

As mentioned in the previous chapter, photo-emissive materials were produced on a simplified Mo substrate (depicted in Fig. 3.4a) in the “R&D” preparation chamber for ease of handling. Whereas INFN-style standard Mo plugs (as shown in Fig. 4.1) are used as a substrate in the new “Production” system in order to enable in-situ testing in the PITZ RF gun. Both the simplified Mo substrate and Mo plugs are prepared from high-purity molybdenum (99.95%) through machining. The "R&D" samples are obtained by cutting thin slabs, while the Mo plugs are obtained by cutting them from a Mo rod (either sintered or arc-cast), followed by shaping them to meet design specifications using a lathe or mill.

After machining, both types of Mo samples undergo Buffered Chemical Polishing to eliminate residuals from the machining process [124]. To enhance its front surface quality and reduce the roughness, the Mo samples undergo lapping procedures. These lapping steps include the use of 6 μm, 3 μm, and 0.05 μm diamond suspensions with a "diamond embedded" disc, followed by successive clothes in three steps. Reflectivity measurements of the Mo samples are taken at each step, with the final goal of reaching a reflectivity $>$ 54% at λ = 543 nm, relative to the theoretical value of 57% [125], which serves as the

Figure 4.1: Photograph of polished standard Mo plugs that are used as substrate in the production system for the deposition process.

standardization criterion.

Once the optical finishing is complete, the Mo samples are then thoroughly rinsed with acetone and alcohol. Subsequently, it is stored in a nitrogen environment to preserve its quality.

4.2 Photocathode Characterization

4.2.1 Photocurrent and Reflected Power Measurements

During the deposition of photocathodes, a He-Ne laser was usually utilized to measure the real-time photocurrent and reflected power at 543 nm. For data standardization, the photocurrent and reflected power data were later converted into quantum efficiency (QE) and reflectivity, respectively, using Equations 2.5 and 2.6 during data analysis. This conversion enables the correlation of physical film characteristics (such as thickness, deposition rate, and crystal structure) with their electronic and optical properties. The real-time measurements provide insights into the photoemissive properties, reaction rate monitor-

ing, and quality control. In addition, these real-time data are compared to evaluate various optimization parameters (such as deposition rate, substrate temperature, and thickness) by analyzing different photocathode films. This comparison across different photocathode films is discussed in the latter part of this chapter.

Fig. 4.2a and Fig. 4.2b illustrate the photographs of the typical setup for measuring the real-time photocurrent and reflected power during the deposition process at the "R&D" and "Production" preparation systems. This setup consists of a He-Ne laser (543 nm), an optical shutter (from Thor Labs), beam routing optics, a calibrated photodiode power meter (from Ophir Optronics), a photocurrent pickup anode (see Fig. 3.4a & 3.6), and a picoampere meter (Keithley 6517a model). The green light produced by the He-Ne laser passes through various mirrors, focusing lenses, and an iris to be well collimated before impinging on the cathode surface. The photoexcited electrons from the cathode are collected by the anode, and the photocurrent is measured by the picoampere meter, while the reflected light is measured using the photodiode. The optical shutter in this setup is operated in a programmed manner during the deposition to facilitate measurements of background reflected power, as well as dark current.

In addition, a multi-wavelength optical diagnostic setup (shown in Fig. 4.2c) is employed in the "Production" system to measure the real-time photocurrent and reflected power at eight different wavelengths (between 254 nm and 690 nm) during the photocathode deposition process (employed only for cathodes 137.1, 137.2, and 137.3, discussed in the latter part of this chapter). This setup, which replaces the He-Ne laser with a Laser-Driven Light Source (LDLS) system (from EQ-77 Energetiq), is similar to the previously described setup but includes a motorized filter wheel. The motorized filter wheel can accommodate up to eight different optical filters, rotating in a programmed manner during deposition to enable real-time monitoring of the photoemissive properties of the deposited films. In this multi-wavelength optical setup, the white light generated by the LDLS system passes through the filter wheel, then through the beam routing optics, and is subsequently projected onto the cathode surface. The photocurrent and reflected power (at eight different wavelengths) are then measured, similar to the previous setup.

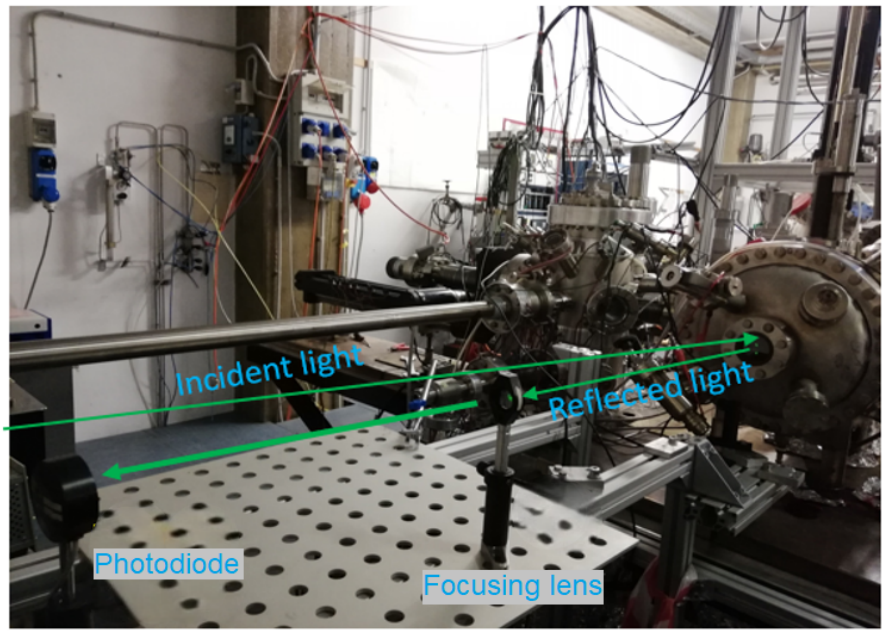
Incident light
Reflected light
Photodiode
Focusing lens

(a)

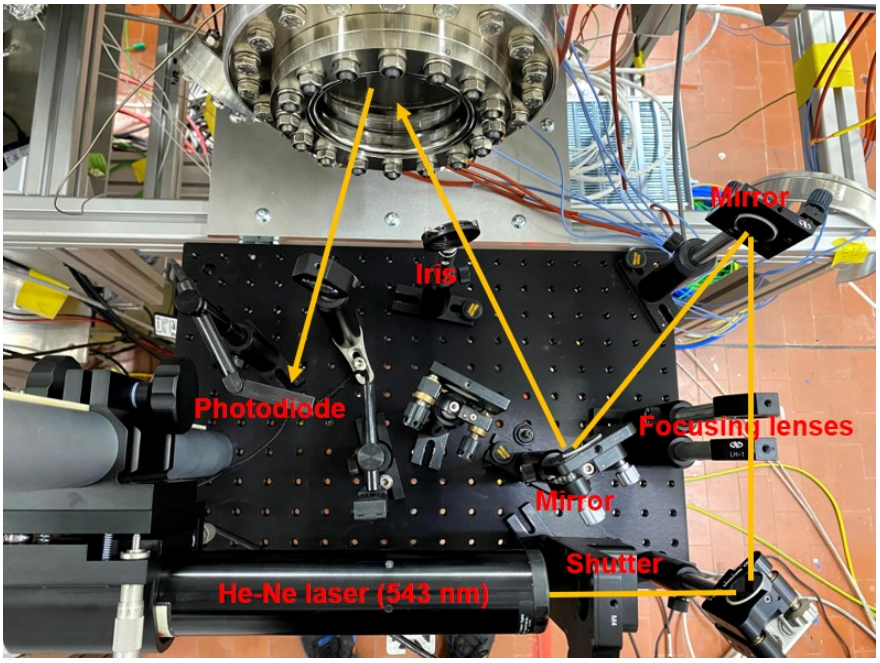
Mirror
Iris
Photodiode
Focusing lenses
Mirror
Shutter
He-Ne laser (543 nm)

(b)

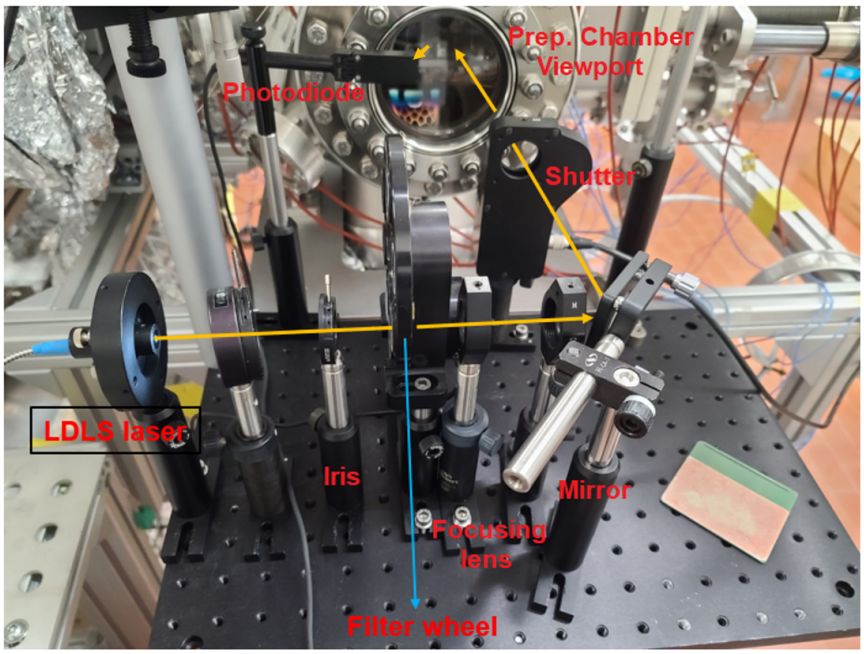

(c)

Figure 4.2: Photographs of the photocurrent and reflected power measurement setups in the (a) "R&D" preparation system and (b) "Production" system. The He-Ne laser and optical shutter are situated behind the photodiode in the "R&D" system, which is not shown in Fig. 4.2a. Figure (c) depicts a multi-wavelength optical diagnostic setup, where a motorized filter wheel containing 8 different optical filters is employed in the "Production" system to facilitate real-time monitoring of photocurrent and reflected power at 8 different wavelengths during deposition.

4.2.2 Spectral Response and Spectral Reflectivity Measurements

As discussed in Chapter 2 (Section 2.2.2), the spectral response of a photocathode material refers to its quantum efficiency measured across incident photon wavelengths. This spectral response curve is crucial as it provides important information about the material's work function, band structure, and quantum efficiency.

The spectral response is determined by measuring two key parameters: the net spectral flux (light power) and the net photocurrent at different wavelengths. The net spectral flux, denoted as $P_{\text{net}}(\lambda)$, is calculated by subtracting the background light power

$P_{\text{background}}(\lambda)$ from the total incident light power $P_{\text{total incident}}(\lambda)$. Similarly, the net photocurrent, $I_{\text{net}}(\lambda)$, is the difference between the total incident photocurrent $I_{\text{total incident}}(\lambda)$ and the dark current $I_{\text{dark}}(\lambda)$. The spectral response measurements are usually recorded after the deposition process.

In practical units, as stated in Section 2.2.1, the Quantum Efficiency (QE) is represented as,

$$QE(\%)(\lambda) = \frac{1240 \cdot (I_{\text{total incident}} - I_{\text{dark}})}{\lambda \cdot (P_{\text{total incident}} - P_{\text{background}})} \times 100 \tag{4.1}$$

where λ is measured in nm.

When taking into account the correction factor $T(\lambda)$ based on the transmittance of viewport material (such as sapphire or N-BK7 at that particular wavelength), QE can be defined as,

$$QE(\%)(\lambda) = \frac{1240 \cdot (I_{\text{total incident}} - I_{\text{dark}})}{\lambda \cdot (P_{\text{total incident}} - P_{\text{background}})} \times \frac{100}{(T(\lambda)/100)} \tag{4.2}$$

The uncertainty in the Quantum Efficiency, denoted as ΔQE, is determined using error propagation, resulting in the following equation:

$$\Delta QE(\lambda) = QE\sqrt{\left(\frac{\Delta I_{\text{net}}}{I_{\text{net}}}\right)^2 + \left(\frac{\Delta P_{\text{net}}}{P_{\text{net}}}\right)^2 + \left(\frac{\Delta\lambda}{\lambda}\right)^2 + \left(\frac{\Delta T}{T}\right)^2} \tag{4.3}$$

Statistical errors are typically below 0.4% for sets of 50 data points taken at each wavelength across all wavelengths.

In our research, we also conducted spectral reflectivity measurements of the photocathode, which holds significant importance in understanding its electronic structure. As described in the Section 2.2.3, optical measurements, including spectral reflectivity, offer crucial insights into the interaction of light with the material and reveal valuable information about its energy band structure, electronic transitions, and optical properties. Therefore, along with the spectral response measurements, we simultaneously obtained spectral reflectivity measurements after the deposition process. Later, we compare this reflectivity data with the theoretical reflectivity (obtained from DFT simulation) values to

gain a deeper understanding of the structure of the grown film, as discussed in Chapter 6.

In practical units, as stated in Section 2.2.3, the reflectivity is represented as,

$$R(\%)(\lambda) = \frac{(R_{\text{total}} - R_{\text{background}})}{(P_{\text{total incident}} - P_{\text{background}})} \times 100 \tag{4.4}$$

Where R_{total} represents the total reflected power and $R_{\text{background}}$ represents the background reflected power. When taking into account the correction factor ($T(\lambda)$ based on the transmittance of viewport material (such as sapphire or N-BK7 at that particular wavelength), Reflectivity R(λ) can be defined as,

$$R(\%)(\lambda) = \frac{(R_{\text{total}} - R_{\text{background}})}{(P_{\text{total incident}} - P_{\text{background}})} \times \left(\frac{100}{(T(\lambda)/100)^2}\right) \tag{4.5}$$

This correction factor takes into account the amount of light that is transmitted through the sapphire (or N-BK7) material at the specific wavelength. The transmittance factor is squared in the reflectivity equation (Equation 4.5) to account for the light's bidirectional journey through the viewport material, considering its passage both to and from the reflecting surface.

The uncertainty in the Reflectivity denoted as ΔR, is determined using error propagation, resulting in the following equation:

$$\Delta R(\lambda) = R\sqrt{\left(\frac{\Delta R_{\text{net}}}{R_{\text{net}}}\right)^2 + \left(\frac{\Delta P_{\text{net}}}{P_{\text{net}}}\right)^2 + \left(\frac{\Delta\lambda}{\lambda}\right)^2 + \left(\frac{\Delta T}{T}\right)^2} \tag{4.6}$$

Just like the spectral response, the error calculation was performed at each wavelength for sets of 50 data points, resulting in statistical errors that are typically below 0.5% across all wavelengths.

Figure 4.3 illustrates the standard optical setup used for conducting spectral response and spectral reflectivity measurements in the production system. Typically, this measurement setup utilizes a monochromator along with an LDLS laser serving as the light source. The LDLS system is equipped with a monochromator that covers a range of 170 nm to 1200 nm. As an alternative, it can also utilize a series of specialized optical filters, which span a range from 239 nm to 690 nm. Additionally, one Ar^+ laser and three He-Ne

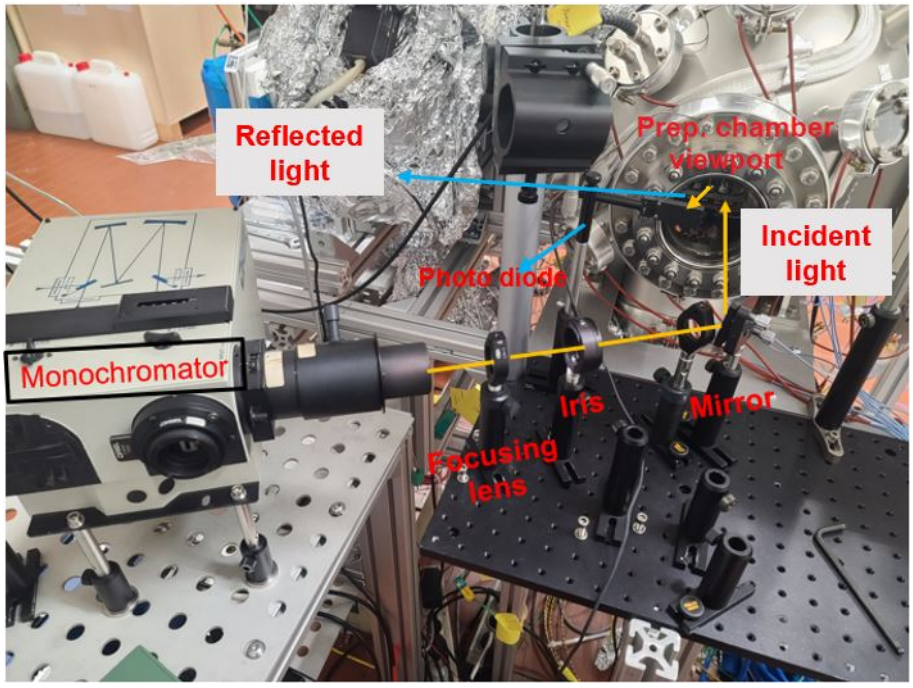

Figure 4.3: Photograph of the measurement setups for spectral response and spectral reflectivity in the "Production" system. The LDLS laser system is situated behind the monochromator, which is not shown in Figure 4.3. A similar setup is used in the "R&D" preparation system to conduct such measurements.

lasers, ranging from 457 nm to 633 nm, can be optionally used.

Similar to the real-time photocurrent and reflected power measurement setup described in the previous section, for spectral response and spectral reflectivity measurement, the white light generated by the LDLS system passes through the monochromator, then through various beam routing optics, and is finally projected onto the cathode surface. Subsequently, the photocurrent and reflected power are measured, as described in the previous section. A similar setup is also employed in the "R&D" preparation system for such measurements.

The front viewport window of the "R&D" chamber is composed of Sapphire material, whereas the front viewport window of the "Production" chamber is made of N-BK7 material. We have conducted transmittance ($T(\lambda)$) measurements for both viewport materials, and the results are shown in Fig. 4.4. It is evident from the data that the transmittance of N-BK7 material drops for $\lambda < 334$ nm, while the transmittance of Sapphire material

drops for $\lambda < 252$ nm. As a consequence, in the production system, we are constrained to perform spectral reflectivity measurements from $\lambda = 334$ nm due to the limitations imposed by the N-BK7 material's transmission characteristics.

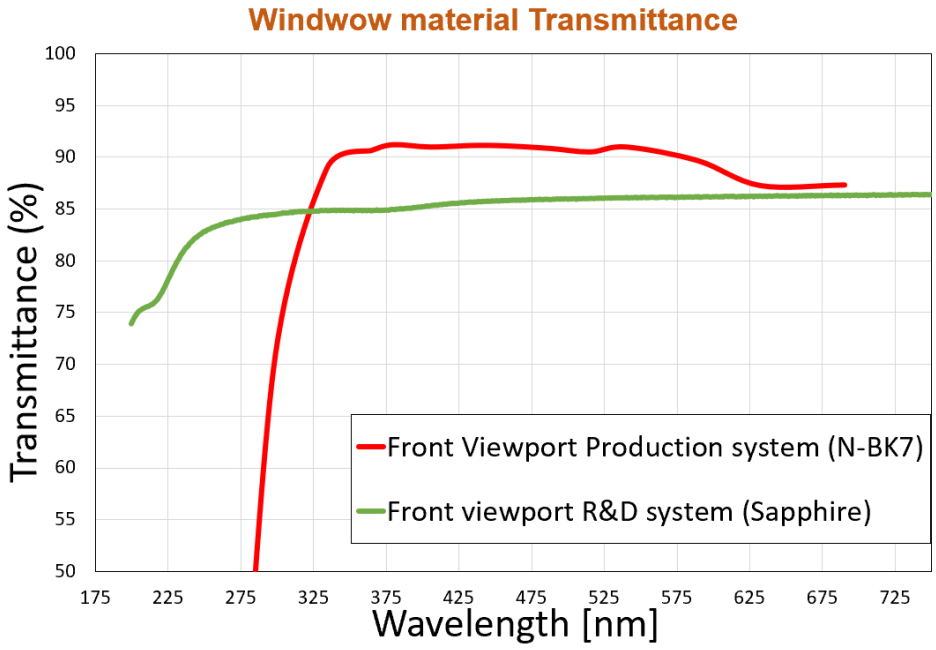

Figure 4.4: illustrates the transmittance ($T(\lambda)$) of the different viewport material with respect to different wavelengths.

4.2.3 Acquisition System

The acquisition system used in green cathode production is built on LabVIEW. This system allows for the capture of reflected power and photocurrent precisely at a wavelength of 543 nm during the deposition process in both the "R&D" and "Production" systems, in addition to gathering all relevant parameters for cathode production. The system records the total photocurrent and reflected power, and, as described in Section 4.2.1, to ensure accuracy, the corresponding background signals are subtracted using the shutter. Furthermore, in the production system, while depositing cathodes 137.1, 137.2, and 137.3 (which will be discussed in subsequent sections of this chapter), the LabVIEW program undergoes slight customization compared to the standard version to capture reflected power

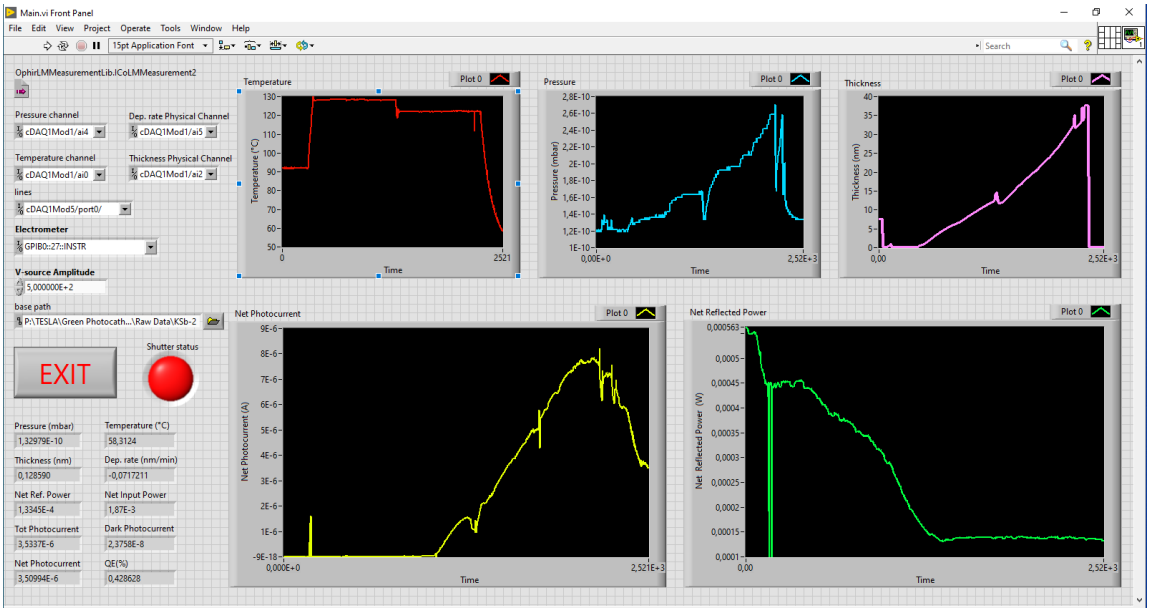

(a)

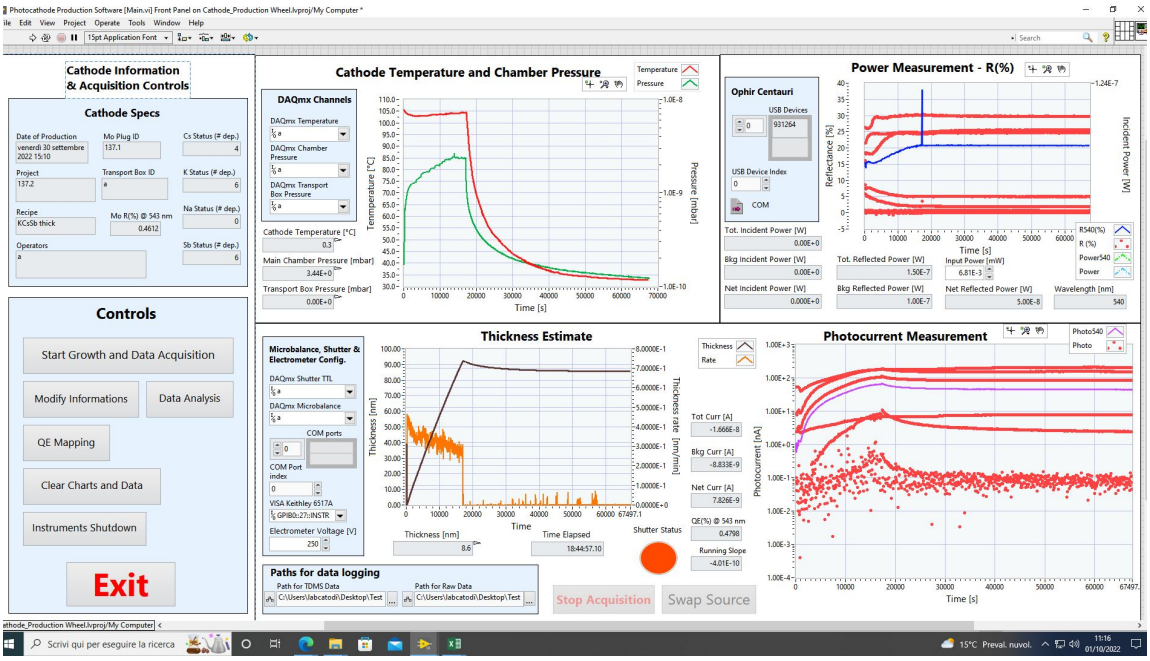

(b)

Figure 4.5: illustrates the screenshot pictures of the acquisition panel captured during the cathode deposition process in both (a) the “R&D” preparation system and (b) the “Production” system.

and photocurrent at eight different wavelengths using the motorized filter wheel. By implementing this modification, the system becomes capable of collecting photocurrent and reflected power data at up to 8 different wavelengths, facilitating the utilization of multi-wavelength measurement techniques. Further details of this procedure will be discussed in subsequent sections of this chapter, and additional information can be found in the reference [126]. Besides recording photocurrent and reflectivity data, the LabVIEW acquisition system also logs other significant parameters such as plug temperature, thickness measured by microbalance, pressures, etc. Figure 4.5 displays screenshot pictures of the acquisition panel used in both the "R&D" and "Production" systems.

4.3 Experimental Results Obtained from the Cathodes Produced in the "R&D" Preparation System

So far, a total number of 8 K-Cs-Sb, 2 Na-K-Sb-Cs, and 2 Na-K-Sb photocathodes have been produced in the "R&D" preparation system. The following section of this chapter provides a comprehensive analysis and discussion of the detailed results and outcomes derived from those photocathodes. As discussed above, due to the better handling, the photoemissive materials were produced on a simplified Mo substrate in the "R&D" preparation chamber. Before the deposition, each sample was heated up to 450 °C for at least one hour to remove possible residuals from the surface. Note that all of the above-mentioned photoemissive films were deposited on the same Mo substrate. Prior to every cathode deposition, the previous film was destroyed by a heating cycle up to 450 °C, and the complete removal was checked by QE and reflectivity measurements before starting with the next film evaporation.

For the deposition process, a custom-made source was used for Sb, while commercially available dispensers (by SAES) were utilized for Cs, Na, and K [127]. To achieve a specific deposition rate (typically 1 nm/min) during cathode growth, each source was calibrated before each cathode deposition. This calibration involved positioning the microbalance at the same location as the substrate. Once the desired deposition rate was achieved, the microbalance was moved out of the axis, and the rate was continuously

measured to have a cross-calibration that was used during the real evaporation process. This calibration procedure was repeated before each growth process to ensure consistent and accurate results.

In order to optimize and better understand the properties of the photoemissive films, as described in the preceding section, we monitored the real-time optical spectra, encompassing photocurrent and reflected power, during the growth process at the green wavelength (543 nm). Post-production, the grown film underwent comprehensive characterization through spectral response and spectral reflectivity measurements across a broader frequency range. Note that 514 nm is the available wavelength from the PITZ photocathode drive laser, corresponding to the second harmonic of the fundamental laser light.

4.3.1 Experimental Results Obtained from KCsSb Photocathodes

4.3.1.1 Fabrication Recipes

The fabrication process of alkali antimonide photocathodes involved a three-step sequential deposition procedure [128–130]. Initially, an Sb film was deposited on the substrate, followed by the sequential evaporation of K until the photocurrent reached its maximum, allowing K to react with the Sb film. Finally, Cs was evaporated onto the K-Sb film until the photocurrent was close to saturation, forming a K-Cs-Sb compound.

It's important to note that the final thickness of the resulting KCsSb film depends on the initial Sb layer thickness. Therefore, to investigate the influence of different thicknesses on the cathode's properties, we decided to grow two different Sb thickness families (i.e., thin as 5 nm and thick as 10 nm), followed by K and Cs. Additionally, to study the effects of different temperatures and deposition rates on the photocathode's properties, we employed varying setup temperatures and deposition rates during the cathode growth process.

During deposition, a 543 nm He-Ne laser with 1.8 mW power was continuously illuminated onto the cathode's surface to enable real-time measurement of photocurrent and reflected power. A bias voltage of 250 V was applied between the anode and the sample

to collect the photocurrent from the cathode. Figure 4.6 illustrates a detailed photocurrent (at 543 nm) and reflected power (at 543 nm) history of a typical photocathode (KCsSb-7) during the growth.

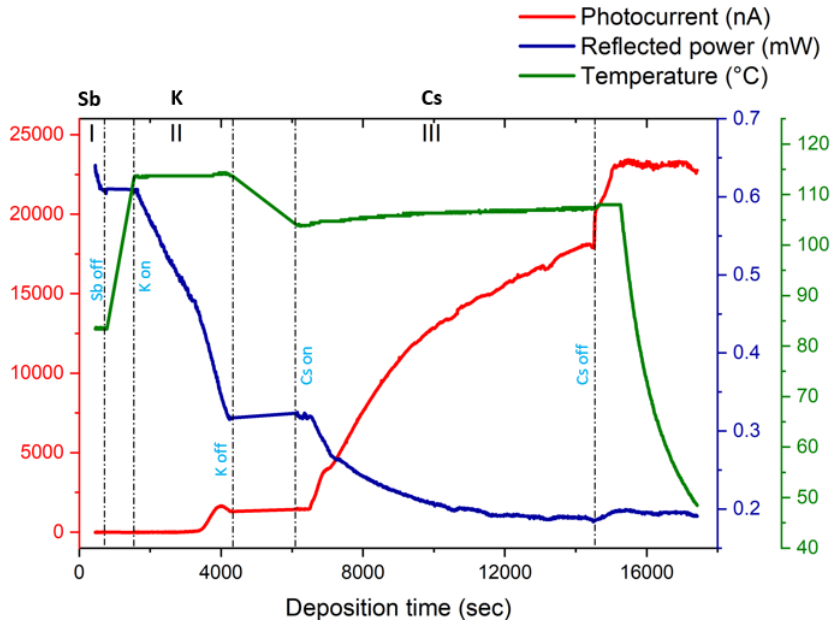

Figure 4.6: Typical photocurrent and reflected power curve recorded during the cathode deposition process. The variations in the reflected power demonstrate the reflectivity behavior throughout the growth. The plot is divided into three sections: section I illustrates the deposition history of Sb, while sections II and III depict the deposition history of K and Cs, respectively.

The key finding from this experiment emphasized the importance of better temperature control and its influence on the overall properties of the cathode. Understanding these variations will aid in optimizing growth recipes to enhance reproducibility. Further details regarding the growth procedure at each deposition stage and the impact of temperature and thickness variations on the photocathode's properties for all cathodes are presented in a subsequent section of this report.

As described earlier in the section, different thicknesses of Sb were initially evaporated onto the Mo substrate. During the K deposition process, the evaporated K atoms typically diffuse into the Sb film, leading to recrystallization into an alkali antimonide structure, often with M_3Sb stoichiometry, where M represents an alkali metal [131]. Sub-

sequently, upon Cs addition, the alkali antimonide film potentially recrystallizes into the cubic or hexagonal phase of the K_2CsSb structure, as explained by Schubert et al. [67].

Based on the Sb evaporation, we classified our photocathodes into two types: thick (with an Sb layer approximately 10 nm thick) and thin (with an Sb layer around 5 nm thick). The growth parameters of the cathodes produced in the "R&D" system are summarized in Table 4.1. Drawing from our experience with Cs_2Te [73] and our current work with K-Cs-Sb photocathodes, we observed that the ratio of evaporated thickness (i.e., K/Sb and Cs/Sb for K-Cs-Sb material), as shown in Table 4.1 demonstrated high reproducibility with their respective recipes. Therefore, this data serves as a valuable addition to evaluating the film's properties.

4.3.1.1.1 Mo Substrate

Conducting the reflectivity measurement of the Mo substrate is crucial as it allows us to assess and compare it with the reflectivity of the grown films. This initial evaluation serves as a reference point to validate and ensure the accuracy of our reflectivity measurements for the thin films. By comparing the reflectivity of the Mo substrate with that of the grown films, we can confidently attribute any observed variations or features (peaks) in the reflectivity spectra to the properties of the thin films (Sb, KSb, KCsSb, etc.). This essential step enables us to make meaningful and accurate analyses of the grown film's optical behavior and performance, ensuring the reliability of our results. Additionally, we performed a comparison between our measured reflectivity data of the Mo substrate and reference data from [125] (depicted in Fig. 4.7), which reveals a substantial agreement between the data sets. This comparison validates the accuracy and precision of our reflectivity measurement system while also confirming the quality of the Mo substrate used in the experiment. Here, it is important to note that the measured spectral reflectivity of Mo substrate used in both the "Production" and "R&D" systems was found to be similar and reproducible.

Table 4.1: Summary of cathode growth parameters and evaporated thicknesses of Sb, K, and Cs. All the thicknesses were measured using a pre-calibrated quartz microbalance (QMB). In the table, ΔR (%) represents the percental changes in the reflectivity after the respective K and Cs deposition.

Cathode	**Sb (nm)**	**K (nm)**	**Cs (nm)**	**K/Sb ratio**	**Cs/Sb ratio**	**TSb-TK-TCs (°C)**	**QE (%) (515 nm)**	ΔR (%) **after K (543 nm)**	ΔR (%) **after Cs (543 nm)**
KCsSb-4	5 ± 0.9	41 ± 0.1	106 ± 0.5	8.2	21.2	90-90-90	5.4	47	37
KCsSb-6	5 ± 0.9	32 ± 0.1	117 ± 0.5	6.4	23.4	90-120-90	5.8	48.5	36.6
KCsSb-7	5 ± 0.9	34 ± 0.5	121 ± 0.5	6.8	24.2	90-120-110	6.6	48.33	38.7
KCsSb-8	5 ± 0.9	43 ± 0.5	31 ± 0.5 *	8.6	6.2 *	90-130-120	8.8	61.19	46.6 *
KCsSb-3	10 ± 0.9	66 ± 0.5	313 ± 0.9	6.6	31.3	60-60-60 **	7.1	65.4	0
KCsSb-5	10 ± 0.5	75 ± 0.1	316 ± 0.5	7.5	31.6	90-90-90	6.3	66.6	-7
NaKSb(Cs)-2	9 ± 0.5	46 ± 0.1	-	5.1	-	90-120	0.3 #	68.8	-

Note: * Due to some technical problem, the Cs deposition was not fully completed for the KCsSb-8 cathode. ** The substrate temperature was increased from 60 °C to 90 °C during the Cs evaporation for the KCsSb-3 cathode, as reported in [130]; # QE is shown only for the K-Sb phase. Since the deposition procedure was similar up to K deposition between the KCsSb and NaKSb(Cs) cathodes, the K-Sb phase data from the NaKSb(Cs)-2 cathode is included in this table.

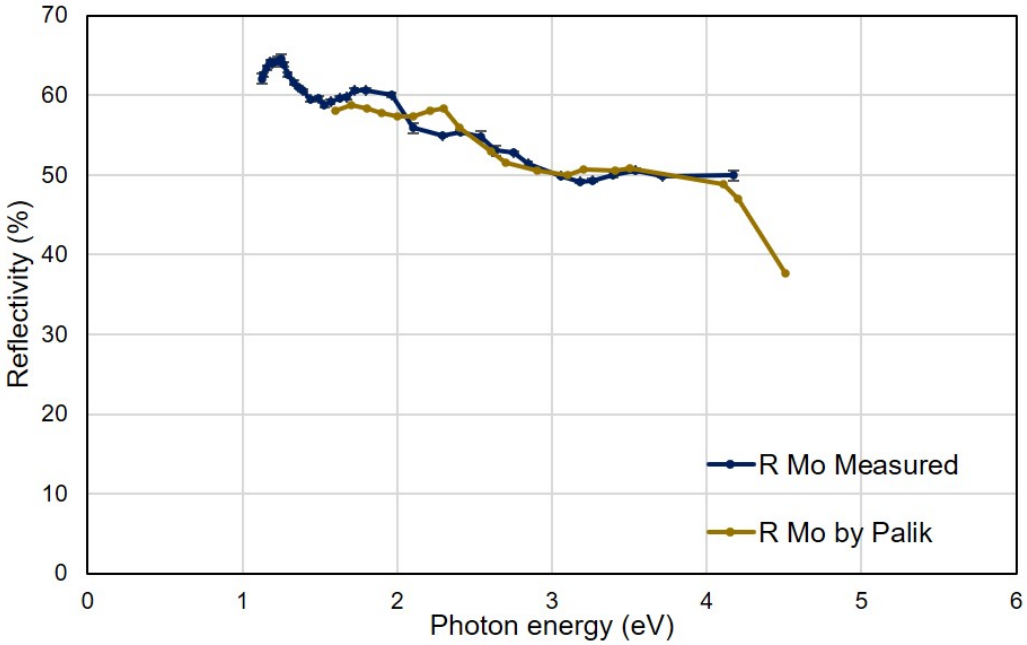

Figure 4.7: Comparison of the spectral reflectivity of Mo between our measurement and the data from Palik [125]. Reflectivity measurements were conducted on the Mo substrate that was used in both the "Production" and "R&D" systems, and we observed a similarity in the spectral reflectivity for both cases. The reflectivity data depicted in the plot are for the Mo substrate derived from the Mo plugs that were used within the "Production" system.

Given the significant impact of sample roughness (σ) on reflectivity, we estimate the roughness of our Mo substrate by assuming bulk properties [125] and utilizing the following Equation 4.7 [132]. In the past, a similar roughness estimation procedure was carried out at INFN LASA and can be found in the reference [133].

$$\frac{R}{R_0} = exp\left[-\left[\frac{4\cdot\pi\cdot\cos(\theta)\cdot\sigma}{\lambda}\right]^2\right] \tag{4.7}$$

Here in Equation 4.7, R represents the measured reflectivity, R_0 represents the reference reflectivity [125], θ represents the angle of incidence, and σ represents the average roughness.

Figure 4.8 illustrates the result of the fitting procedure, which determines a roughness value of 9.26 nm for the Mo substrates.

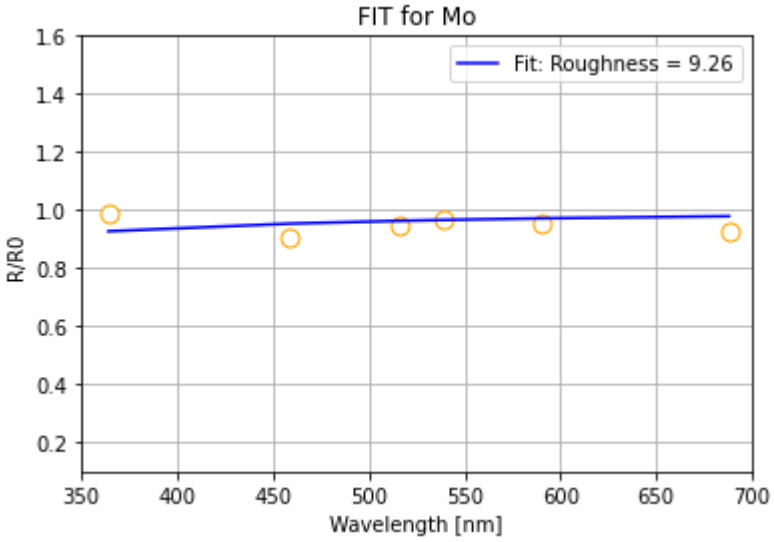

Figure 4.8: The calculated R/R_0 value at $\theta = 6°$ for Mo (yellow circles). The blue curve represents the fit of the data using Equation 4.7

.

4.3.1.1.2 Sb Structure

Numerous studies have demonstrated that the evaporation of antimony (Sb) is a remarkably complex process, and its properties can significantly influence the performance of the cathode [79, 134]. To investigate the effects of varying Sb thicknesses on the cathode's characteristics, we initiated the growth of the K-Cs-Sb photocathode by depositing Sb layers of 5 nm and 10 nm onto the Mo substrate as the initial step. This section presents the results obtained during the Sb deposition of some fully grown cathodes (i.e., KCsSb-4, 5, and 8).

While depositing Sb in the "R&D" preparation system, it was observed that for both thin (Sb = 5 nm) and thick (Sb = 10 nm) Sb films, the reflectivity (at 543 nm) was decreased. However, in the case of thicker Sb films (Sb = 10 nm), a gradual increase in reflectivity was observed after an initial decrease up to approximately 6 nm of evaporated thickness (Fig. 4.9a). For a more comprehensive investigation of this behaviour, we have grown Sb films with two varying thicknesses, 5 nm, and 15 nm, on the Mo substrate. During this process, we tracked the real-time changes in the reflectivity (at 543 nm), as

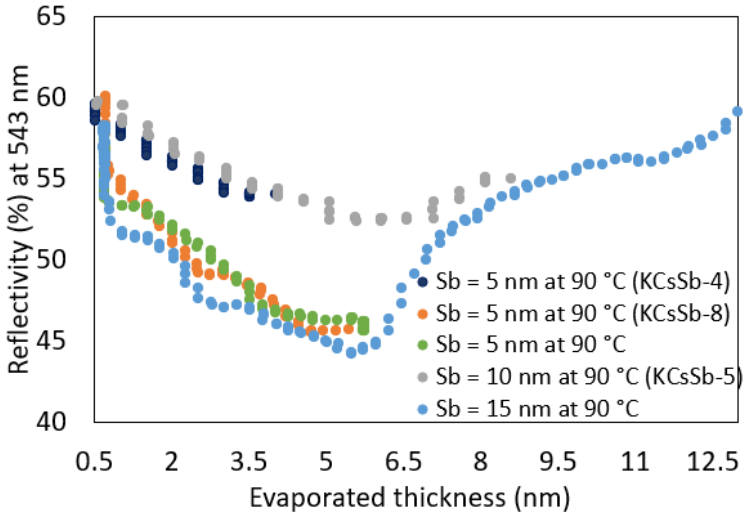

(a)

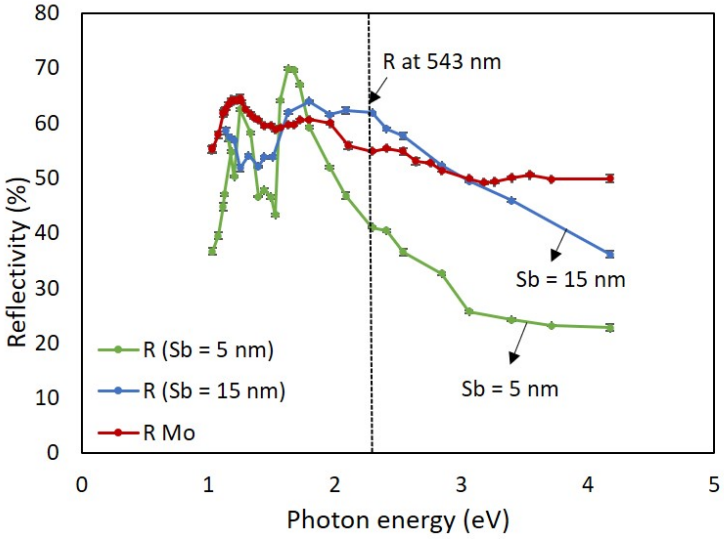

(b)

Figure 4.9: (a) Comparison of real-time reflectivity (at 543 nm) during different Sb depositions. In the plot, the real-time reflectivity history during the Sb deposition of some fully grown cathodes (i.e., KCsSb - 4, 5, 8) is presented. The thicknesses in the plot are the evaporated thickness of Sb. (b) Comparison of full spectral reflectivity between 5 nm and 15 nm Sb films on Mo.

illustrated in Figure 4.9a, and measured the full spectral reflectivity (from 254 nm to 1100 nm) at the end of the deposition, as displayed in Figure 4.9b.

It is important to mention that the deposition conditions (such as substrate temperature and deposition rate) remain similar across all Sb deposition processes. It is evident that the reflectivity (at 543 nm) exhibited a similar rise after reaching a film thickness of around 6 nm for the 15 nm Sb film (Fig. 4.9a). The consistent reproducibility of this behaviour suggests that the film's properties potentially changed around this particular thickness. Furthermore, the distinct behaviour of the full spectral reflectivity (from 254 nm to 1100 nm) between the Sb 5 and 15 nm films (as depicted in Figure 4.9b) gives additional support to this hypothesis. This indicates that Sb films were likely in an amorphous state during its initial stage and subsequently underwent a transition into a crystalline structure as the film's thickness exceeded approximately 6 nm. Several authors have previously reported the presence of this transformation through the utilization of various surface characterization techniques [79, 131, 135]. However, the specific value of this transition thickness might vary, influenced by various factors such as substrate type, substrate temperature, deposition rate, vacuum quality, and residual gases [79].

4.3.1.1.3 K-Sb Structure

The substrate temperature was kept higher during the deposition of K in comparison to Cs deposition due to the relatively lower vapor pressure of K. We generally stopped the K deposition once the photocurrent reached its maximum, as depicted in Figure 4.6. Our observations indicated that both the substrate temperatures and deposition rates played a significant influence on the quantum efficiency (QE) for both thin and thick K-Sb films during the growth. Generally, an elevated substrate temperature results in a more substantial rise in the QE, as depicted in Figures 4.10a and 4.10b. Furthermore, we observed a significant change in the slope of the real-time QE (at 543 nm) and reflectivity (at 543 nm) curves after a certain evaporated thickness (labeled as the transition point), as illustrated in Figure 4.10c and 4.10d. Indeed, the observed change in QE after a specific evaporated thickness indicates the transition of K-Sb from the amorphous phase to the crystalline phase [135]. Furthermore, we noted that these transition points from the amorphous to crystalline phase depended on the substrate temperature and usually occurred at a reduced amount of evaporated K with increasing substrate temperature, as illustrated in Figures 4.10a and 4.10b. This phenomenon could clearly be associated with an accelerated diffusion process between Sb and K, attributed to the elevated temperature, thus initiating the crystallization kinetics within the K-Sb film.

Furthermore, upon comparing the real-time reflectivity (at 543 nm) observed during the K deposition process on both thin and thick cathodes, it was discovered that the pattern of the reflectivity curve is remarkably consistent and correlates with the material's thickness (Fig. 4.11). Additionally, the reflectivity patterns differ between the thin and thick KSb films. This phenomenon is depicted in Figure 4.11 for both the "5 nm Sb" case (Fig. 4.11a) and the "10 nm Sb" case (Fig. 4.11b), and also can be seen in plots 4.10c and 4.10d. The distinctive pattern in reflectivity, particularly during K deposition on thin and thick cathodes, hints at a potential differentiation in crystal orientation between these two types of cathodes. A detailed investigation and analysis will be provided in the subsequent section of this chapter.

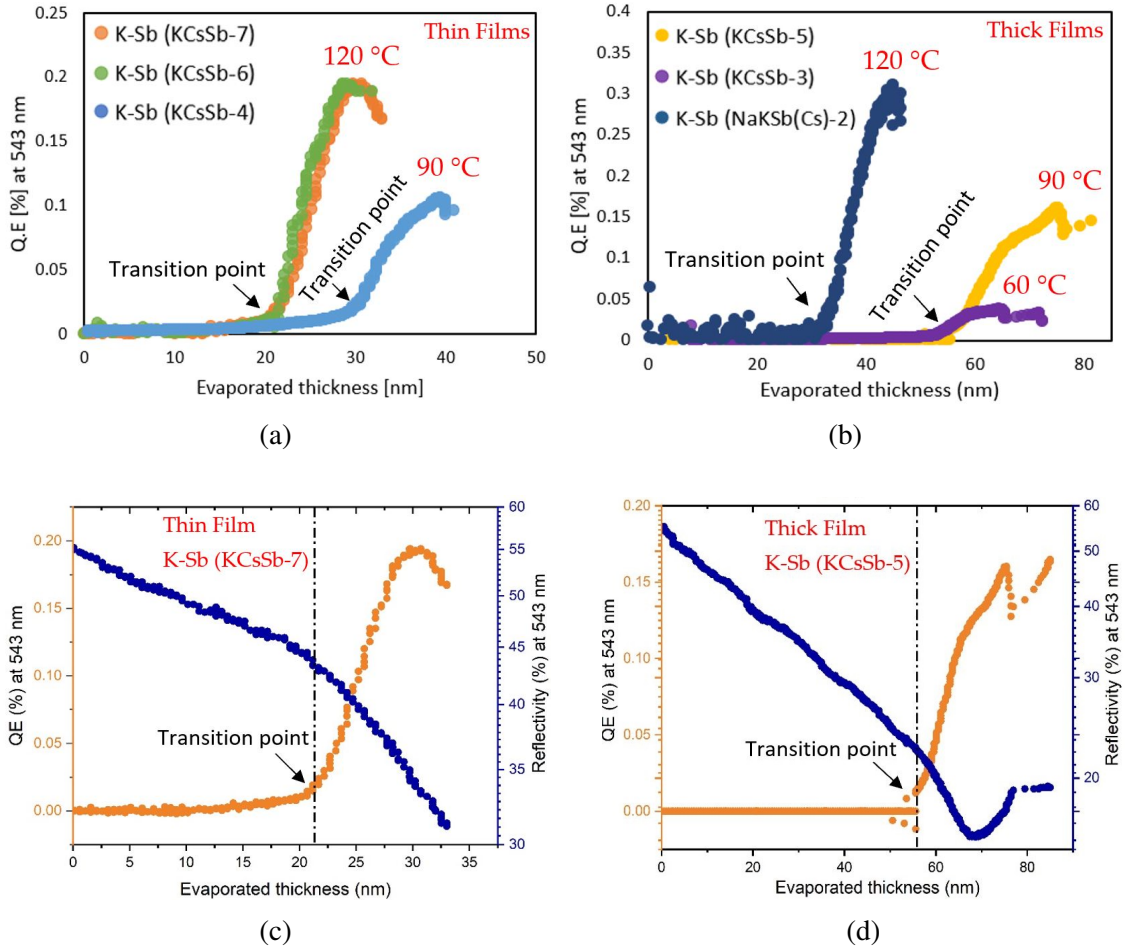

Figure 4.10: Comparison of real-time QE evolution (at 543 nm) during K deposition. (a) represent thin cathodes, and (b) represent thick cathodes. Since the deposition procedure was similar until K, the K-Sb phase data is included from the NaKSb(Cs)-2 cathode in plot b. The thicknesses presented in the plot represent the evaporated thickness of K. Real-time QE (at 543 nm) and reflectivity (at 543 nm) history during K deposition are shown for (c) a thin cathode (i.e., KCsSb-7) and (d) a thick cathode (i.e., KCsSb-5), respectively.

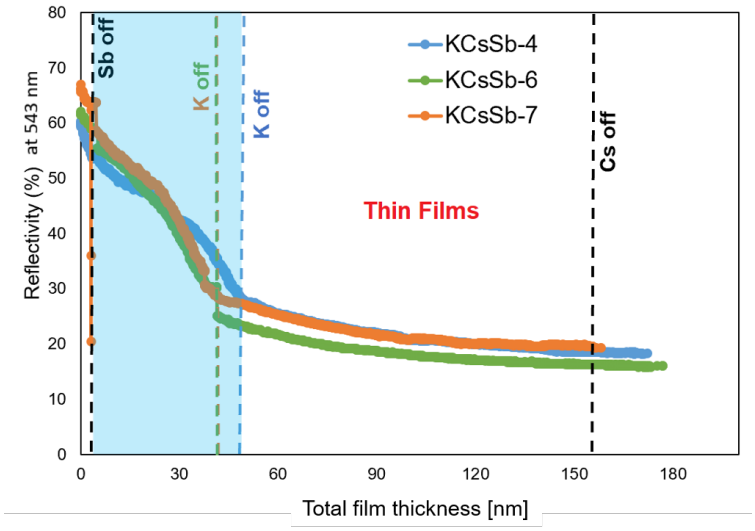

(a)

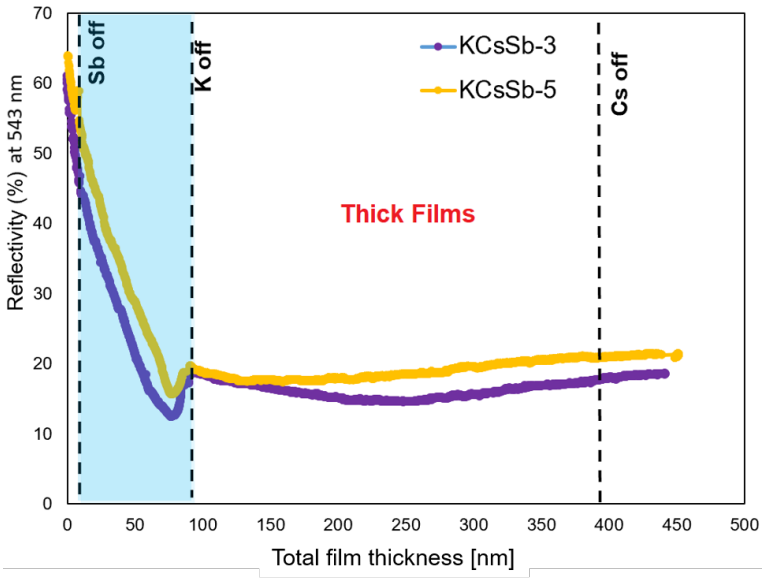

(b)

Figure 4.11: Comparison of real-time reflectivity (%) during the photocathode deposition for both (a) thin cathodes (Sb = 5 nm) and (b) thick cathodes (Sb = 10 nm) at 543 nm. The blue-colored box highlights the reflectivity during the deposition of potassium (K). The reflectivity behaviour observed during the deposition of K for both thin and thick cathodes suggests that the thickness of the Sb layer is the primary factor influencing this behaviour. The two 'K off' annotations in Figure 4.11a stem from the fact that K deposition was terminated at two distinct points of K thickness, as detailed in Table 4.1, which can also be observed in Figure 4.10a.

We also investigated the impact of varying deposition rates on the properties of the K-Sb film. In the case of the KCSb-8 cathode, we maintained a deposition rate of 0.2 to 0.4 nm/min (compared with 1 nm/min before) during the K deposition. As a consequence of modifying the deposition rate and introducing a marginal temperature increase (specifically, 130°C), a noticeable enhancement of QE of roughly 1.2% at 543 nm was detected for the K-Sb film (compared with the previously measured QEs of approximately 0.2% at 543 nm) for this cathode. Figure 4.12a displays a comparison of the real-time QE curve (vs. evaporated thickness) during the K deposition for all produced cathodes in the "R&D" system. Following the approach employed in Sb studies, to investigate the reproducibility of the higher QE associated with the lower deposition rate, we grew two thin (Sb = 5 nm) K-Sb films (KSb-1 and KSb-2) on the Mo substrate with varying deposition rates. We adjusted the deposition rates to 0.6–1 nm/min for KSb-1 and 0.2–0.4 nm/min for KSb-2; both grew at 130°C. Quantum efficiencies of about 0.3% for KSb-1 and 1% for KSb-2 were noted at 543 nm. The spectral response and reflectivity data for these two K-Sb films are presented in Figure 4.12b, illustrating the similar nature of the spectral behaviour (spectral response and reflectivity) for both cathodes. From the spectral response curve, the photoemission threshold ($E_g + E_a$) can be determined as 2.08 eV in both cases. The similarities in the spectral characteristics (reflectivity and spectral response) between the two films imply the potential formation of a similar compound in both cases. The specific mechanisms underlying this behaviour are not yet completely understood and need further investigation. One potential interpretation is that the elevated substrate temperature (130°C) could have increased the diffusive mobility of adsorbed molecules in both cathodes. Whereas, a reduced deposition rate led to a decrease in the arrival rate of the evaporated molecules (in the case of KSb-2). This, in turn, impacted the diffusive mobility of the previously adsorbed molecules, allowing them additional time to organize in a favored configuration [136]. This outcome can result in an enhanced material crystallinity, thereby leading to a significant enhancement in the quantum efficiency observed for the KSb-2 cathode.

Furthermore, we have conducted an examination of the "stopping potential vs. frequency" characteristics of these two films. The stopping potential vs. frequency plot shows how the stopping potential (or kinetic energy of emitted electrons) changes with

varying wavelengths of incident light, providing valuable information about the energy levels of electrons in the material and their interactions with photons. A comprehensive discussion of these two films is elaborated in Appendix A.

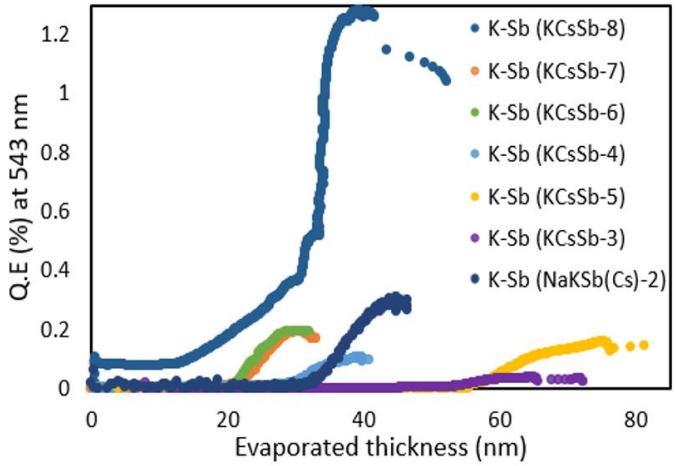

(a)

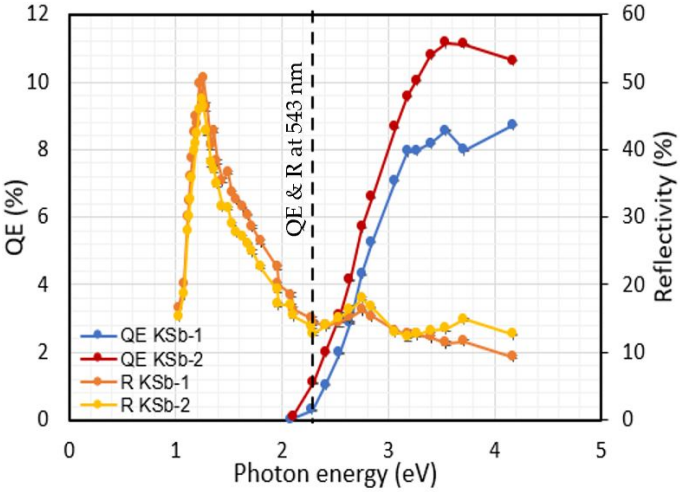

(b)

Figure 4.12: (a) Comparison of the real-time QE vs. evaporated thickness (at 543 nm) measured during K deposition of all produced K-Sb films in the "R&D" preparation system. (b) Spectral response and reflectivity measurements of KSb-1 and KSb-2 cathodes taken after deposition.

At the end of the K deposition, the film commonly exhibited a purple colour, resembling the colour reported by Sommer [137]. The spectral response for all K-Sb films produced within the "R&D" system is displayed in Figure 4.13a. The analysis of the spectral response curve further facilitated the calculation of the (E_g + E_a) value for the photocathode. This value signifies the threshold for photoemission in semiconductor photoemitters. The QE's dependence near the photon energy threshold can be understood by utilizing Equation 4.8, which was documented by W. E. Spicer [75]:

$$QE = \frac{G(h\nu) \cdot (h\nu - (E_g + E_a))^{\frac{3}{2}}}{(h\nu - (E_g + E_a))^{\frac{3}{2}} + \gamma} \tag{4.8}$$

Where, $h\nu$ represents the photon energy, $E_g + E_a$ is the sum of energy gap and electron affinity of the photocathode, and $G(h\nu)$ is a function of the photon energy. The parameter γ can be calculated as $\gamma = (\alpha + \beta)/C$, where β and C are constants, and α represents the absorption coefficient. By fitting Spicer's model (Equation 4.8) to the experimental data (illustrated in Figure 4.13b), we estimated that the photoemission threshold value for the K-Sb film is 2.08 eV. This value closely aligns with findings from other literature sources [75, 79].

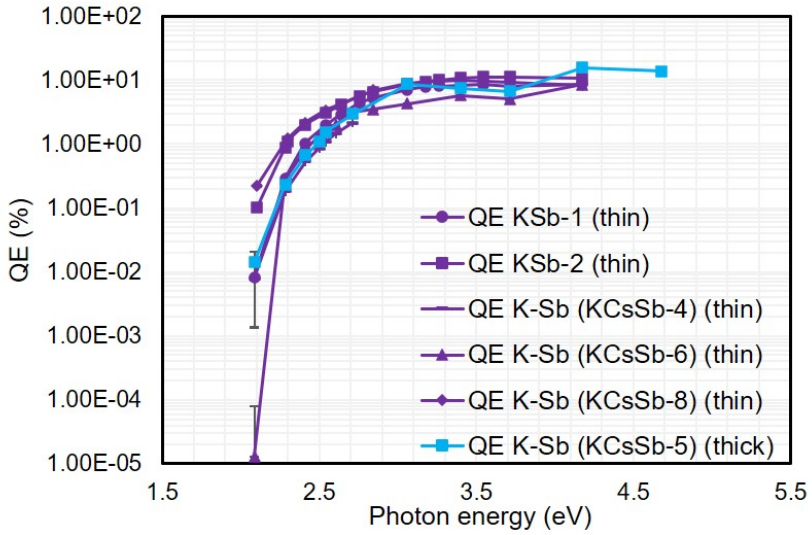

(a)

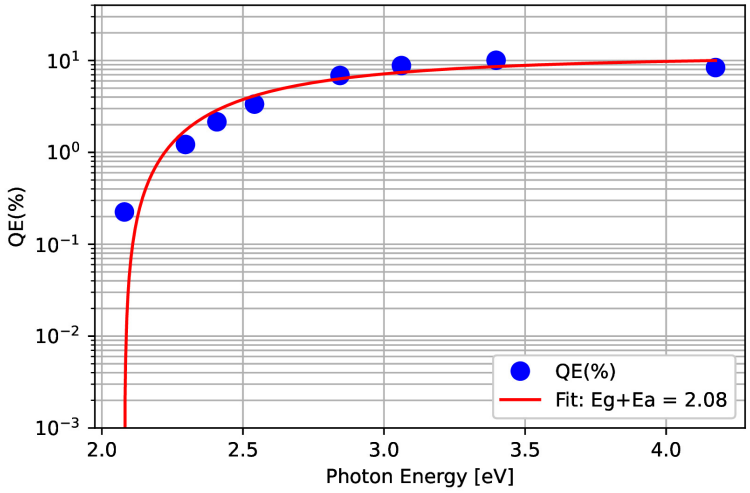

(b)

Figure 4.13: (a) Spectral response of all produced K-Sb films in the "R&D" system. The spectral response of thin and thick cathodes are highlighted in violet (with different symbols) and light blue colors, respectively. Due to some technical problem, the spectral response of K-Sb films of cathodes KCsSb-3 and KCsSb-7 has not been measured. (b) Spectral response of K-Sb film (Sb = 5 nm) of cathode KCsSb-8 (blue markers). The red curve is the fit of the experimental data with Equation 4.8.

4.3.1.1.4 K-Cs-Sb Structure

Finally, the formation of a K-Cs-Sb compound was achieved by sequentially depositing Cs onto the K-Sb films. Cesium was typically evaporated until the photocurrent was close to the saturation level, as depicted in Figure 4.6. Given the consistent reproducibility of the evaporated thickness ratio (i.e., K/Sb and Cs/Sb) with their definite recipes (shown in Table 4.1), we also took into account the Cs/Sb ratio as a supplementary criterion to end the Cs deposition. In this phase, we investigated the influence of substrate temperature and thickness, factors that could potentially affect the properties of the cathode. We observed that the substrate temperature often had a notable influence over the intricate interplay between the rate of compound formation and the displacement rate of pre-existing elements on the substrate. Typically, the quantum efficiency (QE) showed a correlation with the substrate temperature for all six cathodes, as depicted in Figures 4.14a and 4.14b. However, in Figures 4.14a, the QE behavior varied between the KCsSb-4 and KCsSb-6 cathodes, despite being deposited at similar substrate temperatures. This difference can be attributed to the fact that K deposition was carried out at different substrate temperatures for these two cathodes: 120 °C for KCsSb-6 and 90 °C for KCsSb-4, as shown in Table 4.1 and Fig. 4.10a. As explained by Schubert et al., the intermediate K-Sb compound plays a crucial role in determining both the phase structure and QE of the KCsSb compound [67]. It is therefore deduced that variations in the formation of the KSb compound, driven by the different K deposition temperatures, may have led to the different QE behaviors of the KCsSb-4 and KCsSb-6 cathodes during Cs deposition.

Upon analyzing the Cs/Sb ratio (i.e., evaporated thickness ratio) presented in Table 4.1, it becomes apparent that it generally depends on the initial Sb thickness. Our measurements indicate that the ratio was higher in thick photocathodes compared to thin ones. The real-time evolution of the reflectivity (at 543 nm) of all produced cathodes is depicted in Figure 4.14c. As the Cs evaporation started, it was observed that the reflectivity decreased for both thin and thick cathodes. However, in the case of thick cathodes, the reflectivity again increased and stabilized close to the end of the evaporation. The observed variation in such behavior suggested a complex and distinct interplay of stoichiometric and chemical composition that potentially underwent changes during the growth of both

typologies of cathodes. Alternatively, this dissimilarity could be attributed to the film thicknesses of the K-Cs-Sb films, similar to findings observed in the case of Cs_2Te [73].

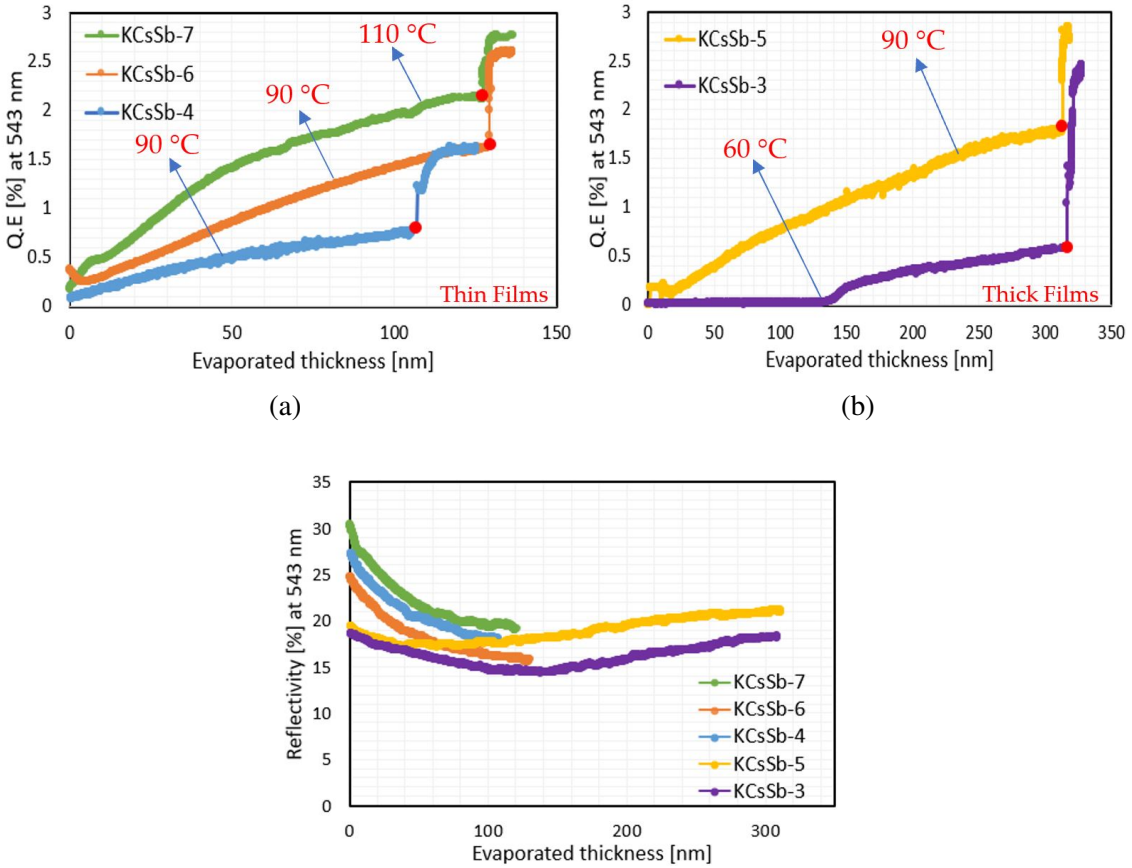

Figure 4.14: Comparison of real-time QE (at 543 nm) evolved during Cs deposition. (a) represent thin cathodes, and (b) represent thick cathodes. Due to some technical problem, the Cs deposition was not fully completed for the KCsSb-8 cathode; therefore, it is not included in plot "a". Red solid circles in plots "a" and "b" show the point where the Cs source was turned off. (c) represents the changes in the real-time reflectivity (at 543 nm) during Cs deposition. The thicknesses shown in the plot represent the evaporated thickness of Cs.

At the end of the Cs evaporation (precisely: after turning off the Cs source), we observed a sudden increase in the QE curve for each cathode, as illustrated in Figures 4.14a and 4.14b. During this particular event, no substantial shifts were observed in the real-time reflectivity. Certainly, such a fast QE response couldn't have been attributed to a modification in the compound's bulk stoichiometry. This suggests that such an anomaly might have originated from the subsurface region of the films. Typically, due to its comparatively lower melting point (28.44 °C) and high vapor pressure [138], a portion of the Cs atoms that were deposited on the sample (where the temperature is around 90–110 °C) should have been prone to evaporate. A similar phenomenon of Cs atom loss due to evaporation over the substrate temperature of 50 °C has been previously reported in the case of K_2CsSb and Cs_3Sb photocathodes [139, 140]. As a consequence of such evaporation, there is a possibility that a temperature-sensitive surface layer may have been formed near the subsurface region of the films during the deposition. This, in turn, could have established a balance between the adsorption (inward Cs being distributed and diffused) and desorption (evaporated Cs from the surface) of cesium atoms near the surface. A sudden decrease in the evaporation rate or any increase in the substrate temperature could disrupt this equilibrium, and it would have impacted the emission barrier via electron affinity; Figure 4.15 attempts to depict such a phenomenon. Table 4.2 displays the absolute percentage of the QE increase after shutting down the Cs source of all cathodes. It is evident that the rate of the QE increase could be related to the substrate temperature. For example, in the case of the KCsSb-4, KCsSb-5, and KCsSb-6 cathodes, the percentage of the QE increase was largely consistent and linked to the equivalent substrate temperature. Furthermore, it's intriguing to observe that this sudden QE increase was primarily correlated to the substrate temperature, irrespective of the evaporated thickness of KCsSb (or Sb), as demonstrated (in Table 4.1) for the T = 90 °C case with the thin (KCsSb-4 and KCsSb-6) and thick (KCsSb-5) cathodes. For cathode KCsSb-7, the increase was minimal (compared to other cathodes, i.e., 30 %) and could likely be associated with the higher substrate temperature. One plausible interpretation is that due to the higher substrate temperature (for KCsSb-7), the loss of Cs due to evaporation might have been compensated by an improved diffusion rate, potentially resulting in a trade-off between

the incoming and outgoing Cs atoms at the surface.

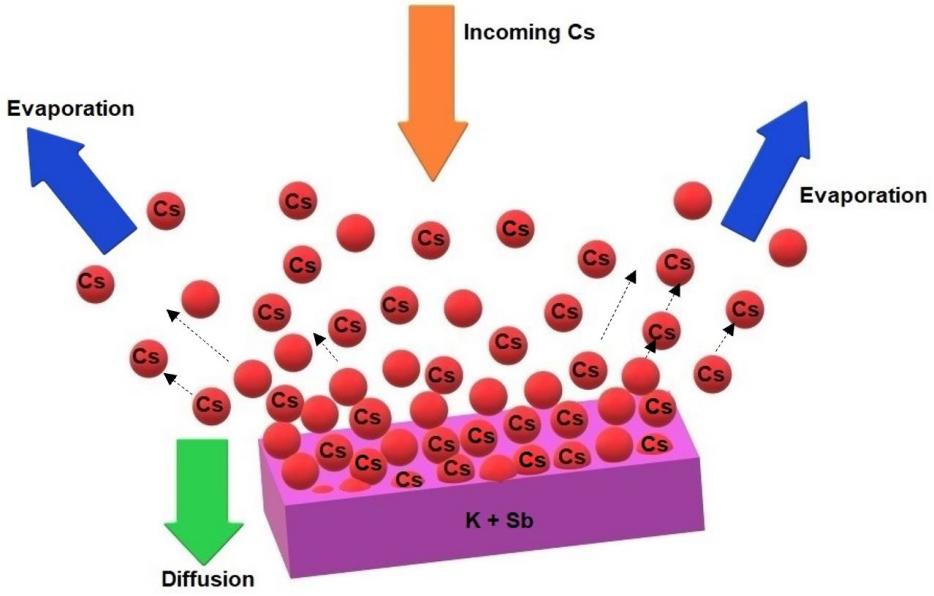

Figure 4.15: The schematic diagram depicts the competing processes of diffusion and evaporation occurring during the deposition of Cs onto the K-Sb compound.

Table 4.2: Summary of the absolute % QE increase after turning off the Cs source and corresponding substrate temperature. * The substrate temperature was increased from 60 °C to 90 °C during the Cs evaporation for the KCsSb-3 cathode, as reported in [130].

Cathode	Substrate temperature (°C) during Cs deposition	% QE Increase
KCsSb-3	60 *	308 ± 0.02
KCsSb-4	90	57 ± 0.02
KCsSb-5	90	55 ± 0.02
KCsSb-6	90	63 ± 0.02
KCsSb-7	110	30 ± 0.02

Figure 4.16 summarizes the spectral responses and reflectivity of all the cathodes produced within the "R&D" preparation system. The spectral response exhibited a consistent pattern across all cathodes. The maximum QE at 514 nm was recorded at 8.8% for the KCsSb-8 cathode. A more comprehensive discussion and interpretation of the spectral response curve are elaborated in Appendix A. However, the comparison of reflectivity revealed a disparity in the behavior at lower photon energies (from 2.28 eV downwards, highlighted by red circles) between the thin and thick cathodes, as depicted in Figure 4.16b. Furthermore, we detected two distinct reproducible colors of films: violet and blue, which were linked to the thin and thick cathodes, respectively, as shown in Figure 4.17.

In an effort to determine the photoemission threshold value, we fit Equation 4.8 to our experimental spectral response data (illustrated in Figure 4.18). This procedure yielded a range of values for $E_g + E_a$, which exhibited variation between 1.93 and 2 eV from cathode to cathode. The values obtained through estimation exhibited notable resemblance to those determined by other studies in the literature (i.e., E_g = 1.2 eV and E_a = 0.7 eV, $E_g + E_a$ = 1.9 eV) [79].

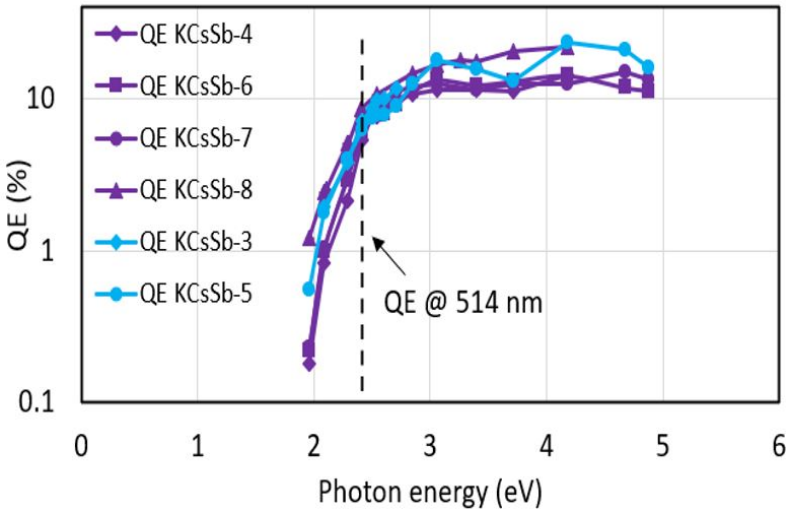

(a)

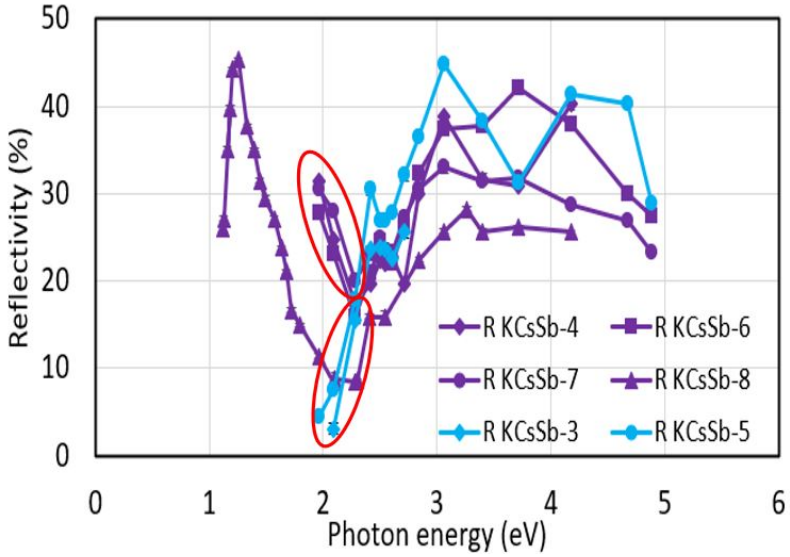

(b)

Figure 4.16: (a) Spectral response and (b) reflectivity of all K-Cs-Sb cathodes produced in the "R&D" system. The spectral response and reflectivity of thin and thick cathodes are highlighted in violet (with different symbols) and light blue (with different symbols) colours, respectively. The red circles in plot "b" highlight the difference in the reflectivity at low photon energy for thin and thick cathodes. Unfortunately, the reflectivity could only be measured over an extended range (up to 1100 nm) for the KCsSb-8 (thin) cathode.

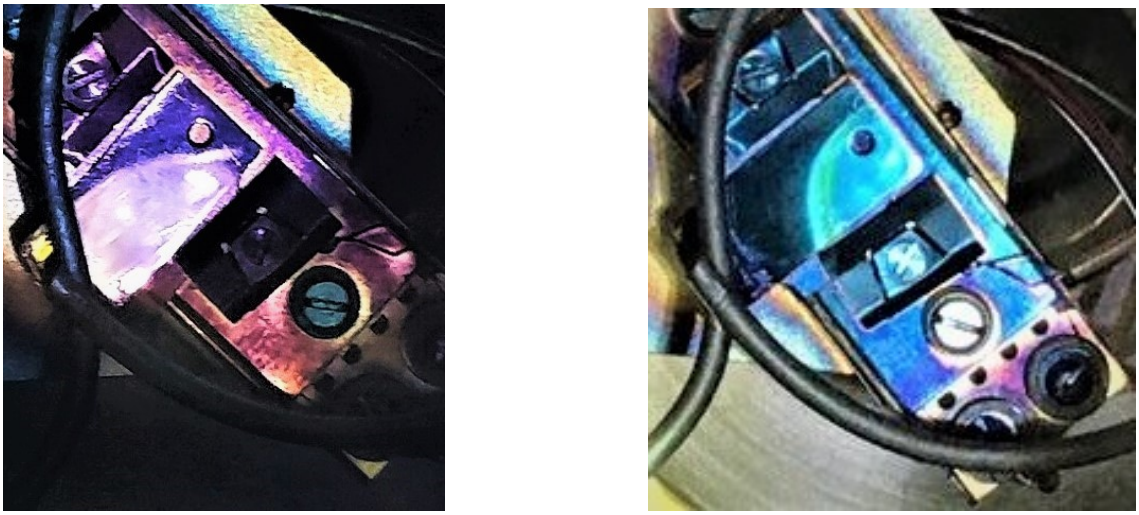

(a) (b)

Figure 4.17: Colors of photocathodes after the deposition (a) thin cathodes, and (b) thick cathodes.

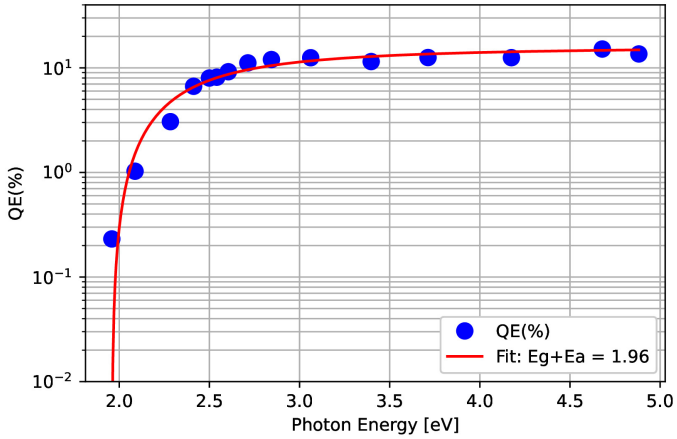

Figure 4.18: Spectral response of KCsSb-7 (thin) cathode (blue markers). The red curve is the fit of the experimental data with Equation 4.8.

4.3.1.2 Effect of Heat Treatment

Concerning the KCsSb-3 cathode, approximately eleven days after its production, we measured the spectral response and observed that the quantum efficiency at various wavelengths remained consistent compared to the measurement obtained one day after production. This observation confirms that maintaining the QE of such a cathode within the chamber is achievable through good vacuum conditions (approximately pressure = 5×10^{-11} mbar).

Thereafter, we elevated the substrate temperature of the KCsSb-3 cathode from room temperature (23 °C) to 120 °C and detected a substantial rise in the photocurrent at 543 nm. Then, the sample was maintained at this temperature for a duration of 30 minutes, followed by a gradual cooling process. The primary objective of this experiment was to assess the impact of heat treatment on the overall quantum efficiency of the photocathode. Following this treatment, a spectral response measurement was conducted, as illustrated in Figure 4.19. A clear significant increase in QE had been observed for the KCsSb-3 cathode; the QE increased from 3.85% to 4.93% at 543 nm (2.28 eV) after the heat treatment. As illustrated in the reference [130], the substrate temperature was increased from 60°C to 90°C during the Cs evaporation for the KCsSb-3 cathode, compared to other cathodes where Cs was deposited at around 90°C to 120°C (Table 4.1). Therefore, it is anticipated that some of the Cs did not fully react at the lower temperature (i.e., 60°C). This increase in QE after the heat treatment implies that as the temperature increases, unreacted or partially reacted Cs may interact with the bulk photocathode, leading to a decrease in the compound's electron affinity. This, in turn, could result in an increase in the QE of the cathode.

A similar heat treatment was also applied to the KCsSb-4 cathode; however, no significant increment in the QE was noticed, as shown in Fig. 4.20. Comparable heat treatment was also applied to other KCsSb cathodes (thick & thin), yielding no major increase in the quantum efficiency, similar to the KCsSb-4 cathode. This indicates that the heat treatment process effectively increases QE only when there is an ample presence of Cs (unreacted or partially reacted) on the cathode surface, regardless of cathode thickness. In the case of KCsSb-3, where a substantial amount of Cs (unreacted or partially reacted) was present

due to the initial Cs deposition being done at a relatively lower temperature (i.e., 60°C), this effect is particularly evident [130].

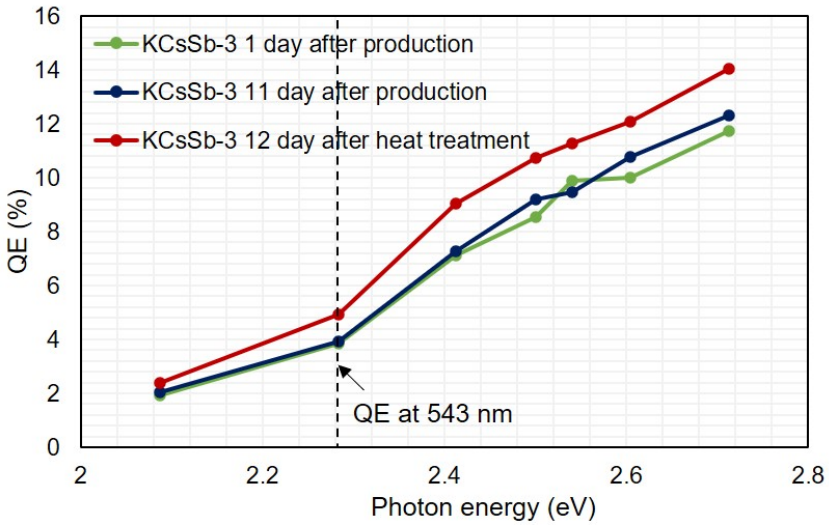

Figure 4.19: Spectral response of photocathode KCsSb-3 before and after the heat treatment.

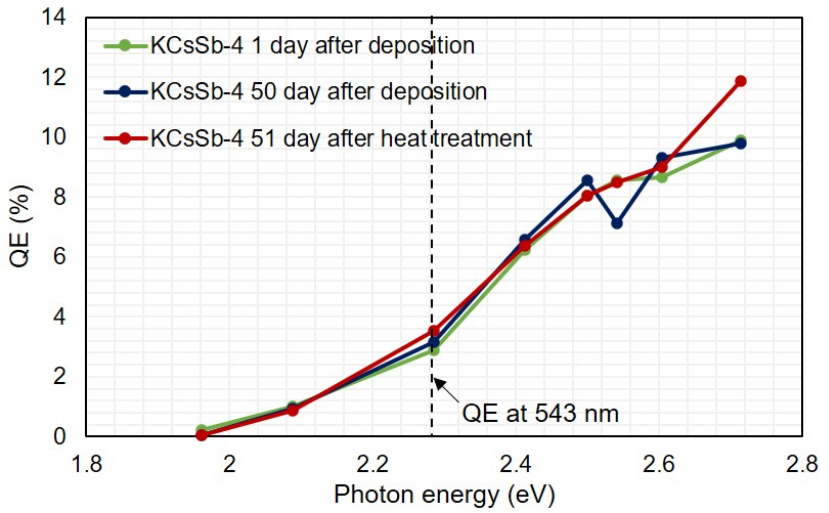

Figure 4.20: Spectral response of photocathode KCsSb-4 before and after the heat treatment.

4.3.1.3 Cathode Degradation Study

All the photocathodes remained quite stable after being produced. The storage lifetime of the cathodes inside our photocathode preparation system (base pressure 10^{-11} mbar) was several months and even years. Nevertheless, various studies, including our own findings, demonstrate a short operational lifetime inside an RF gun [46, 80]. Various factors, such as chemical poisoning, ion back bombardment, laser-induced heating, increased vacuum pressure during operation, and thermal decomposition, might be responsible for this outcome. To assess the impact of laser heating on the properties of the cathode, we exposed the cathode KCsSb-7 to continuous illumination from a He-Ne laser with a wavelength of 543 nm and an optical power of 2 mW (i.e., a power density of 0.4 W/cm^2) on its surface for a duration of 15 days, resulting in an average emitted current of 23 μA, all within the preparation system. No reduction in the quantum efficiency at 543 nm was observed during this process. Furthermore, simulation studies by R. R. Mammei et al. demonstrated that even with high laser power (1.5 W), the temperature of a K_2CsSb photocathode on a Mo substrate could remain below 50 °C [141]. This is because Mo has better thermal conductivity, allowing the absorbed laser power's heat to dissipate efficiently from the surface. Therefore, the degradation of the cathode linked to laser lighting alone is less likely, particularly when the cathode is on a Mo substrate [46].

In order to understand the impact of temperature on the cathode degradation, we heated our cathodes up to 450 °C. Figure 4.21 depicts the changes in real-time quantum efficiency (at 543 nm) and reflectivity (at 543 nm) for both thin (KCsSb-6) and thick (KCsSb-5) cathodes during this process. It can be seen that the quantum efficiency experienced a slight initial increase but subsequently decreased when the substrate temperature exceeded 100 °C for both cathodes. The small initial increase in QE could be attributed to the reaction of excess Cs on the cathode surface with the bulk film, as discussed in the previous section. Then, a sharp decline in the QE (marked as point A in Figure 4.21) was observed when the temperature increased over $\sim$ 140 °C, and $\sim$ 125 °C for thin and thick cathodes, respectively. Comparing the decline rate after the dotted line (the point where QE starts to decline) and after point A in Figure 4.21 for thin and thick cathodes reveals two distinct decay rates in the QE, indicating that the dissociation of the cathode material

was primarily influenced by the substrate temperature.

For the thick cathode (KCsSb-5), the reflectivity initially decreased when the temperature exceeded approximately 130 °C and then gradually increased when the temperature went above about 190 °C (see Fig. 4.21b). However, in the case of the thin cathode (KCsSb-6), the reflectivity kept rising consistently as the substrate temperature went beyond 130 °C (see Fig. 4.21a). This observed difference in the real-time reflectivity behavior during the cathode degradation process between produced thick (i.e., KCsSb-3 & KCsSb-5) and thin (i.e., KCsSb-4, KCsSb-5, KCsSb-6, KCsSb-7) cathodes was found to be consistently reproducible, indicating potential differences in crystal structures between these two types of photocathodes (i.e., thick and thin). Based on the QE curve depicted in Figure 4.21, it is evident that beyond 220 °C, the QE approaches zero for both thin and thick cathodes. However, the reflectivity curve in Figure 4.21 reveals a discrepancy: for the thin film, the cathode materials were nearly completely evaporated as the temperature exceeded 230 °C, whereas for the thick cathode, complete evaporation occurred beyond 420 °C. These observations suggest that the thermal properties and structural response during heating differ between thin and thick cathodes [142]. A further cathode degradation study of KCsSb compound is presented in the forthcoming section 4.4.5.6.

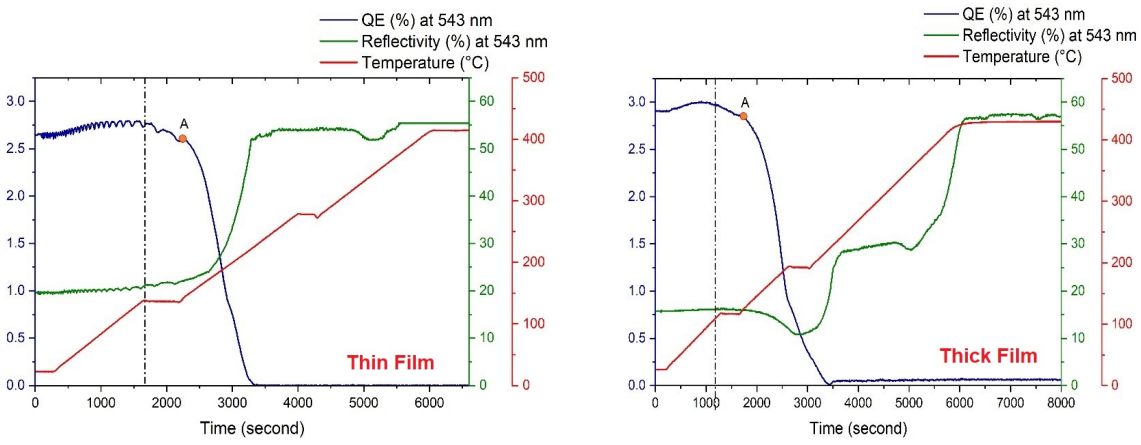

(a) (b)

Figure 4.21: Real-time QE (at 543 nm), reflectivity (at 543 nm), and temperature evolution during the study of the cathode degradation process, (a) for a thin cathode (KCsSb-6) and (b) for a thick cathode (KCsSb-5). The dotted line represents the point where the QE starts to decrease. "A" denotes the point where the QE starts to decrease rapidly.

4.3.2 Experimental Results Obtained from NaKSb(Cs) Photocathodes

NaKSb(Cs) photocathode are valued for their impressive photocathode properties, including high sensitivity, wide spectral response, greater robustness, and the ability to work at higher temperatures. These attributes make it a fitting choice for our present application. Hence, a preliminary attempt was made to develop NaKSb(Cs) photocathodes in our "R&D" preparation chamber. So far, a total number of two photocathodes have been produced. The following section provides the fabrication procedure and presents the experimental outcomes obtained from these two cathodes.

4.3.2.1 Fabrication Recipes

The fabrication process for both photocathodes is identical, except for the varying thicknesses of the deposited Sb layer. For the first cathode (i.e., NaKSb(Cs)-1), we initiated the process by depositing a 5 nm thick Sb layer at 90 °C, followed by K at 120 °C and Na at 130 °C. Subsequently, on top of it, we deposited Sb and Cs at 120 °C. However, the higher substrate temperature during Cs deposition led to a decline in the QE, dropping from an initial 1% to 0.3% (at 543 nm), resulting in a final recorded QE of 0.3% at 543 nm for NaKSb(Cs)-1. In an attempt to enhance the QE, we also experimented with a yo-yo-type deposition of Cs and Sb on the NaKSb(Cs)-1 cathode surface. The detailed deposition procedure is outlined in Appendix B. Post the yo-yo-type deposition, the QE at 543 nm for the NaKSb(Cs)-1 cathode increased from 0.3% to 0.6%.

Due to the low QE obtained for the first cathode, we modified our recipe for the second cathode as follows: initially, we deposited Sb until the reflectivity had dropped to 30% of its initial value (corresponding to an Sb thickness of 9 nm). Subsequently, we deposited K at 120 °C and Na at 90 °C in sequence until the QE reached its peak value. Afterward, a small amount of Sb and K was alternately added at 90 °C until the peak of QE to correct the Na:K ratio. Afterwards, Cs deposition was carried out at 90 °C until the sensitivity reached its maximum value.

The real-time QE (at 543 nm) and reflectivity (at 543 nm) history are depicted in Fig.

4.22. Due to technical difficulties, the reflectivity changes during the first phase of Sb deposition were not captured. Consequently, the reflectivity curve in Figure 4.22 remains constant throughout the first phase of the Sb deposition process.

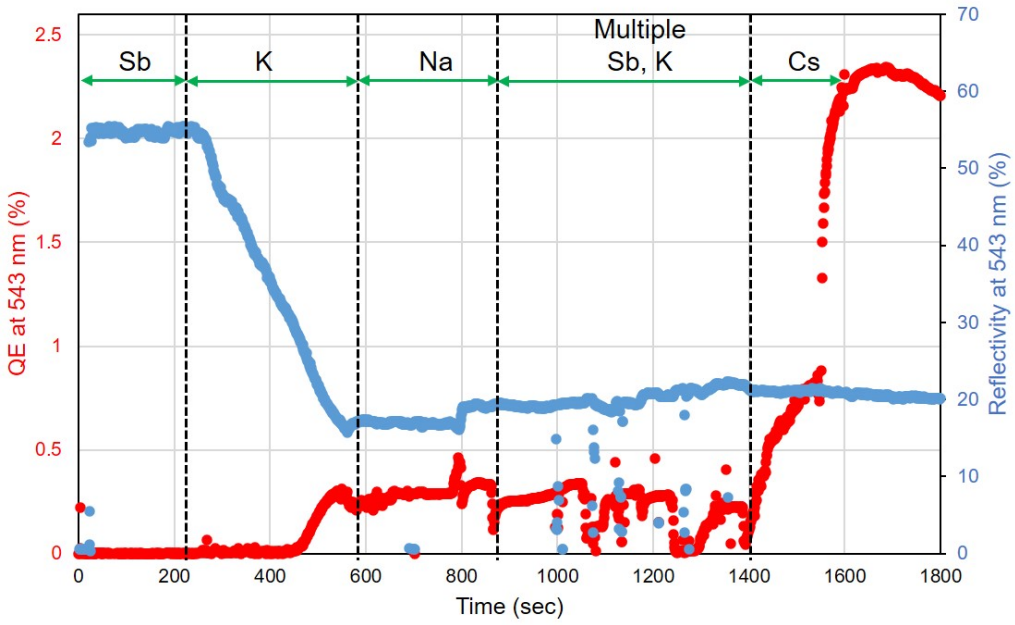

Figure 4.22: Real-time QE (red) and reflectivity (blue) during deposition of cathode NaKSb(Cs)-2.

The spectral response and spectral reflectivity of the NaKSb(Cs)-2 cathode were evaluated post-deposition and are presented in Fig. 4.23. Similar to the KCsSb cathodes, we applied Equation 4.8 to our experimental spectral response data (Figure 4.24) to determine the photoemission threshold value. This analysis yielded a value of 1.80 eV for (E_g + E_a). The value is slightly higher compared to reference [77], and this difference could be attributed to variations in stoichiometry.

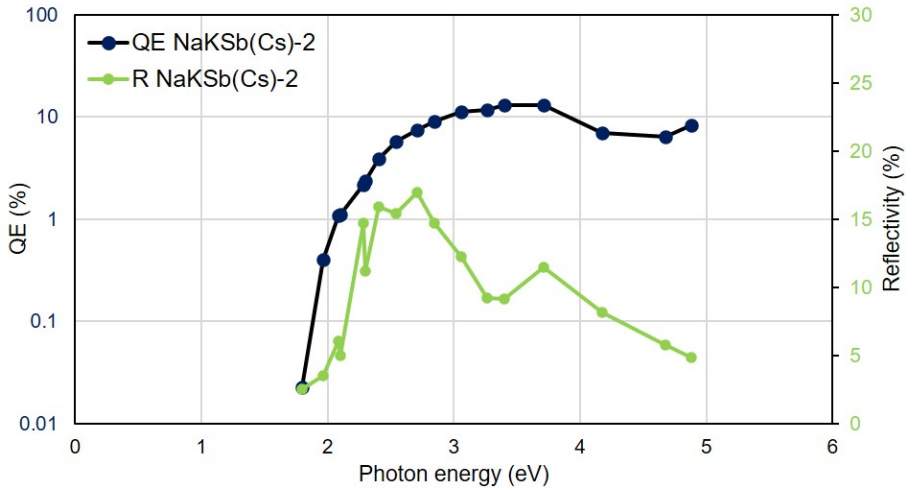

(a)

Figure 4.23: Spectral response and spectral reflectivity plot for the NaKSb(Cs)-2 cathode.

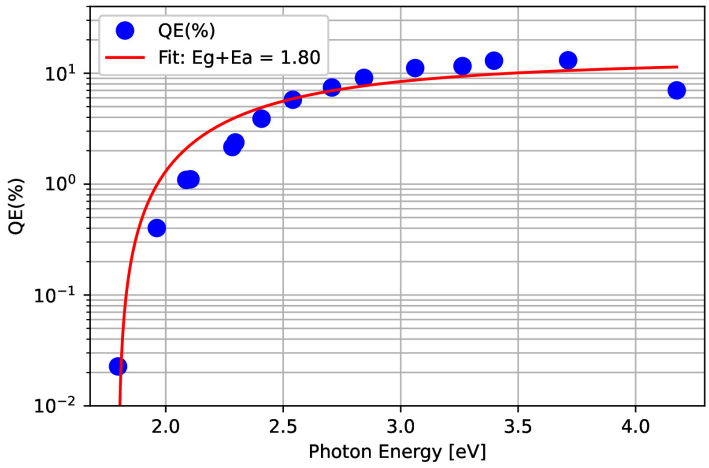

Figure 4.24: Spectral response of NaKSb(Cs)-2 (blue markers). The red curve is the fit of the experimental data with Equation 4.8.

We also made a comparison between the spectral response behaviors of the KCsSb-6 (Sb = 5 nm) and the NaKSb(Cs)-2 photocathodes, illustrated in Fig. 4.25. The results show a slightly improved QE value for the NaKSb(Cs) cathode, particularly at higher wavelengths, typically corresponding to the response to red laser light. Interestingly, electron emission was achieved even when exposed to 690 nm laser light (QE of 0.022%), highlighting the broader spectral response of the NaKSb(Cs) photocathode. This behavior might be attributed to the addition of Cs and Sb into the NaKSb material, potentially leading to a reduction in the material's overall electron affinity [75, 77, 143].

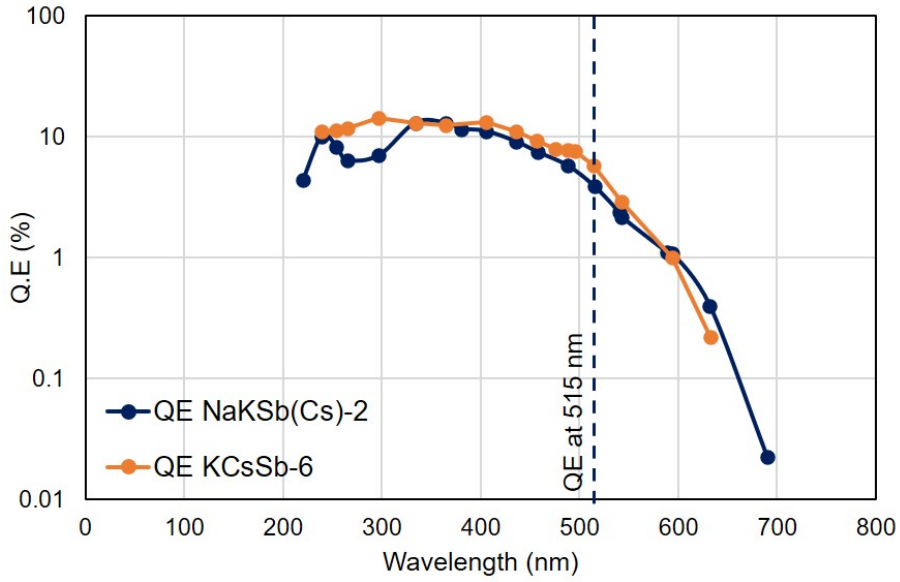

Figure 4.25: Comparison of the spectral response between the NaKSb(Cs)-2 and KCsSb-6 photocathodes.

We also made a comparative analysis regarding the overall evaporated thickness of KCsSb-6 and NaKSb(Cs)-2 photocathodes, and the results are documented in Table 4.3. Our findings indicate that the total evaporated thickness of NaKSb(Cs) is significantly less than that of the KCsSb compound, providing an inherent benefit in terms of the final roughness of this photocathode. In fact, in recent research, it has been demonstrated that the final roughness of a photocathode typically correlates with the film thickness [131]. Therefore, it would be very interesting to test this kind of photocathode within

the operational environment of the PITZ RF gun. The results in terms of QE (at 515 nm), lifetime, and robustness can then be compared with the parameters of the KCsSb photocathode in this environment.

Table 4.3: Cathode Characteristics of KCsSb and NaKSb(Cs) photocathodes. The thickness measurements were obtained using the pre-calibrated Quartz Crystal Microbalance (QCM).

Cathode	Evap. thickness (total) [nm]	QE @ 515 nm [%]
KCsSb-6	154 ± 2	5.8
NaKSb(Cs)-2	93 ± 1	3.9

4.3.2.2 Cathode Lifetime Study

The NaKSb(Cs)-2 cathode was fabricated within the "R&D" preparation system in February 2020. However, due to the COVID-19 pandemic, the cathode destruction study, similar to that conducted for KCsSb cathodes, could not be carried out. As a result, the cathode remained within the preparation system (base pressure of 10^{-11} mbar). In March 2022, we conducted a follow-up spectral response measurement. The corresponding spectral responses and spectral reflectivity plots of the NaKSb(Cs)-2 cathode are displayed in Fig. 4.26. We observed a reduced but still noteworthy quantum efficiency value across all the wavelengths: QE = 0.68% at 540 nm (2.29 eV) compared to the initial value of 3.27%. Notably, we identified a shoulder in the spectral response between 1.79 eV and 2.29 eV (highlighted by the yellow box in Fig. 4.26a). To ensure the accuracy of this observation and to rule out the possibility of measurement errors, we conducted additional QE measurements in April 2022, specifically in the shoulder region. These additional measurements showed QE values consistent with the previous ones, confirming the presence of the shoulder in the spectral response (Fig. 4.26a).

However, when observing the spectral reflectivity data (Fig. 4.26b), it becomes evident that the reflectivity pattern remains almost similar to the initially measured spectral reflectivity, at least up to 3.4 eV. However, some dissimilarities in the reflectivity pattern are observed between 3.71 eV and 4.88 eV. Additionally, it is intriguing to note that the

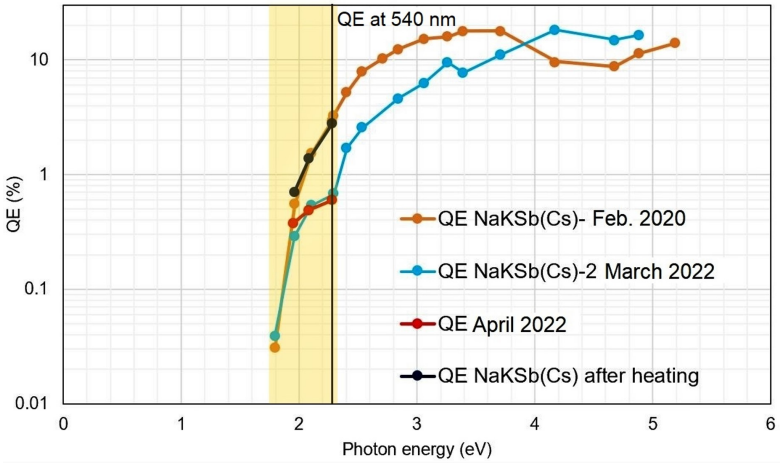

(a)

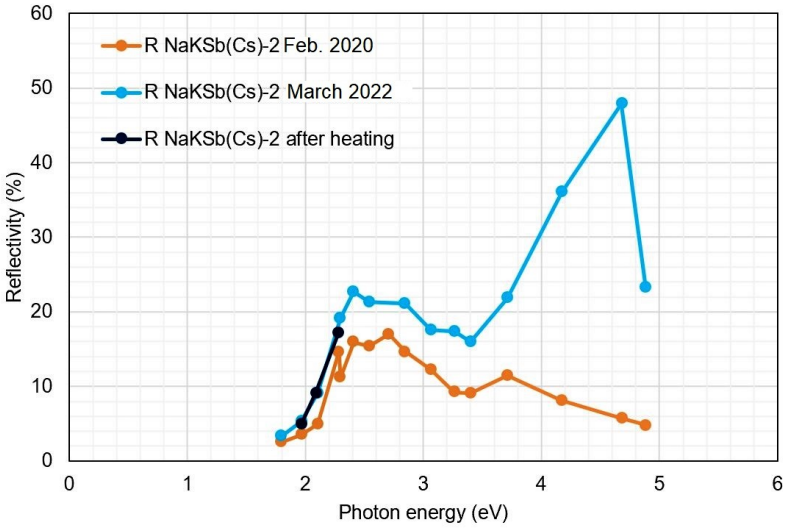

(b)

Figure 4.26: illustrates the (a) spectral response and (b) spectral reflectivity data of the NaKSb(Cs)-2 cathode at different stages.

reflectivity value at almost every wavelength has increased compared to the reflectivity value measured after deposition.

It seems that leaving the cathode in the UHV chamber for a long period might have led to the creation of weak bonds (Van der Waals-like) between the cathode's surface and the gas molecules in the chamber [9]. These bonds are notably delicate and can be effectively broken by raising the temperature of the substrate. This kind of shoulder pattern in the

spectral response curve, stemming from a thin oxide layer, has previously been observed and discussed by Leonardo et al. [144]. Therefore, we raised the substrate temperature to 60 °C, resulting in a significant restoration of the QE, nearly reaching its original level: QE = 2.84% at 540 nm compared to the initial value of 3.27%. This demonstrates that an aged photocathode can be rejuvenated by controlled reheating. It also highlights that these types of the cathode can last for several years as long as the preparation or storage chamber maintains a good vacuum condition ($\sim 10^{-11}$ mbar).

Thereafter, we conducted lifetime measurements on the NaKSb(Cs)-2 photocathode at different substrate temperatures within the "R&D" preparation system. The NaKSb(Cs)-2 cathode was heated at different temperatures for QE degradation measurements. Throughout this process, we consistently illuminated the photocathode using a green laser (543 nm) and measured the real-time photocurrent. Figure 4.27a illustrates the decay curves of the NaKSb(Cs)-2 photocathode at different substrate temperatures, with the initial QE of each experiment normalized to unity. The 1/e lifetime value for each measurement was determined using exponential decay functions to fit the experimental data. The experimental data for these decay temperatures were fitted using a single exponential equation, $QE = QE_0 e^{-\frac{t}{\tau_1}}$ ([32]), where QE represents the QE after a specific time t, QE_0 is the initial QE at t=0, and τ_1 is the amplitude of the exponential decay constant. Fig. 4.27b presents the 1/e lifetime of photocathode as a function of various decay temperatures.

Up to a temperature of 120 °C, no QE degradation is observed, and the photocathode exhibits a lifetime of over 2000 hours. However, a drop in the QE is noticed after reaching 130 °C (see Fig. 4.27a). The 1/e lifetime, calculated from a single exponential fit of the decay data at 130 °C, is 3.84 hours. For 140 °C and 150 °C, the 1/e lifetimes are calculated to be 1.33 and 0.97 hours, respectively (see Fig. 4.27b). These observations clearly indicate a substantial reduction in the cathode's lifetime above a substrate temperature of 120 °C. After the degradation study, the cathode's absolute QE was reduced to almost 0.3% at 543 nm. Due to its lower melting point (28.44°C) and high vapor pressure [138], it is suspected that at higher substrate temperatures, a significant portion of Cs is lost from the bulk photocathode [145]. To address this, a few nanometers of Cs were deposited on the photocathode surface. This resulted immediately in an increased QE to 2.5% (from

0.3% initial value) at 543 nm. The corresponding temperature and QE history during the Cs addition process is shown in Figure 4.28. From this observation, it can be inferred that the temperature-dependent QE decay (Fig. 4.27a) might be linked to the evaporation of Cs from the bulk photocathode.

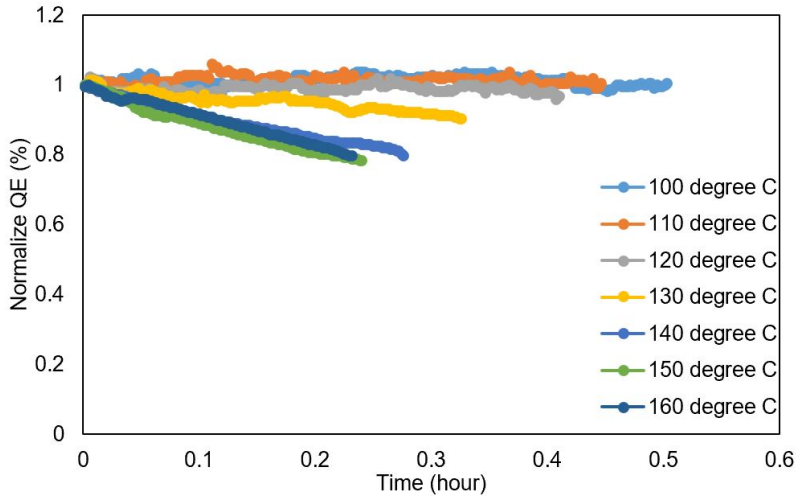

(a)

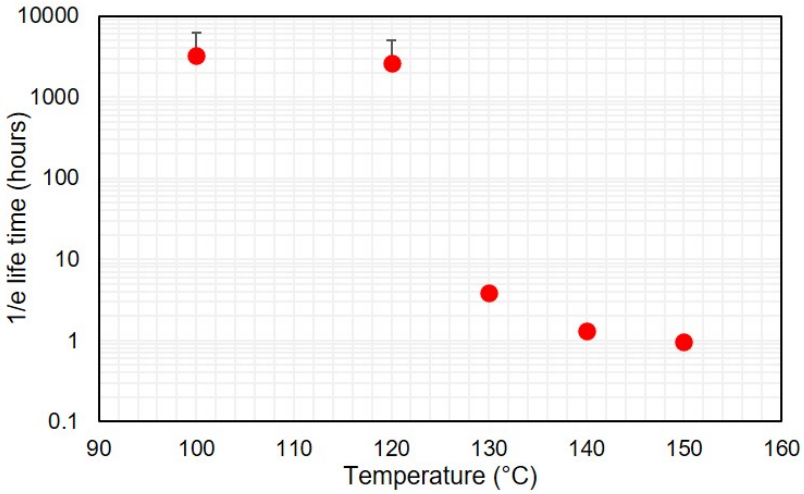

(b)

Figure 4.27: (a) Decay curves of the NaKSb(Cs)-2 photocathode at different temperatures. The quantum efficiency was monitored by illuminating the cathode surface with a 543 nm laser. (b) 1/e lifetime of the NaKSb(Cs)-2 photocathode with respect to different decay temperatures.

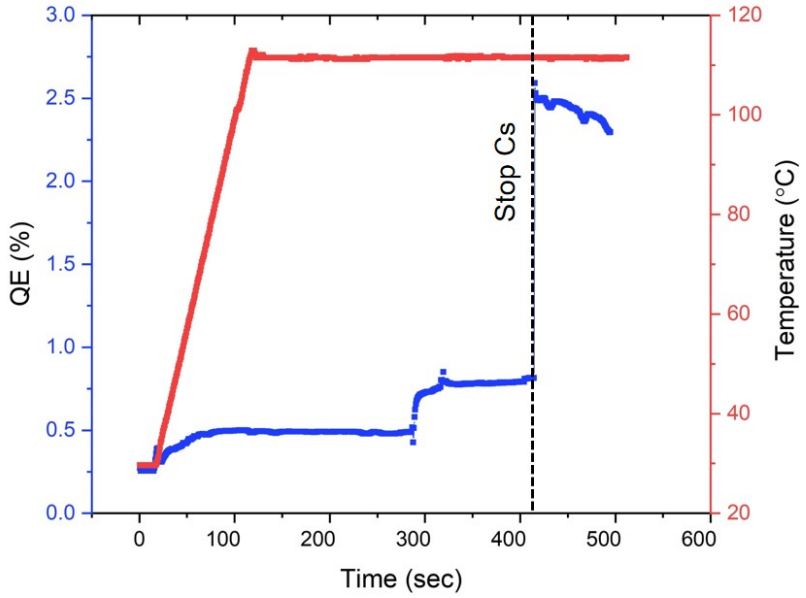

Figure 4.28: QE and temperature history during the Cs addition process. The jump in QE at around 300 s is attributed to variations in the Cs evaporation rate, while the subsequent jump in the QE observed at the end of Cs deposition corresponds to the explanation provided in section 4.3.1.1.4 (page 82).

4.3.3 Experimental Results Obtained from NaKSb Photocathodes

Similar to NaKSb(Cs) cathodes, NaKSb photocathodes also exhibit superior photocathode characteristics, including high sensitivity, broad spectral response, and the ability to function at elevated temperatures. The sole distinction between NaKSb and NaKSb(Cs) cathodes lies in the composition; the NaKSb cathode is fabricated without the addition of Cs. A preliminary attempt was made to develop a NaKSb photocathode in our "R&D" preparation chamber. So far, there is a total number of two photocathodes produced. The following section provides the fabrication procedure and presents the experimental outcomes obtained from these cathodes.

4.3.3.1 Fabrication Recipes

The standard cathode recipe typically involves the initial deposition of Sb, followed by K and Na, to create a NaKSb cathode. However, as we had already produced the KSb-2 cathode using the same procedure up to the K deposition stage (detailed deposition procedure of the KSb-2 cathode is already described in Section 4.3.1.1.3, page 76), we opted to grow the Na on the KSb-2 cathode to produce the NaKSb cathode. Initially, we deposited Sb on the KSb-2 cathode at 120 °C. Following this step, we alternated the addition of small amounts of Na and Sb at the same temperature until we achieved the peak of quantum efficiency to correct the Na: K ratio. During the deposition process, the maximum QE was achieved at 543 nm, reaching 0.80% (Fig. 4.29). However, due to possible excessive deposition of Na during the procedure, the final QE for this cathode at 543 nm was only 0.17%. The corresponding real-time QE (at 543 nm) and reflectivity (at 543 nm) history are depicted in Fig. 4.29.

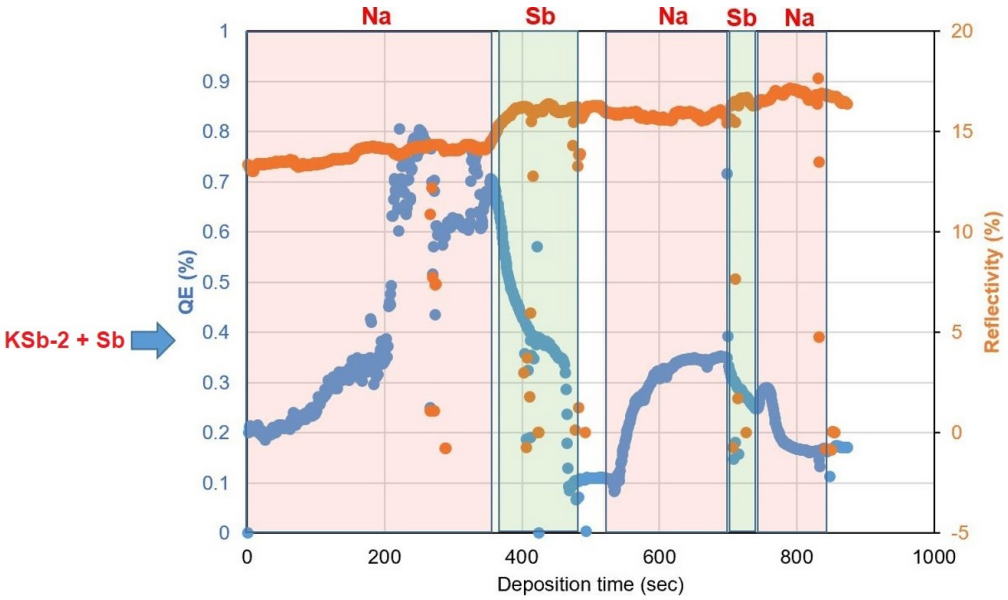

Figure 4.29: Real-time QE (blue) and reflectivity (orange) measurements during the addition of Na and Sb to the pre-existing "KSb-2 film" to form NaKSb-1 cathode. The red boxes highlight the Na depositions, while the green boxes mark the Sb depositions.

The spectral response and spectral reflectivity of the NaKSb-1 cathode were evaluated

post-deposition and are presented in Fig. 4.30. Since the NaKSb-1 cathode was prepared on top of a KSb-2 cathode, we included the spectral response and spectral reflectivity data for the KSb-2 cathode in the same plot for comparison. It's noticeable that the spectral response of the NaKSb-1 cathode decreased when compared to the KSb-2 cathode within the photon energy range of 1.95 eV to 3.39 eV. However, beyond 3.39 eV photon energy (highlighted by red dashed circle), the spectral response of the NaKSb-1 cathode was higher compared to the KSb-2 cathode. The observed difference in the spectral response of the NaKSb-1 cathode compared to the KSb-2 cathode may be attributed to changes in the electronic structure of the compound. In the spectral reflectivity, the onset peak of the NaKSb-1 cathode in the near-infrared region marginally shifted to 1.22 eV, whereas it was 1.26 eV for the KSb-2 cathode. The spectral reflectivity curve of the NaKSb-1 cathode also shows a change in behaviour between 2.29 eV and 3.39 eV (highlighted by black dashed circle), compared to the KSb-2 cathode. This indicates a potential change in the electronic structure of the compound. A more comprehensive analysis of the spectral reflectivity for the NaKSb-1 cathode is discussed in Chapter 6 (Section 6.2). From the spectral response curve, the estimated photoemission threshold (E_g + E_a) is 1.95 eV, which aligns closely with other experimental findings [75].

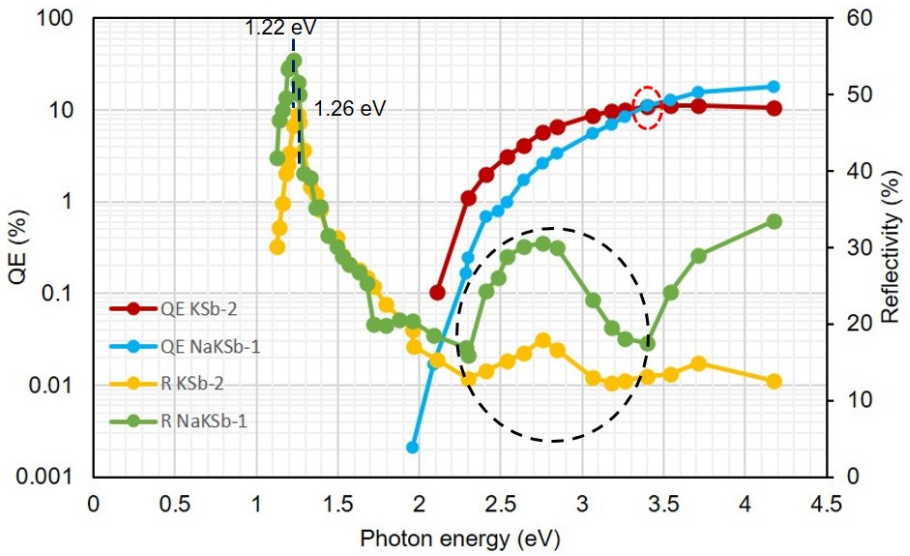

Figure 4.30: Spectral response and spectral reflectivity plot for the NaKSb-1 cathode after the production, with KSb data included for comparison.

For the NaKSb-2 cathode, we attempted deposition at a higher temperature. Initially, Sb was deposited at 180 °C to a thickness of about 5 nm. Then, K was deposited at 160 °C until the QE reached its peak, followed by Na deposition at 160-170 °C. However, at the end of the deposition, we observed a very low QE (5.60×10^{-3} at 543 nm). This lower QE may be attributed to the deposition in a higher substrate temperature compared to NaKSb-1, which likely affected the compound formation, resulting in a lower QE for the NaKSb-2 cathode.

4.3.4 Summary & Discussion

The growth procedure of KCsSb photocathodes produced in the "R&D" preparation system at INFN LASA is explored. The influence of temperature and thicknesses on the photocathode's properties was also examined. It was confirmed that substrate temperature played a significant role in the formation of the cathode film and had an impact on its photoemissive and optical characteristics. Furthermore, it was observed that a different deposition rate has the potential to enhance quantum efficiency, particularly for K-Sb films. The reproducibility of the distinct behaviors in reflectivity and color of the films suggests a possible variation in the chemical composition between the two types of photocathode material (i.e., thin and thick), which may stem from different thicknesses of the Sb layer. The effect of laser heating and substrate temperature on the cathode's degradation is also briefly discussed.

In addition, we also studied the NaKSb and NaKSb(Cs) photocathode materials, and a preliminary cathode recipe has been established. The study on NaKSb(Cs) shows that these photocathodes can survive for several years inside the vacuum chamber (pressure of 10^{-11} mbar). Cathode degradation with respect to different substrate temperatures for NaKSb(Cs) cathode is also analyzed.

4.4 Experimental Results Obtained from the Cathodes Produced in the "Production" Preparation System.

4.4.1 First Batch of KCsSb Photocathodes

As mentioned in the previous section, we have established a reproducible recipe for the KCsSb photocathode in our "R&D" preparation system at INFN LASA. In the new "Production" system, INFN-style standard Mo plugs (shown in Fig. 4.1) are used as substrates to enable in-situ testing of the produced cathodes in the PITZ RF gun. The procedure for growing the KCsSb cathodes in the production system is similar to that in the "R&D" system. Following the R&D experiences, we prepared the first batch of three KCsSb cathodes using a sequential deposition method: two are thin (cathode 112.1, 123.1) (Sb=5 nm), and one is thick (cathode 147.1) (Sb=10 nm). The detailed recipe parameters of produced photocathodes are summarized in Table 4.4. The primary objective is to manufacture these cathodes for subsequent testing at the PITZ RF gun.

Table 4.4: Summary of Cathode Growing Parameters. The temperatures mentioned in the table are measured by the thermocouple positioned in the rear part of the Mo plug (see Section 3.2.2).

Cathode	Sb evaporation	K evaporation	Cs evaporation	QE @ 515 nm
147.1	120 °C, 10 nm	150 °C, 62.4 nm	135 °C, 178.2 nm	5.3%
112.1	120 °C, 5 nm	constant power, 44.6 nm	constant power, 153.6 nm	7.87%
123.1	120 °C, 5 nm	constant power, 44.8 nm	constant power, 156.6 nm	7.58%

It's worth noting that because of the different geometries of the Mo substrates (simplified Mo substrate in the "R&D" system and standard INFN Mo plugs in the "Production" system) and variations in the heating systems (Section 3.2) used in both preparation systems ("R&D" and "Production"), the actual temperature readings may vary between the two systems. Therefore, to grow the first cathode (i.e., cathode 147.1), we decided to set the temperature for growing Sb, K, and Cs according to the temperatures mentioned in Table 4.4. The temperatures mentioned in the table are measured by the thermocouple positioned behind the Mo plug (see Section 3.2.2, page 51). However, when comparing

the temperature readings obtained from the new temperature measuring system that directly touches the plug surface (as explained in Section 3.2.2, page 51), a value of 90 °C was obtained, which corresponds to 120 °C measured by the thermocouple positioned behind the plug. The rear-side thermocouple tends to give slightly higher readings due to its proximity to the plug heater. While growing the two thin photocathodes (112.1 and 123.1), we couldn't measure the actual substrate temperature due to a misalignment in the new temperature reading system. Therefore, we set the plug heating power to match that of the first produced cathode, 147.1.

The spectral response and spectral reflectivity have been measured after the production and are reported in Fig. 4.31a and Fig. 4.31b, respectively. The QE has been recorded at 515 nm to be 5-8 % for thick and thin cathodes. The spectral reflectivity (Fig. 4.31b) shows a similar disparity in the behavior of reflectivity at lower photon energies (highlighted by a red dashed circle) between the thin and thick cathodes, as observed in our R&D systems (see 4.16b).

Figure 4.32 shows photos of the three photocathodes after production. Similar to what was observed in the R&D samples (see Fig. 4.17), a difference in film color is noted: the thick ones appear blue, and the thin ones appear violet. In an attempt to find the photoemission threshold value, Equation 4.8 was used to fit our experimental spectral response data; see Figure 4.33. This process resulted in a value for $E_g + E_a$ of 1.80 eV for all three cathodes. This value is slightly lower than the previous R&D result (1.93 eV, page 84) and also compared to the literature value (1.9 eV) [79]. This difference could be attributed to variations in stoichiometry.

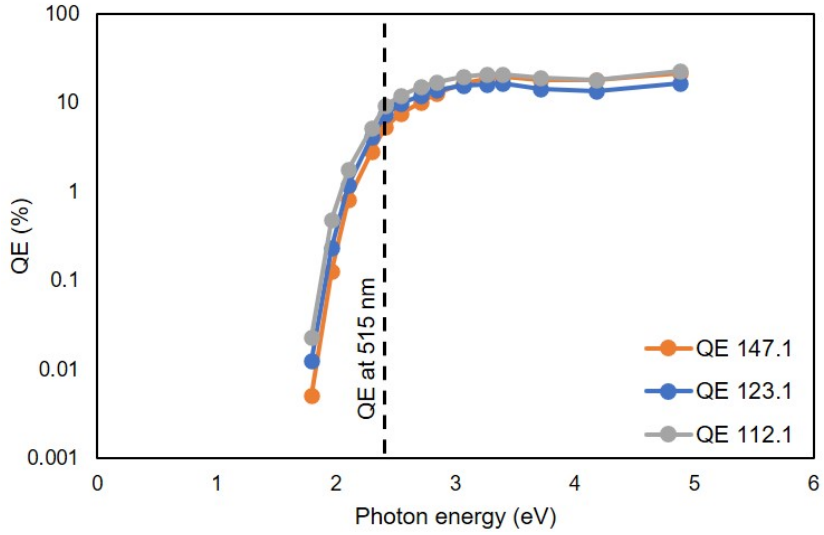

(a)

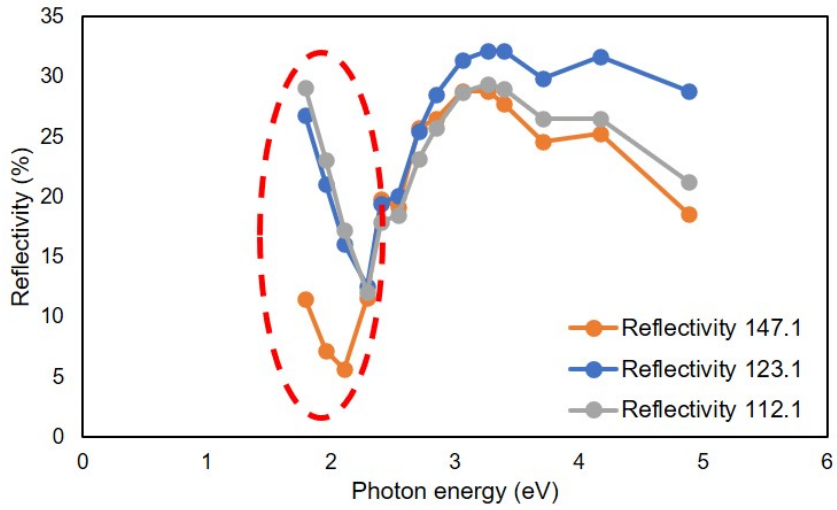

(b)

Figure 4.31: (a) KCsSb photocathode spectral responses: 147.1(thick, 10 nm Sb), 123.1, and 112.1 (thin, 5 nm Sb). (b) spectral reflectivity of the three photocathodes, with the red dashed circle highlighting the variation in spectral reflectivity behavior between the thick (147.1) and thin (123.1, 112.1) cathodes at lower photon energy.

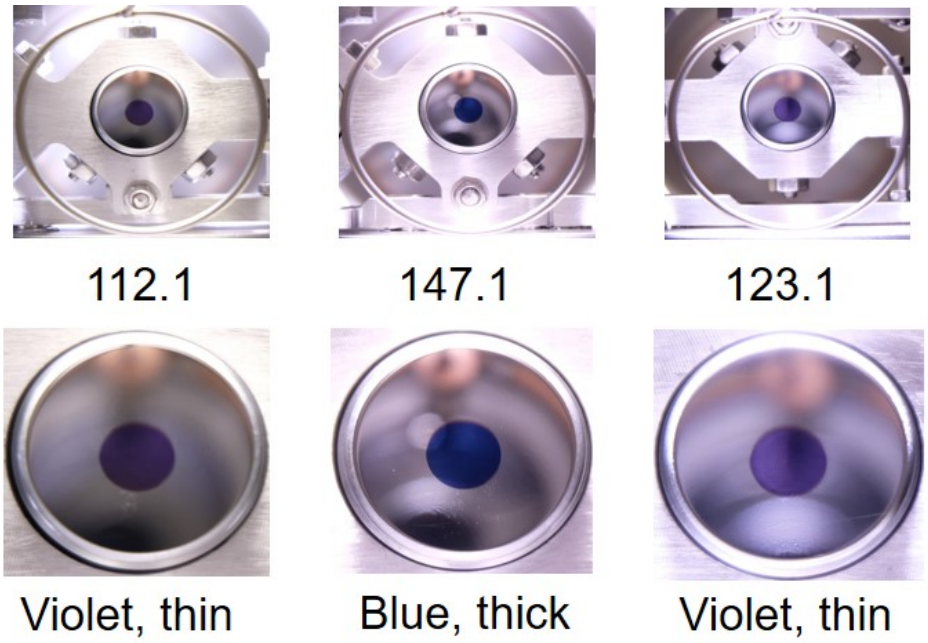

Figure 4.32: Pictures of the three photocathodes in the transport box before delivery to PITZ.

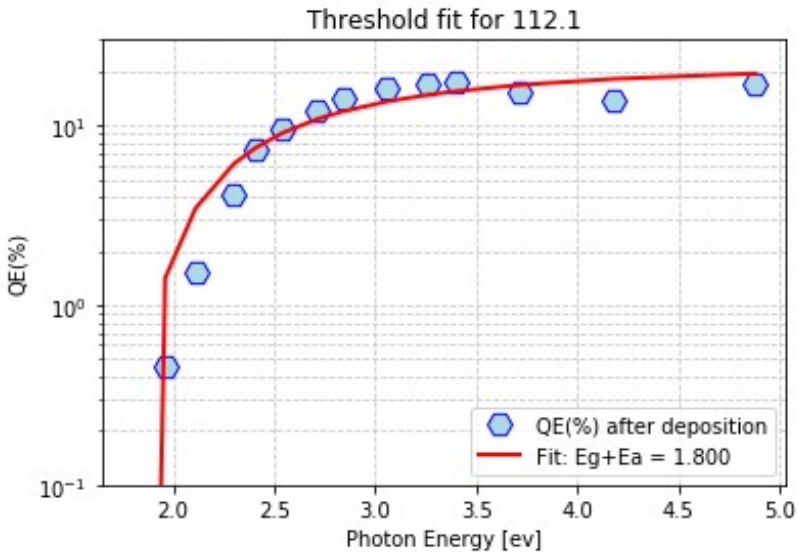

Figure 4.33: Spectral response of cathode 112.1 (Sb = 5 nm) (blue hexagons). The red curve is the fit of the experimental data with Equation 4.8.

4.4.2 Photocathode Studies at PITZ RF gun

After the production, the cathodes were transferred to the portable UHV suitcase box and transported to PITZ for testing. The properties of the cathodes did not change during transport. The QEs (at 515 nm) of the photocathodes were measured upon arrival at the PITZ facility, and the values closely matched those measured at LASA. Afterward, these cathodes were transferred to the gun. The QE maps of these cathodes were uniform throughout the surface, and the map of one of the cathodes is reported in Fig 4.34.

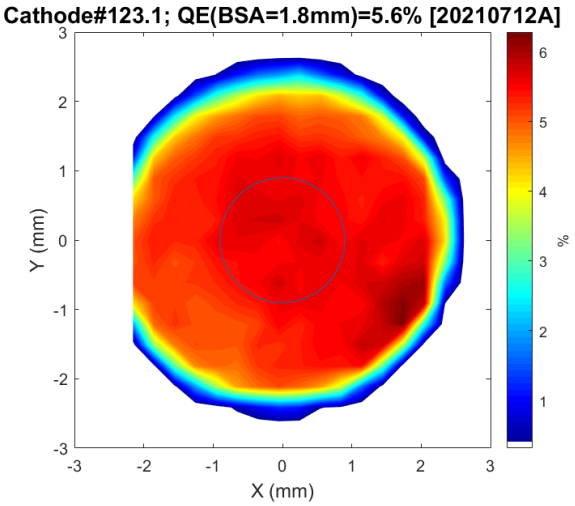

Figure 4.34: QE map of cathode 123.1 (Sb = 5nm) at 515 nm

During cathode conditioning in the RF gun, it was noticed that increasing the cathode gradient beyond 30-40 MV/m resulted in more frequent vacuum trips compared to the previously (standard) used Cs_2Te cathode conditioning. During the trips, the vacuum pressure occasionally reached 1×10^{-7} mbar. These vacuum incidents have a significant impact on the rapid degradation of the QE of the photocathode. The vacuum level and the cathode gradient history during the conditioning of the three cathodes are shown in Figure 4.35. As it can be seen, the QE of all three cathodes drops below 1% within two days after their initial insertion into the gun, probably due to frequent vacuum trips. Additionally, it's worth noting that the cathode remains stable at low gradients ($\leq$ 30 MV/m).

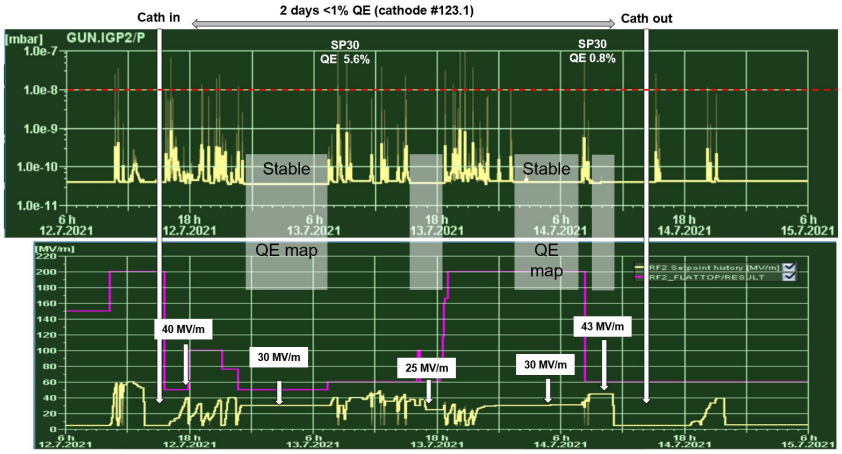

(a)

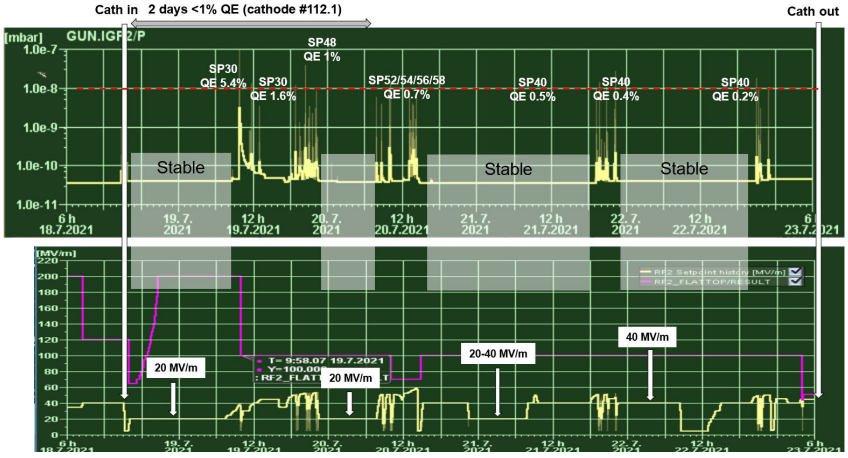

(b)

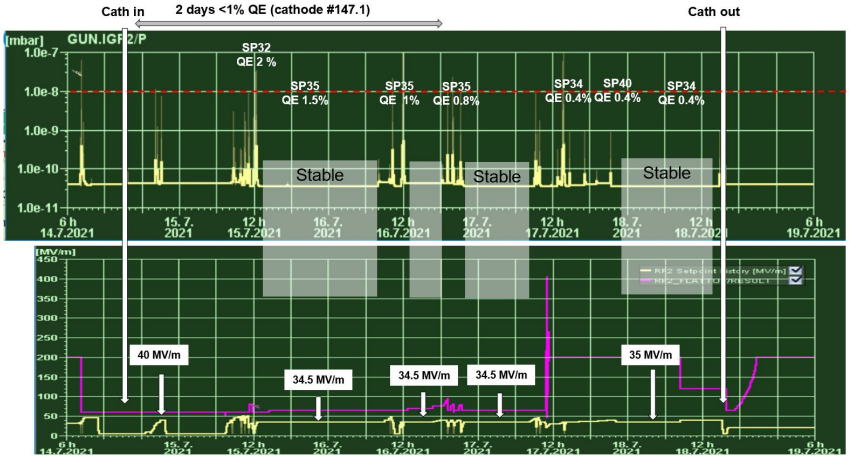

(c)

Figure 4.35: Vacuum level and the cathode gradient history during the conditioning of cathodes (a) 123.1 (thin) (b) 112.1 (thin) (c) 147.1 (thick).

We also noticed that even in the absence of vacuum events, there is still a slow decrease in the QE of these cathodes. The QE gradually drops by about 20% in 12 hours for cathode 147.1 during the overnight run, as shown in Fig. 4.36. This slow decay of QE could potentially result from gradual contamination of the cathode surface within the gun.

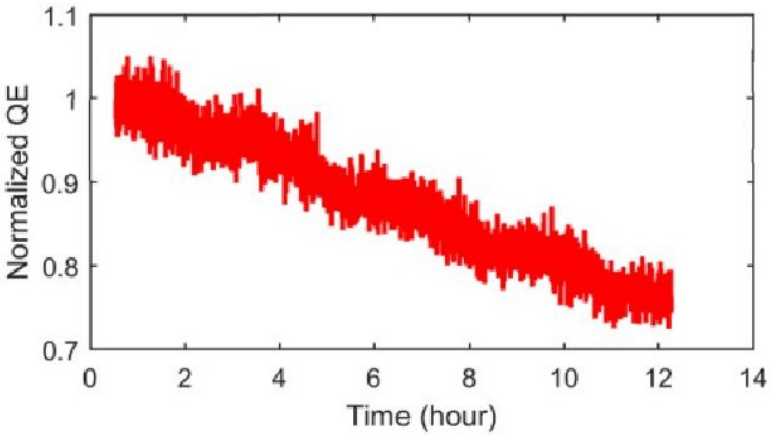

Figure 4.36: QE decay history without vacuum events of cathode 147.1.

We also measured QE maps at various stages during the conditioning of the cathodes. Figure 4.37 illustrates the evolution of QE maps during the conditioning of cathodes 123.1 (thin) and 147.1 (thick). It can be observed that after the vacuum trips, the morphology of the QE maps changed for both thin and thick cathodes. Towards the end of the cathode operation for 147.1, the QE maps were measured at both wavelengths, i.e., 257 nm (UV) and 515 nm (green). Interestingly, at 257 nm (UV), the QE maps appeared quite uniform (Fig. 4.37b), while simultaneously, at 515 nm, the QE maps exhibited non-uniformity. This observation suggests a potential modification of the surface chemistry of cathode 147.1 following the vacuum trips. A more detailed analysis of the post-use characterization is presented in the subsequent section of this report.

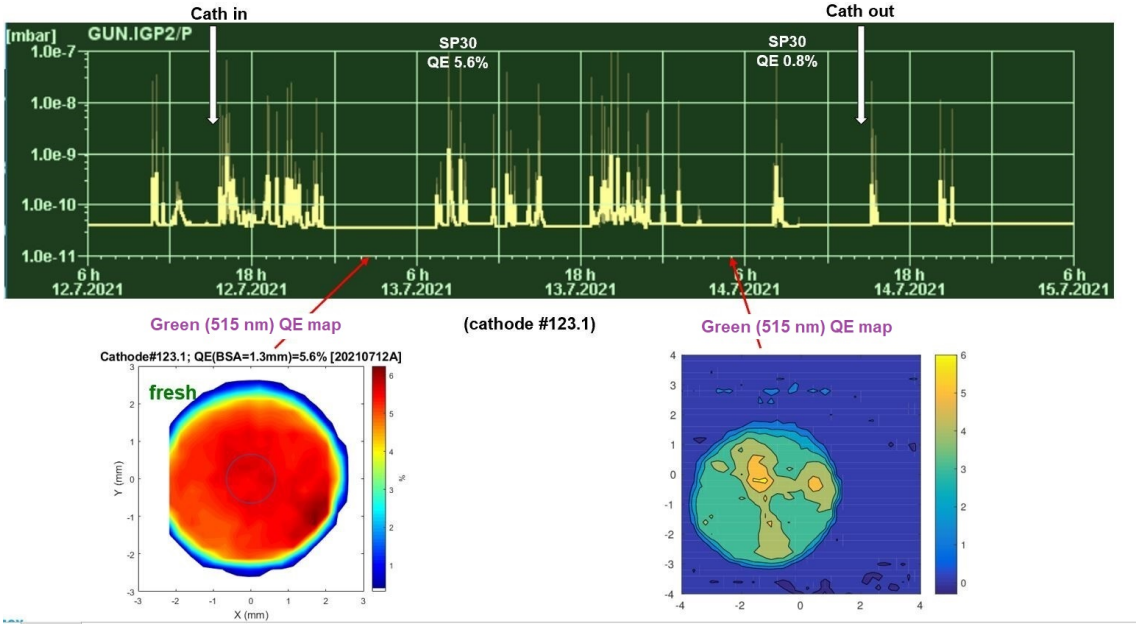

(a)

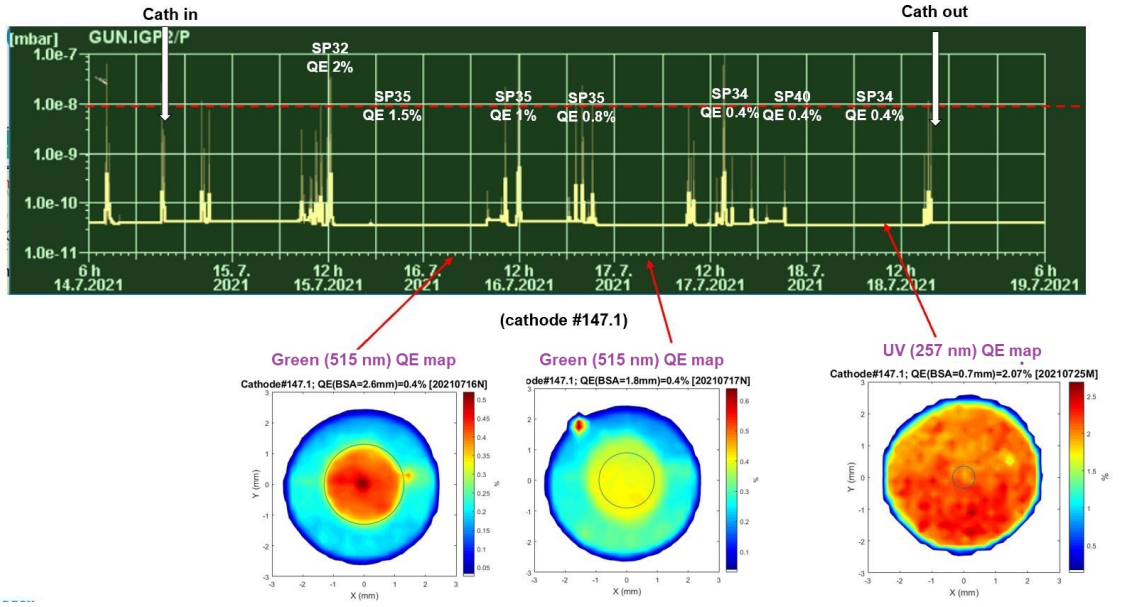

(b)

Figure 4.37: illustrates the evolution of the QE maps during the cathode conditioning of cathode (a) 123.1(thin) and (b) 147.1(thick).

In the case of KCsSb photocathodes, it has been previously demonstrated that their reactivity towards residual gases such as oxygen, carbon dioxide, and hydrocarbons, has a significant role in its short operational lifetime [46, 146]. Figure 4.38 shows the mass spectrum of the residual gas traces in the cavity with and without RF power. It shows a relatively high amount of traces of these critical residual gases inside the gun, and this could be a primary factor contributing to the degradation of the QE of these cathodes.

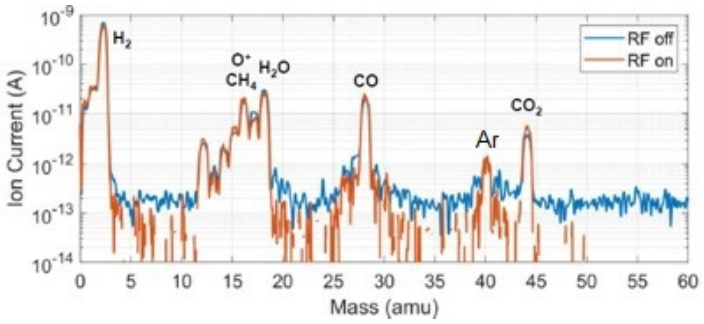

Figure 4.38: Mass spectrum of the residual gas in the cavity with and without RF power

4.4.2.1 Thermal Emittance

Thermal emittance of a photocathode is a measure of the average transverse momentum of the emitted electrons from the photocathode. As discussed in Section 2.2.4, this parameter exerts a significant influence on electron beam quality, thereby impacting accelerator performance.

Thermal emittance measurements have been conducted on all three cathodes using thermal emittance imaging techniques at different cathode emission gradients and light wavelengths (i.e., 515 nm and 257 nm). Emittance imaging techniques typically utilize gun solenoid to direct the emitted electrons onto an observation screen. By manipulating the solenoid strengths, the transverse momentum distribution of the electrons at the cathode can be imaged downstream, allowing for the measurement and analysis of the thermal emittance characteristics. The detailed procedure of this measuring technique can be found in the reference [147]. The measured thermal emittance values for cathode 147.1 is reported in Table 4.5 and presented in Fig. 4.39. It was observed that all three cathodes exhibit a similar thermal emittance value.

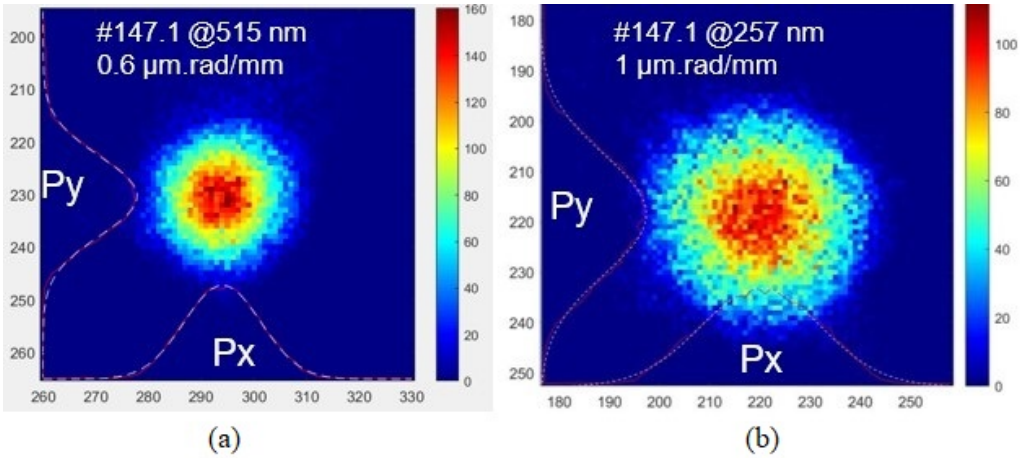

Figure 4.39: illustrates the 2D distribution of photoemission transverse momentum of cathode 147.1 at (a) 515 and (b) 257 nm.

Table 4.5: Thermal emittance of cathode 147.1 at different cathode gradients and wavelengths of light.

Wavelengths	Cathode gradient (MV/m)	Thermal emittance (mm. mrad/mm)
515 nm	19	0.6
	29	0.7
257 nm	19	1

As described in Section 2.3.1.3 (pages 27-30), the thermal emittance of a photocathode is primarily related to the MTE (mean transverse energy) of the emitted electrons, which can be defined at a specific wavelength by Eq. 4.9 [29].

$$MTE = \frac{1}{3}(E_{\text{ph}} - E_{\text{th}}) \tag{4.9}$$

Where E_{ph} is the photon energy, and E_{th} is the photoemission threshold ($E_{\text{th}} = E_g + E_a$, where E_g is the energy gap and E_a the electron affinity). As shown in Table 4.5, the thermal emittance measured at a higher cathode gradient (29 MV/m) was slightly higher than the value measured at 19 MV/m. This difference could potentially be attributed to a reduction in the cathode's work function due to the Schottky effect, which, in turn, may

lead to an increase in the MTE [3, 42].

We then compare the measured thermal emittance with a simple model as described in reference [42], where the theoretical thermal emittance of a semiconductor can be expressed as,

$$\varepsilon_{n_{\text{semiconductor}}} = \sigma_x \sigma_{p_x} = \sigma_x \sqrt{\frac{h\nu - (E_g + E_a)}{3mc^2}} \tag{4.10}$$

In this model, we assumed a photoemission threshold value E_{th} = 1.9 eV [79]. As seen in Fig. 4.40, the measured thermal emittance values are consistent with this model at 2.40 eV (i.e., 515 nm). However, a deviation from this theoretical model is observed in the measurements at higher photon energies, specifically at 4.82 eV (i.e., 257 nm). This deviation at higher photon energies may be attributed to neglected scattering mechanisms, which play a more significant role and result in some electron relaxation before emission [42].

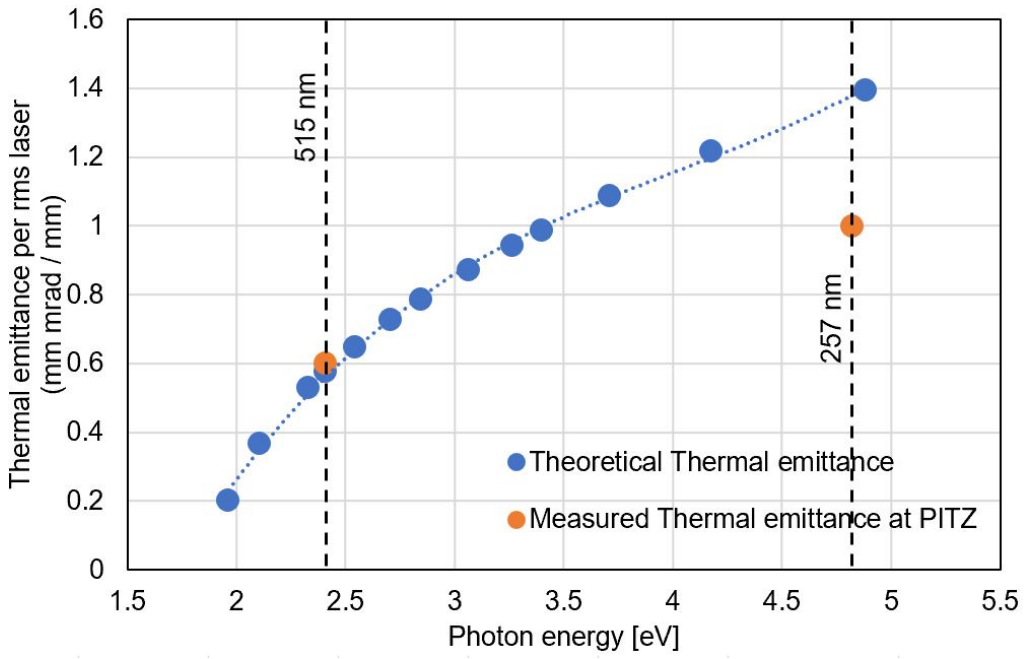

Figure 4.40: Comparison of the thermal emittance of KCsSb photocathodes between the theoretical and measured data. The blue dots represent the theoretically calculated thermal emittance values using Equation 4.10, while the orange dots represent the thermal emittance values measured at PITZ.

4.4.2.2 Projected Emittance

The projected emittance is a measure of the beam quality, specifically the size and divergence of the electron beam. It is defined as the area in phase space occupied by the beam. This approach provides valuable insights into the beam's transverse characteristics, allowing for a comprehensive understanding of its behavior. The projected emittance of 100 pC is measured for three cathodes using slit-scan techniques at a cathode gradient of 40 MV/m; more details regarding the measuring techniques can be found in the reference [148].

In a well-optimized photoinjector, the transverse phase space of the beam is dominated by a high-density Gaussian core distribution and a non-Gaussian low-density tail distribution. This non-Gaussian tail distribution primarily arises from residual nonlinear space charge effects and phase space mismatches in the low-current beam tails [149]. The 95% emittance values were estimated by removing 5% of the total bunch charge from the low-intensity tails of the measured projected transverse phase space distribution [148]. The 95% emittance is much less sensitive to tail particles, as it excludes the worst 5% of particles. The measured 95% emittance of cathode 112.1, along with a comparison between KCsSb and Cs_2Te photocathodes at the same gradient (40 MV/m) is presented in Table 4.6. It was observed that all three cathodes exhibit a similar emittance value. Furthermore, the beam's brightness was evaluated based on this 95% emittance [148]. It has been observed that the overall emittance was reduced by approximately 23%, and the 4D brightness increased by up to 60% for KCsSb cathodes compared to Cs_2Te.

Table 4.6: Comparison of 100 pC Projected Emittance between KCsSb & Cs_2Te Photocathode

Measurements	**Cs_2Te**	**KCsSb**	**Unit**
95% rms emit.	0.36	0.28	μm.rad
4d brightness	760	1209	pC(μm.rad)^2

4.4.2.3 Dark Current

As described in Section 2.2.7, dark current is a critical factor influencing the performance of photoinjectors. The dark current from field emission has been measured for three cathodes at different cathode gradients as a function of the main solenoid current at the first Faraday Cup, located approximately 0.8 meters downstream of the cathode [150, 151]. A comparison of the maximum dark current from the solenoid scans across different gun gradients for (three) KCsSb, Cs_2Te, and Mo cathodes is presented in Fig. 4.41.

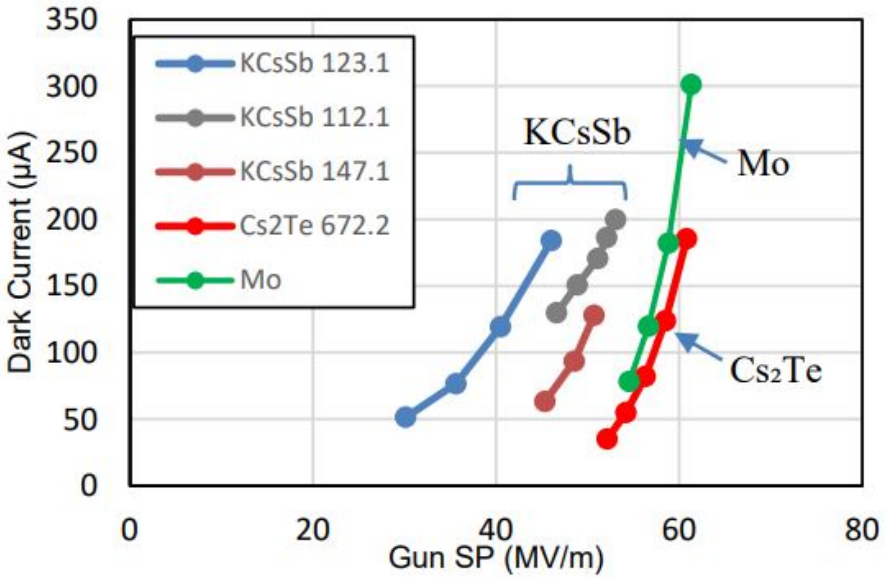

Figure 4.41: Comparison of the maximum dark current as a function of the gun gradient for (three) KCsSb, Cs_2Te, and Mo cathodes. The dark current measurements of Cs_2Te and Mo are presented for comparison purposes.

The dark current measured from KCsSb cathodes was higher by a factor of 2 to 5 compared to that from Cs_2Te cathodes, potentially due to the lower photoemission threshold of KCsSb (1.9 eV) compared to Cs_2Te (3.5 eV) [42]. We also measured the dark current of an uncoated Mo plug prepared in a manner similar to the three Mo plugs used for the three KCsSb cathodes. The lower dark current observed from the uncoated Mo cathode confirms that the primary contribution to the dark current comes from the cathode film itself. We also conducted dark current imaging [151], as illustrated in Figure 4.42, which was performed for cathode 147.1. As evident from the figure, the field emitters

are observed to originate from the KCsSb film itself, serving as the primary source of the observed high dark current.

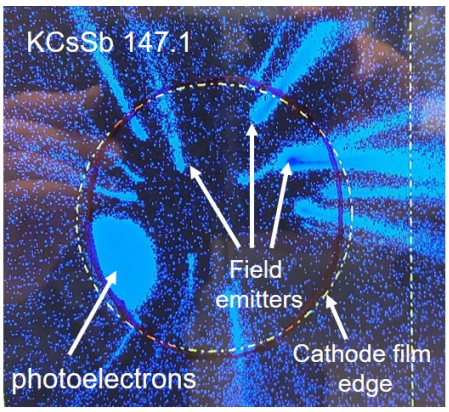

Figure 4.42: illustrates the dark current imaging of Cathode 147.1.

The dark current arising from field emission can be effectively analyzed using the well-established Fowler-Nordheim (FN) theory [152, 153]. The Fowler-Nordheim theory of field emission relies on a quantum mechanical resolution of the Schrödinger equation [154], where electrons tunnel through a barrier in the presence of a high electric field. The FN description for field-emitted current in the context of an alternating field can be written as [155]:

$$\overline{I_F} = \frac{5.7 \times 10^{-12} \times 10^{4.52\phi^{-0.5}} \times A_e(\beta E)^{2.5}}{\phi^{1.75}} \times exp\left(-\frac{6.53 \times 10^9 \times \phi^{1.5}}{\beta E}\right) \tag{4.11}$$

E represents the amplitude of the sinusoidal macroscopic surface field in V/m, β stands for the field enhancement factor, ϕ denotes the work function, and $\overline{I_F}$ is the time-averaged dark current in Amperes from an emitting area A_e. The factor βE accounts for the local field variation due to the microscopic surface roughness via scaling factor β. As discussed in the reference [155], we can extrapolate β and A_e values by plotting the $\frac{\overline{I_F}}{E^{2.5}}$ versus $\frac{1}{E}$. The Fowler-Nordheim theory was formulated for metals, but it can still be useful for visualizing dark current data of semiconductor photocathodes [58]. Using this technique mentioned above, we have calculated the field enhancement factor (β) and

emitting area (A_e) of three cathodes, along with the Cs_2Te photocathode for comparison purposes. The detailed results are presented in Table 4.7.

Table 4.7: Fowler-Nordheim analysis of three KCsSb cathodes, including Cs_2Te for comparison purposes. β represents field enhancement factor and A_e represents emitting area, see Equation 4.11.

Cathode	β	A_e (nm^2)
Cs_2Te 672.2	126	15212
123.1	462	0.002
147.1	97	0.98
112.1	246	0.013

Table 4.7 demonstrates that the β values of the three KCsSb cathodes are comparable to those of the Cs_2Te photocathodes. However, the emitting area (A_e) value is significantly lower compared to the Cs_2Te photocathode. This suggests that the higher dark current observed in KCsSb cathodes may not be primarily attributed to the roughness of the cathode surface, but rather to the lower photoemission threshold being the leading factor.

4.4.2.4 Response Time Measurement

The photoemission mechanism for semiconductor-based photocathodes can be understood by the three-step model as described in Section 2.3.1. During the transport of a photoexcited electron (towards the surface) in a semiconductor photocathode, the electron motion can be affected by numerous scattering processes (i.e., electron-phonon scattering). As a consequence, there is a delay between the photon's arrival at the cathode and the emission of an electron (excited by this photon) from the cathode. This delay causes the lengthening of the extracted electron bunch with respect to the original light pulse. The shape of the emission curve is called the cathode response function, and its characteristic time constant is denoted as the cathode response time. For the response time measurement, two laser pulses with a known optical delay are directed onto the cathode to calibrate the beam temporal response at the photoemission. The detailed procedure is

explained in reference [52].

Because of the high dark current, the response time measurements could only be possible to measure for cathode 147.1(Sb=10 nm). The cathode response time was measured for cathode 147.1 when its QE had already degraded to 0.4%. At this point, there was a possibility of changes in the cathode's surface chemistry. Nevertheless, the results indicate that the response time for the KCsSb cathode is below the 100-fs resolution, compared to a response time of approximately 200 fs for the Cs_2Te photocathode.

4.4.2.5 Visual Inspection After Use

After the test at PITZ, we also conducted a visual inspection of the cathode surface, and the resulting images for cathodes 112.1 (thin) and 147.1 (thick) are shown in Figure 4.43. These images reveal that the photoemissive layer remains intact on the Mo surface, as compared to Figure 4.32 (which depicts the cathodes after production). There are no significant visual differences in the surface morphology of these cathodes found before and after the test in the PITZ RF gun.

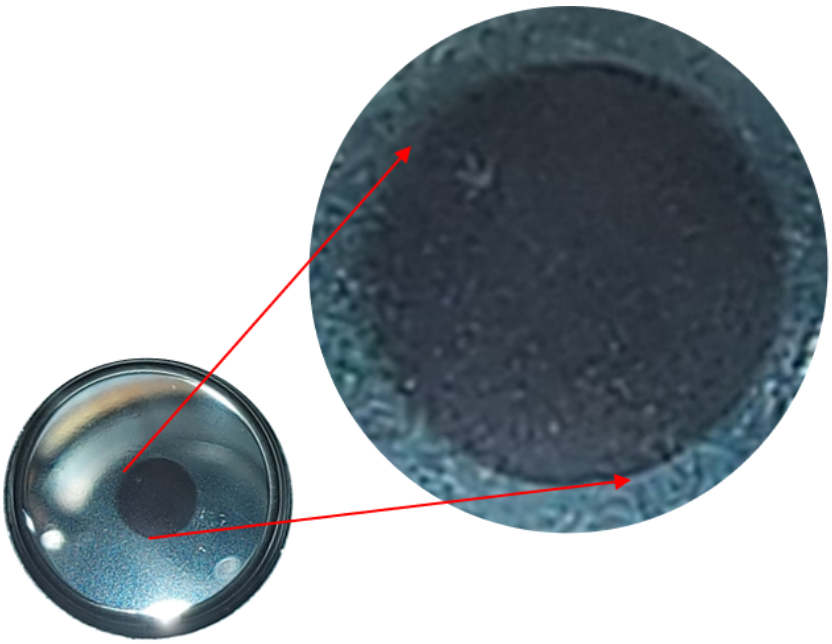

(a)

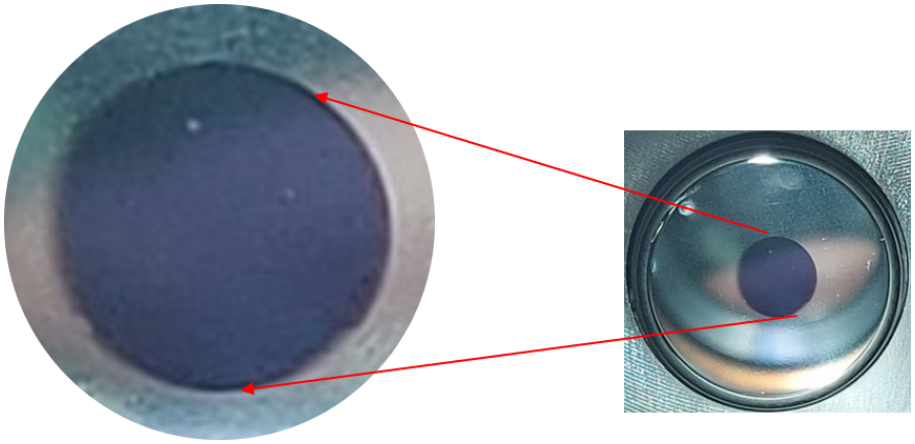

(b)

Figure 4.43: Images of the cathode surface for cathodes (a) 112.1 (thin) and (b) 147.1 (thick) after the test at PITZ.

4.4.3 Post-Usage Spectral Response and Spectral Reflectivity Study at LASA

Following the test of these photocathodes at PITZ, they were transported back to LASA. The spectral response and spectral reflectivity of the "used" cathodes were subsequently measured and are compared in Figure 4.44 with the values obtained immediately after production. The observations from Fig. 4.44a show that the photoemission threshold of cathodes 147.1 and 112.1 has increased from 1.79 eV to 2.08 eV, and a shoulder has appeared at the low photon energy for cathode 123.1 (highlighted by a red dashed circle).

As observed previously in Fig. 4.38, a substantial amount of residual gases, including oxygen, carbon dioxide, and hydrocarbons, is present within the RF gun. A study by A. di Bona et al. has shown that KCsSb cathodes are particularly sensitive to residual gases such as CO_2 and O_2, while remaining unaffected by CH_4, N_2, and CO gases [46]. Interestingly, this study also revealed an increase in the quantum efficiency at lower photon energies (i.e., at 2.33 eV and 2.07 eV) upon exposure to small amounts of oxygen. The authors hypothesized the formation of a Cs-O surface dipole layer at the cathode surface, leading to a reduction in the electron affinity of the bulk material through a band-bending effect near the interface. This observation was further supported by a subsequent X-ray photoelectron spectroscopy (XPS) study conducted by Leonardo et al. [144], where they correlated changes in the spectral response of KCsSb films to varying degrees of oxidation, as revealed by XPS data. This study also demonstrated the appearance of a shoulder at the lower photon energy range (similar to cathode 123.1) in the spectral response upon exposure to lower amounts of oxygen. The XPS data confirmed the formation of a thin suboxide alkali layer, predominantly $Cs_{11}O_3$, on the cathode surface, contributing to the reduction of the surface barrier. Furthermore, a study by P. Michelato et al. affirmed that the increase in QE at lower photon energy is only achievable with O_2 and not with CO_2 [146]. Additionally, in the case of NaKSb(Cs)-2 cathodes, we have previously observed the formation of such a shoulder due to residuals, as illustrated in Fig. 4.26a. Therefore, based on the aforementioned findings and the similarity in spectral behavior, especially at lower photon energies, for cathode 123.1 as compared to the reference [144],

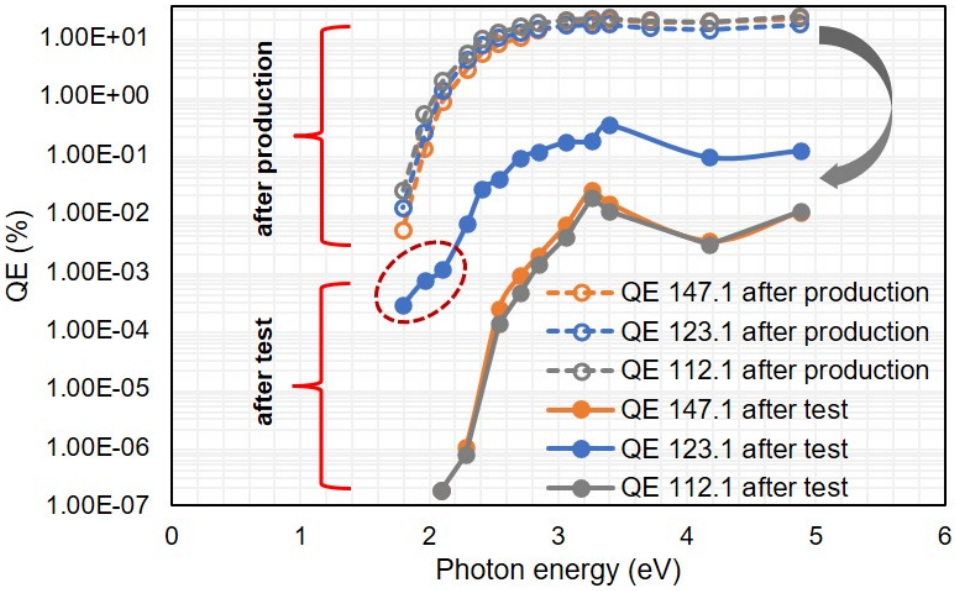

(a)

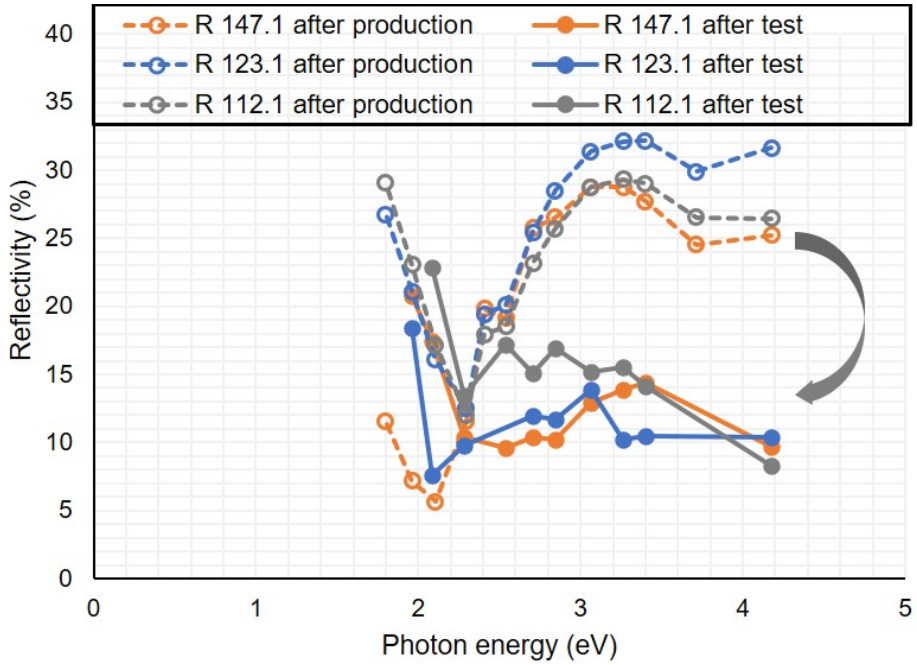

(b)

Figure 4.44: (a) spectral response and (b) spectral reflectivity measurements of the three cathodes after use in the RF gun. The spectral response and spectra reflectivity of the three same cathodes after production are shown in the plot for comparison.

it can be inferred that the shoulder observed in the spectral response of cathode 123.1 could potentially be attributed to a lower level of oxidation.

As previously mentioned, we have observed an increase in the photoemission threshold of cathodes 147.1 and 112.1. This increase in the photoemission threshold potentially is linked to a higher level of contamination within the gun affecting these cathodes. Similar instances of increased photoemission threshold in KCsSb cathodes due to a high degree of oxidation have been documented by Leonardo et al. [144]. This higher level of oxidation leads to the formation of a thicker suboxide layer on the cathode surface, which reduces the probability of photoemission and, consequently, results in an increased photoemission threshold [144]. This phenomenon has also been observed in Cs_2Te photocathodes [156]. Additionally, the fact that both cathodes 147.1 and 112.1 are used for a relatively longer period (i.e., 4 days) compared to cathode 123.1 (i.e., 2 days) inside the RF gun contributes to the likelihood of a relatively higher degree of contamination. Therefore, the increase in the photoemission threshold for cathodes 147.1 and 112.1 can be attributed to the high degree of contamination. Furthermore, the disparity observed in the spectral response behavior among cathodes 112.1, 147.1, and 123.1 can be attributed to varying levels of contamination.

By examining the spectral reflectivity shown in Fig. 4.44b, it is evident that the peak characteristics of the cathodes have altered before and after testing for all three cathodes. This suggests likely modifications in the electronic structure of the cathode material, aligning with the observations from the spectral response analysis provided above. Nevertheless, to further elucidate the underlying mechanisms behind the observed changes in cathode performance during degradation, a further comprehensive surface characterization is essential.

4.4.4 Summary & Discussion

The first batch of 3 KCsSb cathodes (1 thick and 2 thin) was produced in the "Production" system at INFN LASA and transported to PITZ for testing inside the photoinjector. These cathodes survived during the transport. During cathode conditioning in the RF gun, it was noticed that increasing the cathode gradient beyond 30-40 MV/m resulted in more frequent vacuum trips compared to the previous Cs_2Te cathode conditioning. These vacuum incidents significantly impacted the rapid degradation of the photocathode's quantum efficiency, dropping from 3-6% to below 1% within 2 days. The results in terms of thermal emittance and response time are very promising when compared to the Cs_2Te photocathode. Nevertheless, the limiting factors are high dark current and the short operational lifetime. An analysis of post-operational optical spectra conducted at INFN LASA revealed potential oxidation of the cathode films. The analysis also indicated varying levels of oxidation in these cathode films.

4.4.5 Second Batch of KCsSb Photocathodes

Following the testing of the first batch of KCsSb cathodes, our objective is to achieve a more comprehensive insight into the crystal structure of the photocathode both during and after the deposition process, as well as to analyze the impact of varying thickness on the photocathode's electronic structure. This knowledge will allow us to optimize further and improve the cathode recipe. Consequently, we have chosen to grow new cathodes within the new "Production" system, which incorporates a "multi-wavelength" optical diagnostics setup during the deposition process. As already explained in Section 4.2, this "multi-wavelength" optical diagnostics setup employs a motorized filter wheel capable of accommodating up to eight different optical filters (254, 297, 365, 488, 515, 540, 632, 690 nm corresponding to 4.88, 4.17, 3.39, 2.54, 2.40, 2.29, 1.96, 1.79 eV). These filters are used to measure real-time QE and reflectivity within the range of 254 nm to 690 nm during the deposition process, as depicted in Figure 4.2c.

We produced one KSb (137.1, 10nm Sb, i.e., thick) and two KCsSb photocathode (137.2, 10nm Sb, i.e., thick, and 137.3, 5 nm Sb, i.e., thin) in the production system. Table 4.8 and Table 4.9 summarize the detailed recipes for three photocathodes. The three above-mentioned photoemissive films were deposited on the same Mo plug. Prior to the second and third cathode deposition, the previous film had been destroyed by a heating cycle up to 450 °C, and the complete removal was checked by QE and reflectivity measurements before starting with the next film evaporation.

Table 4.8: Summary of evaporated thicknesses of Sb, K, and Cs, along with QE (at 540 nm) and reflectivity (at 540 nm), for cathodes 137.1 (thick), 137.2 (thick), and 137.3 (thin). The QE and R values presented in the table were measured post-deposition.

Cath.	**Film**	**Sb (nm)**	**K (nm)**	**Cs (nm)**	**QE (%)**	**R (%)**
137.1	KSb	10.1	101	-	0.076*	19.72*
137.2	KCsSb	10.1	88.9	181.0	3.3	22.4
137.3	KCsSb	5.3	53.7	85.1	3.8	12.0

* QE and R presented for Cathode 137.1 are representative of the KSb compound.

Table 4.9: Overview of the evaporation rates during Sb, K, and Cs depositions for cathodes 137.1 (thick), 137.2 (thick), and 137.3 (thin).

Cathode	**Evaporation Rate (nm/min)**		
	Sb	K	Cs
137.1	0.9	0.7	-
137.2	0.9	0.7	0.6
137.3	0.9	0.5	0.9

Due to the restrictions posed by the transmittance of the front viewport material in the "Production" system (as detailed in Section 4.2.2 and illustrated in Fig. 4.4), the real-time measurement of QE and reflectivity at 254 nm during deposition cannot be performed for all three cathodes. As for the measurement at 297 nm, it was observed that the real-time reflectivity data obtained was not accurate. This discrepancy likely stems from several factors. Firstly, for reflectivity measurements, the light must travel back and forth through the viewport, leading to a significant reduction in the power of the reflected light due to the low transmittance of the viewport material at 297 nm (i.e., 69%). Additionally, during deposition, the intense heating of alkali and antimony sources emits considerable illumination, potentially introducing background noise. Furthermore, the rotational speed of the filter wheel during measurements may further hinder the accurate capture of the low-intensity reflected light at 297 nm by the photodiode in real-time measurements. The combined effect of these factors – low reflected light intensity, background noise, and the filter wheel speed – makes it difficult to isolate and accurately measure the actual reflected light signal at 297 nm. Consequently, real-time reflectivity at 297 nm could not be measured for any of the three cathodes. However, upon checking the real-time QE value at 297 nm, it was found to be consistent and matched with the QE value obtained by the monochromator (measured without the filter wheel, Fig. 4.3). The consistency observed for QE measurements (at 297 nm) may be attributed to the fact that light travels unidirectionally through the viewport during the QE measurements, resulting in relatively lower power loss. This, in turn, ensures that there is sufficient power remaining to stimulate enough photoelectrons to generate real-time QE data. Therefore, the obtained real-time

QE data at 297 nm was taken into consideration for the characterization of all three cathodes.

In the following section, we will discuss the detailed growth recipe and results of the aforementioned three cathodes (137.1, 137.2, 137.3).

4.4.5.1 Cathode 137.1

Cathode 137.1 was originally planned to be grown as a full KCsSb cathode. However, due to an issue in the preparation system, Cs deposition could not be performed. As a result, we were only able to grow up to the K deposition stage, resulting in a KSb cathode.

The sequential deposition started with 10 nm of Sb (at T = 120 °C), followed by K deposition (at T = 140 °C), until reaching the photocurrent peak. As mentioned in Section 4.4.1, due to a misalignment in the temperature reading system, we set the plug heating power to similar values to match the temperature settings used for the first cathode produced in the "Production" system, i.e., cathode 147.1. As presented in Table 4.9, during Sb deposition, the deposition rate was maintained at 0.9 nm/min, while during K deposition, it was maintained at 0.7 nm/min.

Real-time QE and reflectivity at different wavelengths were monitored during both Sb and K deposition, as detailed in Fig. 4.45. Before the deposition, the input power of light at 7 different wavelengths was measured and implemented in the LabVIEW program to record real-time QE and reflectivity. Due to some technical issues, the real-time reflectivity at 365 nm for cathode 137.1 has not been measured. Prior to the deposition, the spectral reflectivity of the Mo plug was measured.

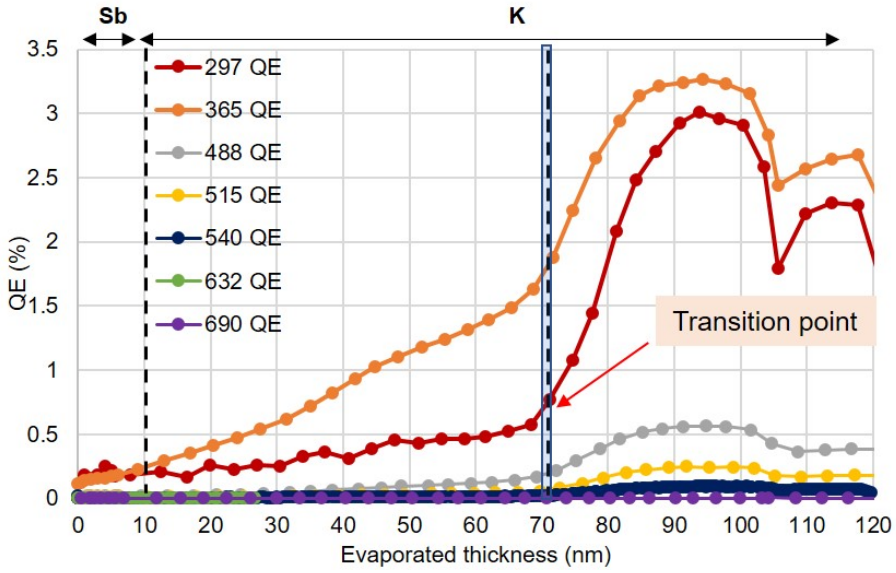

(a)

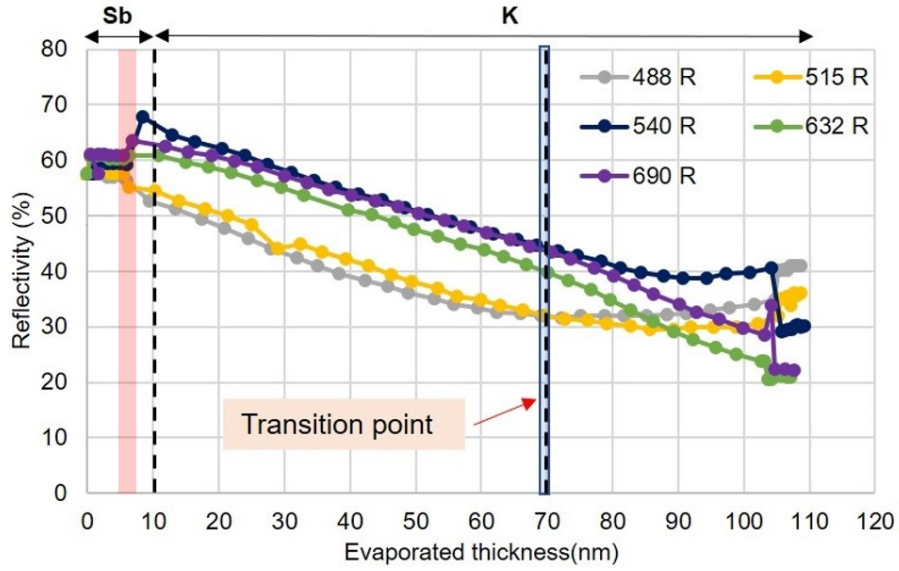

(b)

Figure 4.45: Real-time (a) QE and (b) reflectivity at different wavelengths during Sb and K deposition of cathode 137.1. The thicknesses represented in plots 'a' and 'b' correspond to the evaporated thickness of Sb and K, with a dashed line separating them in the plot. The change in the reflectivity behavior during Sb deposition (at around 6 nm) is highlighted by a red colored box in plot b. The transition point during K deposition is highlighted by a dashed line along with a blue-colored box.

In Figure 4.45b, during Sb deposition, the reflectivity initially experienced a marginal decrease at all wavelengths. However, after around 6 nm (highlighted by the red-colored box), it began to rise (except at 488 nm and 515 nm). This trend is illustrated in Fig. 4.46, which presents the real-time history of reflectivity at different wavelengths during Sb deposition for cathode 137.1. As discussed in Section 4.3.1.1.2 (pages 70-72), these changes in reflectivity could be attributed to the amorphous-to-crystalline transition of the Sb compound [53]. However, as mentioned above, no such increase in reflectivity pattern was observed at 488 nm and 515 nm after 6 nm. Upon checking this behavior with the other two cathodes (i.e., cathode 137.2, Fig. 4.48b and 137.3, Fig. 4.52b), we found that this discrepancy might be due to a potential issue with the instrument or data acquisition process for cathode 137.1. As will be discussed in the upcoming section, since the Sb deposition was carried out under similar conditions for the other two cathodes, and no such discrepancies were observed for 488 nm and 515 nm, we deduce that this issue is likely related to either the instrument or the data acquisition process for cathode 137.1.

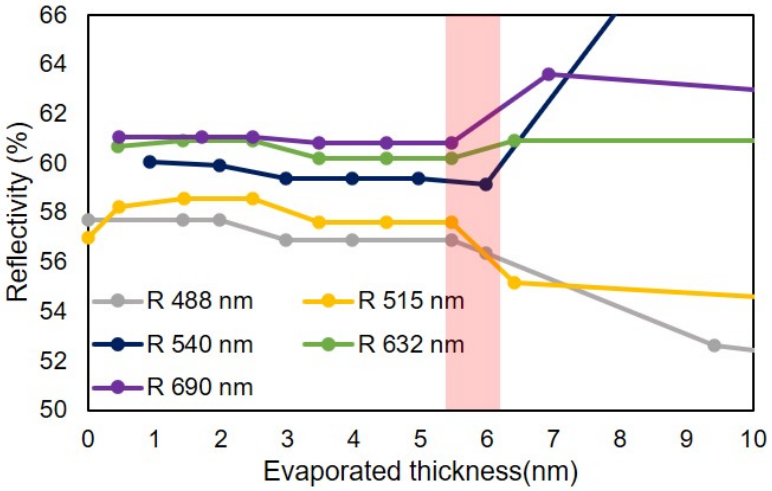

Figure 4.46: A zoom-in plot of the real-time reflectivity history at different wavelengths during the Sb deposition process of cathode 137.1. The change in the reflectivity behavior during Sb deposition (at around 6 nm) is highlighted by a red colored box in the plot.

As depicted in Fig. 4.45a, a significant change in the slope of the real-time QE (across all wavelengths) is evident above 60 nm of K deposition (i.e, equivalent to 70 nm of total evaporated thickness, indicated in the graph), denoted as the transition point (highlighted

by the blue colored box with dashed line). As it was discussed in Section 4.3.1.1.3 (page 73), the observed change in QE after a specific evaporated thickness signified the transition of the K-Sb compound from the amorphous phase to the crystalline phase [135]. Also, it is interesting to notice in Fig. 4.45b that beyond this transition point, there's an observable change in the reflectivity slopes at 488nm, 515nm, and 540nm wavelengths. However, no such slope change is evident in the reflectivity for 632 nm and 690 nm. This discrepancy in behavior between the two sets of wavelengths could potentially originate from the intricate crystallization dynamics of the KSb compound.

Furthermore, as evident in Fig. 4.45a, the QE at 297 nm was lower compared to the QE at 365 nm during K deposition. In principle, higher photon energy efficiently ejects electrons from the cathode compared to a lower photon energy. However, as explained in Appendix A.1 (pages 255-257), when the photon energy is greater than or equal to twice the band gap energy (E_g) of the semiconductor material, the quantum efficiency starts to decline due to electron-electron (e-e) scattering phenomena occurring within the material. It is important to note that the effective decrease in the QE response due to e-e scattering is noticeable only several electronvolts higher than the electron-electron scattering threshold [157]. The band gap of the KSb compound is approximately 1.4 eV (cubic type) and 1.1 eV (hexagonal type) [158]. Therefore, a decrease in QE due to e-e scattering is expected for the KSb compound above the local maximum of photon energies around 3.06-3.54 eV (i.e., 405 nm - 350 nm) ($\because h\nu \geq 2\ E_g$), as seen in Fig. 8.10 (in Appendix A.1) for all produced KSb compounds. Hence, the decrease in QE response at 297 nm (compared to 365 nm) in Fig. 4.45a is related to the KSb band structure and indicates the formation of the KSb compound.

Using the real-time QE (vs. thickness) and reflectivity (vs. thickness) data at 7 different wavelengths shown in Fig. 4.45, we reconstructed the real-time spectral response (vs. photon energy) and reflectivity (vs. photon energy) during Sb and K deposition processes. This reconstruction offers insights into how the spectral response and reflectivity evolve throughout the different phases of Sb and K deposition for cathode 137.1. It provides valuable information about real-time compound formation and enables us to monitor changes in the electronic structure during compound formation. The compre-

hensive analysis of the real-time spectral response and reflectivity during the Sb and K deposition processes is detailed in Appendix C.

As previously mentioned, the spectral reflectivity of Mo was recorded prior to the deposition process. Subsequently, following deposition, measurements of both the spectral response and reflectivity were taken for the grown K-Sb compound, as shown in Fig. 4.47. In Fig. 4.47a, a comparison is presented between the spectral reflectivity of the Mo plug and the deposited KSb compound, highlighting the changes in the spectral reflectivity pattern following cathode deposition.

Furthermore, when we compare the spectral reflectivity and spectral response patterns of the KSb compound (presented in Fig. 4.47) with the reconstructed real-time spectral reflectivity (plot 6 in Fig. 8.17) and spectral response (plot 6 in Fig. 8.16) plots at the end of K deposition, we observe a noticeable similarity. These similarities indicate the accuracy of the real-time data measurements during the deposition.

For cathode 137.1 (KSb compound) the QE was observed 0.17 % at 515 nm (i.e., 2.40 eV).

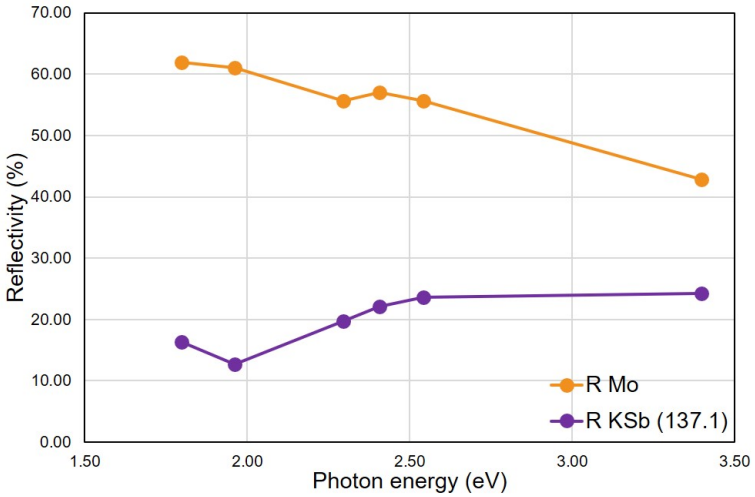

(a)

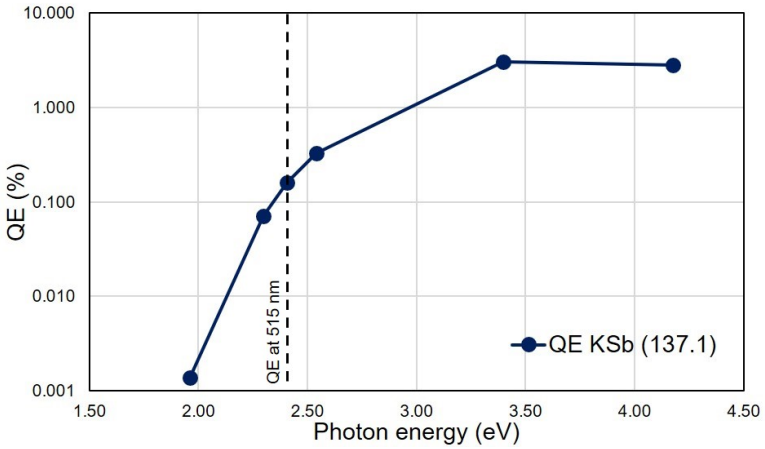

(b)

Figure 4.47: (a) Comparison of the spectral reflectivity between Mo (measured before the deposition) and the KSb compound (measured after the deposition), and (b) the spectral response of the KSb compound measured after the deposition of cathode 137.1.

4.4.5.2 Cathode 137.2

The sequential deposition of cathode 137.2 started with 10 nm of Sb, followed by K, until reaching the photocurrent peak and then evaporating Cs until the photocurrent is close to the saturation level. As presented in Table 4.9, during Sb deposition, the deposition rate was maintained at 0.9 nm/min, while during K and Cs deposition, it was maintained at 0.7 nm/min and 0.6 nm/min, respectively.

As previously discussed, due to a misalignment in the temperature reading system, we adjusted the plug heating power to match the temperature settings used for cathode 137.1, which were set at 120 °C for the deposition of Sb and Cs. However, during the deposition of K, we suspected that the lower QE for the KSb compound in the previous cathode (i.e., cathode 137.1) might have been caused by a higher substrate temperature. As a result, we slightly reduced the plug heating power compared to the previous cathode: the heating power applied during K deposition for cathode 137.1 was 3.1 W, whereas, for cathode 137.2, a power of 2.89 W was used during K deposition.

Similar to the previous cathode, we monitored real-time QE and reflectivity at different wavelengths during the deposition of Sb, K, and Cs. Before the deposition, the input power of light at 7 different wavelengths was measured and implemented in the LabVIEW program to record real-time QE and reflectivity. The following section will discuss the experimental results obtained from the KSb compound for cathode 137.2.

4.4.5.2.1 K-Sb Phase

Fig. 4.48 presents a detailed real-time QE and reflectivity at the different wavelengths during the deposition of Sb and K.

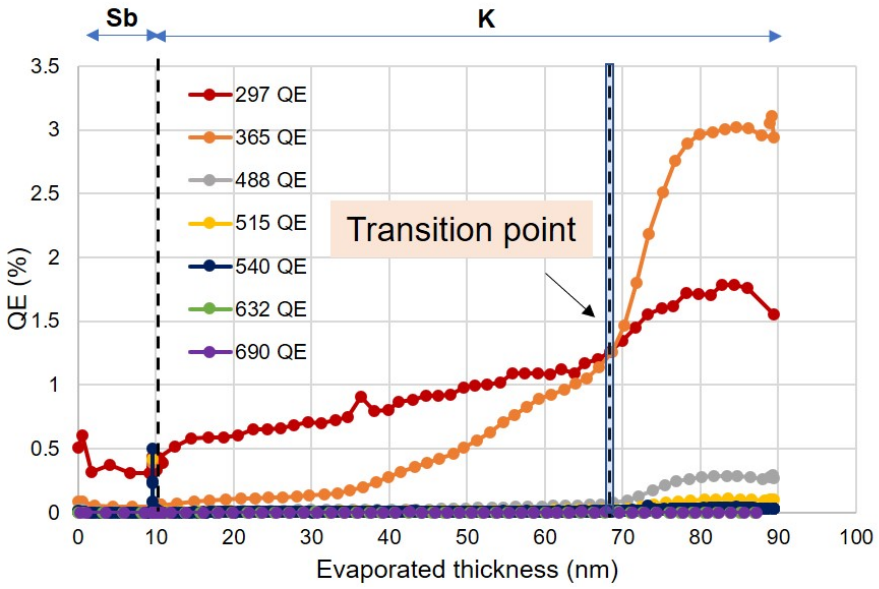

(a)

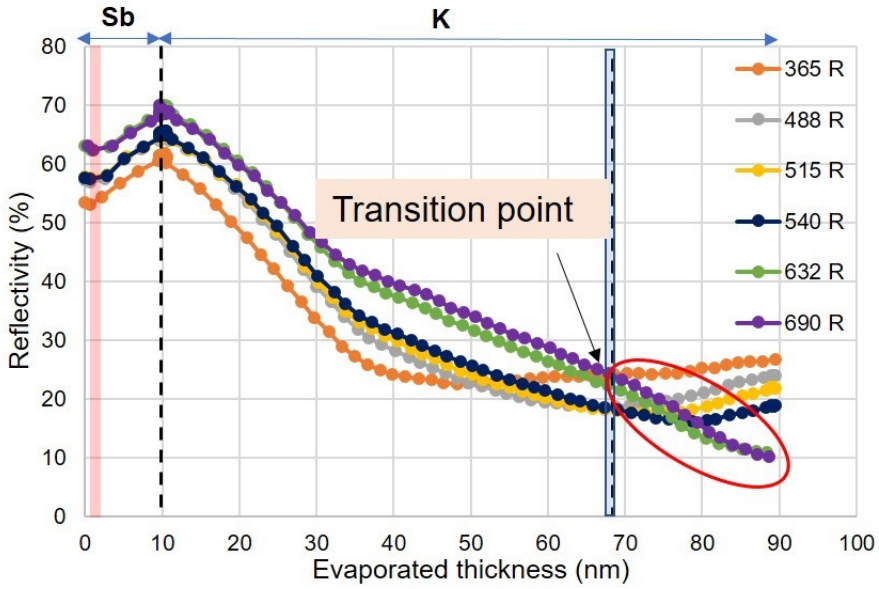

(b)

Figure 4.48: Real-time (a) QE and (b) reflectivity at different wavelengths during Sb and K deposition of cathode 137.2. The thicknesses represented in plots 'a' and 'b' correspond to the evaporated thickness of Sb and K, with a dashed line separating them in the plot. The change in the reflectivity behavior during Sb deposition (at around 2 nm) is highlighted by a red colored box in plot b. The transition point during K deposition is highlighted by a dashed line along with a blue-colored box.

As can be seen in Figure 4.48b, during Sb deposition, the reflectivity first slightly dropped. However, after around 2 nm (highlighted by the red-colored box), it began rising (for all 6 wavelengths) until the end of Sb deposition. As discussed in Section 4.3.1.1.2 (pages 70-72), these changes in reflectivity after a particular evaporated thickness are potentially attributed to the amorphous-to-crystalline transition of the Sb compound [53]. However, compared to cathode 137.1 (refer to Fig. 4.45b), there is a discrepancy in the transition thickness (amorphous-to-crystalline transition of the Sb compound) in the reflectivity plot despite having a similar growth recipe. As discussed in Section 4.3.1.1.2 (pages 70-72), the specific value of this transition thickness might vary due to various factors such as surface quality, substrate type, substrate temperature, deposition rate, vacuum quality, and residual gases [79]. In the case of cathode 137.2, where the cathode is grown on the same Mo plug after destroying cathode 137.1, it is possible that some residuals may remain on the substrate. These potential residuals could influence the observed discrepancy in the transition thickness during Sb deposition for cathode 137.2.

As depicted in Fig. 4.48a, like cathode 137.1, a significant change in the slope of the real-time QE was observed across all wavelengths above 58 nm of K deposition (i.e, equivalent to 68 nm of total evaporated thickness, indicated in the graph), denoted as the transition point (highlighted by the blue colored box with dashed line). As previously discussed, the observed change in QE after a specific evaporated thickness indicates a transition of the K-Sb compound from the amorphous phase to the crystalline phase [135]. Additionally, Figure 4.48b reveals a noticeable change in the reflectivity slope at 488 nm, 515 nm, and 540 nm following this transition point. However, no such slope change is evident in the reflectivity for 632 nm and 690 nm after the transitional thickness (highlighted by a red-colored circle in Fig. 4.48b). This difference in behavior between the two sets of wavelengths may be attributed to the complex crystallization of the KSb compound. If we compare cathode 137.2 with cathode 137.1 (Fig. 4.45), we can observe that this observed behavior in the real-time QE and reflectivity are consistent and reproducible.

When comparing real-time QE behavior during K deposition for cathode 137.2 (Figure 4.48a) with cathode 137.1 (Figure 4.45a), an interesting observation can be made. In Figure 4.45a, the QE at 297 nm (4.17 eV) was initially lower compared to the QE at 365

nm (3.39 eV) at the onset of K deposition. As previously discussed, we attributed this lower QE at 297 nm to the possibility of electron-electron (e-e) scattering, indicating the formation of the K-Sb compound. However, for cathode 137.2, this behavior (lower QE at 297 nm compared to 365 nm) occurred only after 58 nm of K deposition, specifically after the transition point (Fig. 4.48a). It is worth noting that, as mentioned earlier, we deposited K for cathode 137.2 at a lower heating power (i.e., 2.9 W) compared to the heating power (i.e., 3.1 W) used for cathode 137.1. Therefore, this difference between cathode 137.2 and 137.1 suggests that potentially, due to the higher substrate temperature, the reaction rate between Sb and K was higher for cathode 137.1, leading to the observed decrease in QE at 297 nm at the initial stage of K deposition.

Similar to the approach for cathode 137.1, we reconstructed the real-time spectral response and reflectivity for cathode 137.2 during Sb and K deposition. A comprehensive analysis of these real-time measurements during the Sb and K deposition processes is detailed in Appendix D.1.

4.4.5.2.2 K-Cs-Sb Phase

The following section will discuss the experimental results obtained during Cs deposition to form the KCsSb compound for cathode 137.2.

During the deposition of Cs, just as during Sb and K deposition, we monitored the real-time QE and reflectivity at various wavelengths. Fig. 4.49 presents a comprehensive overview of real-time QE and reflectivity at different wavelengths during the Cs deposition.

As shown in Figure 4.49b, a change in slope in the reflectivity is observed after 23 nm of Cs evaporation, with reflectivity increasing at 488 nm and decreasing at 632 nm and 690 nm (both changes highlighted by the red circles). Subsequently, after 30 nm of Cs evaporation, another change in slope is noticed in the reflectivity at 515 nm and 540 nm (highlighted by the red square box). These changes in slope in the reflectivity indicate the complex formation of the KCsSb compound during Cs addition.

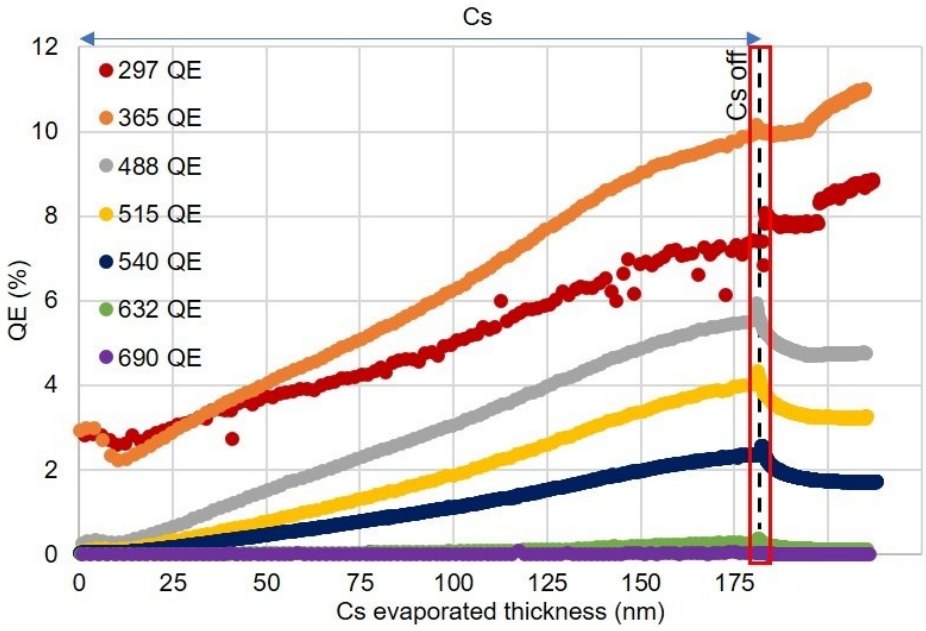

(a)

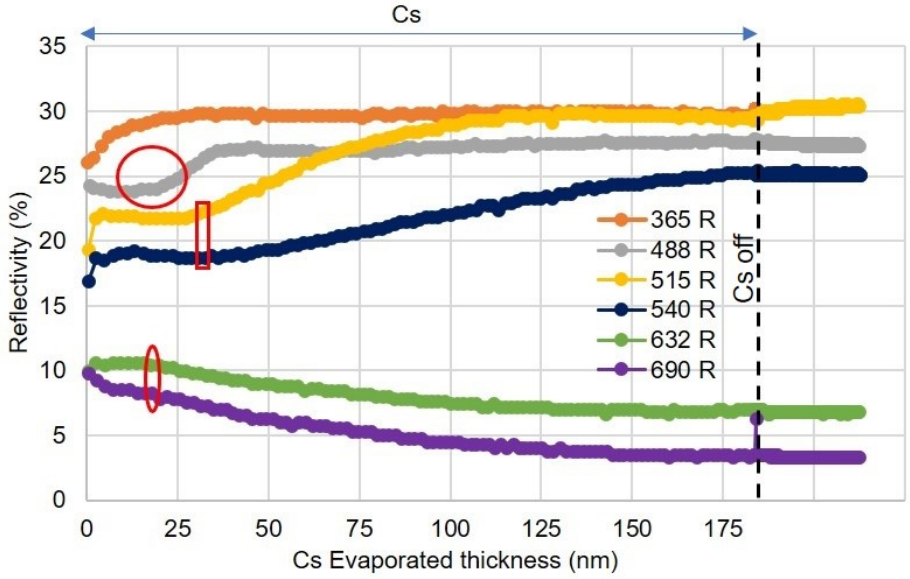

(b)

Figure 4.49: Real-time (a) QE and (b) reflectivity at different wavelengths during Cs deposition of cathode 137.2. The thicknesses represented in plots ‘a’ and ‘b’ correspond to the evaporated thickness of Cs. The small jump in the QE at the end of Cs deposition at all the wavelengths is highlighted by a red colored box in 4.49a.

In Figure 4.49a, at the end of Cs deposition, the QE at 297 nm and 365 nm experiences a minor jump, then it stabilizes for a period before showing a slight increase towards the end. However, for the remaining wavelengths (488 nm, 515 nm, 540 nm, 632 nm, and 690 nm), the QE experiences an initial small jump immediately after the end of Cs deposition, followed by a gradual decrease and stabilization at the end. This small jump at the end of Cs deposition is highlighted by the red colored box in Fig. 4.49a. Table 4.10 shows the absolute percentage of the QE increase after shutting down the Cs source at the different wavelengths.

Table 4.10: Summary of the absolute % QE increase after turning off the Cs source at different wavelengths.

Wavelengths (λ)	ΔQE (%)
297 nm (4.17 eV)	8.9 ± 0.07
365 nm (3.39 eV)	2.1 ± 0.01
488 nm (2.54 eV)	7 ± 0.01
515 nm (2.40 eV)	7.1 ± 0.02
540 nm (2.29 eV)	7.1 ± 0.02
632 nm (1.96 eV)	27 ± 0.11
690 nm (1.79 eV)	100 ± 0.11

The potential explanation for the QE jump observed at the end of Cs deposition has been previously discussed in the Section 4.3.1.1.4 (pages 82-83). We suggested that a temperature-sensitive surface layer might have formed near the subsurface region of the films during deposition, creating a balance between the adsorption (inward Cs distribution and diffusion) and desorption (evaporation of Cs from the surface) of Cs atoms near the surface. Any sudden decrease in the evaporation rate or increase in the substrate temperature could disrupt this balance, impacting the emission barrier through electron affinity. Considering that for cathode 137.2, Cs deposition occurs at a higher substrate temperature (120 °C) and a lower deposition rate (0.6 nm/min) compared to Cs deposition for cathodes prepared in the "R&D" preparation system (temperature range: 60-110 °C, deposition rate: 1 nm/min), the difference in the observed jump (at 540 nm) at the end of Cs deposition is much smaller for cathode 137.2 compared to the R&D cathodes (see Table 4.2).

However, it's noteworthy to observe that there are differences in the rate of QE jump at the different wavelengths, as indicated in Table 4.10. A significantly higher increase at the red wavelengths (632 nm and 690 nm) suggests a potential decrease in electron affinity. Given that these red wavelengths are close to the photoemission threshold of the KCsSb cathodes, they carry less photon energy compared to other wavelengths, making it less efficient to excite electrons from the cathode into the vacuum. Consequently, any decrease in the height of the potential barrier (electron affinity) leads to a higher likelihood of electron excitation into the vacuum, resulting in a significant increase in the QE jump for higher wavelengths (i.e., 632 nm and 690 nm). At wavelengths of 488 nm, 515 nm, and 540 nm, the similarity in photon energy levels leads to an equivalent rate of jump in the QE (as Table 4.10 shows).

Another intriguing observation is that during Cs deposition, the real-time increase in QE at 297 nm is lower than at 365 nm (Fig. 4.49a). As previously explained, this phenomenon is linked to electron-electron (e-e) scattering within the KCsSb compound (e-e scattering possible when $h\nu \geq 2E_g$). However, in Table 4.10, at the end of the Cs deposition, we observe a higher rate of QE jump at 297 nm (8.9 %) compared to 365 nm (2.1 %). This suggests that, due to possible e-e scattering, the excited electrons at 297 nm are initially less efficiently emitted into the vacuum compared to those at 365 nm. Therefore, as the barrier height is reduced (at the end of Cs deposition), it becomes more probable for a greater number of electrons at 297 nm to escape into the vacuum, leading to the observed higher QE increase at 297 nm.

Following this jump in the QE, the quantum efficiency continuously decreased during the cooling process, and later it stabilized for wavelengths 488 nm, 515 nm, 540 nm, 632 nm, and 690 nm. However, for 297 nm and 365 nm, the QE initially stabilized up to a certain point and then increased at the end (Fig. 4.49a). This QE trend suggests that, possibly due to the still higher substrate temperature after Cs deposition, some excess Cs may have evaporated from the surface. Therefore, due to this Cs evaporation, the stoichiometry of the compound re-balanced, and in the end, it likely stabilized.

Similar to the Sb and K depositions, we reconstructed the real-time spectral response and reflectivity during Cs deposition for cathode 137.2. A comprehensive analysis of

these measurements during the Cs deposition process is detailed in Appendix D.2.

We conducted measurements of spectral reflectivity and spectral response after each deposition process (i.e., after the K and after the Cs deposition), including the Mo plug (measured before the deposition). In Fig. 4.50, a comparison is presented between the spectral reflectivity of the Mo plug and the deposited KSb and KCsSb compounds. The changes in the spectral reflectivity pattern following cathode deposition can be observed from the plot. It is evident that the spectral reflectivity pattern of KCsSb closely resembles that of the KSb compound, indicating that the spectral reflectivity pattern observed for KCsSb is essentially a continuation of the pattern observed for KSb, with some modifications, e.g., the appearance of a peak at 2.4 eV for KCsSb.

In Fig. 4.51, the spectral response measurements of KSb and KCsSb compounds, taken after the deposition, are illustrated. An increase in the QE across all wavelengths can be observed for the KCsSb compound compared to the KSb compound.

Additionally, it can be observed that the spectral reflectivity and spectral response patterns of KSb and KCsSb compounds in Fig. 4.50 and 4.51 closely align with the final portion of the real-time spectral reflectivity (plot 6 in Fig. 8.19 and 8.21, present in Appendix D) and spectral response (plot 6 in Fig. 8.18 and 8.20, present in Appendix D) measurements, demonstrating the accuracy of the real-time data measurements during the deposition.

In the case of cathode 137.2, the QE for the KSb compound was measured to be 0.15% at 515 nm (i.e., 2.40 eV), whereas for the KCsSb compound, the QE was 4.25% at 515 nm.

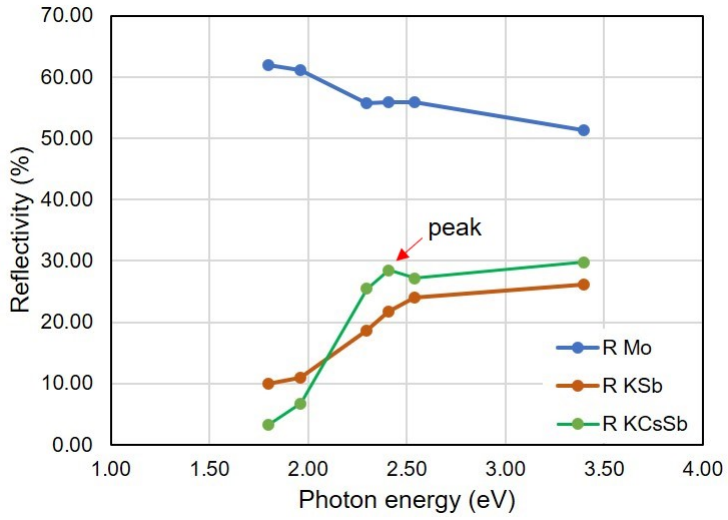

Figure 4.50: illustrates spectral reflectivity of Mo (measured before the deposition), KSb, and KCsSb compounds (measured after their respective depositions) for cathode 137.2.

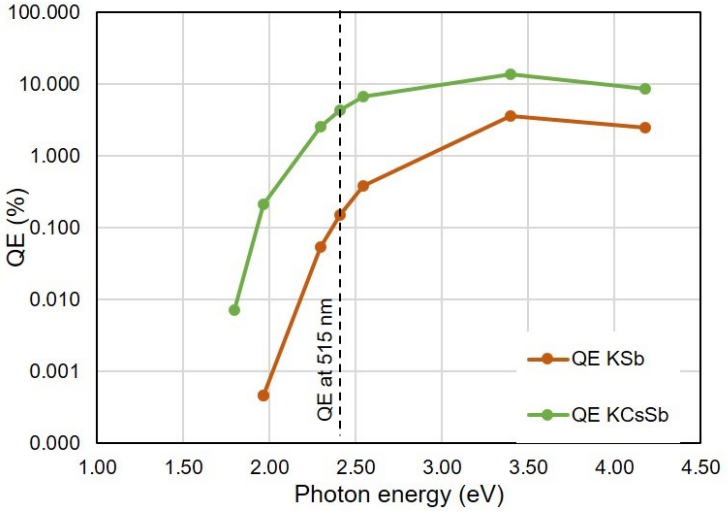

Figure 4.51: Spectral response of the KSb and KCsSb compound measured after the deposition process for cathode 137.2. Since the work function of Mo is approximately 4.6 eV [159], the spectral response of Mo is not included in the plot as it exhibits negligible QE in the given energy range.

4.4.5.3 Cathode 137.3

Similarly to the approach taken for cathode 137.2, we aimed to explore the influence of varying thickness on the cathode's structural and optical properties. To achieve this, we chose to grow a thin cathode (i.e., Sb = 5 nm), referred to as cathode 137.3, on the same Mo plug following the removal of cathode 137.2 (i.e., thick, Sb = 10 nm) through the heating process.

The deposition process for cathode 137.3 was carried out sequentially, starting with 5 nm of Sb deposition, followed by K deposition until reaching the photocurrent peak. Subsequently, Cs deposition was performed until the photocurrent approached saturation levels. As presented in Table 4.9, during the Sb deposition phase, the deposition rate was maintained at 0.9 nm/min. For the K deposition, the deposition rate was maintained at 0.5 nm/min, and during the Cs deposition, it was maintained at 0.9 nm/min.

As previously discussed, due to a misalignment in the temperature reading system, we set the plug heating power for cathode 137.3 to the same values used for cathode 137.2 to match the temperature settings, which were used during Sb, K, and Cs deposition. In summary, the deposition of Sb, K, and Cs occurred for cathode 137.3 at similar substrate temperatures as those used for cathode 137.2.

Similar to the previous cathode, we monitored real-time photocurrent and reflectivity at 7 different wavelengths during the deposition of Sb, K, and Cs. The following section will discuss the experimental results obtained from the KSb compound for cathode 137.3.

4.4.5.3.1 K-Sb Phase

Fig. 4.52 presents a detailed real-time QE and reflectivity at the different wavelengths during the Sb and K deposition.

As can be seen in Figure 4.52b, during Sb deposition, the reflectivity first slightly dropped at all the wavelengths. However, after around 1.5 nm (highlighted by the red colored box in Fig. 4.52b), it began rising until the end of Sb deposition. Considering that all the growth parameters remained identical to cathode 137.2, as discussed in the context of cathode 137.2 (Section 4.4.5.2.1, page 134), these fluctuations in reflectivity beyond a specific thickness of Sb deposition can likely be attributed to the transition from

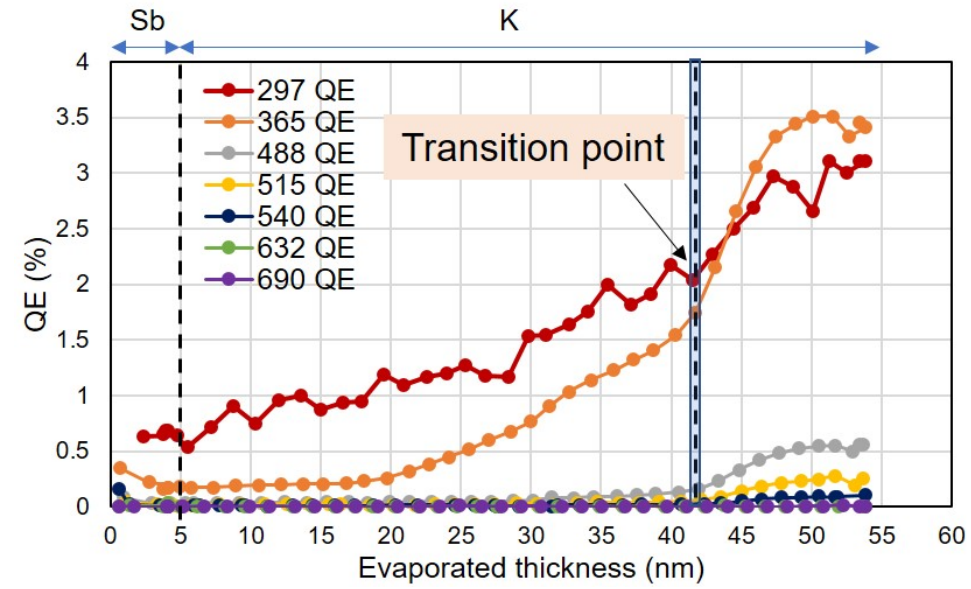

(a)

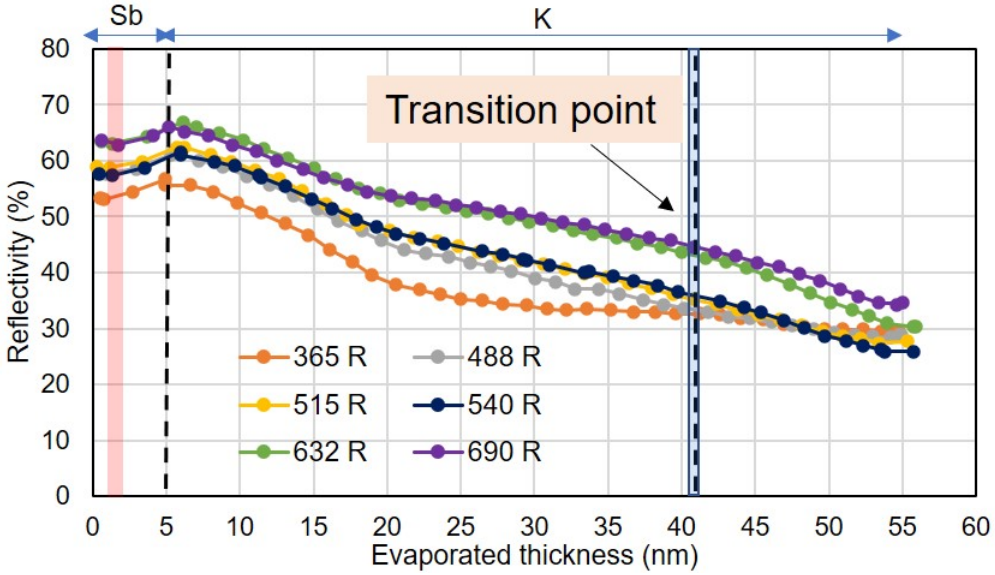

(b)

Figure 4.52: Real-time (a) QE and (b) reflectivity at different wavelengths during Sb and K deposition of cathode 137.3. The thicknesses represented in plots 'a' and 'b' correspond to the evaporated thickness of Sb and K, with a dashed line separating them in the plot. The transition point during K deposition is highlighted by a dashed line along with a blue-colored box.

amorphous to crystalline structure within the Sb compound [53].

As depicted in Fig. 4.52a, a significant change in the slope of the real-time QE (across all 7 wavelengths) is evident after 36 nm of K deposition (i.e, equivalent to 41 nm of total evaporated thickness, indicated in the graph, highlighted by the blue colored box with dashed line), denoted as the transition point. As it is already discussed for the previous cathodes (cathode 137.1 and cathode 137.2, Section 4.4.5.1), the observed change in QE after a specific evaporated thickness is a sign of the transition of the K-Sb compound from the amorphous phase to the crystalline phase [135].

In Figure 4.52b, it is also interesting to observe that after this transition point, there is no discernible change in the slope of reflectivity, and the reflectivity pattern remains consistent across all wavelengths. When comparing this with Figure 4.48b, a discrepancy in the reflectivity behavior becomes apparent between two sets of wavelengths, namely 488 nm, 515 nm, 540 nm and 632 nm, 690 nm after the transition point. This difference in reflectivity behavior during K deposition between the two cathodes, 137.2 (thick) and 137.3 (thin), emerging after the transition point, indicates a potential distinction in the formation of crystal structures between these two cathodes. Additional analysis of the thick and thin KSb compounds can be found in Chapter 6 (Section 6.1).

In Figure 4.52a, the QE at 297 nm (4.17 eV) was initially higher compared to the QE at 365 nm (3.39 eV). However, after the transition point, this pattern reversed. As previously explained, we associated this lower QE at 297 nm with the potential occurrence of electron-electron (e-e) scattering, suggesting the formation of the K-Sb compound. Comparing this behavior with Fig. 4.48a, we observe a similar trend, indicating that both compounds were grown under similar substrate temperature conditions.

Similar to cathode 137.2, we reconstructed the real-time spectral response and reflectivity during the Sb and K deposition for cathode 137.3. A comprehensive analysis of these measurements is elaborated in Appendix E.1.

4.4.5.3.2 K-Cs-Sb Phase

Fig. 4.53 provides a comprehensive overview of real-time QE and reflectivity at different wavelengths during the Cs deposition.

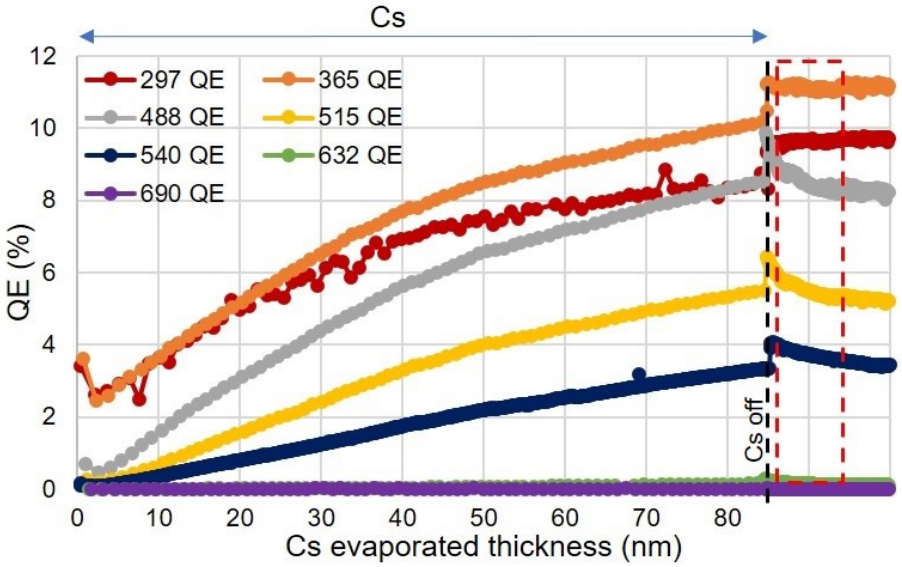

(a)

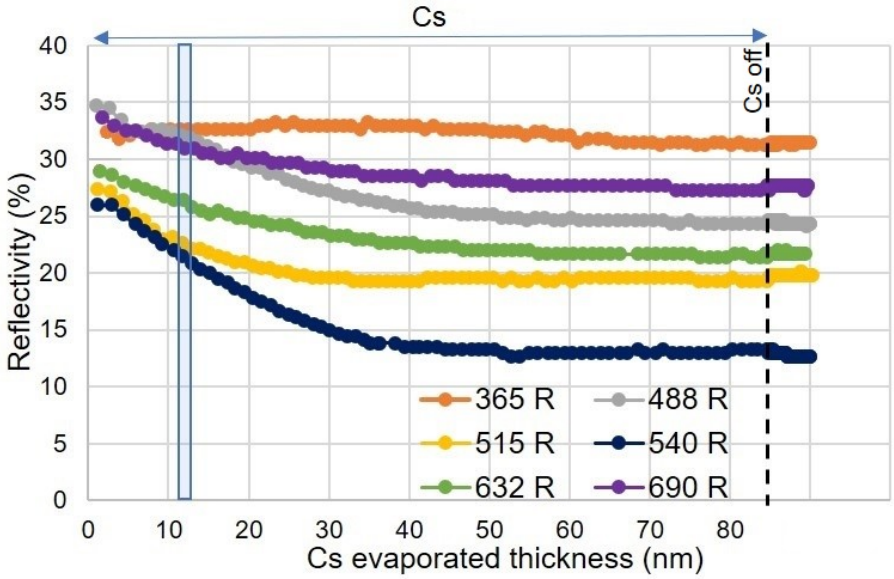

(b)

Figure 4.53: Real-time (a) QE and (b) reflectivity at different wavelengths during Cs deposition of cathode 137.3. The thicknesses represented in plots 'a' and 'b' correspond to the evaporated thickness of Cs. The behavior of the QE after the end of Cs deposition at all the wavelengths is highlighted by a red dashed colored box in 4.53a. The blue box in plot 'b' highlights the point after which the change in the slope of the reflectivity across all wavelengths (except 365 nm) occurred.

As shown in Figure 4.53b, a change in slope in the reflectivity is observed after 13 nm of Cs evaporation in almost all the wavelengths except 365 nm (highlighted by the blue-colored box). Afterwards, the reflectivity stabilizes towards the end of the Cs deposition. These changes in slope in the reflectivity indicate the complex formation of the KCsSb compound during Cs addition. Interestingly, no major change in the slope of the reflectivity behavior at 365 nm is noticed throughout the addition of Cs. However, when we compare the reflectivity behavior of the current cathode (Fig. 4.53b) with cathode 137.2 in Fig. 4.49b, we can observe a significant difference in reflectivity behavior, suggesting the potential formation of different compounds.

In Figure 4.53a, at the end of Cs deposition, the QE at UV wavelengths 297 nm and 365 nm experiences a slight jump, and then it stabilizes. However, for the remaining wavelengths (488 nm, 515 nm, 540 nm, 632 nm, and 690 nm), the QE experiences an initial small jump immediately after the end of Cs deposition, followed by a gradual decrease and stabilize at the end. If we compare this with the behavior observed in cathode 137.2, as shown in Fig. 4.49a, we can notice a similar trend. Table 4.11 shows the absolute percentage of the QE increase after shutting down the Cs source at the different wavelengths.

The potential explanation for the QE jump observed at the end of Cs deposition has been discussed previously in Section 4.3.1.1.4 (pages 82-83), including for cathode 137.2 (Section 4.4.5.2.2, page 137). However, it's noteworthy to observe that, like cathode 137.2, there are differences in the rate of QE increase at the different wavelengths, as indicated in Table 4.11. Comparing this data with the cathode 137.2 (Table 4.10), a similar trend can be observed between the two. A significantly higher increase at the red wavelengths (632 nm and 690 nm) suggests a potential decrease in electron affinity, as described for cathode 137.2. Since these red wavelengths are close to the photoemission threshold of the KCsSb cathodes, they carry less photon energy compared to other wavelengths, making it less efficient to excite electrons from the cathode into the vacuum. Therefore, any decrease in the height of the potential barrier (electron affinity) results in a notable increase in the QE for lower photon energy wavelengths. At wavelengths of 488 nm, 515 nm, and 540 nm, the similarity in photon energy levels leads to an equivalent rate

of increase in the QE. Moreover, like cathode 137.2, we observe a higher rate of QE jump at 297 nm (14.06 %) compared to 365 nm (10.03 %) at the end of Cs deposition. This suggests that, due to possible e-e scattering, the excited electrons at 297 nm are initially less efficiently emitted into the vacuum compared to those at 365 nm. Consequently, when the barrier height is reduced, it becomes more likely for a larger number of electrons at 297 nm to escape into the vacuum.

Interestingly, upon comparing the rate of the jump at different wavelengths between cathode 137.2 (Table 4.10) and 137.3 (Table 4.11), we observe a slightly higher rate of jump for cathode 137.3. As previously explained, this QE jump is sensitive to both substrate temperature and deposition rate. Given that the substrate temperature was similar during Cs deposition for both cathodes, except for the deposition rate (refer to Table 4.9), it suggests that the higher deposition rate in the case of Cathode 137.3 could potentially contribute to the slightly higher rate of QE jump at the end of the Cs deposition.

Table 4.11: Summary of the absolute % QE increase after turning off the Cs source at different wavelengths.

Wavelengths (λ)	Δ QE (%)
297 nm (4.17 eV)	14.06 ± 0.07
365 nm (3.39 eV)	10.03 ± 0.01
488 nm (2.54 eV)	15.61 ± 0.01
515 nm (2.40 eV)	15.32 ± 0.02
540 nm (2.29 eV)	20.95 ± 0.02
632 nm (1.96 eV)	93.33 ± 0.11
690 nm (1.79 eV)	90 ± 0.11

Similar to previous cathodes, we reconstructed the real-time spectral response and reflectivity during the Cs deposition for cathode 137.3. A comprehensive analysis of these measurements is elaborated in Appendix E.2.

We conducted measurements of spectral reflectivity and spectral response after each deposition process (i.e., after the K and after the Cs deposition), including the Mo plug (measured before the deposition). In Fig. 4.54, the spectral response measurements of KSb and KCsSb compounds, taken after the deposition, are illustrated. An increase in the QE across all wavelengths can be observed for the KCsSb compound compared to

the KSb compound. In the case of cathode 137.3, the QE for the KSb compound was measured 0.23% at 515 nm (i.e., 2.40 eV), whereas for the KCsSb compound, the QE was 4.97% at 515 nm.

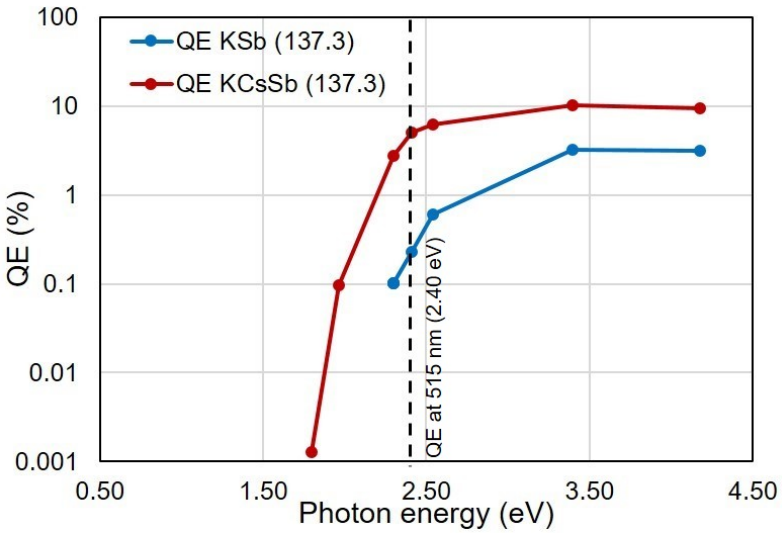

Figure 4.54: Spectral response of the KSb and KCsSb compound measured after the deposition process for cathode 137.3.

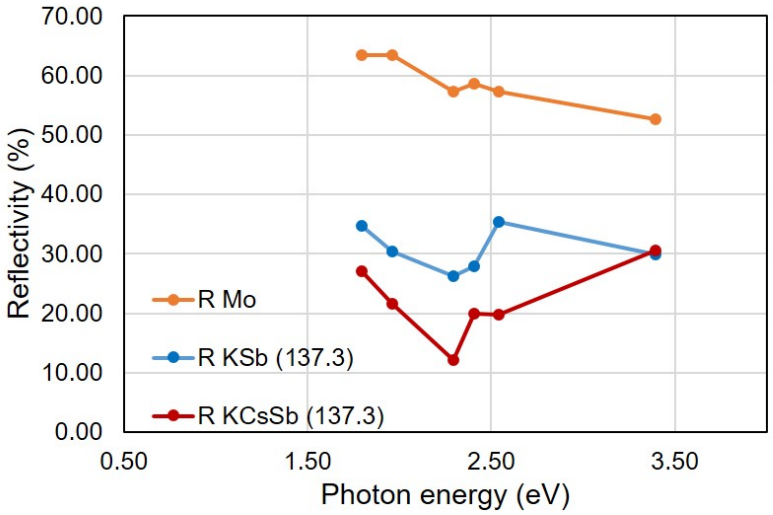

Figure 4.55: Spectral reflectivity of Mo, KSb, and KCsSb compounds for cathode 137.3.

In Fig. 4.55, a comparison is presented between the spectral reflectivity of the Mo plug and the deposited KSb and KCsSb compounds. The changes in the spectral reflectivity pattern following cathode deposition can be observed from the plot. It is evident that the spectral reflectivity pattern of KCsSb closely resembles that of the KSb compound, indicating that the spectral reflectivity pattern observed for KCsSb is essentially a continuation of the pattern observed for the KSb, with some minor modifications, similar to the cathode 137.2 (Fig. 4.50). When comparing the spectral reflectivity plots between the cathodes 137.2 and 137.3 in Fig. 4.50 and 4.55, respectively, it becomes apparent that there are differences in the spectral reflectivity patterns of the KCsSb compound for these two cathodes. Furthermore, it's worth highlighting that this comparison reveals a significant difference in the spectral reflectivity pattern, which only becomes evident after K deposition (i.e., for the KSb compound) between the two cathodes. As detailed in Appendices D.1 and E.1, noticeable differences in the spectral reflectivity patterns between two KSb compounds (cathode 137.2 and cathode 137.3) only became apparent beyond the transition point during K deposition (illustrated in Fig. 8.19 and Fig. 8.23). This occurred during their phase of KSb crystalline development. Consequently, it can be deduced that the variations observed in the spectral reflectivity patterns of the KSb compounds are likely due to differences in the crystal structures of the two cathodes (namely, 137.2 and 137.3). However, in order to get a comprehensive interpretation of these optical spectra results, we compare these experimental findings with a theoretical model. A detailed analysis and interpretation of these results is presented in Chapter 6 (Section 6.1) of this report.

4.4.5.4 Comparative Analysis of Spectral Response and Spectral Reflectivity: Cathode 137.2 (Thick) vs. Cathode 137.3 (Thin)

To gain further insights into the properties of the grown compound, we have measured the spectral response and spectral reflectivity across a broader spectrum after the deposition of cathode 137.2 (thick) and 137.3 (thin), spanning from 297 nm to 1200 nm, employing a monochromator. Fig. 4.56 depicts a comparison of the spectral response and spectral reflectivity of the two cathodes.

In Fig. 4.56, the pattern of the spectral response is similar for both the cathodes. However, in the spectral reflectivity plot, some differences between the two cathodes are evident (highlighted by different colored circles). Two distinct peaks appear in the spectral reflectivity in the near-infrared spectrum for both cathodes (highlighted by red circles). For cathode 137.2, the peak emerges at 1.05 eV, while for cathode 137.3, the peak is observed at 1.22 eV. Furthermore, an additional peak appears at 1.44 eV for cathode 137.2 (highlighted by the black circle), which is not observed for cathode 137.3.

As previously discussed in Section 4.3.1.1.4 & Section 4.4.1, there is a discrepancy in behavior at lower photon energies (from 2.28 eV onward) between the thin and thick cathodes, as shown in Fig. 4.16b & Fig. 4.31b. A similar observation can be made in Fig. 4.56. It's evident that for cathode 137.3 (thin), the spectral reflectivity significantly bends upward at 2.29 eV (highlighted by violet circles), whereas for cathode 137.2 (thick), this occurs at 1.87 eV (highlighted by violet circles). When comparing this behavior with Fig. 4.16b & Fig. 4.31b, it becomes apparent that these characteristics are highly reproducible and intact with their respective cathode recipes (i.e., for thick and thin cathodes). A detailed discussion and interpretation of these results is provided in Chapter 6 (Section 6.1.2).

Additionally, as observed in the "R&D" KCsSb cathodes (see Fig. 4.17), and also for the first batch of KCsSb cathodes produced in the "Production" system (see Fig. 4.32), we noticed two distinct colors for these two cathodes (Cathode 137.2 & Cathode 137.3). Specifically, Cathode 137.2 (thick) appears blue, whereas Cathode 137.3 (thin) appears violet, as illustrated in Fig. 4.57. This demonstrates the reproducibility of the colors, which remain consistent with their respective cathode recipes (thick and thin cathodes).

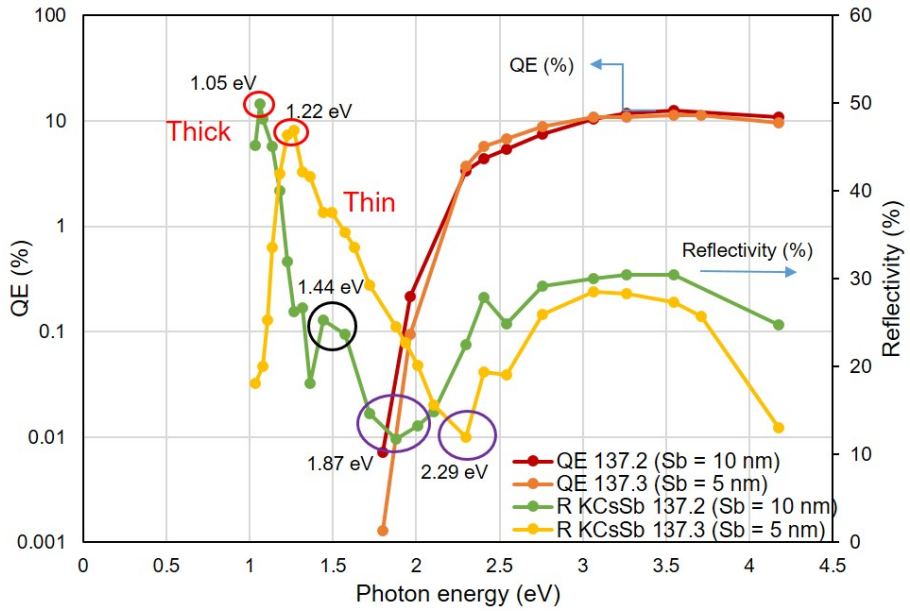

Figure 4.56: Comparison of the spectral response and spectral reflectivity of the KCsSb compound for cathodes 137.2 and 137.3. The colored circles within the plot highlight the observed variations in the spectral reflectivity between two cathodes.

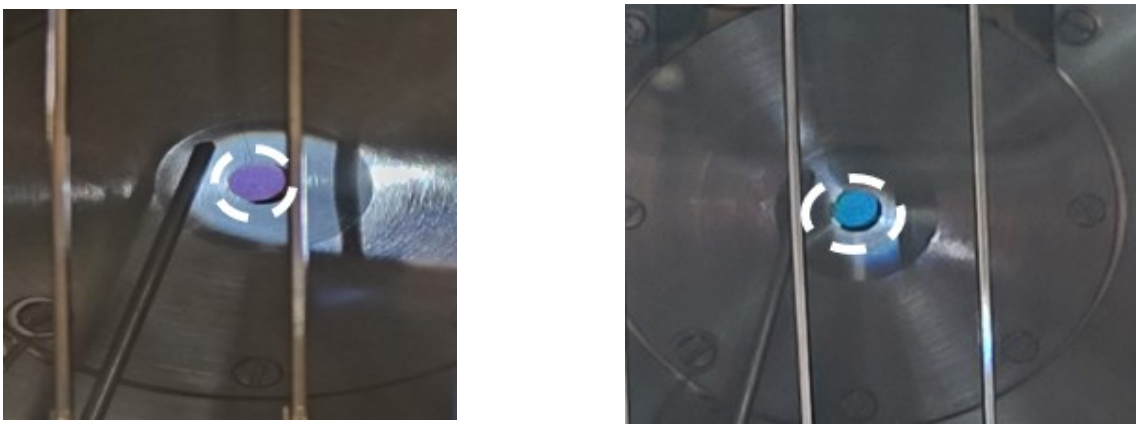

(a) (b)

Figure 4.57: Colors of photocathodes after the deposition (a) 137.3, i.e., thin cathode (violet in color), and (b) 137.2, i.e., thick cathode (blue in color). Since the cathode is placed behind the masking system, the active photoemissive area is highlighted by the white dashed circle for both cathodes.

4.4.5.5 Studies of Cathode's Storage Lifetime

Cathode 137.3 remained in the production preparation system for approximately 14 months. Subsequently, in December 2023—roughly 14 months after its production—we conducted spectral response and spectral reflectivity measurements on cathode 137.3. Figure 4.58 illustrates the comparison between the spectral response and spectral reflectivity of cathode 137.3 obtained after production and following a 14-month storage period. We observed that the QE at lower photon energy (from 1.96 eV to 2.75 eV) has decreased compared to the values measured after production. For example, the QE at 515 nm (2.40 eV) has decreased to 2.31% from the initial value of 4.97% following production. However, at higher photon energy (from 3.06 eV to 4.17 eV), the QE remains similar to the value observed after production (highlighted by green dashed circle). Nevertheless, upon comparing the spectral reflectivity, we observed that the reflectivity patterns are almost similar in both plots. Nonetheless, a slight increase in reflectivity at higher photon energy is noticeable after storage. It's worth noting that during this storage period, the pressure in the "Production" preparation system was maintained at approximately 1.3×10^{-10} mbar. To investigate this change in the spectral response of cathode 137.3, we analyzed the quality of the vacuum level inside our production system using the Residual Gas Analyzer (RGA). Figure 4.59 displays the mass spectrum of the residual gases within the production system, revealing traces of some residual gases present inside the "Production" preparation system. The observed residual peaks in Fig. 4.59 could be attributed to desorption or outgassing from the surfaces and walls within the vacuum system.As discussed in Sections 4.3.2.2 (pages 95-97), such changes in the spectral response for cathode 137.3 may arise from its storage in the UHV system, potentially leading to the formation of weak bonds between the cathode's surface and residual gas molecules, causing surface-level alterations. In the following section, an analysis of the cathode's (cathodes 137.2 and 137.3) lifetime in relation to substrate temperature is presented.

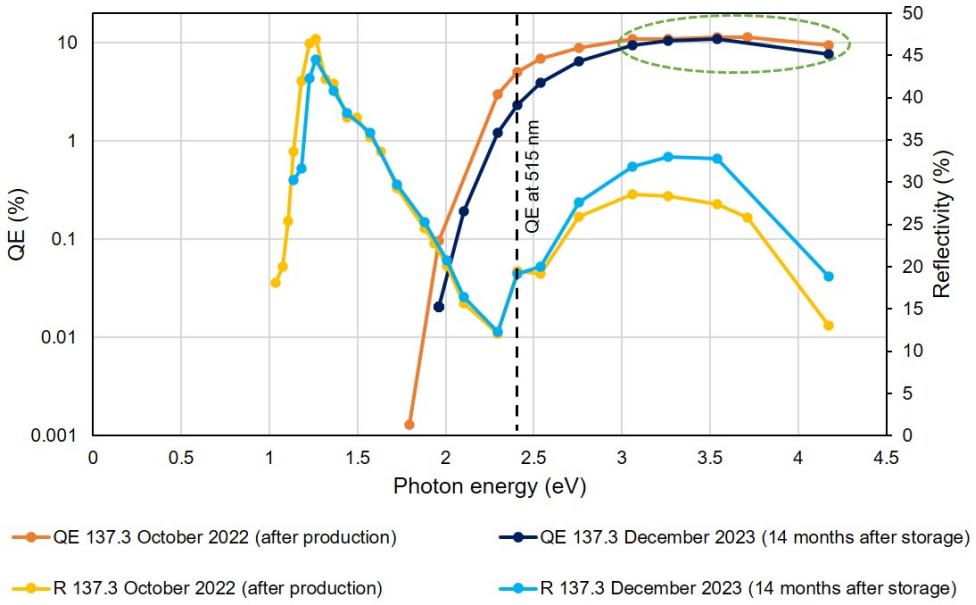

Figure 4.58: Comparison of spectral response and spectral reflectivity of cathode 137.3 after production and after 14 months of storage.

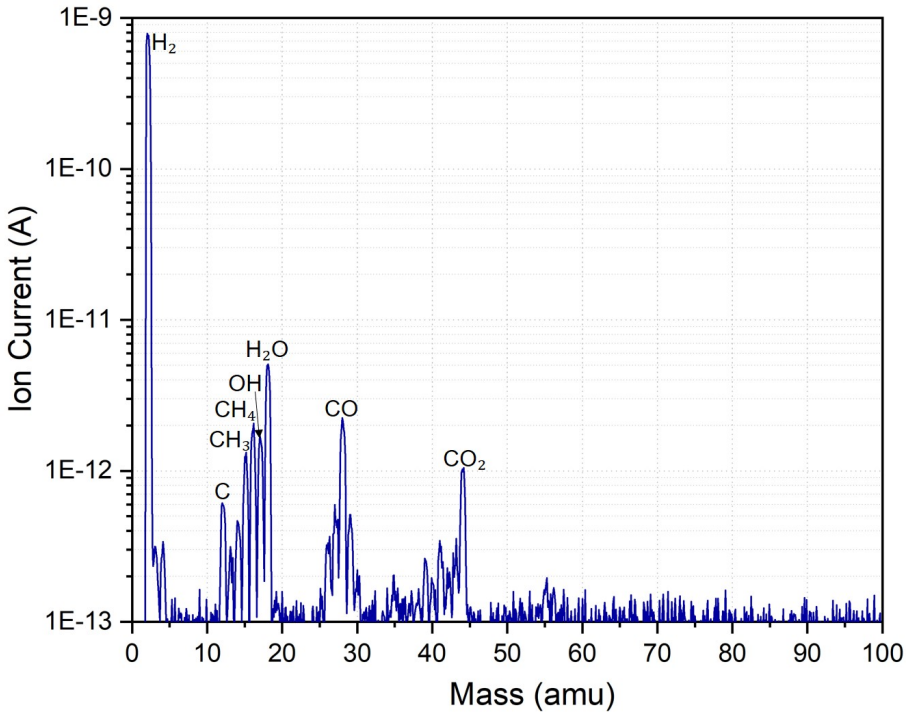

Figure 4.59: Mass Spectrum of the residual gases in the "Production" preparation system.

4.4.5.6 Studies of Cathode Lifetime in Relation to Substrate Temperature

4.4.5.6.1 Cathode 137.2

Lifetime measurements were conducted on cathode 137.2 (Sb = 10 nm, thick cathode) in the production preparation system at various substrate temperatures, mirroring the procedures employed for the NaKSb(Cs) cathode (Section 4.3.2.2) in the "R&D" preparation system. Cathode 137.2 was heated to different temperatures for QE degradation measurements. Throughout this process, we utilized the multi-wavelength setup and consistently illuminated the photocathode at 7 different wavelengths, measuring real-time QE and reflectivity. Figure 4.60a and 4.60b illustrate the history of the QE and reflectivity of cathode 137.2 during the heating process, while Fig. 4.60c represents the temperature history during the cathode heating process. During the lifetime studies, temperature measurements of the Mo plug were taken using the thermocouple positioned at the rear part of the plug (Section 3.2.2, page 51). Unfortunately, due to the malfunction of the new temperature measuring system, we were unable to utilize it to measure the plug's temperature during the process. Note that the life-time studies for cathode 137.2 were conducted a few days after its production.

As shown in Fig. 4.60, we initially raised the substrate temperature to 73 °C and maintained it for 1 hour. However, during this time, we did not observe any changes in both the QE and reflectivity. Subsequently, we increased the temperature to 89 °C and held it for approximately 30 minutes, then further raised it to 109 °C for nearly 15 minutes. Finally, we increased it to 124 °C. Despite these gradual temperature increases, we did not observe any degradation in either the QE or reflectivity, as depicted in Figs. 4.60a and 4.60b. We couldn't raise the substrate temperature beyond 124 °C at the current plug position inside the chamber to avoid potential impacts on the masking system, which is situated near the Mo plug. Details about the positioning of the masking and the Mo plug can be found in the reference [123].

Given the behavior observed for cathode 137.2, where no changes were detected even at 124 ° C, further investigation was necessary to understand the thermal degradation resilience of KCsSb cathodes. Consequently, a comprehensive study was conducted on

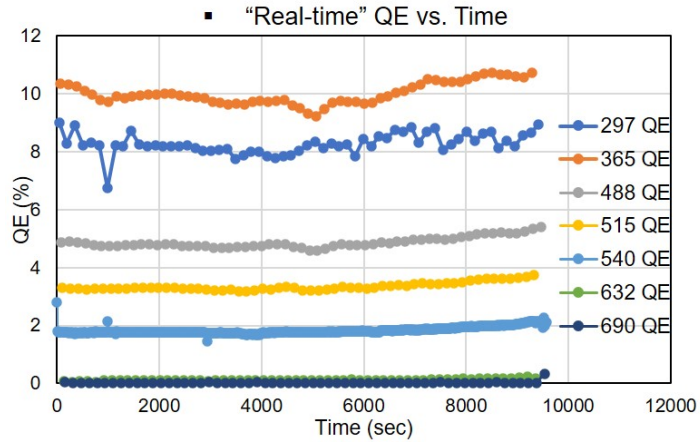

(a)

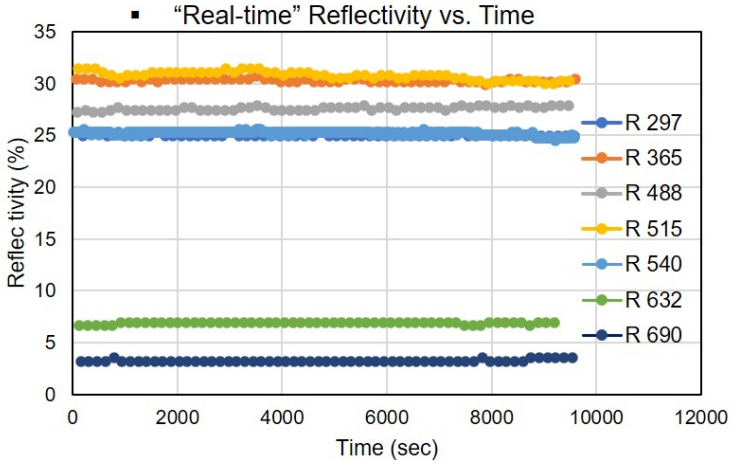

(b)

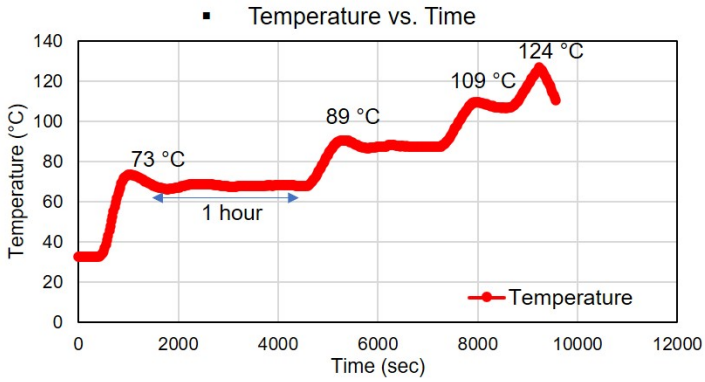

(c)

Figure 4.60: Real-time (a) QE, (b) reflectivity at different wavelengths, and (c) history of the temperature reading during the heating process of cathode 137.2.

cathode 137.3, exposing it to different substrate temperature set points for longer durations. The subsequent section will present the outcomes of the cathode lifetime study for cathode 137.3.

4.4.5.6.2 Cathode 137.3

As detailed in Section 4.4.5.5 (page-151), the QE exhibited some degradation, particularly at lower photon energies, for cathode 137.3 after being stored for 14 months inside the "Production" Preparation system (Fig. 4.58). Afterward, mirroring the approach taken with cathode 137.2, we performed lifetime measurements at various temperatures for cathode 137.3. However, for cathode 137.3, we chose to subject the cathode to different temperatures for a longer duration (about 24 hours). Through this method, our objective is to investigate the impact of prolonged exposure to different temperature conditions on the cathode's QE. Throughout this process, we utilized the multi-wavelength setup and consistently illuminated the photocathode at 7 different wavelengths, measuring real-time QE and reflectivity. Fig. 4.61a presents the decay curves (at 540 nm) of cathode 137.3 at different substrate temperatures, with the initial QE of each experiment normalized to unity. Similar to the NaKSb(Cs)-2 cathode (Section 4.3.2.2, page 97), we have determined the 1/e lifetime of each measurement by using exponential decay functions ($QE = QE_0 e^{-\frac{t}{\tau_1}}$; see Section 4.3.2.2) to fit the experimental data. Fig. 4.61b shows the 1/e lifetime of the photocathode as a function of various substrate temperatures. Note that this lifetime measurement for cathode 137.3 was conducted when the QE had degraded after being stored for 14 months.

As illustrated in Fig. 4.61a, a noticeable decrease in QE is observed beyond a substrate temperature of 110 °C. At 110 °C, the 1/e lifetime, determined from the single exponential fit of the decay data, is 103 hours. At 130 °C and 140 °C, the 1/e lifetimes are calculated to be 38 and 22 hours, as shown in Fig. 4.61b. This observation clearly indicates that prolonged exposure leads to a significant decrease in the lifetime of the cathode at substrate temperatures above 110 °C. For cathode 137.2, the shorter duration of exposure to temperatures above 110 °C potentially resulted in the absence of any observed decrease in QE. Alternatively, the observed reduction in QE above 110 °C for cathode 137.3 could

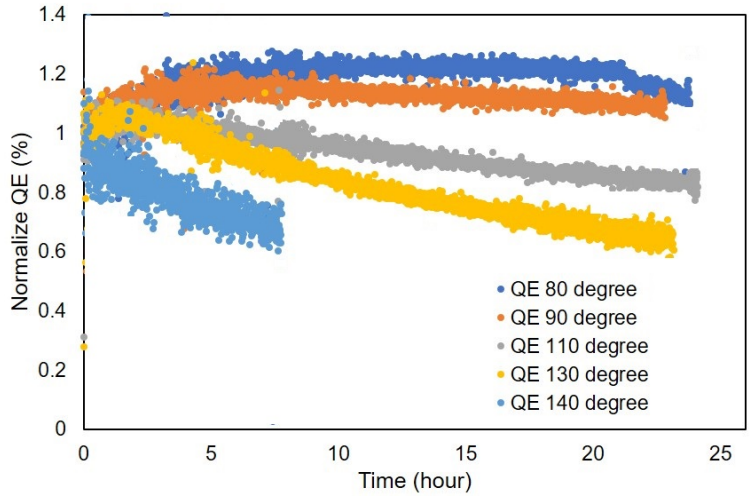

(a)

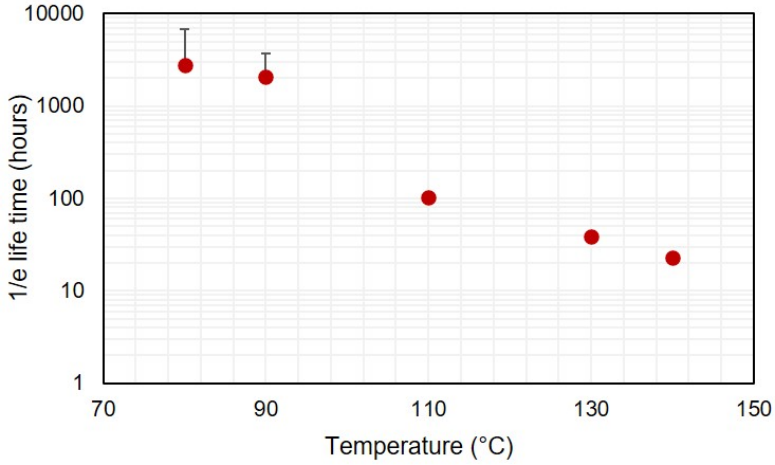

(b)

Figure 4.61: (a) Decay curves of cathode 137.3 at different temperatures are shown in the plot, where the QE mentioned is measured at 540 nm. Due to some technical difficulties, the measurement at 140 °C was limited to 7.6 hours. (b) 1/e lifetime of the cathode 137.3 with respect to different decay temperatures.

be due to the aging of the cathode material. Nevertheless, in summarizing these findings, we can infer that the produced KCsSb can withstand temperatures of at least up to 90 °C, even with prolonged exposure. Moreover, to determine the accuracy of the substrate temperature at which the KCsSb compound degrades and its lifetime with respect to different temperature set points, these experiments should be repeated and carried out in the future

using the "new temperature measurement system" (described in Section 3.2.2, page 51) within the production system.

4.4.6 Summary and Discussion

To gain a deeper understanding of the photocathode structure, three photocathodes (one KSb and two KCsSb compounds) were grown in the production system using a "multi-wavelength" optical diagnostics setup. This setup allowed for real-time measurements of optical responses, such as QE and reflectivity, at different wavelengths during the cathode film deposition. Upon comparing the real-time optical spectra, differences in reflectivity behavior were observed after the transition point during K deposition between cathodes 137.2 (thick) and 137.3 (thin). Additionally, variations in reflectivity behavior during Cs deposition were observed between the two cathodes.

Furthermore, after the cathode deposition, spectral responses and reflectivity across a wider spectrum were measured. Upon analyzing these optical spectra, differences in spectral reflectivity patterns between the two types of KCsSb compounds (i.e., 137.2 (thick) & 137.3 (thin)) became evident. Notably, a substantial difference emerged when comparing the spectral reflectivity pattern of the KSb compound between cathodes 137.2 (thick) and 137.3 (thin), as depicted in Fig. 4.50 and 4.55. Moreover, it was evident that the spectral reflectivity pattern for the KCsSb compound was a continuation of the behavior observed for the KSb compound (with minor modifications) for both cathodes. Therefore, if these changes in spectral reflectivity are linked to differing crystal modifications between the two cathodes (i.e., 137.2 (thick) and 137.3 (thin)), it can be inferred that the major crystal modification occurs during K deposition.

Upon summarizing these results, it can be deduced that variations in thickness influence the optical properties of the KCsSb compound. However, to provide a proper interpretation, these optical spectra results should be further verified using a theoretical model. Therefore, DFT studies were conducted, and a comprehensive discussion and interpretation of these results are presented in Chapters 5 and 6.

Chapter 5

Computational Method

5.1 Motivation

Determining the electronic structure of a material through optical measurements, such as spectral reflectivity and spectral response, is considered an indirect method because it relies on interpretations and correlations rather than direct measurements of electronic states.

In materials science and solid-state physics, direct methods of studying electronic structure involve directly probing the energy levels and electronic states of the material, such as through techniques like photoemission spectroscopy or scanning tunneling microscopy. These methods provide direct information about the distribution of electrons and their energies in the material.

On the other hand, optical measurements, including reflectivity, absorption spectroscopy, and photoluminescence, provide valuable indirect information about the electronic structure. These techniques measure the interaction of light with the material and provide insights into the energy band structure, electronic transitions, and optical properties.

By analyzing the reflectivity of a material across a range of wavelengths or energies, valuable information can be inferred about the electronic structure within the material, including its band gaps, energy levels, and electronic transitions. However, it is crucial

to consider various factors that can impact the observed reflectivity, such as interference effects stemming from the material's thickness or the presence of multiple layers (such as thin films and substrates). These factors can introduce complexities into the interpretation of reflectivity measurements. Therefore, it's important to note that the interpretation of optical measurements requires theoretical models and assumptions about the underlying electronic structure.

To gain insights into the electronic properties of the material, a Density Functional Theory (DFT) study is performed on the various semiconductor photocathode materials such as K_2CsSb, K_3Sb, Na_2KSb, etc., utilizing tools like the *epsilon.x* code within the *QuantumEspresso* package to calculate the complex dielectric function. This complex dielectric function provides information about the material's optical properties and is linked to its electronic band structure, energy levels, and electronic transitions. Using Maxwell's equations, the theoretical reflectivity is calculated based on the complex dielectric function, enabling a comparison with experimental reflectivity data obtained from measurements on the actual material.

By comparing the theoretical and experimental reflectivity data, it becomes possible to assess the agreement between the predicted electronic structure from the DFT calculations and the actual band structure of the material. This comparison also aids in validating whether the characteristics of peaks observed in the experimental reflectivity are intrinsic to the material's electronic structure rather than being caused by other effects. Discrepancies observed between the two reflectivity datasets can offer insights into the limitations of the theoretical model or the influence of additional factors affecting the measured reflectivity, such as surface conditions or material interfaces.

In summary, the approach involves conducting a DFT study, calculating the complex dielectric function, and using it to determine the theoretical reflectivity. This theoretical reflectivity is then compared to the experimental reflectivity data to evaluate the consistency between the predicted electronic structure and the actual band structure of various materials such as K_3Sb, K_2CsSb, and Na_2KSb. This comparison provides valuable insights into the properties of the photoemissive material and allows us to gain a deeper understanding and rationalize its behavior.

5.2 Elements of Electronic Structure Theory

5.2.1 Single Particle Approximation for a Many-body System

The study of systems containing a large number of electrons and nuclei is a key focus in the field of condensed matter physics. The Hamiltonian that describes such systems, in its general form, can be expressed as follows [160]:

$$\hat{H}(\{r_i\},\{R_I\}) = -\frac{\hbar^2}{2m_e}\sum_i \nabla_i^2 - \sum_I \frac{\hbar^2}{2M_I}\nabla_I^2 + \frac{1}{2}\sum_{i\neq j}\frac{e^2}{|\mathbf{r}_i-\mathbf{r}_j|} + \frac{1}{2}\sum_{I\neq J}\frac{Z_I Z_J e^2}{|\mathbf{R}_I-\mathbf{R}_J|} - \sum_{i,I}\frac{Z_I e^2}{|\mathbf{r}_i-\mathbf{R}_I|} \tag{5.1}$$

In the provided expression, the symbols R_I, Z_I, and M_I represent the coordinates, charge, and mass of the I-th nucleus, respectively. On the other hand, the symbol r_i refers to an electron with mass m_e. The first two terms in the expression represent the kinetic energies associated with the electrons and nuclei, respectively. The remaining three terms account for the interactions between electrons (electron-electron interactions), nuclei (nucleus-nucleus interactions), and electrons and nuclei (electron-nucleus interactions). The Schrödinger equation of such system is [160, 161],

$$\hat{H}(\{r_i\},\{R_I\})\Phi(\{r_i\},\{R_I\}) = E\Phi(\{r_i\},\{R_I\}) \tag{5.2}$$

The electron-electron interaction term is typically the most challenging to handle and can vary significantly between different systems. On the other hand, the complexities associated with electron-nucleus and nucleus-nucleus interactions can be mitigated by employing the Born-Oppenheimer or adiabatic approximation [162]. Due to the significant difference in mass between nuclei and electrons, the Born-Oppenheimer approximation assumes that nuclei oscillate around their equilibrium positions at a much slower rate compared to the motion of electrons. Hence, the electrons closely track the motion of the nuclei, residing in the ground states dictated by the electronic Hamiltonian, which takes into account the nuclear coordinates as variables. Now, the many-body wavefunction can be decoupled as [161, 163],

$$\Phi(\{r_i\},\{R_I\}) = \chi(\{R_I\})\Psi_{\{R_I\}}(\{r_i\}) \tag{5.3}$$

Where $\chi(\{R_I\})$ is the nuclear wavefunction and $\Psi_{\{R_I\}}(\{r_i\})$ is the electronic wavefunction. Under the adiabatic approximation, the derivative of the electronic wave function with respect to the nuclear configuration becomes zero. Then the equation of motions for electrons and nuclei can be separated as [163],

$$\left(-\frac{\hbar^2}{2m_e}\sum_i \nabla_i^2 - \sum_{i,I}\frac{Z_I e^2}{|\mathbf{r}_i - \mathbf{R}_I|} + \frac{1}{2}\sum_{i\neq j}\frac{e^2}{|\mathbf{r}_i - \mathbf{r}_j|}\right)\Psi_{\{R_I\}}(\{r_i\}) = E_{\text{el}}(\{R_I\})\Psi_{\{R_I\}}(\{r_i\}) \tag{5.4}$$

and,

$$\left(-\sum_I \frac{\hbar^2}{2M_I}\nabla_I^2 + \frac{1}{2}\sum_{I\neq J}\frac{Z_I Z_J e^2}{|\mathbf{R}_I - \mathbf{R}_J|} + E_{\text{el}}(\{R_I\})\right)\chi(\{R_I\}) = E\chi(\{R_I\}) \tag{5.5}$$

Due to the extremely large number of electrons in a real solid system, solving the equation directly becomes infeasible. As a result, approximate methods are employed to study the ground and excited state properties. Density functional theory (DFT) [164] [165], many-body Green's function method [166], and other techniques have been introduced and have proven to be highly effective in this regard. These methods provide practical approaches for investigating the properties of solid systems, allowing for more feasible and accurate calculations of electronic structures and excitations.

The mean field approximation allows us to treat the electrons as non-interacting "quasi-particles" with effective masses moving in an average potential. Therefore, the many-electron problem Equation 5.4 can be replaced by a set of single-particle equations for each "quasi-particle".

$$\left(-\frac{\hbar^2}{2m_e}\nabla^2 + V_{\text{eff}}(r)\right)\psi_i(r) = \varepsilon_i\psi_i(r) \tag{5.6}$$

where $V_{\text{eff}}(r)$ represents the effective potential energy and ε_i represents the energy eigenvalue associated with the i^{th} quasi-particle. Although it simplifies the treatment of

electron-electron interactions, it provides a useful starting point for understanding the behavior of electrons in a many-electron system. However, it neglects the intricate correlation effects that arise from the true electron-electron interactions, which can be significant in some systems. DFT goes beyond the single-particle approximation by explicitly accounting for electron-electron correlations through the exchange-correlation functional. DFT provides a more accurate description of the electronic structure and properties of many-body systems by considering the collective behavior of electrons through electron density. A detailed discussion of the DFT theory is presented in the following section of this report.

5.2.2 Density Functional Theory (DFT)

5.2.2.1 Hohenberg-Kohn Theorems and Kohn-Sham Equation

The solution of the Schrödinger equation for systems with many interacting atoms has been a longstanding challenge in the fields of theoretical physics and chemistry. In order to address this problem, Density Functional Theory (DFT) offers an approach that maps the interacting system onto a much simpler non-interacting system, which is easier to solve. The central concept of DFT involves replacing the complex many-electron wave function, which comprises 3N variables (where N is the number of electrons, each with 3 spatial coordinates), with the electron density denoted as n(r) (which depends solely on 3 spatial coordinates). By focusing on electron density as the primary variable, DFT simplifies the computational complexity, allowing for efficient calculations of ground-state properties.

The foundation of DFT is based on two fundamental mathematical theorems established by Hohenberg and Kohn in 1964 [164]. These theorems provide the theoretical framework for mapping the quantum mechanical problem of interacting electrons to an equivalent non-interacting problem described by the electron density. In 1965, Kohn and Sham further developed DFT by deriving a set of equations, known as the Kohn-Sham equations, which form the basis for practical calculations within DFT [165]. These equations introduce a fictitious system of non-interacting electrons that reproduce the same

electron density as the original interacting system. This allows for the calculation of various properties and observables. The Thomas-Fermi equation [167, 168], which predates the Kohn-Sham equations of DFT [164,165], can be obtained from DFT as an approximation. It represents an earlier approach within DFT and provides an approximate solution for the electron density based on the kinetic energy of the system.

As described above, DFT is built upon the foundation of two Hohenberg-Kohn theorems, which can be summarized as follows [160]:

Theorem I: For any system of interacting particles under the influence of an external potential V_{ext}, the external potential can be uniquely determined, except for a constant, based on the ground-state particle density, $n_0(r)$.

Corollary I: Since the Hamiltonian is thus fully determined, with the exception of an energy constant shift, the wavefunctions of all states, including ground and excited states, can be fully determined. As a result, by knowing only the ground-state density $n_0(r)$, all properties of the system can be fully determined.

Theorem II: A universal functional, $E[n]$, can be formulated to describe the energy in relation to the density, $n(r)$, which is applicable to any external potential, $V_{ext}(r)$. For any particular $V_{ext}(r)$, the ground state energy of the system can be identified as the minimum value of this functional, representing a global minimum. Simultaneously, the density, $n(r)$, that minimizes the functional corresponds to the exact ground state density, denoted as $n_0(r)$.

Corollary II: The energy functional, $E[n(r)]$, is capable of uniquely determining both the precise ground-state energy and density. However, when it comes to the excited states of electrons, alternative methods are required for their determination.

Based on the above two theorems, all ground-state properties can be written as functional of the ground-state electron density $n(r)$ instead of the many-body wavefunction. The energy functional can be written as follows [164]:

$$E[n] = \int v_{ext}(\mathbf{r}) n(\mathbf{r}) d\mathbf{r} + F[n] \tag{5.7}$$

, where $F[n]$ is the kinetic and interaction energy functional. The Kohn-Sham formalism, first published in 1965, is the most well-known way to approximate the functional

$F[n]$ [165]. It does this by splitting the electronic kinetic energy, the Hartree potential energy, and the exchange-correlation energy ($E_{xc}[n]$) from Equation 5.7. This separation simplifies the problem and makes it computationally tractable while providing a good approximation of the true ground-state energy. The Kohn-Sham energy functional can be written as [165]

$$E[n] = \int v_{\text{ext}}(\mathbf{r}) n(\mathbf{r})\, d\mathbf{r} + T[n] + \frac{1}{2}\int \frac{n(\mathbf{r})n(\mathbf{r}')}{|\mathbf{r}-\mathbf{r}'|}\, d\mathbf{r}\, d\mathbf{r}' + E_{\text{xc}}[n] \tag{5.8}$$

where $T[n]$ represents the kinetic energy of non-interacting electrons and $E_{xc}[n]$ represents the exchange correlation energy, $\int v_{\text{ext}}(\mathbf{r}) n(\mathbf{r})\, d\mathbf{r}$ represents the interaction energy of electrons and the external potential, $\frac{1}{2}\int \frac{n(\mathbf{r})n(\mathbf{r}')}{|\mathbf{r}-\mathbf{r}'|}\, d\mathbf{r}\, d\mathbf{r}'$ represents the classical Coulomb potential of electrons, which is often referred to as the Hartree term. By imposing the constraints of $\int \delta n(\mathbf{r})\, d\mathbf{r} = 0$, we can represent the variational stationary point in the following manner.

$$v_{\text{ext}}(\mathbf{r}) + \frac{\delta T[n]}{\delta n(\mathbf{r})} + \int \frac{n(\mathbf{r}')}{|\mathbf{r}-\mathbf{r}'|} d\mathbf{r}' + \frac{\delta E_{\text{xc}}[n]}{\delta n(\mathbf{r})} = 0 \tag{5.9}$$

which is equivalent to solving the single-particle Schrodinger equation:

$$\left[-\frac{\hbar^2\nabla^2}{2m_e} + v_{\text{ext}}(\mathbf{r}) + \int \frac{n(\mathbf{r}')}{|\mathbf{r}-\mathbf{r}'|} d\mathbf{r}' + v_{\text{xc}}(\mathbf{r})\right] \psi_i(\mathbf{r}) = \varepsilon_i \psi_i(\mathbf{r}) \tag{5.10}$$

where $n(\mathbf{r}) = \sum_i |\psi_i(\mathbf{r})|^2$ is the charge density, and $v_{\text{xc}}(\mathbf{r}) = \frac{\delta E_{\text{xc}}[n]}{\delta n(\mathbf{r})}$ is the exchange-correlation potential.

By utilizing equation 5.10, the N-electron problem can be effectively reduced to the motion of a single electron within an effective potential generated by the collective influence of the other electrons. This simplified formulation allows for the application of self-consistent methods to solve the problem. As a result, it significantly simplifies the complexity of the many-body problem and serves as the fundamental basis for numerous modern DFT calculations [160].

As the Hohenberg-Kohn theorems do not provide specific instructions on obtaining the exchange-correlation potential $v_{xc}(r)$, various approximations have been developed to facilitate practical calculations. A simple approximation, the local density approxima-

tion (LDA) [169], replaces E_{xc} with the exchange-correlation potential obtained from a homogeneous electron liquid. The local spin-density approximation (LSDA) can be considered as a straightforward extension of the LDA to incorporate electron spin. Several parameterizations have been documented in the literature for the LDA energy functional, including notable contributions by Perdew and Zunger [169].

The generalized gradient approximation (GGA) [170] is another frequently employed approximation that offers a more precise approach to incorporate the first-order gradient expansion around the homogeneous density. In recent times, the generalized gradient approximation (GGA) has gained substantial attention due to its simplicity and effectiveness in enhancing first-principles calculations of material properties, surpassing the limitations of the LDA. Several variants of GGA functionals have been proposed, and Filippi et al. [171] have provided a comprehensive compilation of the most significant functionals, along with their respective parameters. An exemplary instance is the Perdew, Burke, and Ernzerhof (PBE) functional [172], which exhibits numerous appealing characteristics. The PBE functional has demonstrated significant improvements in the estimation of cohesive energies for a broad range of molecules [173] and solids [174–176], while also providing accurate predictions of bond lengths in weakly bonded systems [177–180]. However, computational analyses performed on covalent solids demonstrate a consistent tendency of the PBE scheme to underestimate the bulk moduli [175, 176, 181]. In recent times, Perdew and Wang have introduced a novel GGA functional, namely the Perdew-Wang 1991 (PW91) [182], which exhibits numerous characteristics similar to the exact exchange-correlation (XC) functional. From a conceptual standpoint, the PW91 functional is considered to be more satisfactory and is anticipated to provide improvements over prior proposals. Nevertheless, recent applications of the PW91 functional have not consistently validated these anticipated improvements [183].

In more recent times, a highly promising class of DFT functionals has emerged by incorporating additional semi-local information beyond the first-order density gradient present in the GGA. These functionals, known as meta-GGA (M-GGA), explicitly depend on higher-order density gradients. These methods constitute a substantial enhancement in accurately determining properties, such as atomization energies. However, they pose

greater technical complexities and present multiple challenges concerning numerical stability. Numerous M-GGA functionals have been developed for the exchange functional, correlation functional, or both. Examples include B95 [184], KCIS [185], TPSS [186] and VSXC [187].

Another group of functionals known as Hybrid GGA (H-GGA) incorporates a combination of the exchange-correlation (XC) from a conventional GGA method with a certain fraction of Hartree-Fock (HF) exchange. In the conventional GGA functionals, the XC energy is determined based on the local electron density and its gradient. However, the GGA approach often underestimates certain properties, such as reaction energies or weak interactions. To improve the accuracy of calculations, the H-GGA functionals were introduced. By incorporating a fraction of HF exchange, which considers electron-electron interactions in a more accurate way, H-GGA functionals can capture non-local electronic effects and provide better descriptions of electronic structure and properties. The inclusion of HF exchange in the H-GGA functional balances the strengths of GGA and HF approaches, aiming to improve the accuracy of calculations while maintaining computational efficiency. Different H-GGA functionals have been developed, each with a specific formulation for combining GGA and HF exchange. These functionals are typically parameterized to reproduce experimental data or high-level quantum chemical calculations for a range of molecular and solid-state systems. The choice of the fraction of HF exchange in the functional determines the trade-off between accuracy and computational cost. Examples of H-GGA functionals include HSE [188], B3LYP [189], B3P86 [189], B3PW91 [189], B97-1 [190], B97-2 [190], B98 [191], BH&HLYP [189, 192], MPW1K [193], mPW3LYP [193], O3LYP [192] and X3LYP [189, 192]. As the HSE method offers superior accuracy in predicting the band gap of semiconductor materials, it has been extensively utilized as the preferred hybrid functional in our study.

Hybrid meta-GGA (HM-GGA) functionals, similar to M-GGA functionals, are being actively developed and are based on a similar concept. The key distinction is that HM-GGA functionals build upon M-GGA functionals instead of standard GGAs. Therefore, these methods rely on the utilization of the HF exchange, as well as the electron density, its gradient, and the kinetic energy density. Examples of HM-GGA XC func-

tionals include B1B95 [184, 189], BB1K [184, 189], MPW1B95 [184, 193], MPW1KCIS [184, 193], PBE1KCIS [185], TPSS1KCIS [185, 186] and TPSSh [186]. These methods present an advancement over previous formalisms, especially when it comes to accurately determining barrier heights and atomization energies. The previous discussion highlights the wide range of approximations used in density functional calculations for the exchange-correlation (XC) energy functional. The number and complexity of available density functionals are expanding rapidly. As the level of sophistication increases, so does the accuracy of the calculations. However, it should be noted that higher levels of sophistication require also larger computational resources.

5.2.3 Wannier Functions

In this section, we introduce a practical and alternative approach to describe the electronic structure using a set of functions known as Wannier functions (WFs). These WFs provide an efficient representation that allows us to determine the electronic structure at any given point in the momentum space of a crystal.

5.2.3.1 Basic Definition and Properties

The fundamental characteristics of a perfect lattice can be fully captured within a single unit cell, typically a primitive cell, although it is not strictly limited to being primitive. The Hamiltonian operator for such a system consists of two components: a kinetic term representing the motion of particles and a periodic potential term accounting for the periodicity of the system. The Kohn-Sham orbitals constitute a set of mutually orthogonal eigenfunctions known as Bloch waves, which can be expressed as follows [160]:

$$\psi_{n,k}(\mathbf{r}) = \mathbf{u}_{n,k}(\mathbf{r}) \cdot e^{i\mathbf{k}\cdot\mathbf{r}} \tag{5.11}$$

where $u_{n,k}$ represents a periodic function in real space with band index n and wave vector k. A Bloch wave exhibits periodicity in real space, with a phase factor $e^{ik.r}$, where r is a position vector pointing to a neighboring unit cell. This representation in terms of energy eigenfunctions offers significant convenience for various applications, as the

Hamiltonian matrix elements follow the relationship ($H_{mn}(k) = \langle \psi^*_{n,k} | H | \psi_{m,k} \rangle = \varepsilon_{mn}\delta_{mn}$). However, if our goal is to find a localized Hamiltonian operator within a supercell, the plane-wave representation becomes less convenient since Bloch waves are spread-out over-all space.

The delocalized wave nature of Bloch states in real space presents a challenge in developing an intuitive understanding of local chemical and physical processes, such as the nature of crystal bonding. Furthermore, Bloch waves are not efficient in describing phenomena that arise from local electron correlations or other spatially localized entities, such as impurities.

Unlike the Bloch representation of the electronic structure, Wannier functions provide an alternative representation of the electronic structure that is centered and localized in real space [194], which can be more advantageous for certain applications. These functions are developed through a process called Wannierization, which transforms the periodic Bloch waves into a set of orthonormal basis functions known as Wannier functions. This transformation allows us to represent the electronic structure in a localized way, making it easier to understand and analyze the system intuitively. Figure 5.1 provides a schematic comparison illustrating the fundamentally distinct characteristics of Bloch states and Wannier functions in real space.

The Wannier function for the nth isolated energy band, denoted as $|W_{Rn}\rangle$, is essentially subjected to a discrete Fourier transformation of the corresponding Bloch state [195]:

$$W_{Rn}(r) = \frac{1}{N_k} \sum_k e^{-ik\cdot R} \psi_{kn}(r) \tag{5.12}$$

Here, R represents the real space lattice vector, and a summation is performed over crystal momenta originating from the first Brillouin zone. The total number of k-points is designated as N_k.

As the Bloch states of isolated energy bands can be defined with an arbitrary phase, Equation 5.12 does not yield a unique set of Wannier functions. Indeed, multiplying the Bloch states by the phase $e^{i\phi_k}$, where ϕ_k is a real-valued function that is analytically dependent on the crystal momentum, doesn't change any physical effects. However, this gauge transformation typically has a significant impact on the localization characteristics

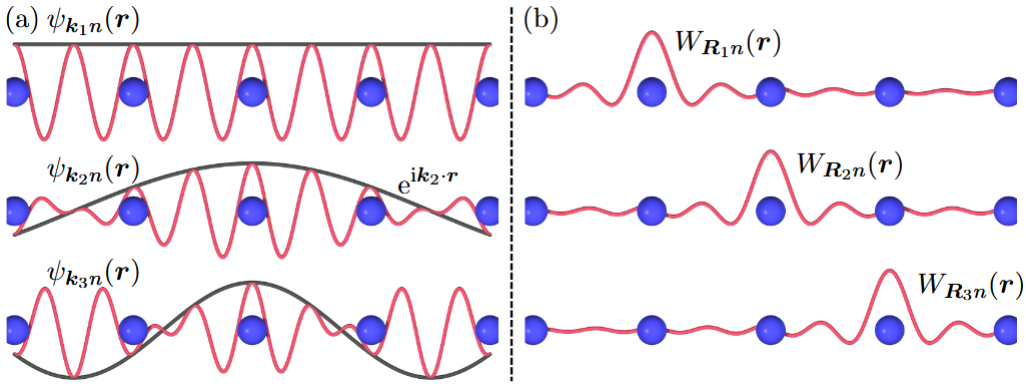

Figure 5.1: Real-space representation of the electronic structure of a periodic crystal with regard to (a) Bloch functions $\psi_{kn}(r)$ and (b) Wannier functions $W_{Rn}(r)$ for various values of crystal momentum k and the lattice vector R. While the Bloch states are spread out in real space, the localized Wannier functions exhibit well-defined centers. The black lines in (a) represent the phase factor e^{ikr} of the Bloch functions. The figure is inspired from [195].

of the Wannier basis. For the case of an isolated group of M energy bands, also referred to as a composite band, the gauge transformation of the Bloch states is facilitated by the unitary *MxM* matrix $U^{(k)}$ such that the Equation 5.12 to be generalized to,

$$W_{Rn}(r) = \frac{1}{N_k} \sum_{k} \sum_{m=1}^{M} e^{-ik \cdot R} U_{mn}^{(k)} \psi_{km}(r) \tag{5.13}$$

In Equation 5.13, the wave functions $\psi_{km}(r)$ that depend on momentum (k) and band index (m) are transformed into a set of Wannier functions $W_{Rn}(r)$ (with Wannier index n) using a unitary transformation. These Wannier functions are assigned to the unit cell located at vector R relative to the origin. The integration is carried out across the complete Brillouin zone.

When dealing with entangled energy bands that don't constitute an isolated group, the transformation matrix $U^{(k)}$ typically becomes rectangular (and therefore non-unitary) because the number of Bloch states at k can be larger than the target number of Wannier functions. Opting for a more smoother gauge for the Bloch states in reciprocal space means that the Wannier functions become more localized in real space due to the inherent properties of the Fourier transformation.

5.2.4 Maximally-Localized Wannier Functions (MLWFs)

Until the late 1990s, although the existence of strongly localized Wannier functions was mathematically proven and widely accepted, they were not commonly utilized in practical applications to support electronic structure theory. This was primarily due to the lack of systematic methods available at that time to construct a unique Wannier basis with desirable localization properties. Significant progress toward practical applications of Wannier functions was achieved by Marzari and Vanderbilt [196]. They introduced the concept of maximally-localized Wannier functions (MLWFs), which marked a substantial leap forward in the field. The concept of maximally-localized Wannier functions was later extended by Souza, Marzari, and Vanderbilt [197] to encompass the treatment of both composite and entangled energy bands. By enforcing the constraint of maximal localization, a unique Wannier basis set is obtained, which in turn establishes an optimally smooth gauge for the Bloch states. The spread, or spatial extent, of the Wannier functions, is determined by the summation of their second moments [195].

$$\Omega = \sum_n \left[\langle W_{0n}|r^2|W_{0n}\rangle - \langle W_{0n}|r|W_{0n}\rangle^2\right] = \sum_n \left[\langle r^2\rangle_n - \langle r\rangle_n^2\right] \tag{5.14}$$

where $\langle\cdot\rangle_n = \langle W_{0n}|\cdot|W_{0n}\rangle$ is the expectation value with respect to the n^{th} reference Wannier function. The sum in the equation runs over all Wannier orbitals that are constructed from the group of energy bands under consideration. The dependence of the spatial extent 5.14 on the gauge transformation $U^{(k)}$ is determined by Equation 5.13. However, in the context of an isolated manifold of Bloch bands, the sum of the Wannier centers, represented by $\langle r\rangle_n$, remains invariant under gauge transformations, except for a lattice translation. The optimal choice of gauge is achieved by minimizing the spatial extent of the Wannier functions, which interestingly corresponds closely to the concept of Boy's localized orbitals in quantum chemistry [198, 199].

The iterative minimization algorithm developed by Marzari and Vanderbilt converts the spatial extent of the Wannier functions, as described by the spread equation 5.14, into an expression in reciprocal space by utilizing specific mathematical identities [195, 196, 200].

$$\langle W_{Rn}|r|W_{0m}\rangle = \frac{iV}{(2\pi)^3}\int_{\mathrm{BZ}} e^{ik\cdot R}\langle u_{kn}^{(W)}|\nabla_k u_{km}^{(W)}\rangle\, d^3k \tag{5.15}$$

$$\langle W_{Rn}|r^2|W_{0m}\rangle = -\frac{V}{(2\pi)^3}\int_{\mathrm{BZ}} e^{ik\cdot R}\langle u_{kn}^{(W)}|\nabla_k^2 u_{km}^{(W)}\rangle\, d^3k \tag{5.16}$$

The integration is performed over the entire Brillouin zone, and the term $|u_{kn}^{(W)}\rangle = \sum_m U_{mn}^{(k)}|u_{km}\rangle$ represents the lattice-periodic part of the Bloch state. It signifies the evolution of the Bloch state's lattice-periodic component during the iterative process of refining the gauge transformation. Although these identities are valid in the continuum limit, practical calculations require discrete k-meshes with uniform spacing. To address this, the gradients in Equations 5.15 and 5.16 are replaced with the finite-difference expressions [196]. This approach leads to practical identities that involve the overlaps between the lattice-periodic parts of the Bloch states at neighboring points k and $k+b$.

$$M_{mn}^{(k,b)} = \langle u_{km}|u_{k+bn}\rangle \tag{5.17}$$

Based on these overlaps, which are obtained from first-principles methods, the important components in Equation 5.14 can be evaluated to [195],

$$\langle r\rangle_n = -\frac{1}{N_k}\sum_{kb} w_b b\ \mathrm{Im}\ \ln \tilde{M}_{nn}^{(k,b)} \tag{5.18}$$

and

$$\langle r^2\rangle_n = \frac{1}{N_k}\sum_{kb} w_b\left[1 - \left|\tilde{M}_{nn}^{(k,b)}\right|^2 + \left(\mathrm{Im}\ln \tilde{M}_{nn}^{(k,b)}\right)^2\right] \tag{5.19}$$

Where the bond weight w_b is used in the calculation, which is associated with $b = b\hat{b}$ originates from the finite-difference approximation of the gradient ∇_k. The efficient method proposed by Marzari and Vanderbilt has been incorporated into the scientific computing software, wannier90 [201]. This software employs a steepest-descent algorithm to reduce the spread, as indicated in equation 5.14.

5.2.5 Wannier Interpolation

5.2.5.1 Band Structure

The Wannier interpolation, as shown in Figure 5.2, is a well-established method for efficiently extracting single-particle operators, such as the Hamiltonian, at any desired point in reciprocal space. This technique relies on the construction of Maximally Localized Wannier Functions, which are obtained from a coarse sampling of the Brillouin zone. To understand the impressive performance of the Wannier interpolation, it is beneficial to examine the relationship between Equation 5.12 and its extension to the continuum limit. By scrutinizing this relation, we can gain insights into its form, which can be expressed as [195, 201],

$$W_{Rn}(r) = \frac{V}{(2\pi)^3} \int_{\mathrm{BZ}} e^{-ik\cdot R} \psi_{kn}^{(W)}(r)\, d^3k \tag{5.20}$$

The integration in the equation is carried out over the first Brillouin zone of the crystal, and the superscript "W" signifies that the gauge transformation is embedded in $|\psi_{kn}^{(W)}\rangle$. Since the Fourier transformation is invertible, the Bloch state can be obtained at any k-point once the "true" orbital $|W_{Rn}\rangle$ is given by utilizing the inverse of Equation 5.20.

$$\psi_{kn}^{(W)}(r) = \sum_R e^{ik\cdot R}\, W_{Rn}(r) \tag{5.21}$$

The remarkable effectiveness of the Wannier interpolation technique can be attributed to the key observation that the shape of the Wannier orbital $|W_{Rn}\rangle$, as defined by Equation 5.12, exhibits rapid convergence towards the "true" function 5.20 as more discrete k-points are included in the construction of $|W_{Rn}\rangle$.

Beginning with the Kohn-Sham eigenvalues ε_{kn}, which are determined from the coarse first-principles mesh, we can deduce the single-particle Hamiltonian on an extremely dense interpolation mesh using the Wannier interpolation method. The matrix components of the Hamiltonian within the Wannier basis, commonly referred to as "hopping" terms, serve to describe how electrons transition between distinct Wannier orbitals. These hopping terms are fundamental elements in electronic structure calculations utilizing the

Wannier basis.

$$H_{nm}(R) = \langle W_{0n}|H|W_{Rm}\rangle = \frac{1}{N_k}\sum_k e^{-ik\cdot R}\left[U_{n'n}^{(k)}\right]^* \varepsilon_{kn'} U_{n'm}^{(k)} \tag{5.22}$$

The Equation 5.22 is utilized to compute these matrix elements of the Hamiltonian in the Wannier basis [195, 201]. Where the $U^{(k)}$ holds the maximal-localization gauge, and the summation is performed over the coarse grid that represents a sampling of the Brillouin zone. Due to the system's translational symmetry, the hoppings rely solely on the distance vector R, which distinguishes the separation between the two Wannier orbitals. As the distance $|R|$ grows, the matrix elements in the Equation 5.22 diminish rapidly. This is because the Maximally Localized Wannier Functions are highly concentrated in real space and their overlap is minimal. By performing an inverse Fourier transformation, we obtain the following expression [195, 201],

$$H_{nm}^{(W)}(k) = \langle u_{kn}^{(W)}|H_k|u_{km}^{(W)}\rangle = \sum_R e^{ik\cdot R} H_{nm}(R) \tag{5.23}$$

This expression provides an interpolation of the single-particle Hamiltonian for any given point k, even if that point is outside the original coarse mesh that was used to construct the maximally localized Wannier functions (MLWFs). While the finite sum in Equation 5.23 accounts for all lattice vectors, this process can be executed even more effectively by remembering that the hoppings decrease quickly over distance. The desired interpolated band energies ε_{kn} can be obtained by diagonalizing the Hamiltonian:

$$\langle u_{kn}^{(H)}|H_k|u_{km}^{(H)}\rangle = [V^{(k)\dagger} H^{(W)}(k) V^{(k)}]_{nm} = \varepsilon_{kn}\delta_{nm} \tag{5.24}$$

where $V^{(k)}$ represents the unitary matrix of eigenstates $|u_{kn}^{(H)}\rangle = \sum_m |u_{km}^{(W)}\rangle V_{mn}^{(k)}$. The interpolation method ensures that the Kohn-Sham eigenvalues are accurately reproduced at every point within the original coarse mesh. This method, which uses a significantly smaller number of basis functions to represent the Hamiltonian compared to the comprehensive full-potential linearized augmented-plane-wave (FLAPW) basis set, is remarkably efficient. Indeed, the Wannier interpolation can deliver the electronic structure with the precision of first-principles methods but at the computational expense akin to a tight-

binding approach.

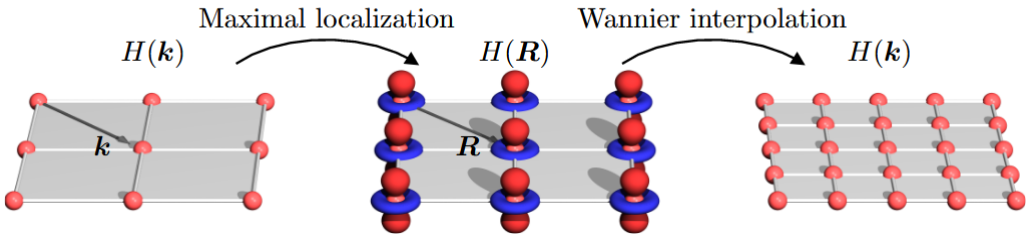

Figure 5.2: represents the Wannier interpolation scheme. Starting with the electronic structure represented by the Hamiltonian H(k) on a coarse k-grid. From this information, we construct Wannier functions that are localized in real space at specific positions R. By utilizing these Wannier functions as a basis, we can effectively represent the electronic structure in terms of the hoppings H(R). This enables us to derive the Hamiltonian on a significantly denser mesh of k-points through the application of an inverse Fourier transformation. This figure is adapted from [195].

5.3 Computational Techniques

In the upcoming sections, we will describe the computational methods employed to investigate the band structure, density of states (DOS), and optical properties of alkali antimonide materials. The electronic band structure calculations were performed using the open-source software Quantum Espresso [202, 203], which is based on the plane wave and pseudopotential methods. For the computation of the maximally localized Wannier functions, the open-source software Wannier90 [201] was utilized.

5.3.1 Quantum Espresso

Quantum Espresso is a computational method used for performing first-principles calculations on both periodic and disordered systems. In Quantum Espresso, the size of the unit cell and the desired atom configuration within that unit cell are indeed the main physical input parameters needed to perform calculations. These parameters define the basic geometry and composition of the system under study. Due to the periodic nature of the system, the Kohn-Sham equations in Quantum Espresso are solved in reciprocal

space (also known as k-space) using a Plane Wave (PW) basis set. This choice of basis allows for efficient representation of the electronic wavefunctions and facilitates the numerical solution of the equations. In Quantum Espresso, the pseudopotential approximation is utilized to reduce the computational requirements by replacing the electron-ion interaction with a modified effective potential term in the Schrödinger equation for core electrons. This approximation is achieved through the use of pseudopotentials, which come in two types: ultrasoft pseudopotentials and norm-conserving pseudopotentials. In the pseudopotential approximation, the Kohn-Sham equations are solved by considering the radial equation, which includes the contribution from valence electrons. This approximation effectively accounts for the interaction between valence electrons and the atomic cores, allowing for a reduction in computational complexity.The Density Functional Theory (DFT) calculations in this thesis were carried out utilizing the open-source software Quantum Espresso.

5.3.2 Wannier90

The Wannier90 code, which is part of the Quantum Espresso package, was employed in this study to perform the Wannier transformation on a selected subset of bands from a given electronic structure. Wannier90 is an Open Source software that is widely used for generating maximally localized Wannier functions from the Bloch states obtained through first-principles calculations. Wannier90, which is fully compatible with Quantum Espresso, relies on the overlaps between the cell periodic part of the Bloch states, denoted as $M_{mn}^{(k,b)}$, and the projections of the initial guess for the localized orbitals on the Bloch states, represented as $A_{mn}^{(k)}$. These quantities serve as input parameters for the Wannier transformation process. By utilizing this information, Wannier90 effectively generates maximally localized Wannier functions from the electronic structure data obtained from Quantum Espresso calculations. To perform band structure interpolation, the calculation follows the steps outlined in Fig. 5.3.

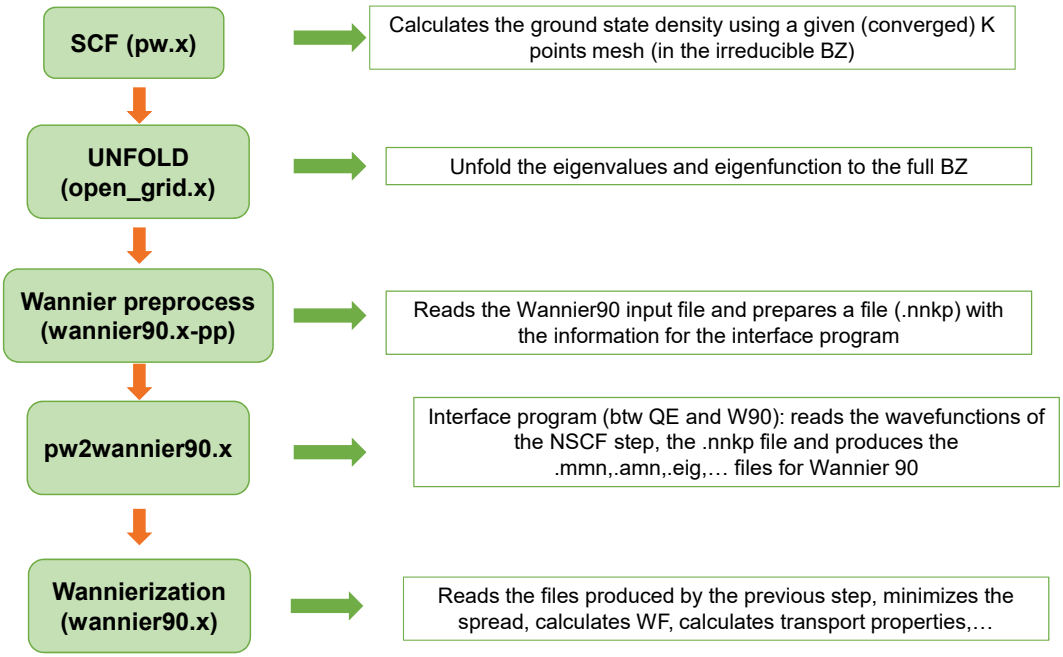

Figure 5.3: Flowchart to perform band structure interpolation using Wannier Functions.. This flowchart is inspired from [204, 205].

5.3.3 epsilon.x

Optical properties of the alkali antimonide materials were investigated in this study using the epsilon.x code from the Quantum-Espresso package. Within the random phase approximation (RPA) framework [206], we calculated the complex dielectric function $\varepsilon(\omega)$ based on the DFT ground state calculation using the HSE functional (mentioned in the Section 5.2.2). More details of this code can be found in the reference [207]. In

the following section of this chapter 5.5, a more comprehensive discussion of the optical properties of individual alkali antimonide compounds can be found.

5.4 Optical Properties

In a neutral atom or molecule, the center of charge of the negative electrons and the positive nucleus typically coincide. However, when an external electromagnetic field is applied, the electron cloud undergoes oscillation in response to the applied frequency, resulting in a displacement of the center of charge and leading to polarization. This degree of polarization is described by the dielectric function, which characterizes the material's response to the applied electric field [208].

In semiconductors, the valence band electrons are relatively loosely bound to the nucleus, making them susceptible to polarization when exposed to an external electromagnetic field (like photon). The extent of this polarization is measured by the dielectric function. This function illustrates how the material interacts with electromagnetic waves, including their reflection and transmission. The dielectric function is represented as a complex quantity, consisting of a real part and an imaginary part. The real part corresponds to the refractive index of the material, governing the phase shift experienced by electromagnetic waves as they pass through the material. On the other hand, the imaginary part represents the absorption coefficient, quantifying the amount of energy absorbed by the material [208].

In semiconductors, if the energy of the external electromagnetic field (like photon) matches or exceeds the material's band gap, electrons can transition from the valence band to the conduction band. This results in absorption and dispersion phenomena in the real and imaginary parts of the dielectric function. Therefore, by examining the dielectric function, valuable insights into various aspects of a material, including its polarization characteristics, band structure, and optical properties can be obtained.

As described in the Section 5.3.3, the optical properties of the material were analyzed using the epsilon.x code from the Quantum-Espresso package. Within the random phase approximation framework [206], we calculated the complex dielectric function

$\varepsilon(\omega)$ based on the DFT ground state calculation using the HSE functional. The imaginary part $\varepsilon_2(\omega)$ is determined by calculating the momentum matrix elements between the occupied, and unoccupied wave functions [207], and was computed by using the following Equation 5.25:

$$\varepsilon_2(\omega) = \frac{4\pi e^2}{\Omega N_k m^2} \sum_{n,k} \frac{df(E_{k,n})}{dE_{k,n}} \frac{\eta\omega \hat{M}_{\alpha,\beta}}{\omega^4 + \eta^2\omega^2} + \ldots + \frac{8\pi e^2}{\Omega N_k m^2} \sum_{n\neq n'} \sum_{k} \frac{\hat{M}_{\alpha,\beta}}{(E_{k,n'} - E_{k,n})} \cdots \frac{A\omega f(E_{k,n})}{[(\omega_{k,n'} - \omega_{k,n})^2 - \omega^2] + A^2\omega^2} \tag{5.25}$$

In the equation, the symbol e represents the electron charge, m represents the mass of the electron, and Ω represents the volume of the lattice cell. The variables n and n' correspond to the valence and conduction bands, respectively. $E_{k,n}$ represents the eigenvalues of the Hamiltonian, while $f(E_{k,n})$ represents the Fermi distribution function that accounts for the occupation of the bands. $\hat{M}_{\alpha\beta}$ represents the transition momentum from α (valance with energy $E_{k,n}$) to β (conduction with energy $E_{k,n'}$); A and η are coefficients, and N_k represents the number of electrons within the unit cell volume. By utilizing the Kramers-Kronig relation and taking into account the imaginary part, the real part $\varepsilon_1(\omega)$ of the complex dielectric function can be computed [207]:

$$\varepsilon_1(\omega) = 1 + \frac{2}{\pi} P \int_0^{\infty} \frac{\omega' \varepsilon_2(\omega')}{\omega'^2 - \omega^2} d\omega \tag{5.26}$$

where P represents the Cauchy principal value. As it described above, the real and imaginary components of the dielectric function have important applications in calculating various optical properties. According to the Maxwell model, the refractive index $n(\omega)$ and the extinction coefficient $k(\omega)$ can be expressed in terms of the real and imaginary parts of the dielectric function as follows [208],

$$n(\omega) = \left(\frac{1}{\sqrt{2}}\right) \left[\sqrt{\varepsilon_1^2(\omega) + \varepsilon_2^2(\omega)} + \varepsilon_1(\omega)\right]^{\frac{1}{2}} \tag{5.27}$$

$$k(\omega) = \left(\frac{1}{\sqrt{2}}\right) \left[\sqrt{\varepsilon_1^2(\omega) + \varepsilon_2^2(\omega)} - \varepsilon_1(\omega)\right]^{\frac{1}{2}} \tag{5.28}$$

Furthermore, the reflectivity $R(\omega)$ can be described in relation to the refractive index $n(\omega)$ and extinction coefficient $k(\omega)$ using the following expression [208],

$$R(\omega) = \frac{(1-n)^2 + k^2}{(1+n)^2 + k^2} \tag{5.29}$$

Likewise, the electron energy loss spectroscopy (EELS) spectrum $L(\omega)$ [209] can be formulated in relation to the real and imaginary components of the dielectric function as follows,

$$L(\omega) = \frac{\varepsilon_2(\omega)}{\varepsilon_1^2(\omega) + \varepsilon_2^2(\omega)} \tag{5.30}$$

The real and imaginary parts of the dielectric function can be described using three tensor components: epsilon xx (ω), epsilon yy(ω), and epsilon zz(ω). As described, the equations mentioned above are used to calculate various optical properties, including the refractive index, extinction coefficient, reflectivity, and the electron energy loss function, for different photoemissive materials such as K_2SbCs, Cs_2KSb, cubic K_3Sb, hexagonal K_3Sb, and Na_2KSb. These calculations and their discussion are presented in the following section.

5.5 Simulation Results

First-principles calculations using DFT are presently among the most crucial computational methods for studying the atomic properties of materials [210, 211]. These calculation methods not only assist in interpreting experimental data but also predict and access properties that are challenging to measure with high accuracy. Furthermore, DFT calculations have been utilized to evaluate the optical properties of various materials, with a significant amount of optical spectra derived from these calculations being documented [212–216]. Optical-function calculations, such as dielectric functions and absorption coefficients, using DFT have primarily been validated through comparisons with experimental data [212–217].

Following this methodology, we present the outcomes of our DFT simulations in this

section, focusing on the electronic and optical characteristics of various semiconductor photocathode materials, including cubic K_3Sb, hexagonal K_3Sb, K_2CsSb, Cs_2KSb and Na_2KSb. As previously explained in Section 5.1, the optical properties, particularly the simulated reflectivity data of the aforementioned compound, will be compared with experimental data to evaluate the peak characteristics. This comparison is particularly significant given that, in experimental setups, the photoemissive compounds are usually deposited on a Mo substrate, which introduces the potential for interference effects. Additionally, the presence of potential defects and roughness in the deposited film could also contribute to the observed peaks in the experimental spectral reflectivity. Thus, this approach will allow for an evaluation of whether the observed peak characteristics in the experimental reflectivity are intrinsic to the material's electronic structure or significantly influenced by various factors, including interference effects. The following section will present these calculations along with their respective discussion.

5.5.1 K_2CsSb Photocathode

5.5.1.1 Electronic Properties

With the K_2CsSb material being the primary focus of this study, the DFT calculations were specifically conducted on this material, utilizing a monocrystalline structure for the cathodes. In this study, our focus was on analyzing the electronic and optical properties of the K_2CsSb material in its face-centered cubic (FCC) phase, which belongs to the F m-3-m space group. Through volume optimization and fitting the results using the Birch-Murnaghan equation [218, 219] , a lattice parameter of a = 8.7587 Å was determined for the system. This value exhibited good agreement with both previous experimental studies [220] and theoretical investigations [221–223] . Figure 5.4a illustrates the spatial arrangement of the atoms in the cell. The Sb atoms, represented by the blue color, were positioned at the Wyckoff position (0, 0, 0). On the other hand, the alkali species Cs and K, depicted in red and orange colors respectively, were located at crystal coordinates $(\frac{1}{2},\frac{1}{2},\frac{1}{2})$ and $\pm\,(\frac{1}{4},\frac{1}{4},\frac{1}{4})$, respectively.

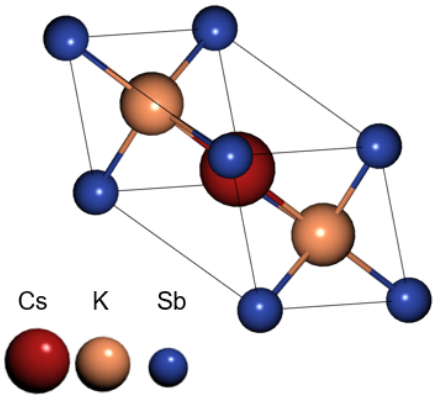

(a)

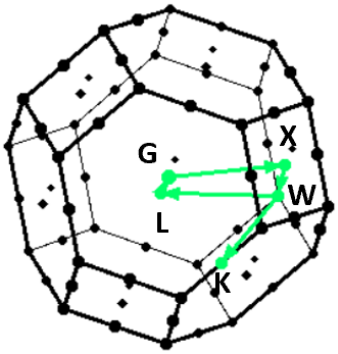

(b)

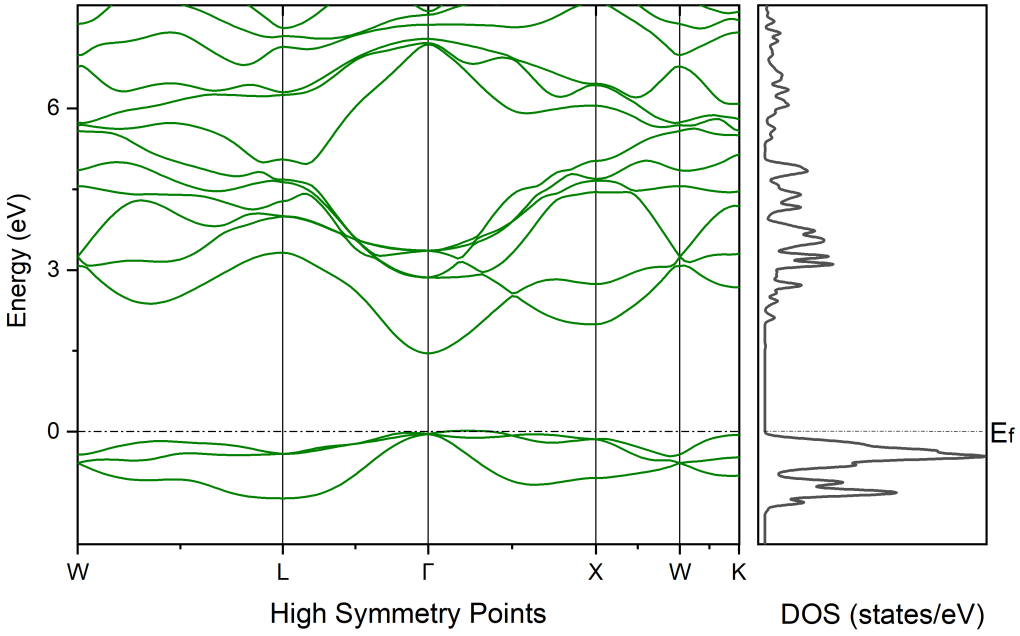

(c)

Figure 5.4: (a) unit cell of K_2CsSb is depicted using a ball and stick representation. (b) Brillouin zone of K_2CsSb is shown, with high symmetry points and the corresponding path connecting them highlighted in color. (c) computed electronic band structure of K_2CsSb material along with the corresponding density of states (DOS) plot using the HSE functional. The Fermi energy (E_f) was set to zero at the valence band maximum.

In this study, for the K_2CsSb material, the band structure calculation was conducted using two different computational approaches: the generalized gradient approximation (GGA) based on the Perdew-Burke-Ernzerhof (PBE) functional [172], and the hybrid Heyd-Scuseria-Ernzerh (HSE) functional which includes the exact exchange contribution [188]. To model the interaction between electrons and ions, optimized norm-conserving Vanderbilt (ONCV) pseudopotentials [224] were employed. Additionally, a $4 \times 4 \times 4$ k-mesh was utilized to sample the Brillouin zone during the calculation. For this calculation, a plane wave kinetic energy cutoff of 70 Ry and a charge density plane wave cutoff of 280 Ry were employed. As mentioned earlier in the Section 5.3.2, the computation of Maximally Localized Wannier Functions [195] was performed using the Wannier90 code. These functions were subsequently utilized to interpolate the band structure [201].

The band gap calculated using the HSE functional was 1.49 eV (with a direct band gap at the point Γ). On the other hand, the PBE results underestimated the gap and yielded a value of 0.84 eV (with a direct band gap at the point Γ). The band structure presented in Fig. 5.4c is calculated using the HSE functional. Due to the consistent underestimation of band gaps using the PBE functional for band gap calculations [225–227], we have opted to utilized the HSE functional in the DFT calculations for all the remaining cathode materials studied in this report. The band gap obtained from the HSE functional agrees well with previous DFT studies [228] and closely matches the experimental value of 1.2 eV [79]. When analyzing the band structures (Fig. 5.4c), it is observed that the valence bands show a dispersion that covers a range of about 1.25 eV. Particularly, there is a specific valence band that stands out with a significant minimum near point L. Moreover, in the area around this point, the band takes on a roughly parabolic shape along the path from point W to Γ point. Also, a parabolic shape in the nature of the conduction band minimum can be noticed in Fig. 5.4c.

Density of states (DOS) analysis allows for the investigation of the contribution of various electronic states in the valence and conduction bands, providing insights into the electronic band structure of a material. Furthermore, DOS analysis helps determine interband and intraband transitions between quantized electronic levels in the valence and conduction bands, shedding light on optical spectra phenomena. Figure 5.4c illustrates

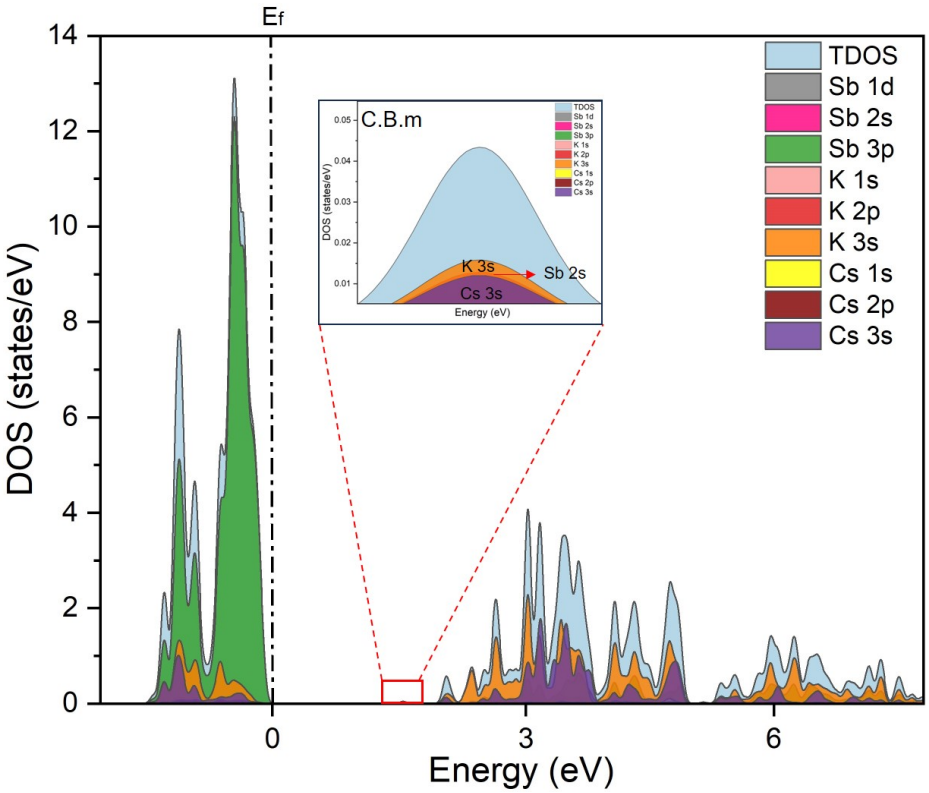

Figure 5.5: Atom projected density of states (PDOS) of K_2CsSb, with the Total density of state (TDOS) represented by the light blue area. The contribution of different atoms is depicted in various colors. In the plot, 'C.B.m' denotes the conduction band minimum.

the electronic band structure of K_2CsSb material along with the corresponding density of states plot. Furthermore, Figure 5.5 displays the atom-projected density of states (PDOS) for the K_2CsSb material. An interesting characteristic of the K_2CsSb material is the limited number of valence states near the band gap. This feature can be observed in the Figure 5.4c. Additionally, there are lower-energy bands that exhibit nearly flat dispersion, primarily dominated by the Sb 2s state, along with a minor combination of K 3s and Cs 3s, 2p states, at approximately 7.7 eV below the Fermi energy (not depicted in the figures). This pattern echoes observations made in earlier DFT findings [221, 222, 229, 230]. It indicates that the electrons in those bands are relatively localized and do not participate in the extensive delocalized electronic motion. As seen in Fig. 5.5, the valence band is primarily governed by the Sb 3p states, with a minor contribution stemming from the 3s-

states of K and Cs. The main contribution to the conduction band predominantly stems from the 3s states of both K and Cs, while the Sb 2s and 3p states make only a minimal contribution. The major contribution to the conduction band minimum (CBm) arises from the K and Cs 3s states, as well as the Sb 2s states.

To understand the charge distribution and chemical bonding between the constituent atoms, it is crucial to have an understanding of the electronic charge allocations. Figure 5.6 displays the electronic charge density distribution of K_2CsSb material within the (100) plane. The figures show that the electronic charge is mainly concentrated around the ionic sites, as indicated by the scale. This behavior suggests that the compounds exhibit a predominant ionic bond character. The charge distributions of both alkali and antimonide atoms exhibit a spherical shape, indicating significant charge transfer between the anions and cations. Additionally, there is a comparatively high charge distribution observed between potassium K and Sb atoms, as well as between Cs and Sb atoms, in comparison to the charge distribution between K and Cs. This lower charge distribution between K and Cs can be attributed to the smaller electronegativity difference between these two elements. As alkali metals, K and Cs have low electronegativity values and a tendency to donate electrons, which can result in a weaker effect on the charge distribution between them. However, it's important to note that charge distribution is a complex phenomenon influenced by multiple factors, including electronegativity, atomic sizes, the arrangement of atoms, the crystal lattice, and bonding interactions.

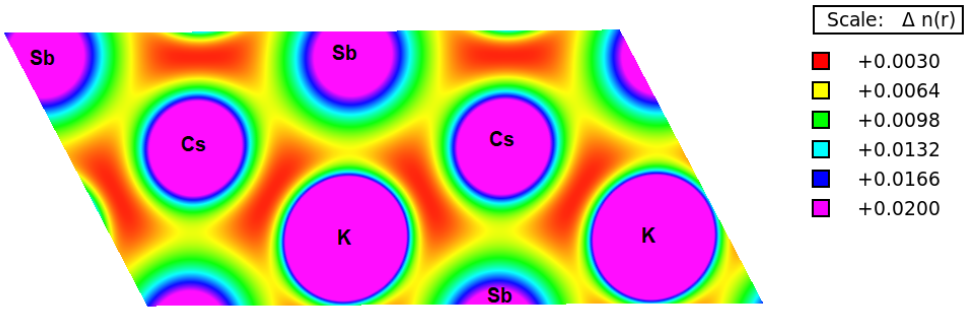

Figure 5.6: Side view of the calculated charge density plot of the K_2CsSb material with colors scale n(r) indicating ranges of charge accumulation and depletion in a.u.

5.5.1.2 Optical Properties

Figure 5.7a displays the calculated real and imaginary parts of the dielectric function for the K_2CsSb material as a function of photon energy obtained using the HSE hybrid functional. It is observed that the real part of the dielectric function generally increases with increasing frequency, which is referred to as normal dispersion. However, there are specific regions (highlighted in blue colored box), where the real part of the dielectric function decreases with increasing frequency. This phenomenon is known as anomalous dispersion [208]. It is interesting to note that within this narrow region of anomalous dispersion, the imaginary part of the dielectric function sharply increases. The significant increase in the imaginary part indicates a high level of absorption, reflecting the absorption processes occurring within that frequency range. The presence of peaks in the spectra (Figure 5.7a, 5.7b, 5.7c, 5.7d) is attributed to the permitted transitions between the valence and conduction bands of electrons.

In the imaginary part of the dielectric function (Figure 5.7a), the first peak (labelled A) appears at approximately 1.49 eV. This peak is generated by an exciton that is three-fold degenerate, owing to the cubic symmetry of the crystal. This transition can be attributed to the direct optical transition (Γ-Γ) that occurs between the valence band maximum (VBM) and the conduction band minimum (CBm). The imaginary part and the extinction coefficient provide valuable information about the absorption characteristics at the band edges. Consequently, at this specific point (i.e., around 1.49 eV), a notable rise in the extinction coefficient $k(\omega)$ (Fig. 5.7c) is detected, indicating the presence of fundamental absorption. The following peaks, marked as B, C, D, and E, are found within the visible-UV spectrum, roughly at energy values of 2.13 eV, 2.60 eV, 2.93 eV, and 3.68 eV, respectively, in Figure 5.7a. Similar to peak A, the intensity of peak B is relatively weak, suggesting that it is likely formed by a manifold of excitations that exhibit three-fold degeneracy due to the crystal's symmetry. This suggests that this interaband transition (peak B) could potentially occur near the Γ-point, along the Γ-L, or the Γ-X paths from the valence band to the vicinity of the lowest level of the conduction band [230] (Fig. 5.4c). Our findings exhibit strong consistency with previous DFT studies [230] and demonstrate closer alignment with our experimental observations (discussed later).

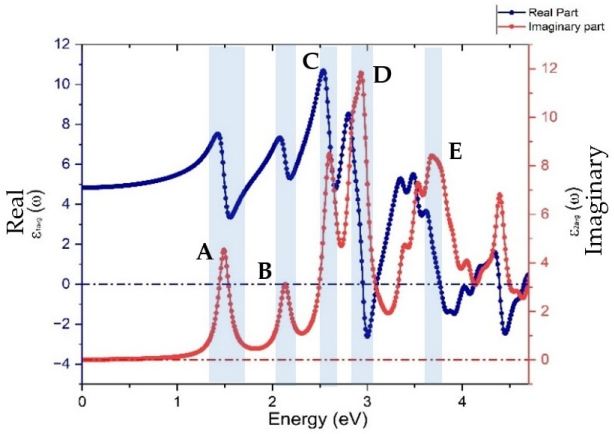
Real Part
Imaginary part
Real
Imaginary
A
B
C
D
E
Energy (eV)

(a)

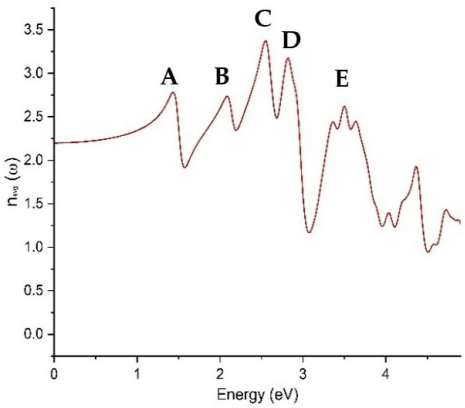
A
B
C
D
E
Energy (eV)

(b)

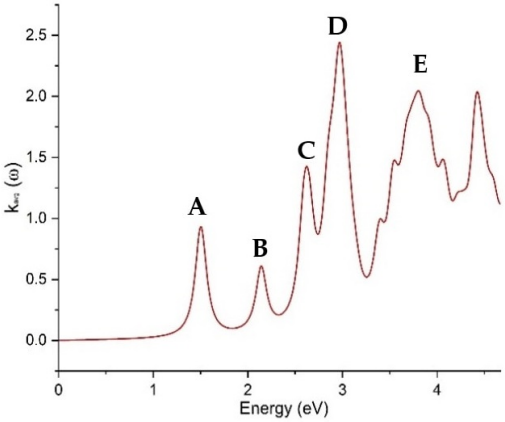
A
B
C
D
E
Energy (eV)

(c)

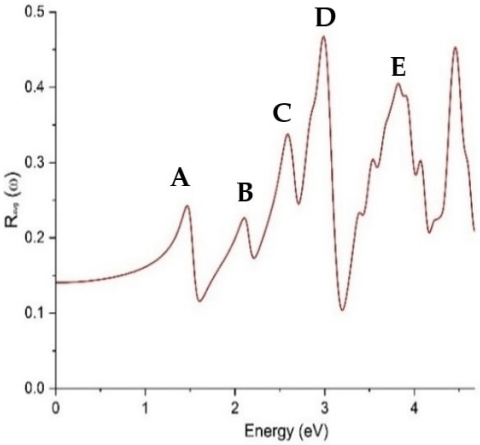
A
B
C
D
E
Energy (eV)

(d)

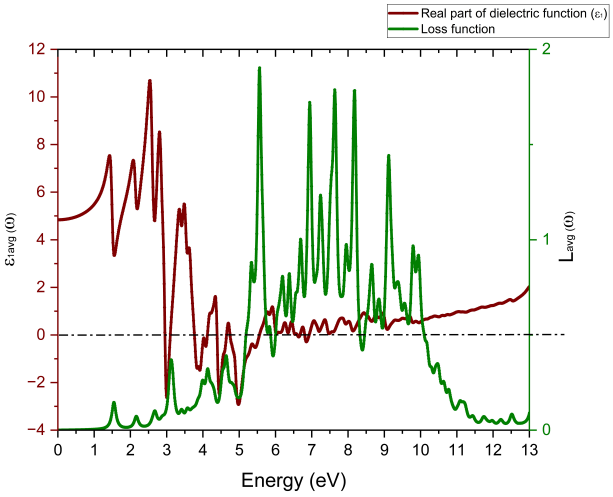
Real part of dielectric function (ε)
Loss function
Energy (eV)

(e)

Figure 5.7: Optical spectra of the K_2CsSb film as a function of the photon energy, where it shows the (a) real and imaginary parts of the dielectric function, (b) refractive index $n(\omega)$, (c) extinction coefficient $k(\omega)$, (d) reflectivity $R(\omega)$, and (e) electron energy loss spectrum (green color). The real part of the dielectric function (shown in red wine color) in Figure 5.7e is presented for comparison purposes.

Based on the values of ε_1 and ε_2, the refractive index $n(\omega)$ for the studied K_2CsSb compound was calculated (according to Equation 5.27), and the corresponding plot is shown in Figure 5.7b. The refractive index is defined as a physicochemical property as its value changes upon irradiation of light due to the interaction between atoms in a material. As previously mentioned in the Section 5.4, it has been emphasized that there is a direct relationship between the dielectric function and the complex refractive index. The refractive index is usually used to measure the response of a material upon transmission of light through it. From Fig. 5.7b it has been observed that the refractive index of the K_2CsSb compounds follows the similar pattern with the real part of the dielectric function (ε_1). The obtained refractive index values exhibit good agreement with the previous experimental measurements [231]. In the refractive index plot, the peaks are appeared at 1.43 eV, 2.08 eV, 2.54 eV, 2.81 eV, and 3.50 eV, corresponding to the A, B, C, D, and E peaks, respectively.

Both the imaginary part of the dielectric function and the extinction coefficient (Fig. 5.7c) provide insights into the absorption behavior at the band edges. As a result, we observe analogous peaks in the extinction coefficient (Fig. 5.7c), mirroring those in the imaginary part of the dielectric function. This suggests that absorption characteristics are present at those particular energy levels.

The reflectivity plot in Figure 5.7d shows the calculated variations of reflectivity for the K_2CsSb compound in relation to photon energy. Within this plot, we observe peaks at energy levels of 1.46 eV, 2.10 eV, 2.58 eV, 2.98 eV, and 3.81 eV, which are labeled as A, B, C, D, and E, respectively. The reflectivity plot was obtained by calculating the reflectivity by using Equation 5.29, which involves the real and imaginary components of the dielectric function of the K_2CsSb material. Consequently, the resulting plot closely resembles the patterns observed in the real and imaginary plots, with only minor devia-

tions. These peaks in the reflectivity plot indicate transitions occurring within the band structure, specifically between the valence band and the conduction band. In Chapter 6 (Section 6.1), the presented DFT calculated reflectivity plot (Fig. 5.7d) is compared with the experimental reflectivity data of the K-Cs-Sb compound grown in the laboratory, followed by a discussion of the results.

Figure 5.7e presents the electron energy loss spectrum (EELS) of the K_2CsSb compound, depicting the variations with photon energy. The electron energy loss spectrum (EELS) corresponds to the energy loss experienced by fast-moving electrons as they interact with a material, primarily due to plasmon excitations. Plasmons are collective oscillations of the electron density in a material, and when fast electrons interact with these plasmons, energy transfer occurs, resulting in energy loss. In the shown electron energy loss spectrum, significant characteristics are primarily noticed beyond approximately 5 eV, with local maxima in the loss function occurring within the energy range of 5 to 10 eV. The observation of an increase in the real part of the dielectric function within this frequency range strongly indicates the presence of plasmonic behaviour in the excitation [230]. In the range of lower energy, local fluctuations in the real component of the dielectric function, ε_1, correspond to absorption peaks in the imaginary component, ε_2.

5.5.2 Cs_2KSb Photocathode

The literature indicates that a Cs_2KSb compound can form under conditions of excess cesium [232]. Furthermore, as detailed in Section 4.4.5.4 (pages 149-150), noticeable differences were observed in the spectral reflectivity peaks between thick and thin KCsSb cathodes (Fig. 4.56). These discrepancies in experimental spectral reflectivity may arise from stoichiometric differences (i.e., Cs_2KSb compound). To investigate this hypothesis, we performed a comparable DFT analysis on the Cs_2KSb material. The following sections detail the optical and electronic properties of Cs_2KSb as derived from our DFT calculations.

5.5.2.1 Electronic Properties:

Here, we focused on the face-cantered-cubic (FCC) phase (which belongs to the space group of F m-3-m) of the Cs_2KSb material and investigated the electronic and optical properties. The lattice parameter a = 8.88 Å was taken directly from the reference [229]. As shown in Figure 5.8a, the Sb atoms (depicted in blue color) were located at the Wyckoff position (0, 0, 0), while the alkali species K and Cs (depicted in orange and red colors, respectively) were located at the crystal coordinates $(\frac{1}{2}, \frac{1}{2}, \frac{1}{2})$ and ± $(\frac{1}{4}, \frac{1}{4}, \frac{1}{4})$, respectively. In this study, the band structure calculation was conducted using the HSE hybrid functional, which includes the incorporation of exact exchange [188]. A similar procedure is applied here for this calculation as it was for the previous cathode. To model the interaction between electrons and ions, optimized norm-conserving Vanderbilt pseudopotentials [224] were employed, and a 4 × 4 × 4 k-mesh was utilized to sample the Brillouin zone during the calculation. For this calculation, a plane wave kinetic energy cutoff of 70 Ry and a charge density plane wave cutoff of 280 Ry were employed. Like for the K_2CsSb material, Maximally localized Wannier functions [195] were computed with the Wannier90 code and used to interpolate the band structure [201].

The band gap calculated using the HSE functional was 1.06 eV (indirect gap). Figure 5.8c presents the electronic band structure of the Cs_2KSb material, accompanied by the corresponding density of states plot. The band structure of this material reveals an indirect band gap that occurs between the X and Γ points in the Brillouin zone (Fig. 5.8c). By comparing K_2CsSb compound (Fig.5.4c), it can be inferred that decreasing the proportion of K (potassium) in the material results in the displacement of the valence-band maximum from the center of the Brillouin zone (Γ) towards the zone edge (X), as it was also seen in previous DFT studies [223].

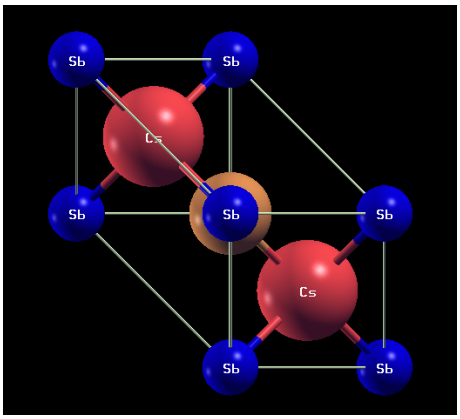

(a)

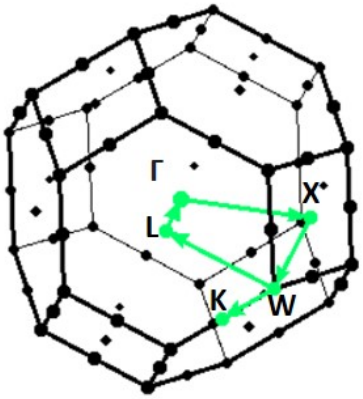

(b)

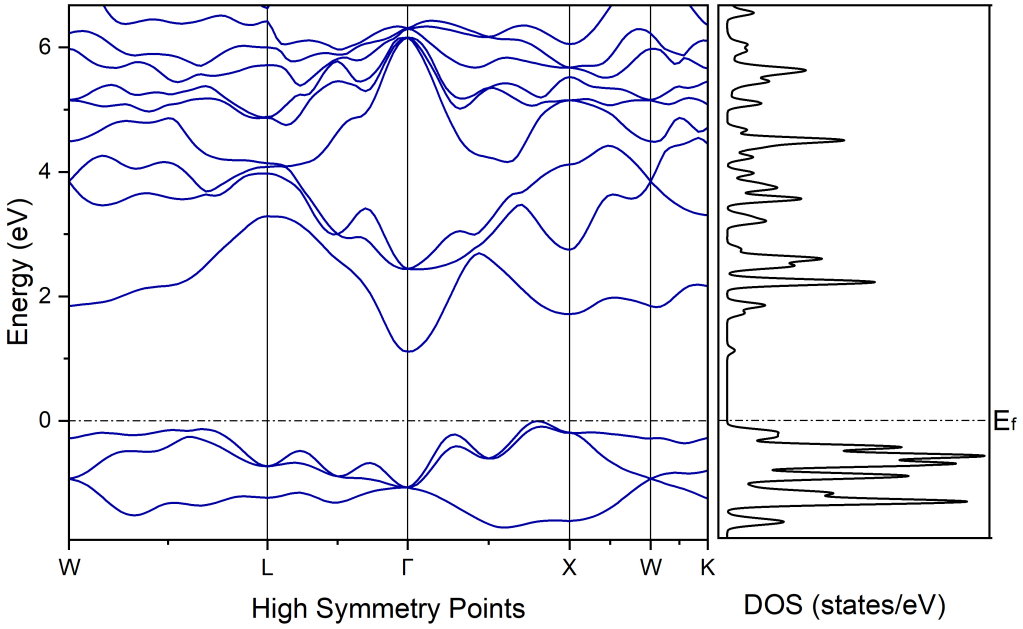

(c)

Figure 5.8: (a) unit cell of Cs_2KSb is depicted using a ball and stick representation. (b) Brillouin zone of Cs_2KSb is shown, with high symmetry points and the corresponding path connecting them highlighted in color. (c) computed electronic band structure of Cs_2KSb material along with the corresponding density of states (DOS) plot using the HSE functional. The Fermi energy (E_f) was set to zero at the valence band maximum.

Figure 5.9 illustrates the atom-projected density of states (PDOS) for the Cs_2KSb material. Like the K_2CsSb compound, there are lower-energy bands that exhibit nearly flat dispersion primarily dominated by the Sb 2s state, with a slight mix of Cs 2p and 3s states, situated roughly 7.6 eV beneath the Fermi energy (this is not shown in the figures). This observation is consistent with previous DFT findings [229]. Figure 5.9 demonstrates that the valence band of the material is primarily governed by the Sb 3p states, while the 3s states of K and Cs, along with the Cs 2p state, make a smaller contribution (similar to the K_2CsSb compound). The dominant influence on the conduction band minimum (CBm) comes from the 3s states of both K and Cs, along with the Sb 2s state, while the Cs 1s state makes a minimal contribution. Furthermore, the analysis of Figure 5.9 reveals that the lower part of the conduction band is primarily governed by the K 3s state, while the Cs 3s state predominantly influences the upper part. By comparing the PDOS data of K_2CsSb and Cs_2KSb compounds (as shown in Figure 5.5 and Figure 5.9, respectively), it becomes apparent that the 3s-state of K atom makes a more substantial contribution to the lower conduction band region in the Cs_2KSb compound compared to the K_2SbCs compound.

Similarly, to the K_2SbCs compound, the electronic charge density distribution has been computed for the Cs_2KSb compound. The distribution of electronic charge density within the (100) plane of the Cs_2KSb material is depicted in Figure 5.10. The figures indicate that the electronic charge is primarily localized around the ionic sites, as evident from the scale. This observation suggests that the compounds possess a dominant ionic bond nature, similar to the K_2SbCs compound. Additionally, there is a relatively higher charge distribution observed between Cs and Sb atoms, as well as between K and Sb atoms (like for the K_2CsSb compound), compared to the charge distribution between K and Cs. The lower charge distribution between K and Cs can be attributed to the smaller electronegativity difference between these two alkali metals. This is a result of their low electronegativity values and their tendency to donate electrons, which results in a relatively weaker effect on the charge distribution between K and Cs.

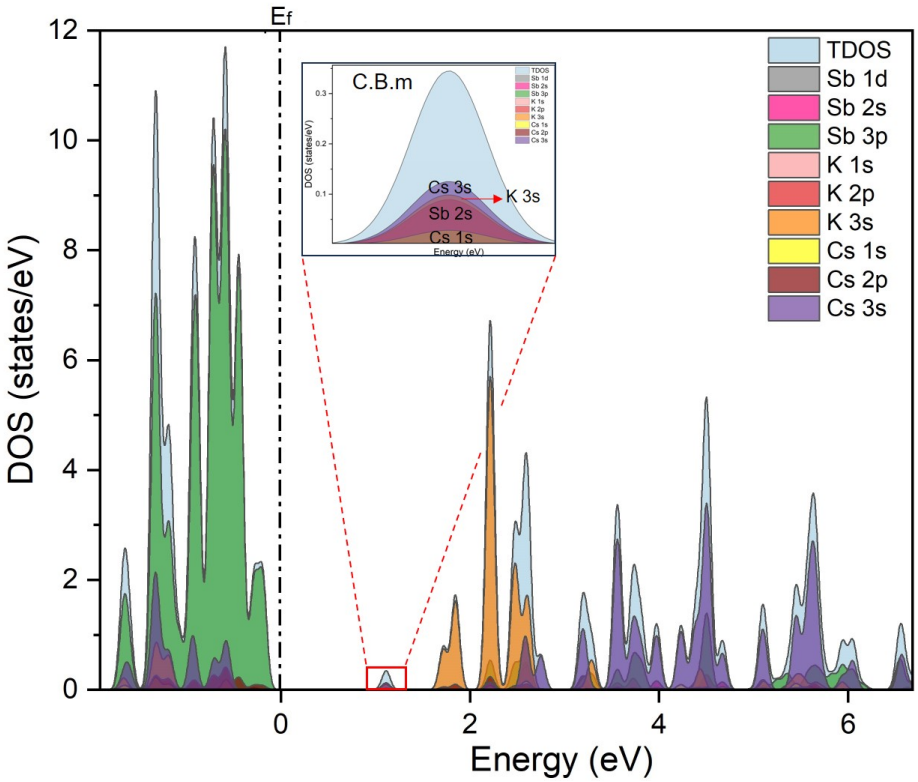

Figure 5.9: Atom projected density of states (PDOS) of Cs_2KSb, with the TDOS represented by the light blue area. The contribution of different atoms is depicted in various colors. In the plot, 'C.B.m' denotes the conduction band minimum.

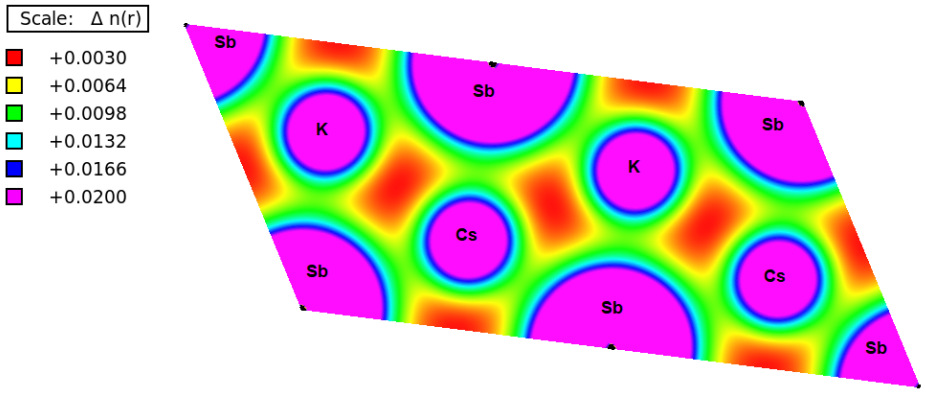

Figure 5.10: Side view of the calculated charge density plot of the Cs_2KSb material with colors scale n(r) indicating ranges of charge accumulation and depletion in a.u.

5.5.2.2 Optical Properties

Similar to the analysis performed on K_2CsSb material, the optical properties of the Cs_2KSb compound were studied utilizing the epsilon.x code available in the Quantum-Espresso package. Within the random phase approximation framework [206], we calculated the complex dielectric function $\varepsilon(\omega)$ based on the DFT ground state calculation using the HSE functional.

In Figure 5.11a, the variation of the real and imaginary parts of the dielectric function with photon energy is shown for the Cs_2KSb material. In the imaginary part of the dielectric function, the first peak (labeled A) appears at approximately 1.77 eV. However, the band gap calculated using the HSE functional was determined to be 1.06 eV. The reason for this shift in the position of the imaginary dielectric peak compared to the band gap in Cs_2KSb can be attributed to the nature of the optical transitions involved. In materials with an indirect band gap, such as Cs_2KSb, the valence band maximum, and the conduction band minimum occur at different points in the Brillouin zone. As a result, an electron transitioning between these states requires a change in momentum in addition to the energy difference. Therefore, these transitions may occur through phonon-assisted processes or involve momentum changes in addition to the energy difference. This change introduces an additional energy component, resulting in a shift in the observed peak in the dielectric function. The subsequent peaks, labeled B, C, D, E, and F, are observed in the visible-ultraviolet (UV) spectrum at approximately 2.27 eV, 2.61 eV, 2.86 eV, 3.27 eV, and 4.15 eV, respectively in Fig. 5.11a. These peaks arise from electron transitions originating from various positions within the valence band to the conduction band.

The refractive index $n(\omega)$ for the Cs_2KSb compound was calculated based on the values of ε_1 and ε_2, and the resulting plot shows peaks that closely resemble the real and imaginary plots with minor deviations. The corresponding plots can be observed in Figure 5.11b. Peaks A, B, C, D, E, and F were observed in the refractive index plot at energy values of 1.72 eV, 2.22 eV, 2.56 eV, 2.81 eV, 3.23 eV, and 4.10 eV, respectively. These peaks correspond to inter-band transitions occurring between the valence band and the conduction band.

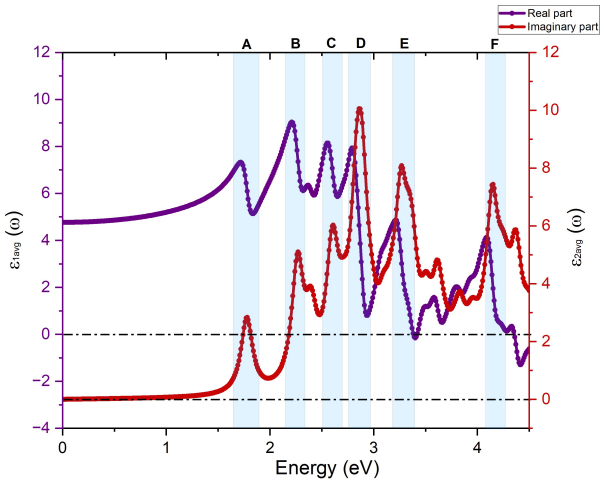
Real part
Imaginary part
A
B
C
D
E
F
ε_{1avg} (ω)
ε_{2avg} (ω)
Energy (eV)

(a)

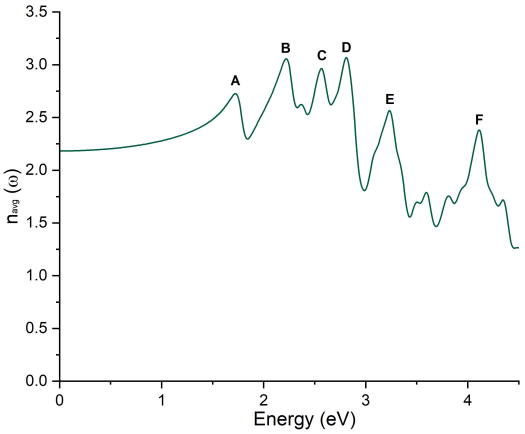
A
B
C
D
E
F
n_{avg} (ω)
Energy (eV)

(b)

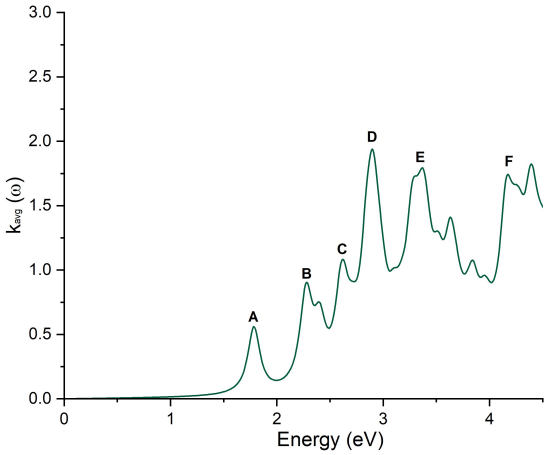
A
B
C
D
E
F
K_{avg} (ω)
Energy (eV)

(c)

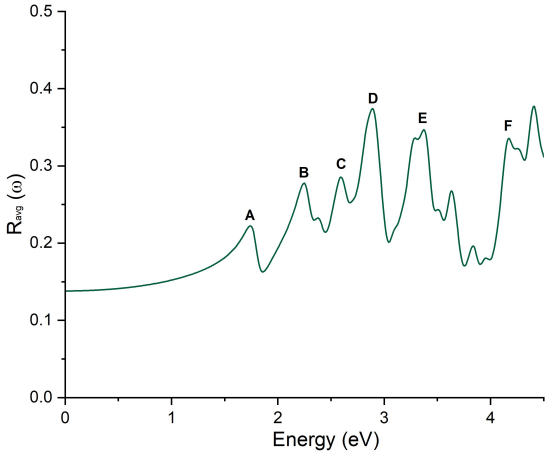
A
B
C
D
E
F
R_{avg} (ω)
Energy (eV)

(d)

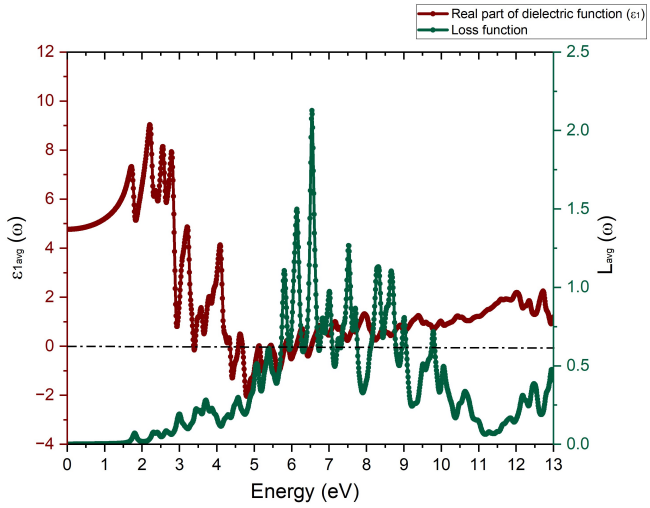
Real part of dielectric function (ε1)
Loss function
ε_{1avg} (ω)
L_{avg} (ω)
Energy (eV)

(e)

Figure 5.11: Optical spectra of the Cs_2KSb film as a function of the photon energy, where it shows the (a) real and imaginary parts of the dielectric function, (b) refractive index $n(\omega)$, (c) extinction coefficient $k(\omega)$, (d) reflectivity $R(\omega)$, and (e) illustrates the real part of the dielectric function (red wine color) and the electron energy loss spectrum (green color), calculated through HSE hybrid functional.

Both the imaginary part of the dielectric function and the extinction coefficient provide insights into the absorption behavior at the band edges. As a result, like K_2CsSb compound, we observe analogous peaks in the extinction coefficient (Fig. 5.11c), mirroring those in the imaginary part of the dielectric function (Fig. 5.11a). This suggests that absorption characteristics are present at those particular energy levels.

Figure 5.11d illustrates the calculated variation of reflectivity for the Cs_2KSb compound with respect to photon energy. In the reflectivity plot, the peaks appeared at 1.74 eV, 2.24 eV, 2.59 eV, 2.89 eV, 3.37 eV, and 4.17 eV, corresponding to the A, B, C, D, E, and F peaks, respectively. These peaks in the reflectivity plot correspond to transitions within the band structure, specifically between the valence band and the conduction band. A detailed analysis and interpretation of these peaks are provided in comparison with the experimental reflectivity data, as presented in Chapter 6 (Section 6.1).

The variations in the electron energy loss spectrum (EELS) with respect to photon energy for the Cs_2KSb compound are illustrated in Figure 5.11e. Prominent features in the electron energy loss spectrum of the Cs_2KSb compound are primarily observed in the high-energy range beyond the visible region, particularly at frequencies above approximately 6 eV. At 6.55 eV, a local maximum is observed in the loss function, an increase in the real part of the dielectric function is also detected within this frequency range. This observation strongly suggests the presence of plasmonic behavior in this excitation, similar to the K_2CsSb compound. At lower energy levels, the local fluctuations seen in the real component of the dielectric function, ε_1, correspond to the locations of absorption peaks in the imaginary component, ε_2.

5.5.3 K_3Sb Cubic & Hexagonal Photocathode

As previously discussed, the formation of the K_2CsSb compound is influenced by the presence of intermediate phases, namely Sb and K_3Sb, which can influence the properties of the final compound [67]. As outlined in Section 4.4.6, during the analysis of the thick and thin KCsSb cathodes, a significant difference in spectral reflectivity was observed for KSb compounds. This disparity was attributed to potential variances in the crystal structure between them. Additionally, existing literature has confirmed the presence of distinct crystal structures in the K_3Sb compound, encompassing both cubic and hexagonal forms [158, 233]. As indicated by references [158, 233], these variations in the crystal structure in the K-Sb film can be ascribed to either an excess or deficiency of potassium (K) atoms. Therefore, to investigate the hypothesis, we conducted a DFT analysis on the K_3Sb material, considering both the cubic and hexagonal phases. Subsequently, we compared these DFT results with the experimental data, particularly the reflectivity results, to gain a deeper understanding. In the following section, we have discussed the DFT results obtained for both the K_3Sb cubic & Hexagonal compounds.

5.5.3.1 K_3Sb (Cubic) photocathode:

5.5.3.1.1 Electronic Properties:

Here, we focused on the face-cantered-cubic (FCC) phase (with a space group of F m-3-m) of the K_3Sb material and investigated the electronic and optical properties. The lattice parameter a = 8.493 Å was taken directly from the reference [158]. As shown in Figure 5.12a, the Sb atoms (depicted in blue color) were located at the Wyckoff position (0, 0, 0), while the alkali species K (depicted in orange color) were located at the crystal coordinates $(\frac{1}{2}, \frac{1}{2}, \frac{1}{2})$ and $\pm\,(\frac{1}{4}, \frac{1}{4}, \frac{1}{4})$, respectively. In this study, the band structure calculation was conducted using the HSE hybrid functional, which includes the incorporation of exact exchange [188]. Like previous compounds, to model the interaction between electrons and ions, ONCV pseudopotentials [224] were employed, and a $4 \times 4 \times 4$ k-mesh was utilized to sample the Brillouin zone during the calculation. For this calculation, a plane wave kinetic energy cutoff of 70 Ry and a charge density plane wave cutoff of

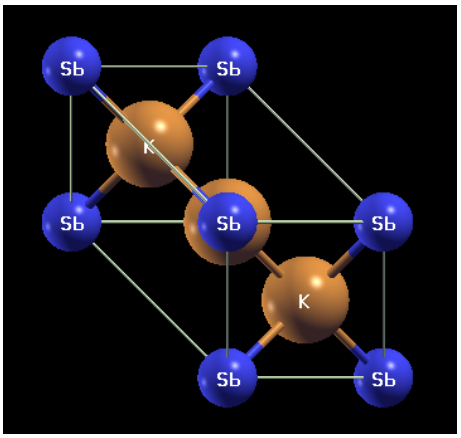

(a)

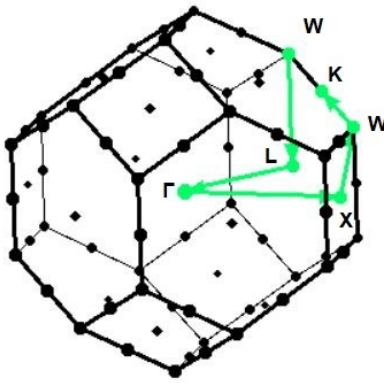

(b)

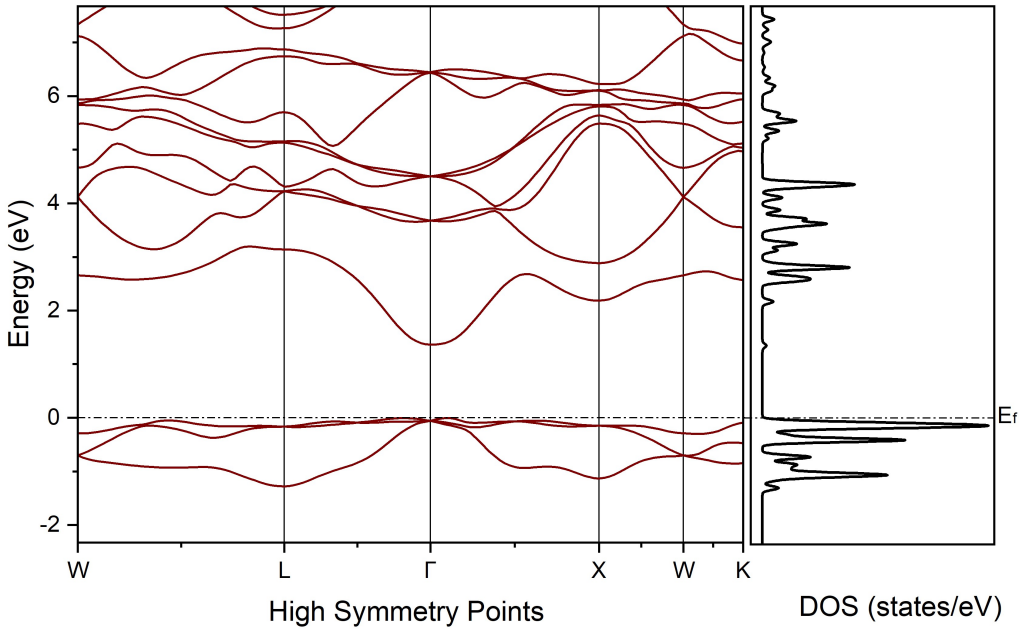

(c)

Figure 5.12: (a) unit cell of K_3Sb (cubic) is depicted using a ball and stick representation. (b) Brillouin zone of K_3Sb (cubic) is shown, with high symmetry points and the corresponding path connecting them highlighted in color. (c) computed electronic band structure of K_3Sb (cubic) material along with the corresponding density of states (DOS) plot. The Fermi energy (E_f) was set to zero at the valence band maximum.

280 Ry were employed. Like previous compounds, Maximally localized Wannier functions [195] were computed with the Wannier90 code and used to interpolate the band structure [201]. The band gap calculated using the HSE functional was 1.42 eV (direct gap) and almost identical matches with the experimental value of 1.4 eV [158]. The band structure of this material reveals a direct band gap that occurs between the Γ and Γ points in the Brillouin zone, where the valence-band maximum and the conduction-band minimum appear, respectively (see Fig. 5.12c).

Figure 5.12c presents the electronic band structure of the K_3Sb (cubic) material, accompanied by the corresponding density of states plot. Additionally, Figure 5.13 illustrates the atom-projected density of states (PDOS) for the K_3Sb (cubic) material. Like the previous compounds, there are lower-energy bands that exhibit nearly flat dispersion, primarily dominated by the Sb 2s state, with a slight mix of K 3s state, situated roughly 7.7 eV beneath the Fermi energy (this is not shown in the figures). This indicates that the electrons in those bands are relatively localized and do not participate in extensive delocalized electronic motion. Figure 5.13 reveals a noticeable influence of the Sb 3p state on the valence bands, while the contributions from the K 3s, Sb 2s, and K 2p states (Sb 2s and K 2p states are overshadowed by the Sb 3p and K 3s states in the figure) are comparatively smaller. Furthermore, it can be observed that the conduction band is predominantly influenced by the K 3s state, with a relatively minor contribution from the 2s and 3p states of the Sb atoms. The primary contribution to the conduction band minimum (CBm) originates from the K 3s and Sb 2s states.

Similarly, to the K_2SbCs & Cs_2KSb compounds, the electronic charge density distribution has been computed for the K_3Sb (cubic) compound. The distribution of electronic charge density within the (100) plane of the K_3Sb (cubic) material is depicted in Figure 5.14. Based on the figures, it is apparent that the electronic charge is concentrated predominantly around the ionic sites, as indicated by the scale. This finding implies that the compounds exhibit a prevailing ionic bond character. Furthermore, the charge distribution analysis reveals a relatively higher charge distribution between the Sb and K atoms compared to the charge distribution between K and K within the compound. The relatively lower charge distribution observed between K atoms can be attributed

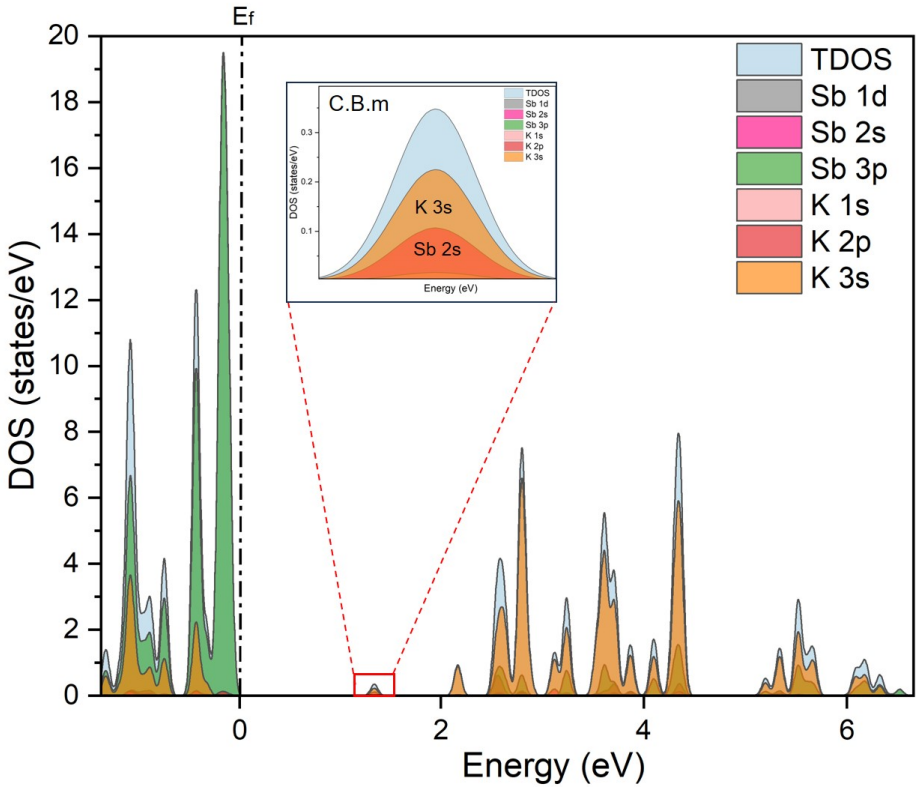

Figure 5.13: Atom-projected density of states (PDOS) of K_3Sb (cubic), with the TDOS represented by the light blue area. The contribution of different atoms is depicted in various colors. In the plot, 'C.B.m' denotes the conduction band minimum.

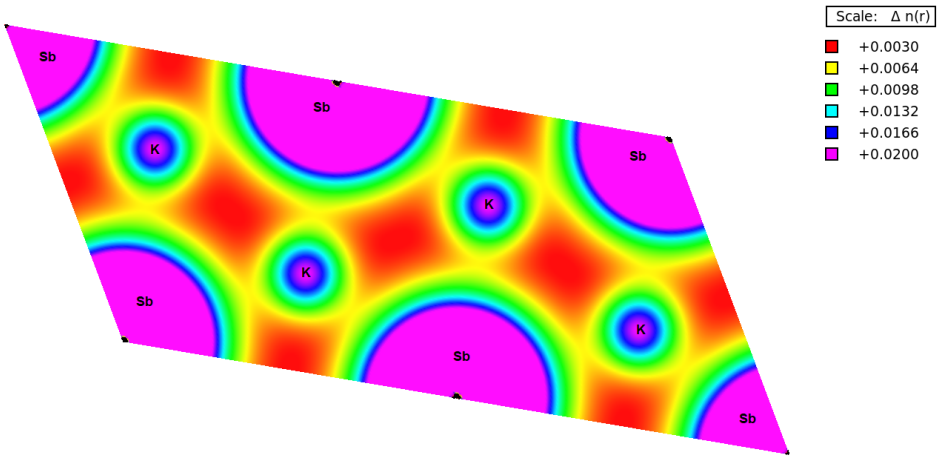

Figure 5.14: Side view of the calculated charge density plot of the K_3Sb (cubic) material with colors scale n(r) indicating ranges of charge accumulation and depletion in a.u.

to their similar electronegativities. As a result of the similar electronegativity, the charge distribution between the potassium atoms is reduced.

5.5.3.1.2 Optical Properties:

The optical properties of the K_3Sb (cubic) compound were studied using the epsilon.x code available in the Quantum-Espresso package, similar to the approach employed for K_2CsSb and Cs_2KSb materials. Within the random phase approximation framework [206], we calculated the complex dielectric function $\varepsilon(\omega)$ based on the DFT ground state calculation using the HSE functional.

Figure 5.15a illustrates the change in the real and imaginary components of the dielectric function as a function of photon energy for the cubic K_3Sb material. In the imaginary part of the dielectric function, the first peak (labeled A) appears at approximately 1.42 eV. The observed peak arises from a three-fold degenerate exciton due to the cubic symmetry of the crystal. This particular transition, labeled as the direct optical transition (Γ-Γ), originates between the valence band maximum and the conduction band minimum. The following peaks, marked as B, C, D, E, and F, are found within the visible-UV spectrum, roughly at energy values of 2.33 eV, 2.67 eV, 2.95 eV, 3.32 eV, and 3.77 eV, respectively in Fig. 5.15a. These peaks result from electron transitions originating from distinct locations within the valence band and extending into the conduction band.

Similar to the approach employed for the K_2CsSb and Cs_2KSb materials, the refractive index $n(\omega)$ of the K_3Sb (cubic) compound was determined by evaluating the values of ε_1 (real part) and ε_2 (imaginary part). The resulting plot (see Fig. 5.15b) shows peaks that closely resemble the real and imaginary plots with minor deviations. Peaks A, B, C, D, E, and F were observed in the refractive index plot at energy values of 1.36 eV, 2.29 eV, 2.62 eV, 2.91 eV, 3.28 eV, and 3.61 eV, respectively.

The imaginary part of the dielectric function and the extinction coefficient offer valuable information regarding the absorption behavior at the band edges. Consequently, we observe similar peaks in the extinction coefficient (see Fig. 5.15c) that correspond to the peaks observed in the imaginary part of the dielectric function (Fig. 5.15a). This similarity indicates the presence of absorption characteristics at those specific energy levels.

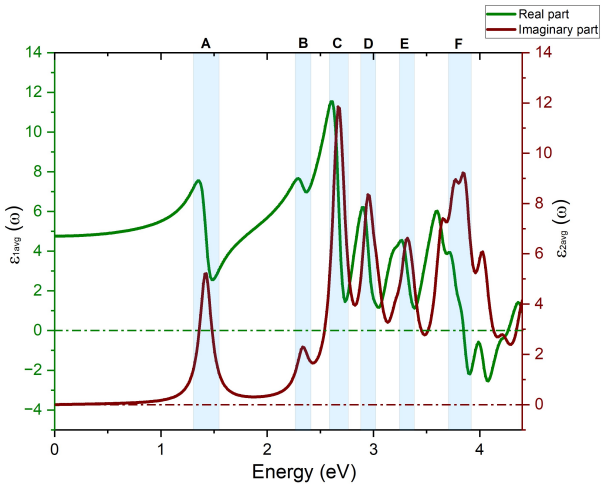
Real part
Imaginary part
A
B
C
D
E
F
ε_{1avg} (ω)
ε_{2avg} (ω)
Energy (eV)

(a)

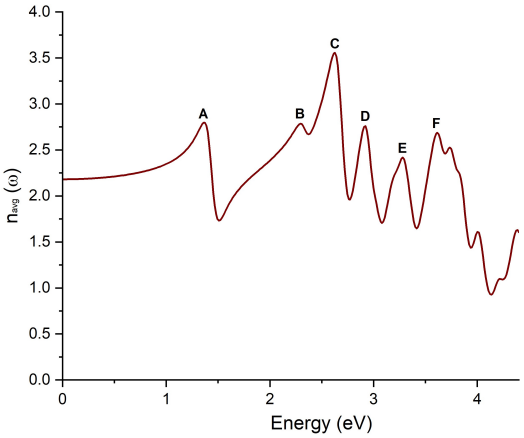
A
B
C
D
E
F
n_{avg} (ω)
Energy (eV)

(b)

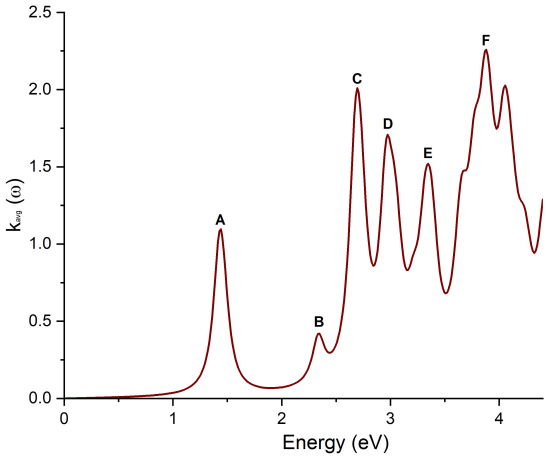
A
B
C
D
E
F
k_{avg} (ω)
Energy (eV)

(c)

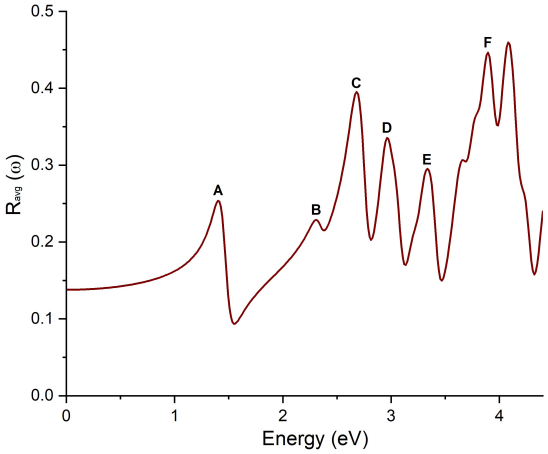
A
B
C
D
E
F
R_{avg} (ω)
Energy (eV)

(d)

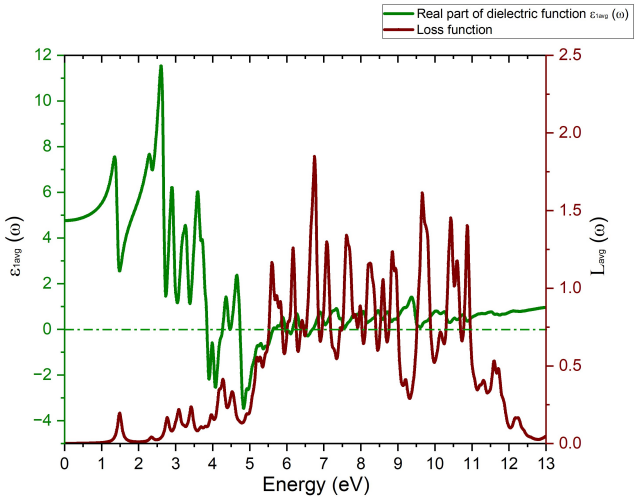
Real part of dielectric function ε_{1avg} (ω)
Loss function
ε_{1avg} (ω)
L_{avg} (ω)
Energy (eV)

(e)

Figure 5.15: Optical spectra of the K_3Sb (cubic) compound as a function of the photon energy, where it shows the (a) real and imaginary parts of the dielectric function, (b) refractive index $n(\omega)$, (c) extinction coefficient $k(\omega)$, (d) reflectivity $R(\omega)$, (e) the real part of the dielectric function (green color) and the electron energy loss spectrum (red wine color), calculated through HSE hybrid functional.

Figure 5.15d illustrates the DFT calculated variation of reflectivity for the K_3Sb (cubic) compound with respect to photon energy. In the reflectivity plot, the peaks appeared at 1.40 eV, 2.30 eV, 2.67 eV, 2.97 eV, 3.33 eV, and 3.89 eV, corresponding to the A, B, C, D, E, and F peaks, respectively. These peaks in the reflectivity plot correspond to transitions between the valence band and the conduction band. Additional analysis and comparison of these reflectivity results are presented in Chapter 6 (Section 6.1.1.1).

The variations in the electron energy loss spectrum (EELS) with respect to photon energy for the K_3Sb compound are illustrated in Figure 5.15e. Prominent features in the electron energy loss spectrum of the K_3Sb (cubic) compound are primarily observed in the high-energy range beyond the visible region, particularly at frequencies above ~ 5 eV. At 6.75 eV, a local maximum is observed in the loss function, an increase in the real part of the dielectric function is also detected within this frequency range. This observation strongly suggests the presence of plasmonic behavior in this excitation. At lower energy levels, the local fluctuations seen in the real component of the dielectric function, ε_1, correspond to the locations of absorption peaks in the imaginary component, ε_2.

5.5.3.2 K_3Sb (Hexagonal) Photocathode

5.5.3.2.1 Electronic Properties:

Here, we focused on the hexagonal structure (with a space group of $P6_3$ / mmc (No 194)) of the K_3Sb material and investigated the electronic and optical properties. The lattice parameter a = 6.025 Å and c = 10.690 Å was taken directly from the reference [233]. As shown in Figure 5.16a, two Sb atoms (depicted in blue color) were located at the 2c position with coordinates $(\frac{1}{3},\frac{2}{3},\frac{1}{4})$ and $(\frac{2}{3},\frac{1}{3},\frac{3}{4})$, while the alkali species K (depicted in orange color) occupies the 2b position at coordinates $(0,0,\frac{1}{4})$, $(0,0,\frac{3}{4})$ and the 4f position $(\frac{1}{3},\frac{2}{3},z)$, $(\frac{2}{3},\frac{1}{3},z+\frac{1}{2})$, $(\frac{2}{3},\frac{1}{3},-z)$, and $(\frac{1}{3},\frac{2}{3},-z+\frac{1}{2})$ with positional parameter u = 0.582. In this study, the band structure calculation was conducted using the HSE hybrid functional, which includes the incorporation of exact exchange [188]. Like the previous compounds, to model the interaction between electrons and ions, optimized norm-conserving vanderbilt pseudopotentials [224] were employed, and a $4\times4\times4$ k-mesh was utilized to sample the Brillouin zone during the calculation. For this calculation, a plane wave kinetic energy cutoff of 70 Ry and a charge density plane wave cutoff of 280 Ry were employed. Like K_2CsSb, Cs_2KSb, and K_3Sb (cubic) material, Maximally localized Wannier functions [195] were computed with the Wannier90 code, and used to interpolate the band structure [201]. The band gap, calculated as 1.05 eV (direct gap) using the HSE functional, closely corresponds to the experimental value of 1.1 eV [158], indicating a strong agreement between the two.

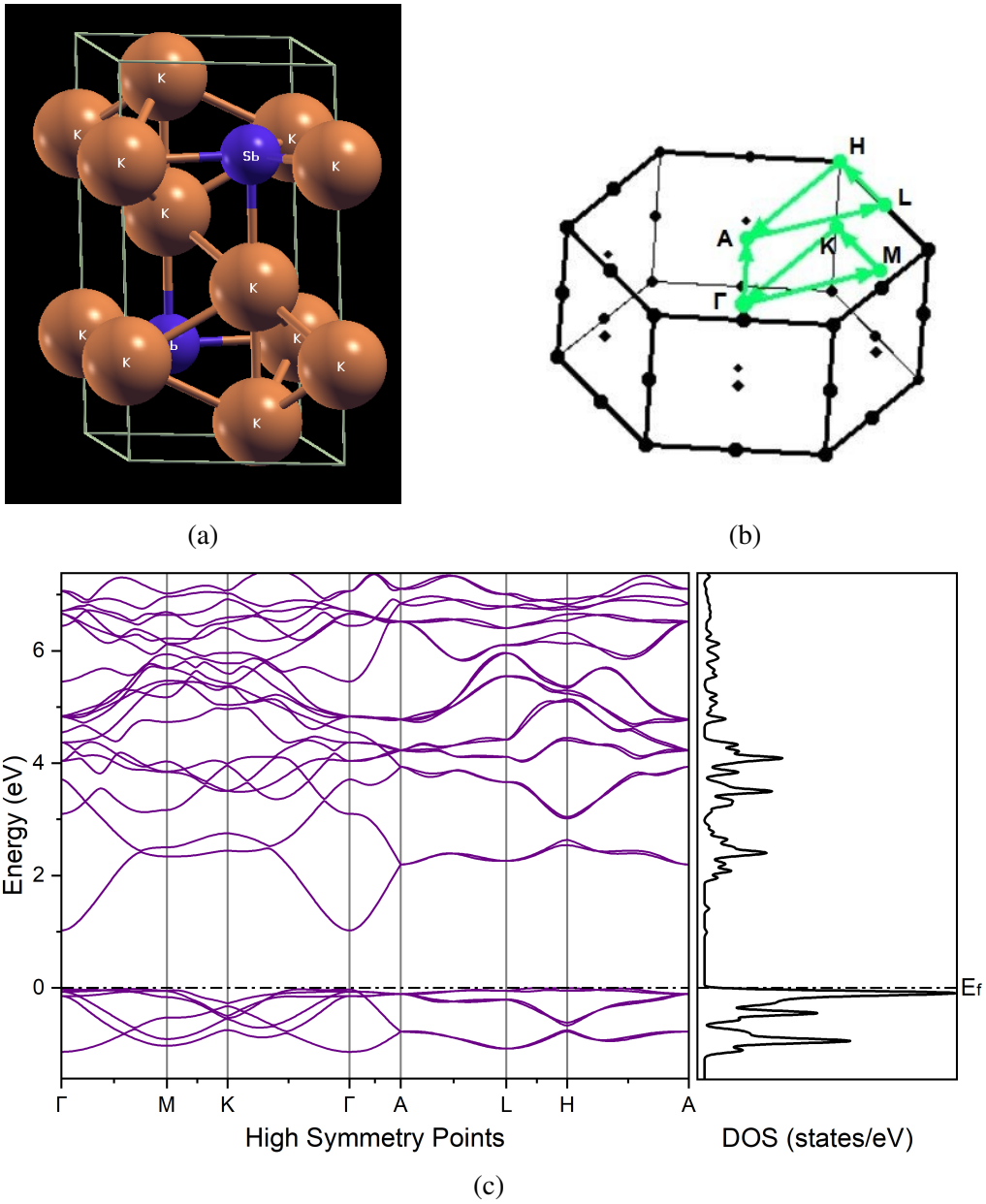

(a) (b)

(c)

Figure 5.16: (a) unit cell of K_3Sb (hexagonal) is depicted using a ball and stick representation. (b) Brillouin zone of K_3Sb (hexagonal) is shown, with high symmetry points and the corresponding path connecting them highlighted in color. (c) computed electronic band structure of K_3Sb (hexagonal) material along with the corresponding density of states (DOS) plot. The Fermi energy (E_f) was set to zero at the valence band maximum.

Figure 5.16c presents the electronic band structure of the K_3Sb (hexagonal) material, accompanied by the corresponding density of states (DOS) plot. Additionally, Figure 5.17 illustrates the atom-projected density of states (PDOS) for the K_3Sb (hexagonal) material. Like other studied compounds, there are lower-energy bands that exhibit nearly flat dispersion primarily dominated by the Sb 2s state, with a slight mix of K 3s state, situated roughly 7.72 eV beneath the Fermi energy (this is not shown in the figures). This indicates that the electrons in those bands are relatively localized and do not participate in extensive delocalized electronic motion. In Figure 5.17, it is evident that the valence bands are significantly influenced by the Sb 3p state, while the contributions from the K 3s and K 2p states, as well as the Sb 2s state (K 2p and Sb 2s states are overshadowed by the Sb 3p and K 3s states in the figure), are comparatively smaller. In addition, it is apparent that the conduction band is primarily governed by the dominant influence of the K 3s states, while the contributions from the 2s and 3p states of the Sb atoms (Sb 2s and 3p states are overshadowed by the K 3s state in the figure) are relatively minor. The main contribution to the conduction band minimum (CBm) arises from the combined effects of the K 3s and Sb 2s states. These findings exhibit similarities to the K_3Sb (cubic) structure (see Fig. 5.13).

Similar to previously studied compounds, the electronic charge density distribution for the K_3Sb (hexagonal) compound has been computed. The distribution of electronic charge density within the (100) plane of the K_3Sb (hexagonal) material is depicted in Figure 5.18. Based on the figures, it is apparent that the electronic charge is concentrated predominantly around the ionic sites, as indicated by the scale. This finding implies that the compounds exhibit a prevailing ionic bond character. Additionally, there is a relatively higher charge distribution observed between Sb atoms and K atoms compared to the charge distribution between K and K in the compound. As mentioned earlier for the K_3Sb (cubic) compound, the relatively lower charge distribution between potassium K atoms (K-K) in the compound can be attributed to the fact that both potassium atoms have similar electronegativity. Since both potassium atoms have similar electronegativity, the charge distribution between them is lower. This similar pattern in the charge density was also observed in previous findings for the K_3Sb (cubic) compound (see Fig. 5.14).

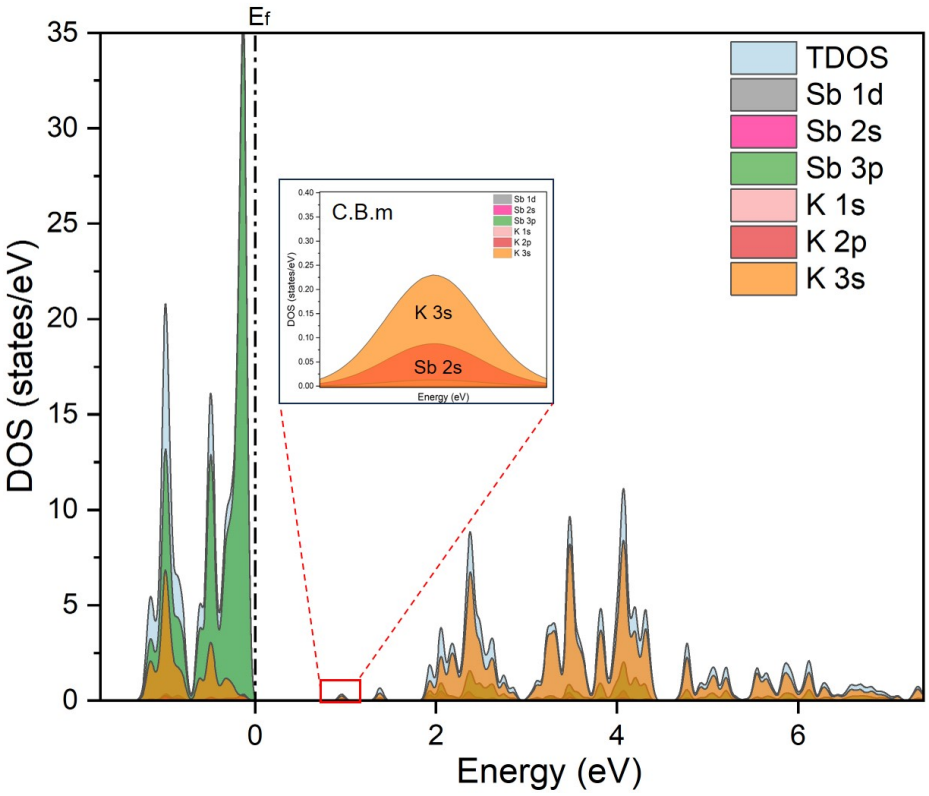

Figure 5.17: Atom-projected density of states (PDOS) of K_3Sb (hexagonal), with the TDOS represented by the light blue area. The contribution of different atoms is depicted in various colors. In the plot, 'C.B.m' denotes the conduction band minimum.

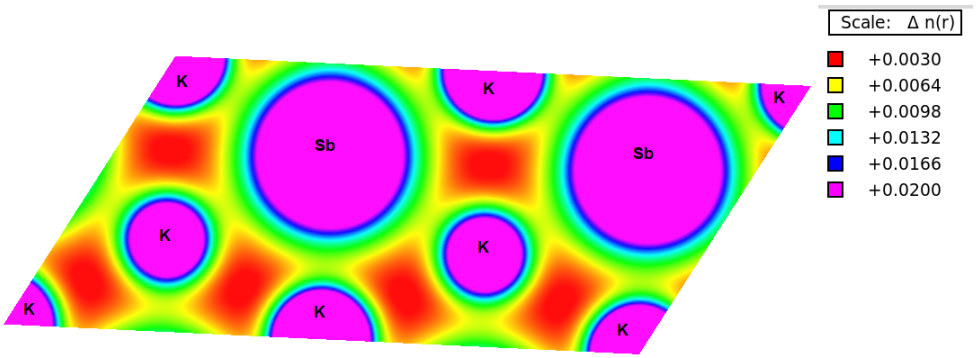

Figure 5.18: Side view of the calculated charge density plot of the K_3Sb (hexagonal) material with colors scale n(r) indicating ranges of charge accumulation and depletion in a.u.

5.5.3.2.2 Optical Properties:

Similar to previously studied compounds, the optical properties of the K_3Sb (hexagonal) compound were investigated using the epsilon.x code available in the Quantum-Espresso package. Within the random phase approximation framework [206], we calculated the complex dielectric function $\varepsilon(\omega)$ based on the DFT ground state calculation using the HSE functional.

Figure 5.19a illustrates the changes in the real and imaginary components of the dielectric function as a function of photon energy for the hexagonal K_3Sb material. The plot includes highlighted violet-colored boxes that represent the peaks of interest. In the imaginary part of the dielectric function, the presence of the first peak (labeled A) is observed at approximately 1.05 eV, indicating its association with the fundamental absorption process. Following the onset of this peak, an additional peak emerges at around 1.14 eV (present in the violet color box of peak A). Considering the dominant presence of Sb in the upper valence band, as evident from the PDOS plot (Figure 5.17), the doublet structure observed may be associated with the spin-orbit splitting phenomenon. The following peaks, marked as B, C, D, E, F, G, H, I, and J, are found within the visible-UV spectrum, roughly at energy values of 1.55 eV, 2.17 eV, 2.46 eV, 2.85 eV, 3.33 eV, 3.55 eV, 3.90 eV, 4.14 eV, and 4.38 eV, respectively. These peaks result from electron transitions originating from distinct locations within the valence band and extending into the conduction band.

Similar to the approach employed for previously studied compounds, the refractive index $n(\omega)$ of the K_3Sb (hexagonal) compound was determined by evaluating the values of ε_1 (real part) and ε_2 (imaginary part). The resulting plot (see Fig. 5.19b) shows peaks that closely resemble the real and imaginary plots with minor deviations. Peaks A, B, C, D, E, F, G, H, I, and J were observed in the refractive index plot at energy values of 0.99 eV, 1.49 eV, 2.13 eV, 2.42 eV, 2.81 eV, 3.26 eV, 3.52 eV, 3.87 eV, 4.09 eV, and 4.34 eV, respectively. These peaks correspond to inter-band transitions occurring between the valence band and the conduction band.

The imaginary part of the dielectric function and extinction coefficient provide valuable insights into the absorption behavior at the band edges. As a result, we observe a

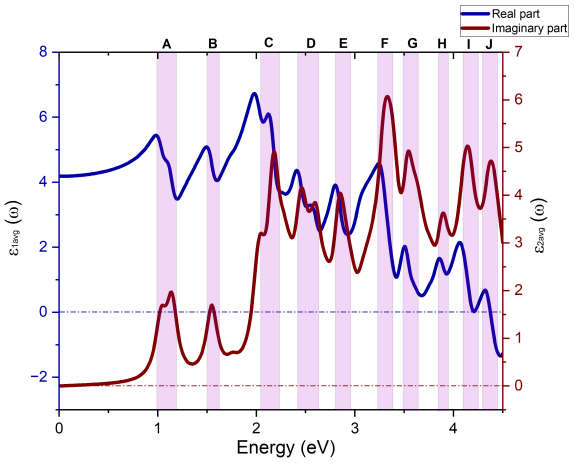
Real part
Imaginary part
A B C D E F G H I J
Energy (eV)

(a)

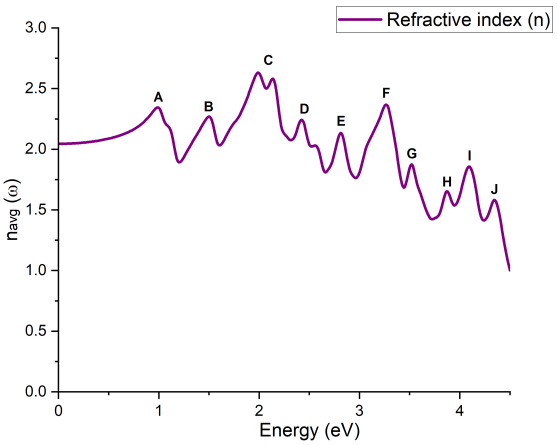
Refractive index (n)
A B C D E F G H I J
Energy (eV)

(b)

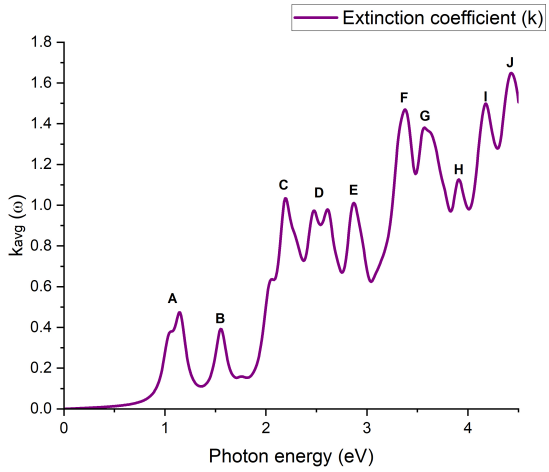
Extinction coefficient (k)
A B C D E F G H I J
Photon energy (eV)

(c)

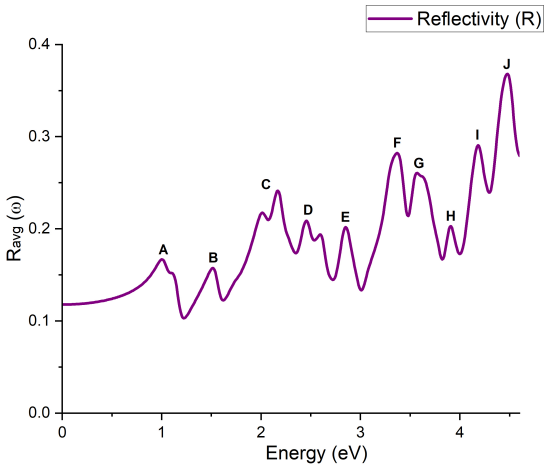
Reflectivity (R)
A B C D E F G H I J
Energy (eV)

(d)

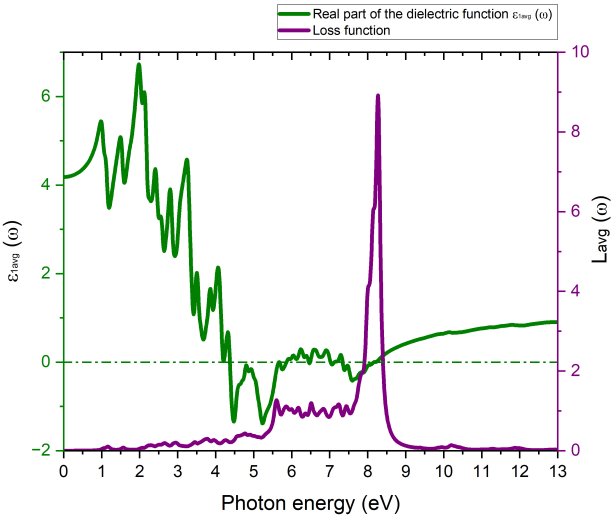
Real part of the dielectric function
Loss function
Photon energy (eV)

(e)

Figure 5.19: Optical spectra of the K_3Sb (hexagonal) compound as a function of the photon energy, where it shows the (a) real and imaginary parts of the dielectric function, (b) refractive index $n(\omega)$, (c) extinction coefficient $k(\omega)$, (d) reflectivity $R(\omega)$, and (e) illustrates the real part of the dielectric function (green color) and the electron energy loss spectrum (violet color), calculated through HSE hybrid functional.

comparable peaks in the extinction coefficient (refer to Fig. 5.19c) that align with the peaks observed in the imaginary part of the dielectric function (Fig. 5.19a). This similarity suggests the existence of absorption features at those particular energy levels.

Figure 5.19d illustrates the DFT calculated variation of reflectivity for the K_3Sb (hexagonal) compound with respect to photon energy. In the reflectivity plot, the peaks appeared at 1.00 eV, 1.51 eV, 2.16 eV, 2.45 eV, 2.85 eV, 3.36, 3.56 eV, 3.90 eV, 4.18 eV, and 4.47 eV, corresponding to the A, B, C, D, E, F, G, H, I and J peaks, respectively. These peaks in the reflectivity plot correspond to transitions within the band structure, specifically between the valence band and the conduction band. Additional analysis and comparison of these reflectivity results are presented in Chapter 6 (Section 6.1.1.1).

The variations in the electron energy loss spectrum (EELS) with respect to photon energy for the K_3Sb (hexagonal) compound are illustrated in Figure 5.19e. Prominent features in the electron energy loss spectrum of the K_3Sb (hexagonal) compound are primarily observed in the high-energy range beyond the visible region, particularly at frequencies above $\sim$ 7.5 eV. At 8.28 eV, a local maximum is observed in the loss function, along with a notable increase in the real part of the dielectric function within this frequency range. This observation strongly suggests the presence of plasmonic behavior in this excitation.

5.5.4 Na_2KSb Photocathode

5.5.4.1 Electronic Properties:

As part of our investigation into the Na_2KSb photocathodes, we also conducted a DFT study focusing on the Na_2KSb compound.

Here, we focused on the face-cantered-cubic (FCC) phase (with a space group of F m-3-m) of the Na_2KSb material and investigated the electronic and optical properties. The lattice parameter a = 7.7235Å was taken directly from the reference [234]. As shown in Figure 5.20a, the Sb atoms (depicted in blue color) were located at the Wyckoff position (0, 0, 0), while the alkali atoms K (depicted in orange color) were located at the crystal coordinates $(\frac{1}{2}, \frac{1}{2}, \frac{1}{2})$, and Na atoms (depicted in green color) are located at the crystal coordinates $\pm$ $(\frac{1}{4}, \frac{1}{4}, \frac{1}{4})$, respectively. In this study, the band structure calculation was conducted using the HSE hybrid functional, which includes the incorporation of exact exchange [188]. To model the interaction between electrons and ions, optimized norm-conserving vanderbilt pseudopotentials [224] were employed, and a 4 × 4 × 4 k-mesh was utilized to sample the Brillouin zone during the calculation. For this calculation, a plane wave kinetic energy cutoff of 70 Ry and a charge density plane wave cut-off of 280 Ry were employed. Like other discussed compounds, Maximally localized Wannier functions [195] were computed with the Wannier90 code and used to interpolate the band structure [201].

The band gap calculated using the HSE functional was 1.49 eV (direct gap), has a good agreement with previous DFT studies [235]. The band structure of this material reveals a direct band gap that occurs between the Γ and Γ points in the Brillouin zone, where the valence-band maximum and the conduction-band minimum appear, respectively, as can seen in Fig. 5.20b.

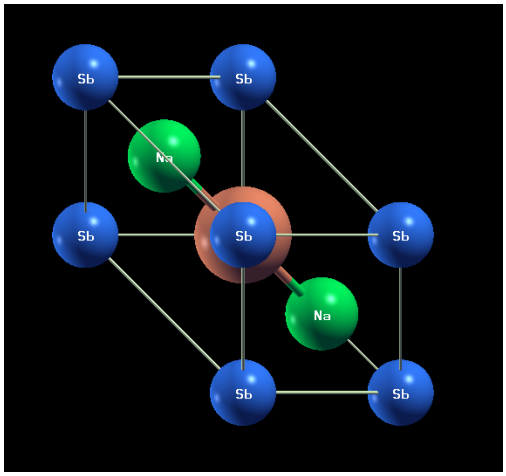

(a)

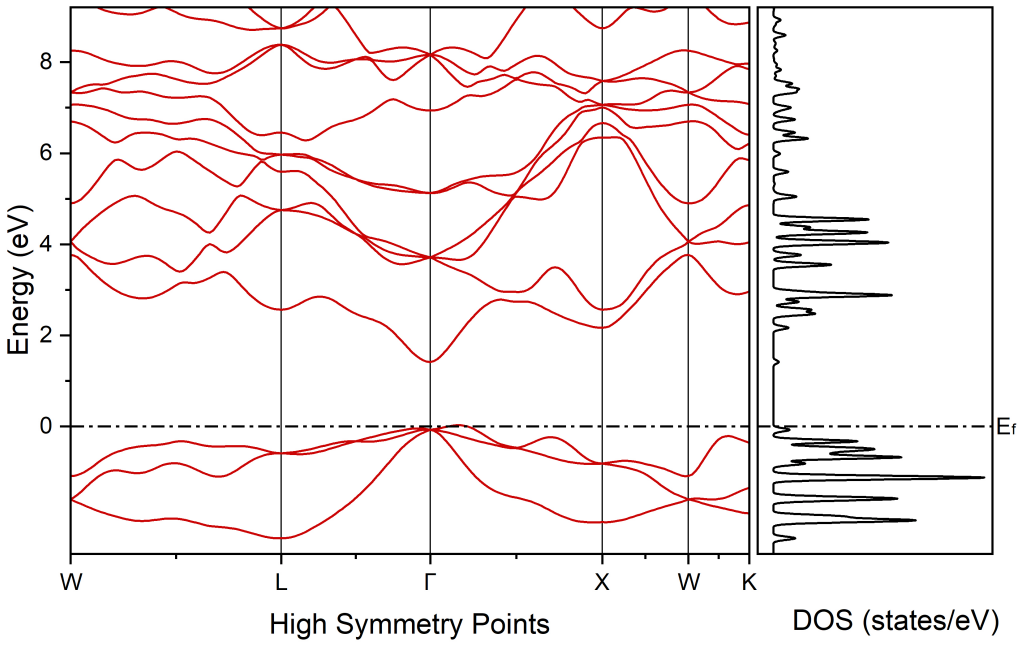

(b)

Figure 5.20: (a) unit cell of Na_2KSb is depicted using a ball and stick representation. (b) computed electronic band structure of Na_2KSb material along with the corresponding density of states (DOS) plot. The Fermi energy (E_f) was set to zero at the valence band maximum.

Figure 5.20b presents the electronic band structure of the Na_2KSb material, accompanied by the corresponding density of states plot. Additionally, Figure 5.21 illustrates the atom-projected density of states (PDOS) for the Na_2KSb material. Like previous compounds, there are lower-energy bands that exhibit nearly flat dispersion, primarily dominated by the Sb 2s state, with a slight contribution from the K 3s state and Na 3s state, situated roughly 8.28 eV beneath the Fermi energy (this is not shown in the figures). This indicates that the electrons in those bands are relatively localized and do not participate in extensive delocalized electronic motion. In Figure 5.21, it is evident that the valence bands are significantly influenced by the Sb 3p state, while the contributions from the Na 3s, K 3s state, and Sb 2s state are relatively less pronounced. Moreover, it is evident that the upper bands of the valance band are exclusively dominated by the Sb 3p state. In addition, it is apparent that the conduction band is primarily governed by the dominant influence of the Na and K 3s states, while the contributions from the 2s and 3p states of the Sb atoms are relatively minor. The primary origin of the conduction band minimum (CBm) can be attributed to the Na 3s, K 3s, and Sb 2s states.

Similarly to the other previous compounds, the electronic charge density distribution has been computed for the Na_2KSb compound. The distribution of electronic charge density within the (100) plane of the Na_2KSb material is depicted in Figure 5.22. Based on the figures, it is apparent that the electronic charge is concentrated predominantly around the ionic sites, as indicated by the scale. This finding implies that the compounds exhibit a prevailing ionic bond character. Furthermore, a relatively higher charge distribution is observed between the Sb and K atoms, as well as between the Sb and Na atoms, compared to the charge distribution between the K and Na atoms in the compound. This is because of the fact that K and Na are alkali metals with relatively low electronegativity values, whereas Sb possesses a higher electronegativity. Due to this difference, antimony tends to attract electrons more strongly than potassium and sodium.

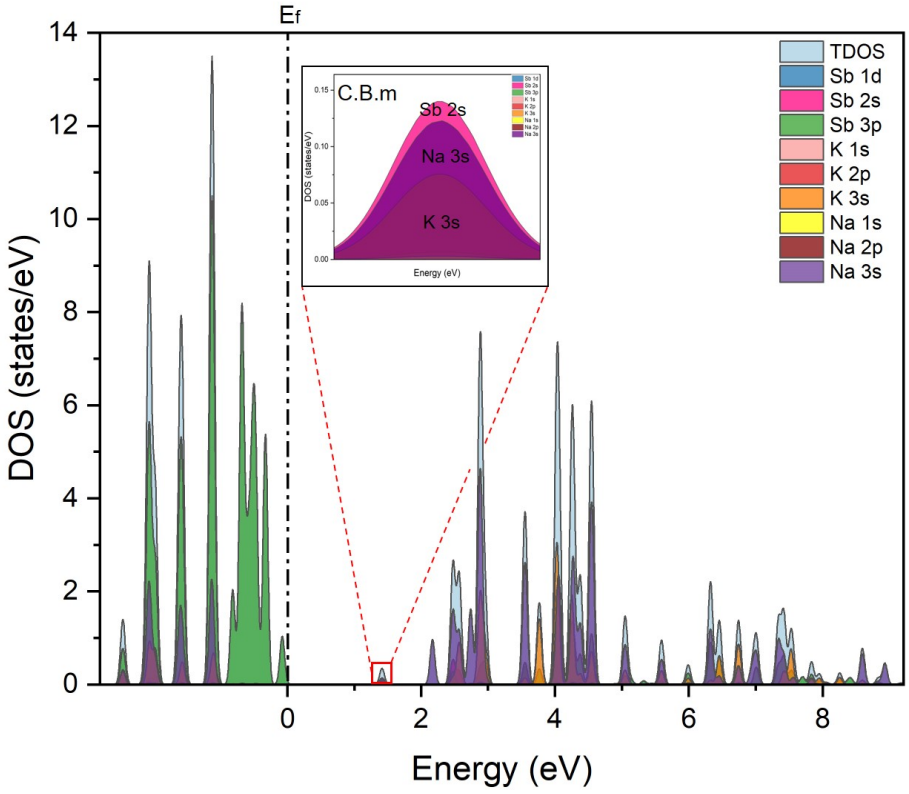

Figure 5.21: Atom-projected density of states (PDOS) of Na_2KSb, with the TDOS represented by the light blue area. The contribution of different atoms is depicted in various colors. In the plot, 'C.B.m' denotes the conduction band minimum.

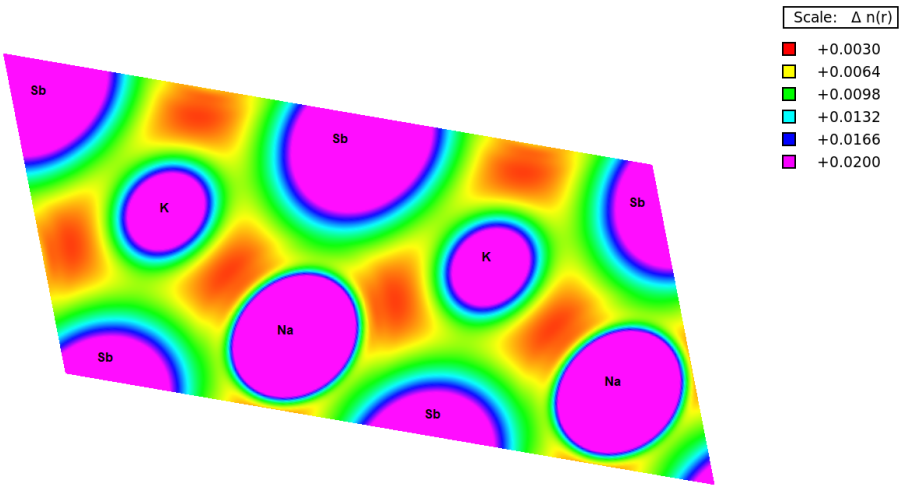

Figure 5.22: Side view of the calculated charge density plot of the Na_2KSb material with colors scale n(r) indicating ranges of charge accumulation and depletion in a.u.

5.5.4.2 Optical Properties:

Like it was done for previously studied materials, the optical properties of the Na_2KSb compound were studied utilizing the epsilon.x code available in the Quantum-Espresso package. Within the random phase approximation framework [206], we calculated the complex dielectric function $\varepsilon(\omega)$ based on the DFT ground state calculation using the HSE functional.

Figure 5.23a illustrates the change in the real and imaginary components of the dielectric function as a function of photon energy for the Na_2KSb material. In the imaginary part of the dielectric function, the first peak (labeled A) appears at approximately 1.49 eV. The observed peak can be attributed to a three-fold degenerate exciton (Fig. 5.20b), which arises from the cubic symmetry of the crystal, as seen in compounds like K_2CsSb and K_3Sb(cubic). This particular transition, labeled as the direct optical transition (Γ-Γ), originates between the valence band maximum and the conduction band minimum. The following peaks, marked as B, C, D, E, and F, are found within the visible-UV spectrum, roughly at energy values of 2.80 eV, 3.18 eV, 3.55 eV, 4.07 eV, and 4.55 eV, respectively. These peaks result from electron transitions originating from distinct locations within the valence band and extending into the conduction band.

Similar to the approach employed for other materials, the refractive index $n(\omega)$ of the Na_2KSb compound was determined by evaluating the values of ε_1 (real part) and ε_2 (imaginary part). The resulting plot (Fig. 5.23b) shows peaks that closely resemble the real and imaginary plots with minor deviations. Peaks A, B, C, D, E, and F were observed in the refractive index plot at energy values of 1.43 eV, 2.75 eV, 3.13 eV, 3.52 eV, 4.04 eV, and 4.52 eV, respectively. These peaks correspond to inter-band transitions occurring between the valence band and the conduction band.

Like previously studied materials, we observe similar peaks in the extinction coefficient (see Fig. 5.23c) that correspond to the peaks observed in the imaginary part of the dielectric function (Fig.5.23a). This similarity indicates the presence of absorption characteristics at those specific energy levels.

Figure 5.23d illustrates the DFT calculated variation of reflectivity for the Na_2KSb compound with respect to photon energy. In the reflectivity plot the peaks are appeared at

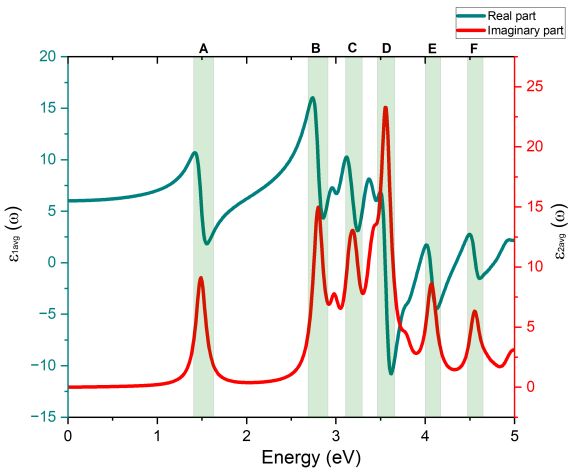
Real part
Imaginary part
A
B
C
D
E
F
Energy (eV)

(a)

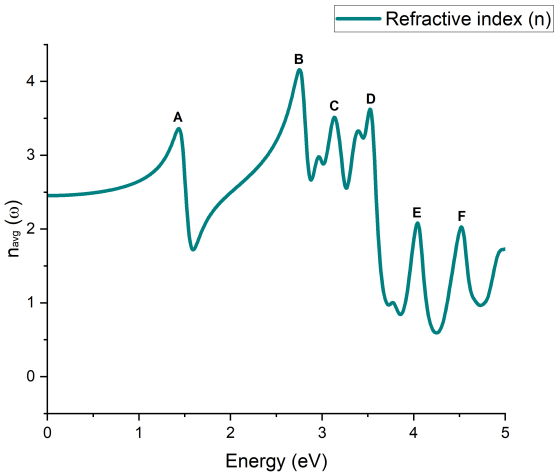
Refractive index (n)
A
B
C
D
E
F
Energy (eV)

(b)

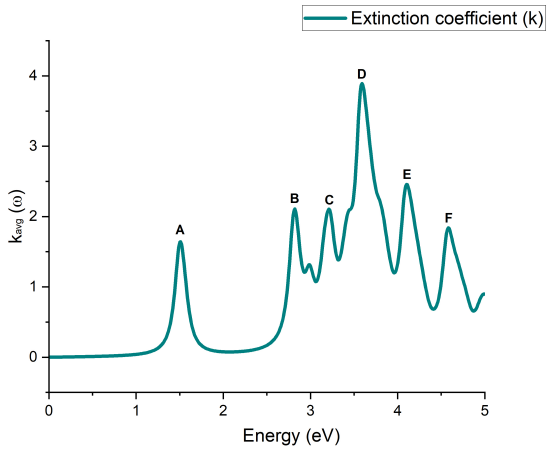
Extinction coefficient (k)
A
B
C
D
E
F
Energy (eV)

(c)

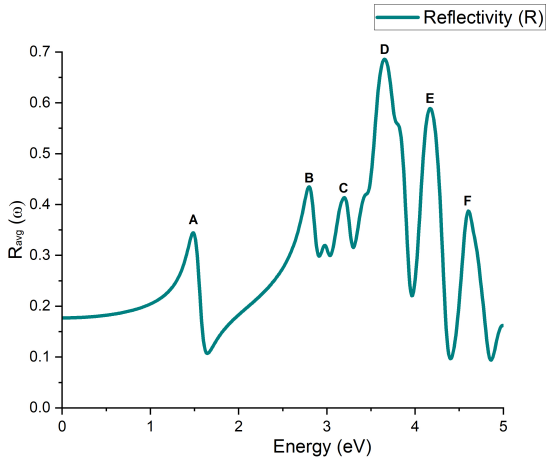
Reflectivity (R)
A
B
C
D
E
F
Energy (eV)

(d)

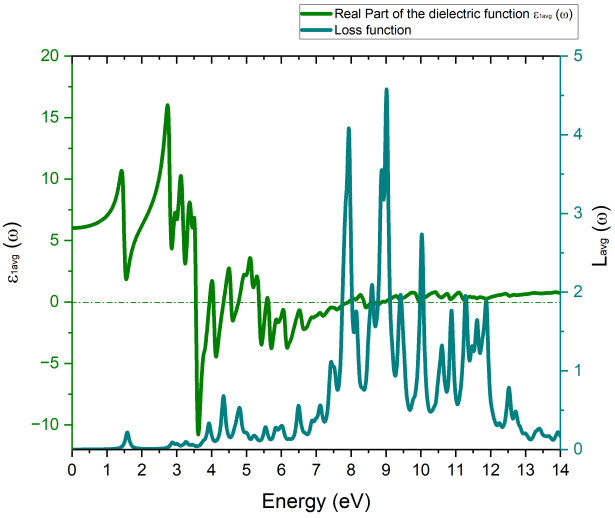
Real Part of the dielectric function
Loss function
Energy (eV)

(e)

Figure 5.23: Optical spectra of the Na_2KSb compound as a function of the photon energy, where it shows the (a) real and imaginary parts of the dielectric function, (b) refractive index $n(\omega)$, (c) extinction coefficient $k(\omega)$, (d) reflectivity $R(\omega)$, and (e) the real part of the dielectric function (green color) and the electron energy loss spectrum (cyan color), calculated through HSE hybrid functional.

1.48 eV, 2.80 eV, 3.20 eV, 3.65 eV, 4.17 eV, and 4.60 eV, corresponding to the A, B, C, D, E, and F peaks, respectively. These peaks in the reflectivity plot correspond to transitions within the band structure, specifically between the valence band and the conduction band. A comprehensive discussion about the reflectivity of the Na_2KSb compound is presented in Chapter 6 (Section 6.2).

The variations in the electron energy loss spectrum (EELS) with respect to photon energy for the Na_2KSb compound are illustrated in Figure 5.23e. Prominent features in the electron energy loss spectrum of the Na_2KSb compound are primarily observed in the high-energy range beyond the visible region, particularly at frequencies above approximately 7 eV. At 9.01 eV, a local maximum is observed in the loss function, along with an increase in the real part of the dielectric function within this frequency range. This observation suggests the presence of plasmonic behavior in this excitation. At lower energy levels, the local fluctuations seen in the real component of the dielectric function, ε_1, correspond to the locations of absorption peaks in the imaginary component, ε_2.

Chapter 6

Comparative Analysis of Simulation versus Experimental Data

6.1 Comparison and Discussion of Simulation and Experimental Results for KSb and KCsSb Compounds

In this section, we compare the simulation results with experimental data to further evaluate and rationalize the peak characteristics. The initial part involves a comparison of DFT simulation data with experimental results for the KSb compound, followed by a similar comparison for the KCsSb compound. The latter part of this section summarizes the relevant findings and discussions.

6.1.1 K-Sb Compound

In the literature, there are experimental results available, including the imaginary part of the dielectric function, and transmittance for both cubic and hexagonal K_3Sb compounds [233, 236]. In the first half of this section, a comparative analysis was conducted between our DFT results and the experimental data presented in the literature to validate the accuracy of our simulations. These datasets were then compared to our own experimental plots for result interpretation. In the sections below, we will begin with the

comparison and analysis of the K_3Sb (cubic) compound.

Note that, in the following section, for clarity, we will denote the peaks observed in the experimental plot as A', B', C', ... etc., the peaks in the DFT simulated plots as A, B, C, ... etc., and the peaks in the plot comparing the experimental and DFT simulated curves as A_1, B_1, C_1, ... etc.

6.1.1.1 Comparison and Analysis of K_3Sb Compound

The experimental findings of the imaginary part of the dielectric function for the K_3Sb cubic compound were reported by Ebina and Takahashi et al. and A. H. Sommer [233], as shown in Figure 6.1a. The plot reveals multiple peaks, including two prominent peaks at 2.75 eV (i.e., C') and 3.65 eV (i.e., F'). These peaks are visually highlighted by a violet-colored box and labeled as A', B', C', E', and F'. A shoulder appeared at 1.45 eV, referred to as A', is observed, followed by peaks at 2.41 eV, 2.75 eV, 3.35 eV, and 3.65 eV, denoted as B', C', E', and F', respectively. In Figure 6.1b, the imaginary part of the dielectric function of K_3Sb (cubic) compound obtained through DFT calculations is presented. As already reported Section 5.5.3.1.2 (page 200, Fig. 5.15a), several peaks are observed at specific energy values in the simulated imaginary part of the dielectric function plot in Fig. 6.1b: 1.42 eV, 2.33 eV, 2.67 eV, 2.95 eV, 3.32 eV, and 3.77 eV (highlighted by a violet-colored box). These peaks are labeled as A, B, C, D, E, and F, respectively. Figure 6.1c illustrates the comparison between the experimental (literature) and simulated plots of the imaginary dielectric function of K_3Sb (cubic) compound. The peaks in both curves show a noticeable similarity, as depicted by the light blue-colored boxes highlighting the corresponding peaks in Fig. 6.1c. Nevertheless, a marginal deviation is observed in the simulated plot, particularly for the peak labeled F_1, when compared to the experimental plot (Fig. 6.1c). However, the overall agreement between the two plots validates the accuracy of the simulation and confirms the presence of specific electronic transitions or excitations in the material at those energy levels. Nevertheless, it is worth noting that the peak labeled D in the simulated plot (Fig. 6.1b) is not as prominently visible as it corresponds to the peak in the experimental plot (Fig. 6.1a). This difference could be attributed to limitations inherent to the experimental measurement process, such as

sensitivity or resolution issues. However, it is intriguing to note the similarity between two prominent peaks between the simulation and experimental plots, specifically point C_1 and point F_1 in Fig. 6.1c. Notably, when calculating the ratio between these two peaks (i.e., between peak C_1 & F_1) observed in both simulated and experimental plots, the ratios exhibit similarity in both the simulated and experimental datasets.

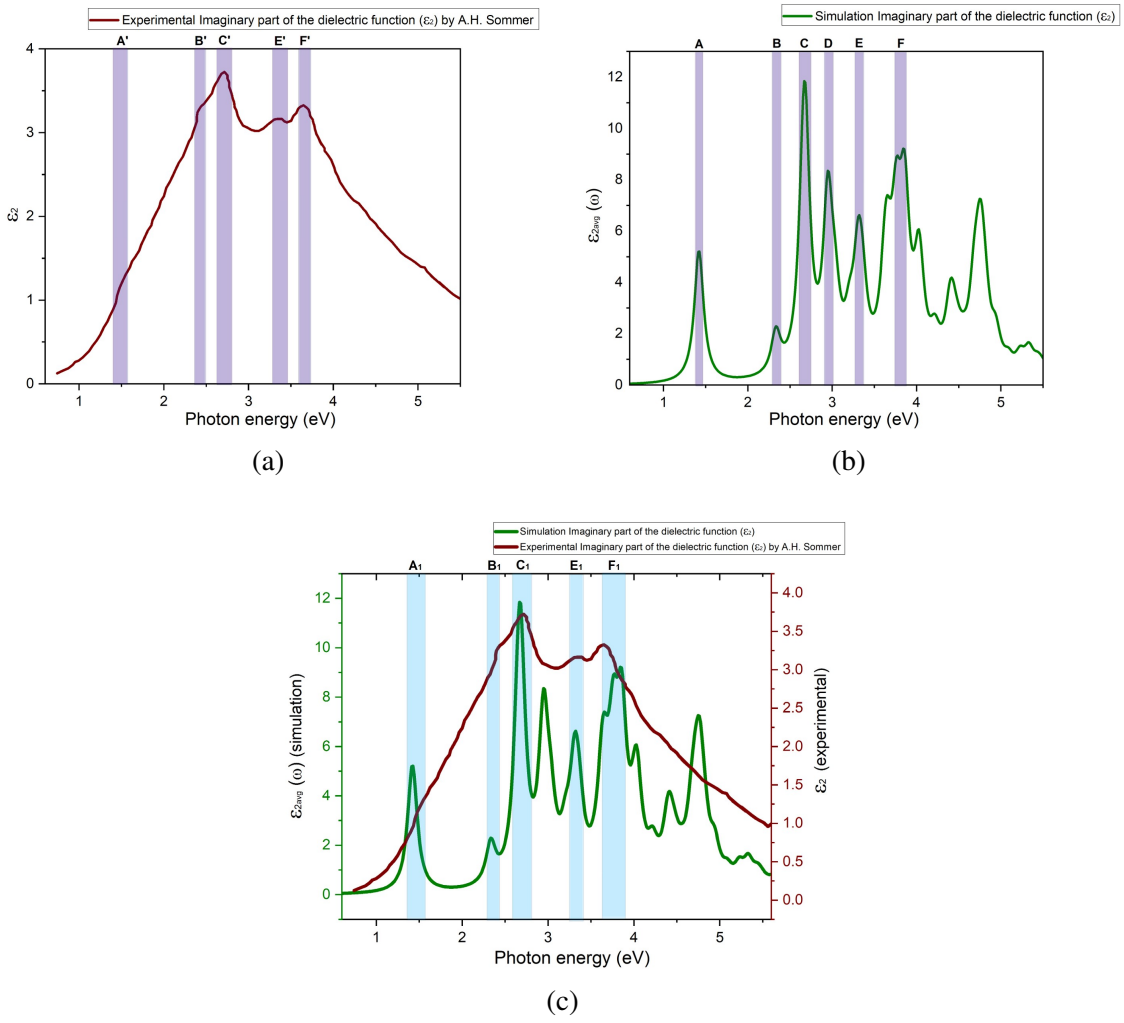

Figure 6.1: (a) presents the experimental imaginary part of the dielectric function (ε_2) of K_3Sb (cubic) compound as reported in reference [233], (b) DFT calculated imaginary parts of the dielectric function of K_3Sb (cubic) compound, as previously shown in Fig. 5.15a (c) depicts a comparison between the imaginary part of the dielectric function obtained experimentally (by A.H. Sommer [233]) and through simulation. The plot presented in this work has been generated with permission using data from reference [233].

The experimental measurements of the transmittance curve for the K_3Sb cubic compound, as obtained by Ebina and Takahashi et al. [233]), are presented in Appendix F.1.

Then, we compared our experimental results of lab-grown K-Sb compounds, including both thin and thick samples, with the K_3Sb (cubic) datasets. In this comparison, we examined the agreement between our experimental datasets and both DFT simulated results and literature experimental results. From this comparison, we observed that the peak characteristics of KSb-thin films are in good agreement with those of the K_3Sb (cubic) compound. While we also analyzed the peak characteristics of KSb-thick compounds, however, no such resemblance with the K_3Sb (cubic) compound was observed.

Figure 6.2a illustrates the experimental reflectivity of KSb (thin) films obtained from both the R&D system (thin films: KSb-1&2, and KSb-(NaKSb(Cs)-2)) and the Production system (thin film: KSb (KCsSb-137.3)) at LASA. Figure 6.2b illustrates the DFT calculated reflectivity of K_3Sb (cubic) compound, which has been previously presented in Section 5.5.3.1 (Fig. 5.15d). In Figure 6.2a, the first peak labeled A' appears in the near-infrared spectrum at 1.26 eV. Upon comparing with the DFT reflectivity plot (Fig. 6.2b), it can be inferred that the initial peak observed in the reflectivity spectrum corresponds to the fundamental absorption [53]. This absorption arises from the electron transitions between the valence band maximum and the conduction band minimum. Notably, this experimental value is closer to our DFT reflectivity results (Fig. 6.2b), where the first peak is observed at 1.40 eV. The following peaks, denoted as C' and F', were observed at energy levels of approximately 2.75 eV and 3.71 eV, respectively, in Figure 6.2a. Upon comparing these peaks with the corresponding DFT plots in Figure 6.2b, it becomes evident that the two prominent peaks observed in our KSb-thin reflectivity plot closely align with the DFT data. The corresponding peaks C and F appear at 2.67 eV and 3.89 eV, respectively, in the DFT plot. This similarity of the peaks with the DFT results and their reproducibility suggest the existence of similar absorption characteristics and electronic transitions in our experimental results. Nevertheless, the absence of peaks B', D', and E' in our experimental reflectivity plot (refer to Fig. 6.2a) compared to Figures 6.2b may be attributed to experimental variations, including factors such as sample thickness, stoichiometric variations, as well as limitations inherent in the measurement

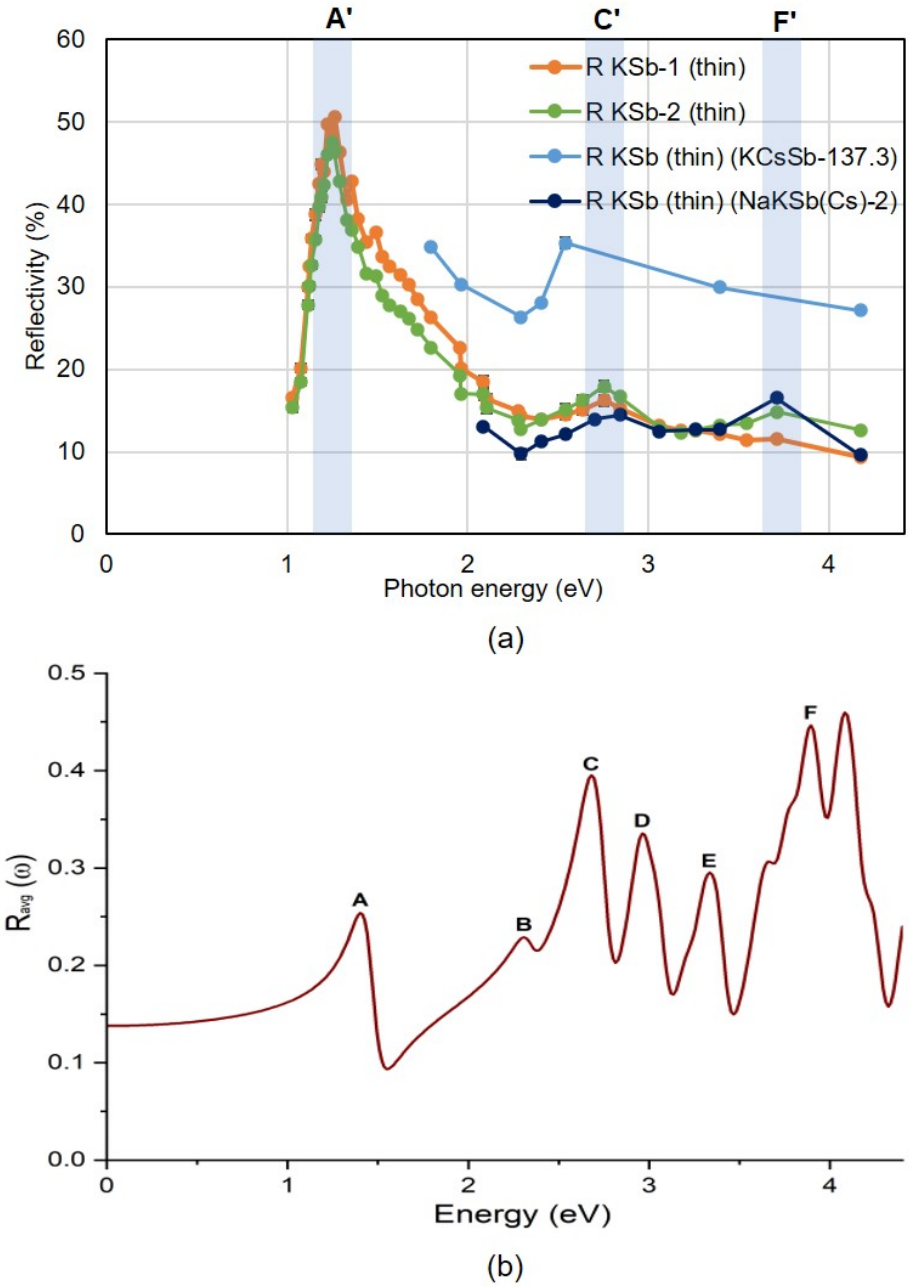

Figure 6.2: (a) experimental reflectivity data obtained from the KSb (thin) photocathodes produced in both the "R&D" and "Production" systems at LASA. The thin cathode KSb-(KCsSb-137.3) was produced in the new "Production" system, while the KSb-1&2 and KSb-(NaKSb(Cs)-2) thin films were produced in the "R&D" system [53]. Due to technical issues, the reflectivity for the KSb-(KCsSb-137.3) cathode was not measured across a wide spectrum. (b) the DFT-calculated reflectivity $R(\omega)$ of K_3Sb (cubic) compound (already been presented in Fig. 5.15d).

process, such as sensitivity or resolution issues.

We expanded our analysis by comparing our KSb-thin film data with literature results from A.H. Sommer [233]. Considering the interconnections between reflectivity and the imaginary part of the dielectric function peak characteristics [208], our study aims to compare the peak characteristics observed in the reflectivity data of our experimental KSb thin films with the corresponding dielectric function data of K_3Sb (Cubic) reported by A.H. Sommer [233]. In Fig. 6.3 such a comparison is presented.

As it can be seen in Fig. 6.3, there is a notable agreement between peaks A', C', and F' in both plots. In the dielectric function plot (ε_2), a shoulder (corresponding to peak A') is observed at 1.45 eV, which closely aligns with the experimental reflectivity value where the corresponding peak is seen at 1.26 eV. Additionally, peaks C' and F' are observed in the dielectric function plot (ε_2) at 2.75 eV and 3.65 eV. Upon comparison with the reflectivity plots, it was found that the peaks almost exactly match with each other (peaks C' and F' in the reflectivity plot appeared at 2.75 eV and 3.71 eV, respectively). This similarity confirms the presence of similar absorption characteristics and electronic transitions in our experimental data. Furthermore, the reproducibility of these peaks and their similarities with the reference data suggest that our KSb thin cathodes may exhibit a crystal orientation similar to that of a K_3Sb cubic structure. Upon comparing the band diagram plot (Fig. 5.12c), we can infer that the first pronounced peak at 2.75 eV likely arises from the electron transition between the highest level of the valence band and the lowest level of the conduction band. Similarly, the secondary peak at 3.71 eV can be attributed to the electron transition between the highest level of the valence band and the second-lowest level of the conduction band [233].

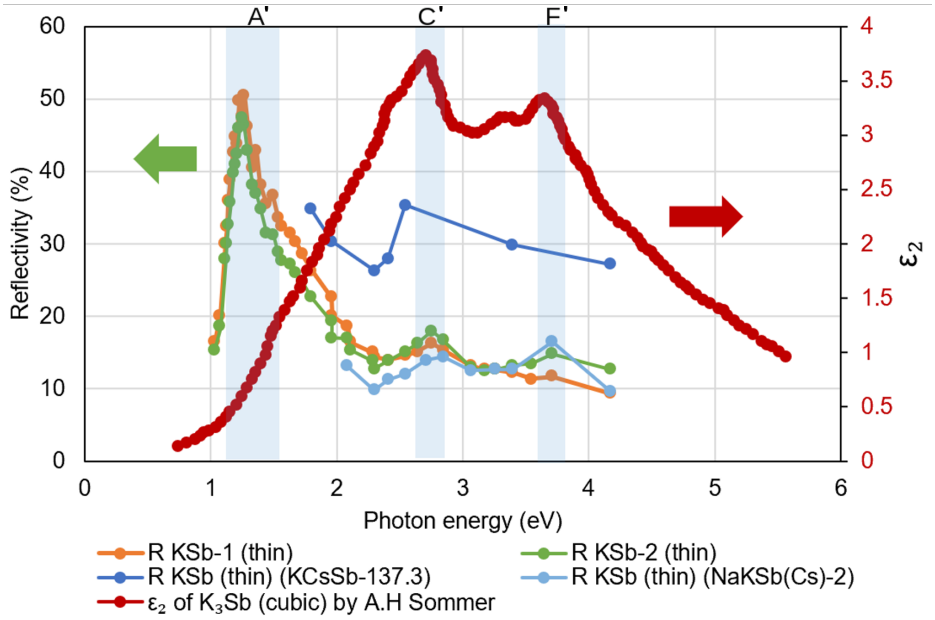

Figure 6.3: illustrates a comparison between the reflectivity data of KSb-thin cathodes produced at INFN and the imaginary part of the dielectric function (red color) of the K_3Sb (cubic) material as reported by A.H. Sommer [233]

As described, unlike the thin films, the peak characteristics observed in our lab-grown KSb-thick cathodes show no significant resemblance to the K_3Sb (cubic) data. Hence, we chose to compare and analyze the data for the K_3Sb (hexagonal) compound. The following section presents the relevant findings and discussions on this matter.

Similar to the K_3Sb (cubic) compound, to ensure the reliability of our DFT results we conducted a comparison between our DFT results and the experimental data presented in the literature. The experimental findings of the imaginary part of the dielectric function for the K_3Sb hexagonal compound were reported by Ebina and Takahashi et al. and A. H. Sommer [233], as shown in Figure 6.4a. The plot exhibits a series of peaks, with particular emphasis on two notable peaks at energy values of 2.24 eV (peak C') and 3.41eV (peak F').

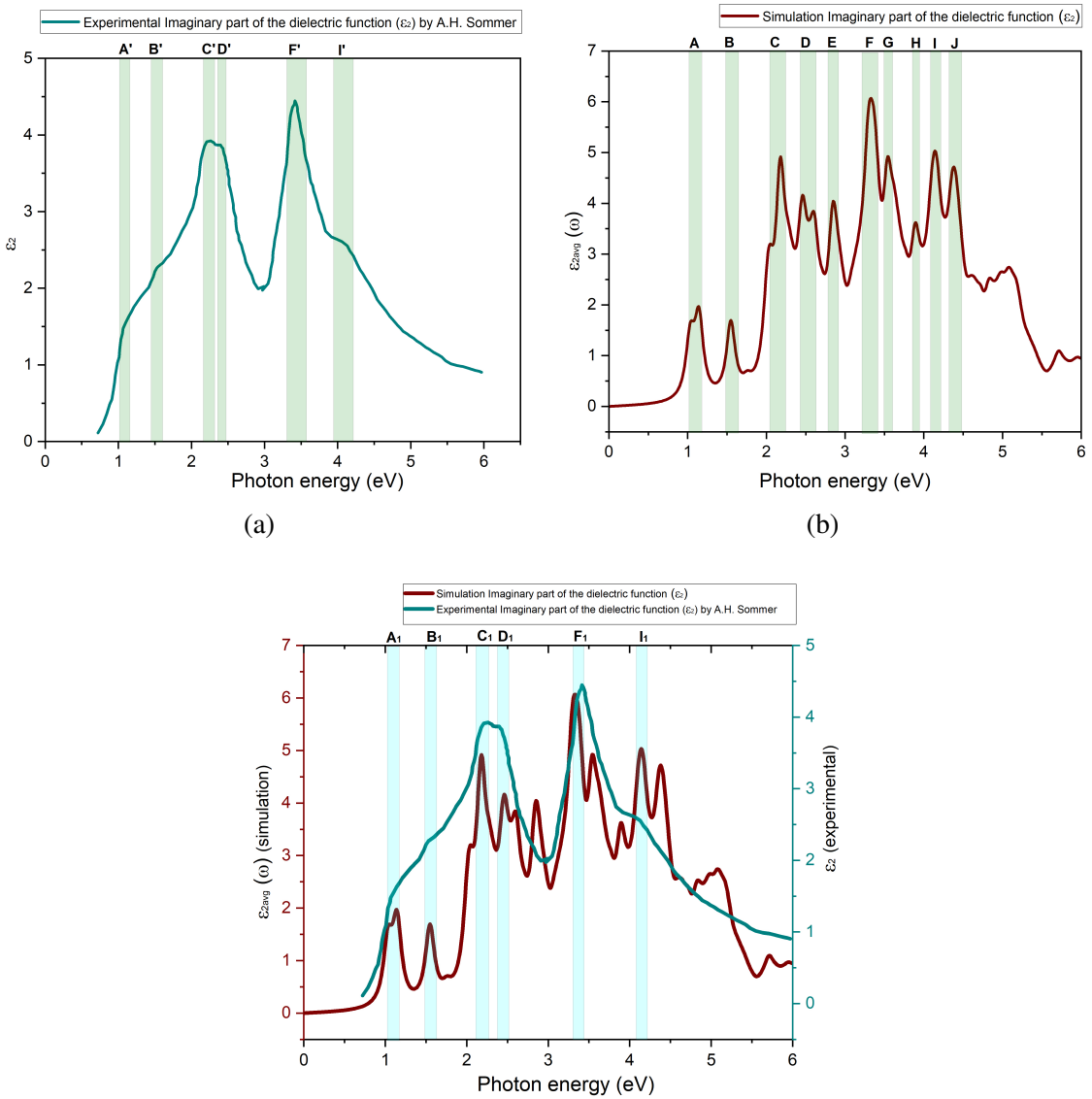

Figure 6.4: (a) presents the experimental imaginary part of the dielectric function (ε_2) of K_3Sb (hexagonal) as reported in reference [233], (b) the imaginary parts of the dielectric function of K_3Sb (hexagonal) obtained from DFT calculations, (c) depicts a comparison between the imaginary part of the dielectric function obtained experimentally (by A.H. Sommer [233]) and through simulation. The plot presented in this work has been generated with permission using data from reference [233].

This characteristic pattern closely resembles the peak distribution observed in the K_3Sb (cubic) compound (refer to Fig. 6.1). These peaks in Fig.6.4a are visually highlighted by a light green-colored box and labelled as A', B', C', D', F', and I'. The spectrum reveals the presence of a shoulder at 1.06 eV, labelled as A', which is followed by distinct peaks at 1.51 eV, 2.24 eV, 2.40 eV, 3.41 eV, and 4.08 eV. These peaks are denoted as B', C', D', F', and I', respectively. In Figure 6.4b, the imaginary part of the dielectric function obtained through DFT calculations is presented. As already reported in the DFT results section (Section 5.5.3.2.2, Fig. 5.19d), several peaks are observed at specific energy values in the simulated imaginary part of the dielectric function plot: 1.05 eV, 1.55 eV, 2.17 eV, 2.46 eV, 2.85 eV, 3.33 eV, 3.55 eV, 3.90 eV, 4.14 eV, and 4.38 eV (highlighted by a green-colored box). These peaks are labelled as A, B, C, D, E, F, G, H, I, and J, respectively. Figure 6.4c illustrates the comparison between the experimental (literature [233]) and simulated plots of the imaginary dielectric function. The peaks in both curves show a noticeable similarity, as depicted by the light blue-colored boxes highlighting the corresponding peaks. The agreement between the two plots validates the accuracy of the simulation and confirms the presence of specific electronic transitions or excitations in the material at those energy levels. However, it should be noted that the peak labelled E,G, and H in the simulated plot is not as visibly pronounced as it is in the corresponding experimental plot. This discrepancy could be attributed to certain limitations in the measurement process, such as sensitivity or resolution issues. However, it is intriguing to note the similarity between two prominent peaks between the simulation and experimental plots, specifically point C_1 and point F_1 in Fig. 6.4c. Notably, when calculating the ratio between these two peaks (i.e., between peak C_1 & F_1) observed in both simulated and experimental plots, the ratios exhibit similarity in both the simulated and experimental datasets. Additionally, upon observing Figure 6.4c, it becomes evident that both the experimental and simulated plots exhibit a local minimum occurring at a point close to 3 eV between the peaks C and F.

Similar to the comparison of dielectric function data, we also conducted a comparison of reflectivity data between experimental (literature) and DFT simulated datasets for the K_3Sb (hexagonal) compounds, which are presented in Appendix G.

Thereafter, similar to the process for KSb-thin cathodes, we conducted a comparative analysis to determine the crystal orientation of the KSb-thick cathodes. This involved comparing our experimental reflectivity data of KSb-thick with the data of the K_3Sb (hexagonal) compound. Based on our previous observation of a strong agreement between the experimental (literature [236]) and DFT simulation data of the K_3Sb hexagonal compound, we chose to directly compare our experimental reflectivity data with the available literature experimental data. Given the readily available reflectivity data of the K_3Sb hexagonal compound in the literature, we directly compared it with the reflectivity data of the KSb-thick cathodes to simplify the analysis. The relevant plot can be found in Figure 6.5. However, this comparison revealed that the two prominent peaks, namely D_1' (appeared at 3.06 eV) and F_1' (appeared at 4.67 eV), in our experimental KSb-thick plot do not closely correspond to the two peaks, D' (appeared at 2.42 eV) and F' (appeared at 3.52 eV), of the reference K_3Sb (hexagonal) plot. Hence, we could not determine if our KSb-thick films align with the hexagonal structure of K_3Sb. Unfortunately, at LASA, we have not measured the full spectral reflectivity for the KSb-thick cathodes. However, it is important to highlight that the local minimum (highlighted by the red dashed circle) in the reflectivity curve of K_3Sb (hexagonal), which appeared at approximately 2 eV, closely resembled the behavior observed in our KSb-thick cathodes, where the local minimum (highlighted by the red dashed circle) appeared at 1.96 eV.

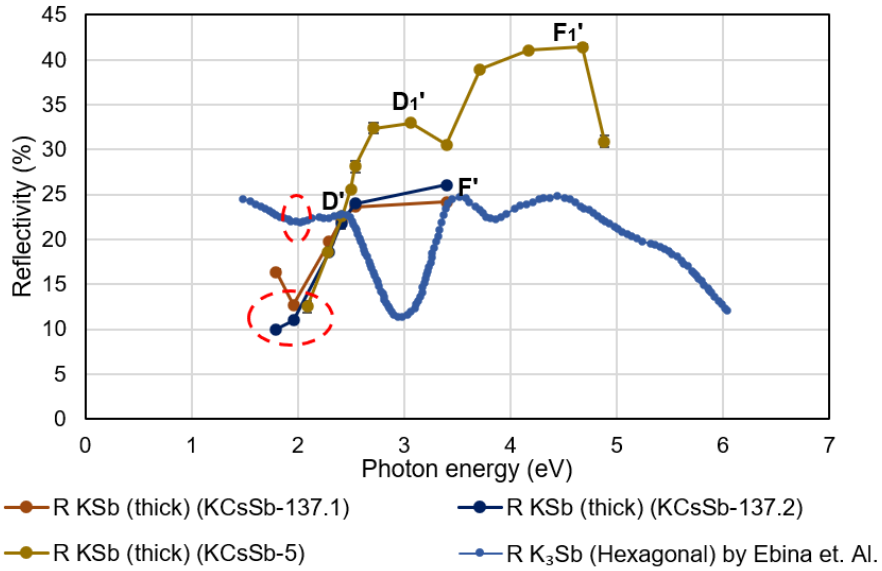

Figure 6.5: illustrates a comparison between the reflectivity data of KSb-thick cathodes produced at INFN and the reflectivity data of the K_3Sb (hexagonal) material as reported by Ebina and Takahashi et al. [236]. The thick KSb-(KCsSb-137.1) and KSb-(KCsSb-137.2) compounds were produced in the "Production" system while KSb-(KCsSb-5) was produced in the "R&D" system.

Thereafter, we compared the experimental reflectivity graphs of lab-grown thick and thin KSb cathodes to identify the discrepancies in their optical properties. As evident from Figure 6.6, a noticeable shift in the respective peaks (peaks D and F) can be observed between the two types of KSb cathodes (thick and thin). The peaks of KSb thick cathodes are observed to be shifted towards higher photon energy. If we examine the transmittance data (presented in Appendix F.3), we can observe a similar shift in the peaks within the transmittance curve between the cubic and hexagonal forms of K_3Sb compound. However, in the transmittance plot (Fig. 8.28), unlike our experimental reflectivity plot (Figure 6.6), the peaks of K_3Sb (cubic) are shifted towards higher photon energy. Furthermore, a noticeable shift in the local minimum (highlighted by red dashed circles) is observed between the two types of KSb cathodes (Figure 6.6). The local minimum points (highlighted by red dashed circles) appeared for KSb-thick and thin cathodes at around 1.96 eV and 2.29 eV, respectively. Considering the aforementioned data, it is evident that the observed shifts in peak positions between KSb thick and thin cathodes indicate potential

variations in composition or crystal structure between the two.

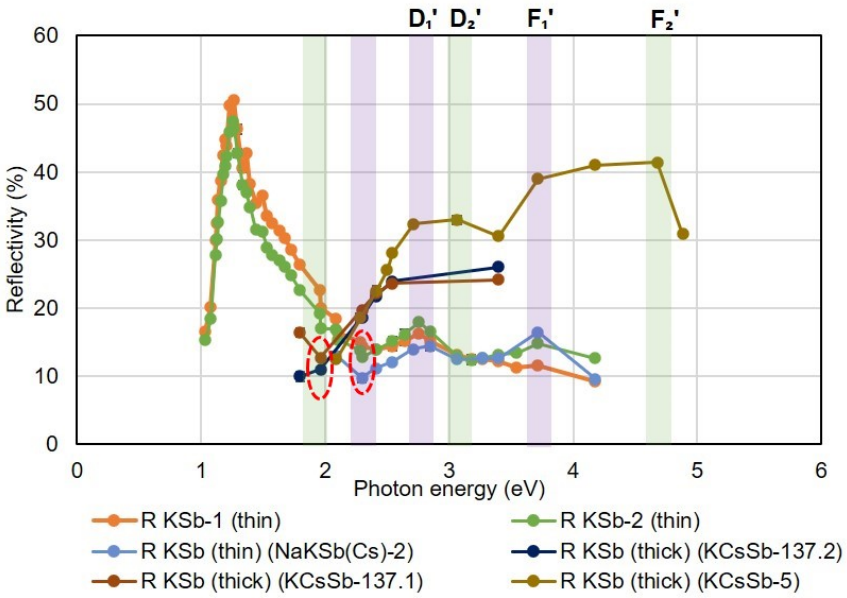

Figure 6.6: presents a comparative analysis of the reflectivity data obtained from the KSb-thick and thin cathodes. The similarities of peaks between the two graphs are highlighted using letters D, and F. Furthermore, these similar peaks are visually marked with different colored boxes, where violet-colored boxes represent the peaks in the KSb thin cathodes, and green-colored boxes represent the peaks in the KSb thick cathodes.

In summary of the aforementioned comparison, we deduce that the KSb-thin compound likely possesses a crystal orientation similar to that of K_3Sb cubic compounds. However, in the case of the KSb-thick compound, we were unable to conclusively establish its crystal orientation. The comparison of reflectivity between thick and thin KSb compounds suggests a potential difference in composition or crystal structure between the two.

Subsequently, we analyze the reflectivity data of KCsSb thin and thick cathodes in a manner similar to that of KSb cathodes.

6.1.2 K-Cs-Sb Compound

Based on numerous research findings, it is observed that the K-Cs-Sb compound, produced through sequential deposition, typically exhibits a multiphase polycrystalline material structure, as indicated by X-ray diffraction (XRD) studies [67, 135]. Modeling such a multiphase polycrystalline structure using DFT poses significant computational challenges due to the high computational cost involved in performing a large number of calculations [237,238]. Additionally, the lack of available data for the specific multiphase polycrystalline material compound presents significant challenges for accurate DFT modelling. Therefore, considering these limitations, the cubic phase of K_2CsSb emerges as a suitable alternative for computational analysis. While the cubic phase might not perfectly capture all aspects due to the potential presence of the hexagonal K_3Sb phase and the polycrystalline nature of the samples, it offers a simplified yet representative model for comparison with the experimental observations. Through comparison with experimental reflectivity data, our objective is to analyze the peak characteristics of grown K-Cs-Sb compounds and evaluate the similarity between the cubic phases. Furthermore, any observed differences can indicate the presence of polycrystallinity in the grown compound. In the following section, we begin with a comparative analysis between the experimental reflectivity of lab-grown KCsSb compounds and DFT-calculated reflectivity data. Subsequently, we compare peak characteristics between thin and thick lab-grown KCsSb cathodes.

In the analysis of peaks, we initially compared the experimental reflectivity of lab-grown thick and thin KCsSb cathodes with the DFT reflectivity results of the K_2CsSb (cubic) compound. Figure 6.8a & b depict the experimental reflectivity of KCsSb photocathodes produced in both the "R&D" system (thin: KCsSb-4, KCsSb-7, and KCsSb-8; thick: KCsSb-3 and KCsSb-5) and the "Production" system (thin: 123.1, 112.1, and 137.3; thick: 147.1 & 137.2) at LASA. Figure 6.8c depicts the DFT simulated reflectivity of the K_2CsSb (cubic) compound.

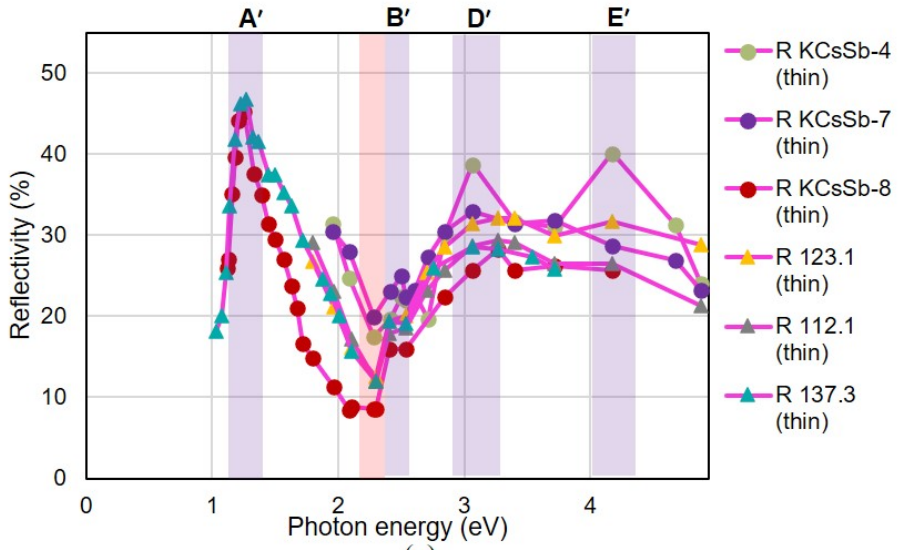
A′
B′
D′
E′
Reflectivity (%)
Photon energy (eV)
R KCsSb-4 (thin)
R KCsSb-7 (thin)
R KCsSb-8 (thin)
R 123.1 (thin)
R 112.1 (thin)
R 137.3 (thin)

(a)

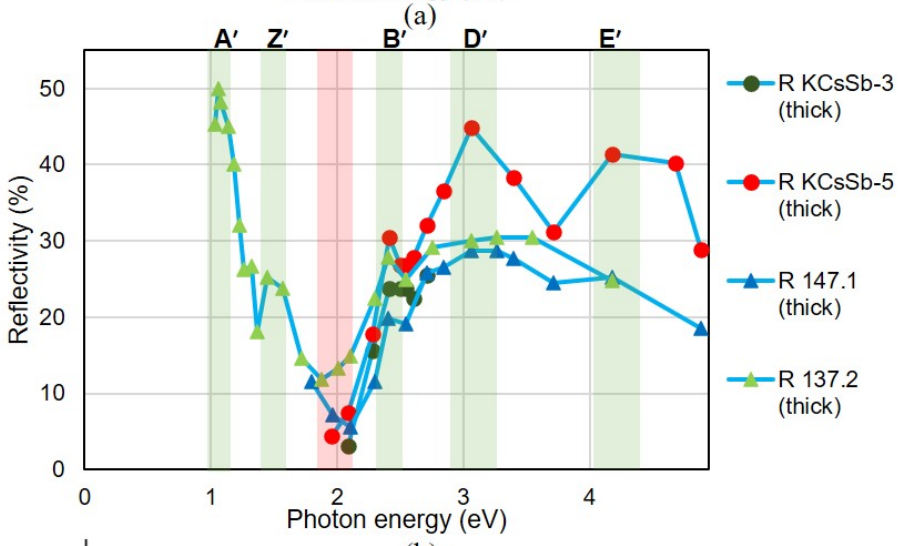
A′
Z′
B′
D′
E′
Reflectivity (%)
Photon energy (eV)
R KCsSb-3 (thick)
R KCsSb-5 (thick)
R 147.1 (thick)
R 137.2 (thick)

(b)

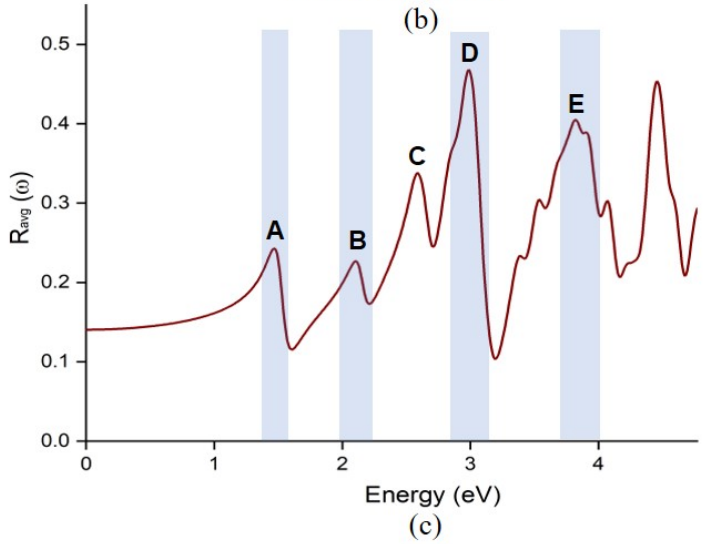
A
B
C
D
E
Ravg (ω)
Energy (eV)

(c)

Figure 6.8: presents a comparative analysis of the reflectivity data obtained from the lab-grown KCsSb (a) thin and (b) thick cathodes. Cathodes 123.1 (thin), 112.1 (thin), 137.3 (thin), and 147.1 (thick), 137.2 (thick) were produced in the new "Production" system [53]. Cathode KCsSb-4,7 & 8 (thin) and KCsSb-3,5 (thick) are produced in the "R&D" system. (c) DFT-calculated reflectivity ($R(\omega)$) for the K_2CsSb (cubic) compound, as previously presented in 5.7d, is shown here for comparison. The peaks are visually marked with different colored boxes, where violet-colored boxes represent the peaks in the KCsSb-thin cathodes, green-colored boxes represent the peaks of the KCsSb-thick cathodes, and blue-colored boxes represent the peaks of the DFT calculated K_2CsSb compound. In Fig. 6.8a, thin cathodes are highlighted by magenta lines, while in Fig. 6.8b, sky blue lines highlight thick cathodes. Due to some technical issues, the complete spectral reflectivity was only measured for the KCsSb-8 (thin), 137.3 (thin) & 137.2 (thick) cathodes.

In Figure 6.8a & b, the first peak labeled A' appears in the near-infrared spectrum. Upon comparing the DFT reflectivity results, it can be inferred that the onset of the reflectivity peak is associated with fundamental absorption, which involves electrons transitioning between the valence band maximum and conduction band minimum [53]. For thick cathode films (Fig. 6.8b), this peak occurs at an energy of 1.05 eV. However, for thin cathode films (Fig. 6.8a), the peak shifts to a higher energy of 1.22 eV. This discrepancy suggests the possibility of different band gaps in these two types of cathodes. Notably, this experimental value is closer to our DFT reflectivity plot (Fig. 6.8c), where the corresponding peak A appears at 1.46 eV. A further comprehensive analysis and interpretation of these findings are provided in the following part of this section. The subsequent peaks B', D', and E' were observed at energy levels of approximately 2.40, 3.06-3.26, and 4.17 eV, respectively, for both thin and thick cathodes in Figures 6.8a & b. In the DFT reflectivity plots, the corresponding peaks B, D, and E were observed at 2.10 eV, 2.98 eV, and 3.81 eV, respectively. Upon comparison, it becomes evident that the peaks observed in the experimental reflectivity plot (Fig. 6.8a & b) exhibit a reasonable agreement with the DFT reflectivity results of the K_2CsSb (cubic) compound, as presented in Fig. 6.8c, especially for peaks B, D, and E.

Despite the experimental reflectivity data showing some similarities with the DFT reflectivity datasets, notable differences are observed between the two types of KCsSb cathodes (i.e., thick and thin) within the 1 to 2.3 eV frequency range of the spectral

reflectivity (Fig. 6.8a & b). Therefore, to identify the differences, we compared the experimental reflectivity between the KCsSb thick and thin cathodes, shown in Figure 6.8a & b.

As observed, there is a difference in the near-infrared region, particularly in the first peak (A') between the two types of cathodes. As described earlier, the first peak appears at 1.05 eV for thick cathodes, whereas for thin cathodes, it occurs at 1.22 eV. Through comparison with the DFT results, it is inferred that there may be different band gaps present in these two types of cathodes.

Then, we noticed that the second peak (Z') is exclusively present in the thick cathodes (Fig. 6.8b) at around 1.44 eV and absent in the thin cathodes. This observation strongly suggests the presence of potential differences in crystal structure or compositional variations between the two types of KCsSb cathodes. If we compare with the data of the K_3Sb hexagonal DFT reflectivity data (Fig. 5.19d), such an intermediate peak is there at around 1.51 eV. As per the XRD study conducted by Schubert et al. [67], the K_3Sb film produced through the sequential deposition process typically exhibits a combination of both cubic and hexagonal phases. Then, during the deposition of Cs to form a K_2CsSb compound, Cs rapidly reacts with the cubic phase of K_3Sb, while the reaction with the hexagonal phase of K_3Sb occurs at a later stage [239]. This is because the hexagonal K_3Sb structure is more stable and undergoes a more difficult transformation to convert into the K_2CsSb structure. The dissimilarity in the transformation of the two K_3Sb phases can be elucidated by examining their crystal structures. When transitioning from cubic K_3Sb to cubic K_2CsSb, one K-atom must be replaced by cesium, a process relatively simpler due to the less compact arrangement of the cubic lattice. However, in the case of the closely packed hexagonal lattice of K_3Sb, this transformation becomes more challenging. Also, in the cubic phase, there is typically a natural deficiency of alkali atoms, which makes it easier for Cs atoms to be incorporated during the transformation to K_2CsSb [240]. On the other hand, transforming the hexagonal structure involves not only replacing atoms but also disrupting a highly stable crystal structure and forming a new one. As a result, the conversion of K_3Sb (hexagonal) to K_2CsSb is less favorable compared to the cubic structure. Consequently, due to the difficulty in this conversion process, some remnants of the K_3Sb

hexagonal structure are expected to remain unreacted in the final K_2CsSb compound, as observed in the XRD studies [67]. Therefore, the presence of the observed second peak (Z') may be attributed to the potential existence of the KSb hexagonal structure in the KCsSb thick cathodes or to the bulk modification of the crystal structure.

As described in Chapter 4 (Section 4.4.6), the spectral reflectivity plots for the two cathodes—thick (137.2) and thin (137.3)—reveal that the most significant changes occur during the addition of potassium (K). However, during the Cs addition, the spectral reflectivity behavior shows only minor changes (in shape), which can be considered as a continuation of the reflectivity behavior observed after the K deposition. This observation aligns with the findings from the XRD study, which indicates that the major change in the crystal structure happens during the K addition [67]. The interaction between the Sb film and K vapour involves a redox reaction, resulting in the formation of K_3Sb compounds. During the process of Cs addition, the Cs atoms, which have a larger ionic radius compared to K atoms, replace the K atoms, resulting in the formation of a K_2CsSb compound.

Upon analyzing the local minimum (highlighted by red colored boxes) in Fig. 6.8a & b, we observed that for KCsSb-thick cathodes, the local minimum appeared in the range of 1.87-2.08 eV (Fig. 6.8b), while for KCsSb-thin cathodes, it occurred at around 2.29 eV (Fig. 6.8a). Interestingly, when we compare the reflectivity plots of KSb films in Fig. 6.6, we notice the presence of similar local minimum at the similar energy points for both thick and thin KSb films, just like in the case of KCsSb cathodes. This observation provides another indication that some of the reflectivity behavior observed after the K deposition continues even after the Cs deposition. However, upon comparing certain major peaks, specifically peak D' and E', in both KCsSb thick and thin cathodes in Fig. 6.8a & b (D', E' for thick and thin KCsSb appears at around 3.06-3.26 eV and 4.17 eV, respectively), with corresponding peaks D' and F' in KSb thick and thin cathodes in Fig. 6.6 (D', F' for KSb-thick appears at around 3.06 eV and 4.67 eV and corresponding D', F' for KSb-thin appears at around 2.75 eV and 3.71 eV), it is evident that there is a shift in these peak positions between KSb and KCsSb. The observed shift in peak positions can be attributed to the distinct electronic structures between the KSb and KCsSb cathodes, signifying the formation of KCsSb cathodes from the initial KSb film. This shift in peaks

reflects changes in the material's optical properties, highlighting the transformation and the differences in the electronic band structures during the conversion process from KSb to KCsSb.

Then, upon analyzing the peak B' in Fig. 6.8a & b, in both KCsSb thick and thin cathodes, we observed that it appears at the same position, approximately 2.40 eV. However, for thick cathodes, usually, this particular peak is more pronounced compared to thin KCsSb cathodes. This observation can also be seen in Fig. 4.56 for thick and thin KCsSb cathodes.

Then, we compared the following peaks, namely D' and E', for both thick and thin KCsSb cathodes (Fig. 6.8a & b). Upon examination, we found that both peaks are nearly identical in position for both thick and thin KCsSb cathodes.

Afterward, we also analyzed the spectral response data of KCsSb (thick and thin) cathodes, as illustrated in Figure 6.9. As can be seen, there is a sharp increase in the slope of the quantum yield above a threshold energy of $\sim$ 1.8-1.9 eV observed in the plot. This sharp threshold indicates that both cathodes possess a direct band gap. Furthermore, the observed sharp threshold in the spectral response data also suggests a finite width of the valence band (VB), indicating a narrow valence band. This can be supported by referencing the DFT band structure plot (Fig.5.4c) of the K_2SbCs compound, where the width of the valence band is approximately 1.25 eV (page 182). Based on these observations, it can also be inferred that both the thin and thick KCsSb compounds do not exhibit a Cs_2KSb structure. This conclusion is supported by the fact that Cs_2KSb is known to be an indirect gap semiconductor (Section 5.5.2, page 189). For indirect gap semiconductors, a sharp increase in the photoemission threshold is not typically observed (often leading to a gradual increase rather than a sharp threshold) due to the nature of their band structure [241, 242]. The presence of a sharp threshold in the spectral response plot for both thick and thin KCsSb cathodes contradicts the behavior expected for an indirect gap semiconductor like Cs_2KSb. Therefore, our findings strongly suggest that both thin and thick KCsSb compounds exhibit direct band gaps, further supporting their distinct crystal structures.

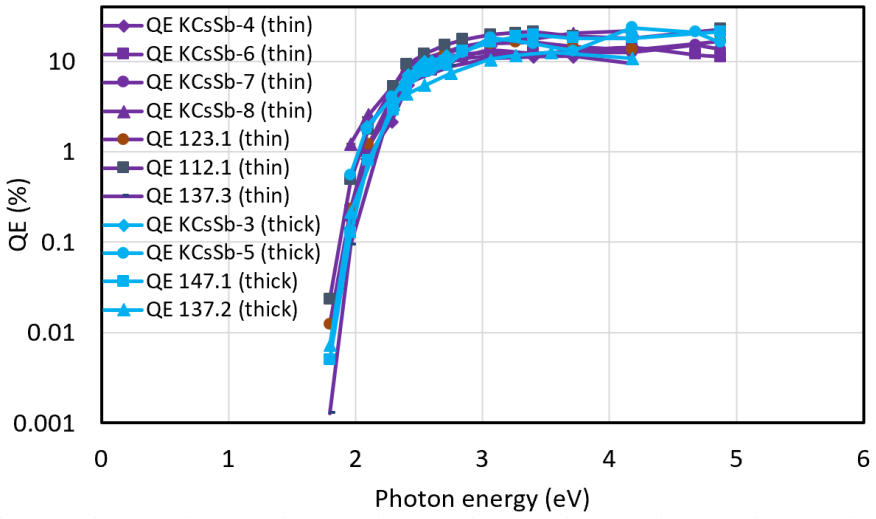

Figure 6.9: presents the spectral response of all K-Cs-Sb cathodes produced in both the "R&D" and "Production" systems. The spectral response of thin and thick cathodes is highlighted in violet (with different symbols and colors) and light sky (with different symbols) color lines, respectively.

6.1.3 Summary & Discussion

As described in the above section, significant similarities were observed in the optical data between our experimental and DFT datasets, particularly in the reflectivity, which closely corresponded to the definite crystal structures of K_3Sb and K_2CsSb compounds. These similarities suggest that the observed peaks are likely not significantly influenced by other factors, such as interference effects, at least within the studied energy range, but rather arise from the electronic structure of the materials. The reproducibility of these peaks, associated with their specific crystal structures (K_3Sb and K_2CsSb), further supports this argument. Furthermore, it is important to note that interference effects typically result in a periodic gap between the observed peaks in reflectivity data (a regular pattern of alternating peaks and crests in the reflectivity data as a function of wavelength). However, upon analyzing our reflectivity data, we found no such periodic gap between the peaks. This significant observation strongly suggests that interference effects have minimal influence on our reflectivity results.

As discussed in the preceding section, there is a similarity of the reflectivity peaks between KSb-thin and K_3Sb (cubic) compounds. However, in the case of the KSb-thick films, the reflectivity peaks do not align with the simulation and reference experimental data of K_3Sb (hexagonal) compound. Nevertheless, intriguingly, we observe certain similarities, such as the appearance of the local minimum around 2 eV for KSb-thick cathodes, which closely resembles the points seen in the reference experimental data (see Fig. 6.5). As discussed earlier, XRD studies reveal that the K_3Sb film produced through the sequential deposition process typically exhibits a combination of both cubic and hexagonal phases [67]. Therefore, based on this observation, it can be deduced that the similarities between KSb-thin films and the cubic phase of K_3Sb suggest a larger proportion of cubic crystal orientation present in our KSb-thin films compared to hexagonal or other phases. Likewise, in the case of KSb-thick cathodes, there may exist a different proportion of hexagonal, cubic, and other phase crystal orientations (unlike KSb-thin compounds). This difference in crystal orientation could be the reason why we have observed a different spectral reflectivity for the two types (thick and thin) of KSb compounds for cathodes 137.2 (thick) and 137.3 (thin), as described in Chapter 4 (Section 4.4.6).

Upon analyzing the reflectivity data of the KCsSb compounds (thick and thin) with the K_2CsSb (cubic) DFT results, certain similarities between the two datasets are evident, suggesting the presence of cubic orientations in the KCsSb compounds. However, notable differences are observed between the two types of KCsSb cathodes (i.e., thick and thin) within the 1 to 2.3 eV frequency range of the spectral reflectivity. These differences, especially the varying onset points in the reflectivity spectra, hint at potentially different band gaps for the two types of cathodes. Moreover, the presence of an additional peak (peak Z') in the thick cathodes (see Fig. 6.8) further supports the hypothesis of different crystal orientations between the thick and thin KCsSb cathodes. Furthermore, comparing the spectral reflectivity results of the KCsSb compound with the KSb compound also reveals similarities in characteristics, albeit with shifts in peak positions. As discussed earlier, the XRD study indicates that when Cs is deposited on the KSb compound, Cs reacts more favorably with the cubic-type of K_3Sb compound compared to K_3Sb hexagonal compound, resulting in a portion of K_3Sb hexagonal compound remaining unreacted in

the final K_2CsSb compound [239]. As described above, both thick and thin KSb films likely possess varying ratios of cubic, hexagonal, and other phases. Therefore, the differences in spectral reflectivity between our thick and thin KCsSb cathodes may be attributed to the varying proportions of cubic, hexagonal, and other mixed phases present in the final KCsSb compound of each type. These differences in phase composition are likely a consequence of the underlying KSb compound phases, suggesting that the thickness of the film could influence the crystal orientation and, consequently, the optical properties.

However, to gain a more comprehensive understanding of the underlying mechanism, further surface characterization is required to investigate and elucidate the detailed structural differences and their impact on the optical properties. Moreover, additional investigation is necessary to determine the nature of the semiconductor in both types of cathodes, specifically whether they exhibit p-type or n-type characteristics. Such findings would be highly valuable in facilitating and optimizing the design of heterostructure-type depositions.

6.2 Comparison and Discussion of Simulation and Experimental Results for NaKSb Compounds

In a similar manner to previous studies on KSb and KCsSb compounds, we have conducted a comparative analysis of the DFT simulation results with the experimental data of Na_2KSb compound. Initially, to validate the accuracy of the DFT simulations, we compared the simulated results with the existing experimental data in the literature for the Na_2KSb compound. Subsequently, these datasets were compared with the experimental results obtained from our in-house lab-grown NaKSb cathodes. The following sections present the relevant findings and discussions.

The experimental findings of the imaginary part of the dielectric function for the Na_2KSb compound were reported by Ebina and Takahashi et al. [233], as shown in Figure 6.10a. The plot reveals multiple peaks, including two prominent peaks at 3.06 eV (peak B') and 4.81 eV (peak D'). These peaks are visually highlighted by a green-colored box and labeled as A', B', D', and E'. A shoulder appeared at 1.36 eV, referred to as A', followed by peaks at 3.06 eV (denoted as B'), 4.81 eV (D'), and 5.25 eV (E'). In Figure 6.10b, the imaginary part of the dielectric function obtained through DFT calculations is presented. As presented earlier in the DFT results section (Fig. 5.23a), several peaks are observed at specific energy values in the simulated imaginary part of the dielectric function plot: 1.49 eV, (group of three peaks: 2.80 eV, 3.18 eV, 3.55 eV), 4.07 eV, 4.55 eV and (group of two peaks: 5.16 eV,5.36 eV); highlighted by a green-colored box. These peaks are labeled as A, B (group of three peaks), C, D, and E (group of two peaks), respectively. The combination of three peaks (B) and two peaks (E) within a single box allows for a more straightforward comparison with the experimental plot, as the multiple peaks are not as prominently visible in the experimental data.

Figure 6.10c illustrates the comparison between the experimental (literature) and simulated plots of the imaginary dielectric function. The peaks in both curves show a noticeable similarity, as depicted by the light blue-colored boxes highlighting the corresponding peaks. The agreement between the two plots validates the accuracy of the simulation and confirms the presence of specific electronic transitions or excitations in the material at

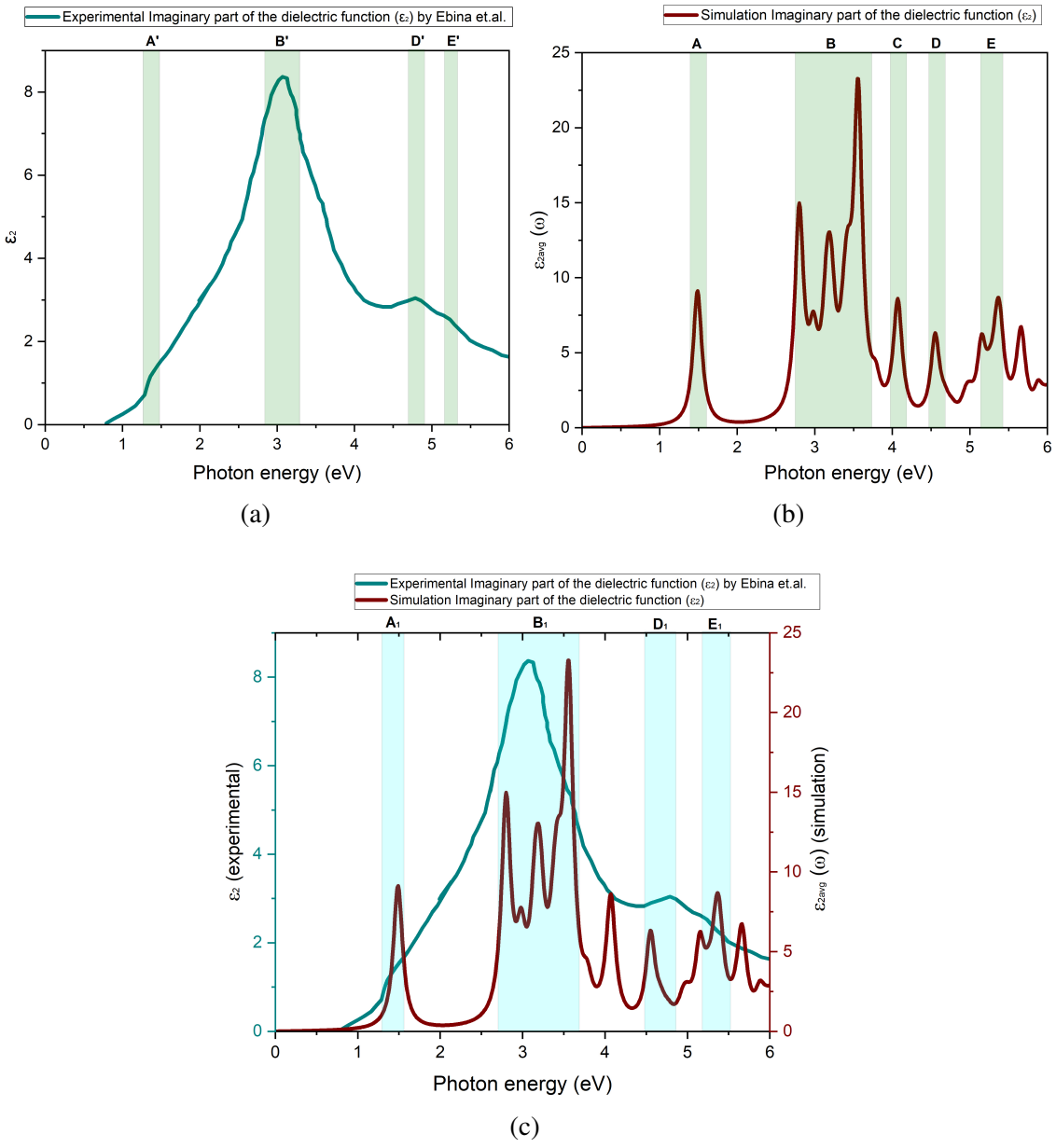

Figure 6.10: (a) presents the experimental imaginary part of the dielectric function (ε_2) of Na_2KSb as reported in reference [233], (b) the imaginary parts of the dielectric function of Na_2KSb obtained from DFT calculations (c) depicts a comparison between the imaginary part of the dielectric function obtained experimentally (by Ebina et.al. [233]) and through simulation. The plot shown in (a) of this study has been replotted with permission using data from reference [233].

those energy levels. Nevertheless, a marginal deviation is observed in the simulated plot, particularly for the peaks labeled A_1, B_1, and D_1, when compared to the experimental plot in Fig. 6.10c. Also, it should be noted that the peak labeled C in the simulated plot is not as visibly pronounced in the experimental plot. This discrepancy could be attributed to certain limitations in the measurement process, such as sensitivity or resolution issues. However, it is intriguing to note the similarity between three peaks—points A_1, B_1, D_1, and E_1—in both the experimental (literature) and DFT plots. Regarding peak B_1, in the experimental dielectric function plot (Fig. 6.10c), a single peak is observed (nearly at 3.06 eV). However, upon analyzing the experimental transmittance data of the same film, as presented in the reference paper [233] (also depicted in Fig. 6.11), two peaks (i.e., at 3.25 eV and 3.56 eV, highlighted by red dashed circles) are observed within the corresponding energy range of peak B_1 in the transmittance plot. Upon comparison with our DFT imaginary dielectric function plot (Fig. 6.10b) with Fig. 6.11, we can observe a good agreement of these peaks, especially in the section corresponding to peak B (group of three peaks: appeared at energy level of 2.80 eV, 3.18 eV, 3.55 eV) in plot 6.10b, as compared to the B' peak (group of two peaks: appeared at energy level of 3.25 eV, 3.56 eV) in plot 6.11. The doublet peak (peak B') in the transmittance curve might be attributed to the spin-orbit splitting [233]. As a point of reference, the transmitted curve (Fig. 6.11) displays several peaks at distinct energy values: 1.40 eV (Peak A'), a group of two peaks: 3.25 eV and 3.56 eV (Peak B'), 4.86 eV (Peak D'), and 5.25 eV (Peak E').

Figure 6.12 illustrates the experimental reflectivity of our NaKSb films (NaKSb-1) obtained from the "R&D" system at LASA. Then, a comparison was made between the experimental reflectivity results from our NaKSb films and the experimental results of Na_2KSb with a cubic orientation conducted by Ebina et al. [233], as well as with the DFT results. The main aim of this comparison is to comprehend the underlying origin of the observed peaks in the reflectivity curves of our NaKSb cathode. However, since we only have spectral reflectivity data for one NaKSb film (i.e., NaKSb-1 cathode), the reproducibility of the observed peaks in our experimental plot (Fig. 6.12) could not be verified. In the future, the reproducibility of the peaks will be assessed in subsequently produced NaKSb films. For reference, as detailed in Section 4.3.3.1, the NaKSb-1 cathode

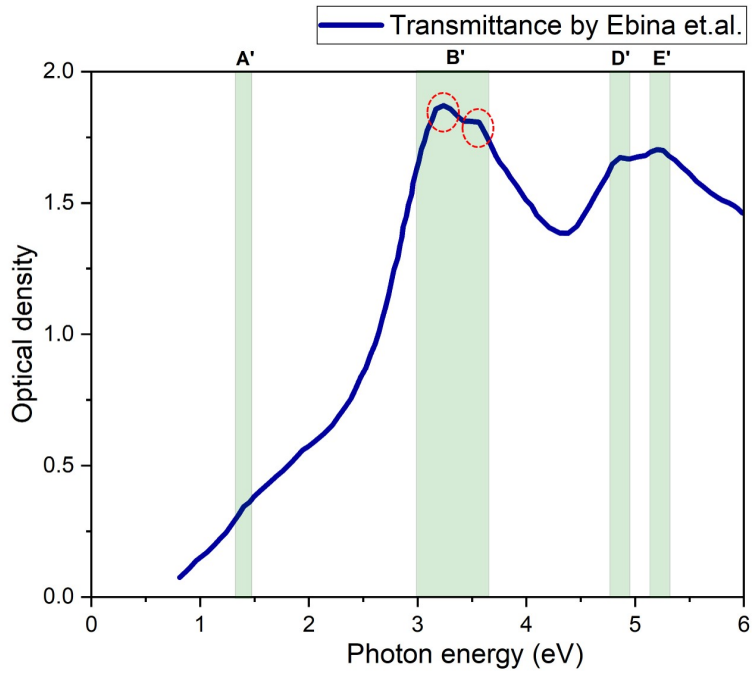

Figure 6.11: Transmittance curve of the Na_2KSb compound. The plot presented here has been recreated with permission using data from reference [233].

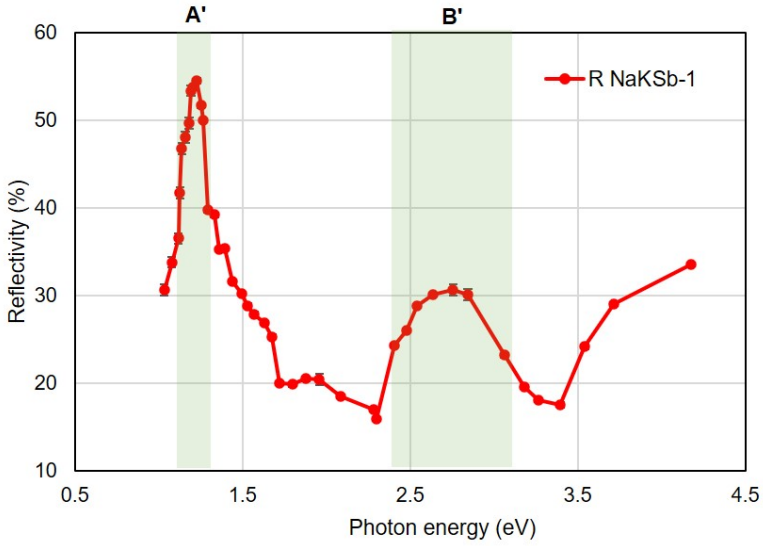

Figure 6.12: Experimental reflectivity data obtained from the NaKSb-1 photocathode fabricated in the "R&D" preparation systems at LASA.

was produced on the KSb-2 film.

Considering the interconnections of the peaks between reflectivity and the imaginary part of the dielectric function, like it was done for KSb cathodes (Section 6.1.1.1, pages 222-223), we compare the peak characteristics observed in our reflectivity data of NaKSb film with the dielectric function data of the Na_2KSb film reported by Ebina et al. [233], shown in Fig. 6.13.

In Figure 6.13, the first peak labeled A_1 appears in the near-infrared spectrum at 1.22 eV in the reflectivity plot of the NaKSb compound. By comparing with DFT results (Fig.5.23d), it can be inferred that the initial peak observed in the reflectivity spectrum potentially corresponds to the fundamental absorption. This absorption arises from the electron transitions between the valence band maximum and the conduction band minimum. The corresponding peak A appeared in the DFT reflectivity plot at 1.48 eV (Fig.5.23d), whereas in Ebina's results, the corresponding peak appeared at around 1.36 eV in the imaginary dielectric function (ε_2) plot (Fig.6.13).

Furthermore, in Figure 6.13, a noticeable shift is evident for peak B_1 between the reflectivity of the NaKSb-1 sample and the imaginary dielectric function of the Na_2KSb compound. This observed discrepancy may be attributed to variations in the stoichiometric or chemical composition of our produced NaKSb film. Nonetheless, as mentioned earlier, to gain a more comprehensive understanding and assess the reproducibility of these peaks in our experimental reflectivity plot, they will be further evaluated in future productions of NaKSb films.

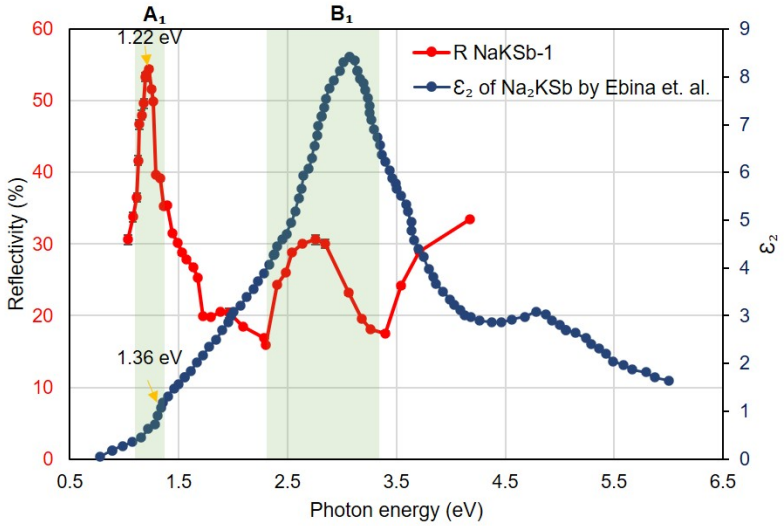

Figure 6.13: Comparison between the reflectivity data of the NaKSb-1 cathode produced at INFN and the imaginary part of the dielectric function (ε_2) of the Na_2KSb material as reported by Ebina et.al. [233]. The imaginary part of the dielectric function (ε_2) plot presented here has been recreated with permission using data from reference [233].

Chapter 7

Conclusions

7.1 Summary

This study concentrated on the application of high QE alkali antimonide photocathodes as electron sources for high-brightness RF photoinjectors. However, this presented challenges such as developing a reliable cathode deposition process, handling the highly reactive cathode surface under ultra-high vacuum conditions, and maintaining the required surface quality for both the substrate and cathode material to meet the photoinjector's specifications.

In this dissertation, comprehensive insights into the growth procedures of all produced photocathodes within both the "R&D" and "Production" preparation systems at INFN LASA in Milan, Italy are provided. A reproducible recipe using the three-step sequential method has been developed in the "R&D" preparation system. The influence of temperature, deposition rate, and thickness on the properties of the photocathode has been investigated and discussed. It has been observed that the substrate temperature played a crucial role in the formation of the cathode film and affected its photoemissive and optical properties. Notably, we've observed that varying the deposition rate can enhance quantum efficiency, particularly for the K-Sb films, as discussed in Chapter 4. The effects of laser heating and substrate temperature on cathode degradation are briefly discussed, revealing that laser heating has no impact on cathode lifetime. In addition, we also studied

the NaKSb and NaKSb(Cs) photocathode materials, and a preliminary cathode recipe has been established. The study on NaKSb(Cs) shows that these photocathodes can survive for several years inside the vacuum chamber (pressure of 10^{-11} mbar). Stopping potential studies were also conducted on the produced cathodes inside the "R&D" preparation system (Appendix A).

A newly dedicated preparation system has been built to enable the deposition of alkali antimonide films onto INFN Mo plugs for testing in the PITZ RF gun. The first batch of three KCsSb cathodes was produced at INFN LASA and successfully transported and tested in a high-gradient RF gun at PITZ. These cathodes' performance was compared to the previously utilized Cs_2Te photocathodes, revealing that the thermal emittance and response time are quite good in comparison. Notably, the overall emittance was reduced by approximately 23%, and the 4D brightness was increased by up to 60% for KCsSb cathodes compared to Cs_2Te. However, challenges include a high dark current and a short operational lifetime. During cathode conditioning in the RF gun, observations were made that raising the cathode gradient beyond 30-40 MV/m resulted in a higher number of vacuum trips compared to past Cs_2Te cathode conditioning. These vacuum events significantly contribute to the rapid QE degradation of these KCsSb photocathodes. Additionally, a higher dark current was observed from these KCsSb photocathodes compared to the Cs_2Te photocathodes, primarily due to the low photoemission threshold of these cathodes. The post-usage analysis done at LASA revealed varying degrees of contamination of these used cathode films.

To further optimize and gain a deeper understanding of the photoemissive film properties, two KCsSb cathodes with varying thicknesses were deposited using the new 'multi-wavelengths' diagnostic setup in the "Production" system. Upon analyzing the optical spectra, it was evident that a significant difference in spectral reflectivity arose for KSb compounds (thick and thin). The spectral reflectivity pattern for the KCsSb compound continued the observed behavior for the KSb compound (with slight modifications) for both cathodes. Furthermore, we also noticed variations in the final spectral reflectivity of these two cathode types.

In order to interpret these optical results, a density functional theory (DFT) study

was conducted for K_3Sb, K_2CsSb, Cs_2KSb, and Na_2KSb compounds, focusing on their electronic and optical properties. The optical properties such as dielectric function, reflectivity, refracting index, and extinction coefficient have been evaluated. A comparison study was made between the DFT-calculated reflectivity of K_3Sb, K_2CsSb, and Na_2KSb compounds and the reflectivity obtained experimentally for KSb, KCsSb, and NaKSb compounds. Significant similarities were observed between the two data sets. These similarities suggest that the observed peaks are likely to arise from the electronic structure of the materials not significantly influenced by other factors, such as interference effects. Moreover, this analysis indicated the potential presence of different crystal structures in thick and thin KCsSb cathodes. However, these results should be substantiated through additional material characterization techniques, such as X-ray photoelectron spectroscopy (XPS) and X-ray diffraction (XRD).

By analyzing optical spectra, particularly spectral reflectivity, and comparing them with theoretical models (DFT results), we have developed a valuable method for predicting the electronic structure of the grown compound. This approach can be further incorporated into the automated growth process to produce these types of cathodes [243]. The portability and convenience of these optical setups for in-situ measurements make them particularly advantageous. However, optical measurements, such as spectral reflectivity and spectral response, offer an indirect method for analyzing a material's electronic structure. As described in the dissertation, validating these findings necessitates additional comparisons with theoretical models and further verification through spectroscopic results. In the future, if material characterization techniques, such as XPS and XRD studies, establish a clear relationship between the evolving crystal structure of these photocathodes during growth and the observed changes in optical spectra (spectral response and reflectivity), it may enable fine-tuning the cathode recipe to achieve a monocrystalline cathode structure.

7.2 Outlook

The upcoming batch of KCsSb photocathodes is planned to be produced at INFN LASA and subsequently subjected to testing at PITZ in the near future. The performance of these newly produced cathodes will undergo analysis, and any identified limitations will drive further efforts to optimize and improve the cathode recipe. Notably, our study has observed significant variations in the spectral reflectivity pattern after the transition point during potassium (K) addition for both thick and thin KCsSb cathodes, which likely stem from crystal structural differences between these two KSb compounds. Therefore, we have planned to stop the K deposition precisely at this transition point for both types of cathodes in the new recipe for the forthcoming production cycle of KCsSb cathodes. This approach aims to achieve a more uniform crystalline structure across the cathodes [67], thereby enabling a focused study on how this uniformity affects the photocathode's lifetime.

Moreover, in the future, it is essential to conduct more comprehensive studies on cathode degradation, such as exploring different setup temperatures, residual gases, and other factors, in order to gain insights into the reasons for degradation within the gun and ultimately enhance the longevity of these cathodes in this environment.

In the future, it is planned to explore the use of a new deposition method, specifically the two-step alkali co-evaporation process, for producing these photocathodes. These results should then be compared to those of the cathodes currently created using the sequential method.

Further efforts are required to establish a reliable recipe that can consistently achieve a high QE for NaKSb(Cs) and NaKSb photocathodes. These cathodes exhibit a broader spectral response (with a QE of 0.022% at 690 nm, which can be comparable to metallic cathodes). It's well-known that alkali-antimonide photocathodes can achieve very low emittances when the excitation energy is close to the photoemission threshold (due to less excess energy of photoexcited electrons). Therefore, it's worth exploring the operation of these Na-based cathodes in the red or near-infrared wavelengths (for instance, by utilizing a Ti:Sapphire laser that operates at 800 nm).

In the future, it's worth considering the exploration of heterostructure-type photocathodes. For instance, since Cs_2Te is known to be a relatively robust cathode, a thin layer of Cs_2Te could be deposited onto the KCsSb cathode film, similar to the approach used for GaAs cathodes [83, 244, 245]. This thin Cs_2Te layer would serve as a protective barrier to shield the bulk KCsSb cathodes from contamination and thereby extending their overall operational lifetime. However, it's important to note that implementing this approach would likely result in a reduction in the overall QE of the photocathode. Despite this trade-off, it's a valuable direction for investigation, and the potential outcomes merit further exploration.

Lastly, at INFN LASA, the development of a new device called TRAnsverse Momentum Measurement (TRAMM) is underway, with plans for its integration into the green cathode production system. This device allows for the measurement of the thermal emittance of produced photocathodes. This advancement allows for further refinement of the cathode recipe to achieve lower thermal emittance values.

Appendix 8

Appendices

A Analysis of Stopping Potential Versus Photon Energy for Different Multi-alkali Photocathodes

The stopping potential refers to the minimum negative voltage applied to the anode in a photoelectric experiment to completely stop the emission of electrons from a photoemissive material [246]. This phenomenon occurs when the kinetic energy of the emitted photoelectrons is reduced to zero due to the opposing electric field created by the stopping potential. This voltage is a measure of the maximum kinetic energy of the emitted electrons and is closely related to the work function of the material. It provides valuable information about the energy distribution of emitted electrons and can be used to determine properties of the material's surface, such as its work function.

In simpler terms, when we shine a light on a metal plate or a semiconductor material with photons carrying energy greater than the work function (for metals) or the photoemission threshold (E_g+E_a) (for semiconductors), electrons absorb these photons and break free from the surface, as extensively described in Chapter 2. Some of the released electrons travel across the tube, hit the anode at the other end, and register as a current in the ampere meter. The current tells us the quantity of emitted electrons but not their kinetic energy. To extract the initial kinetic energy, we convert it into potential energy by applying an opposing electric field through an electric voltage across the tube. While

the electrons, being negatively charged, are repelled by the negative anode, some still manage to reach it, especially those with high kinetic energy. As the negative potential on the anode increases, fewer electrons can reach it. Finally, when none can reach it, the photocurrent becomes zero, and the applied potential is called the stopping potential. This phenomenon is depicted in Figure 8.1. In the context of our experiment, utilizing low laser power (in μW) is strategic to minimize the space charge effect of electrons, ensuring minimal impact on the measurement of the stopping potential.

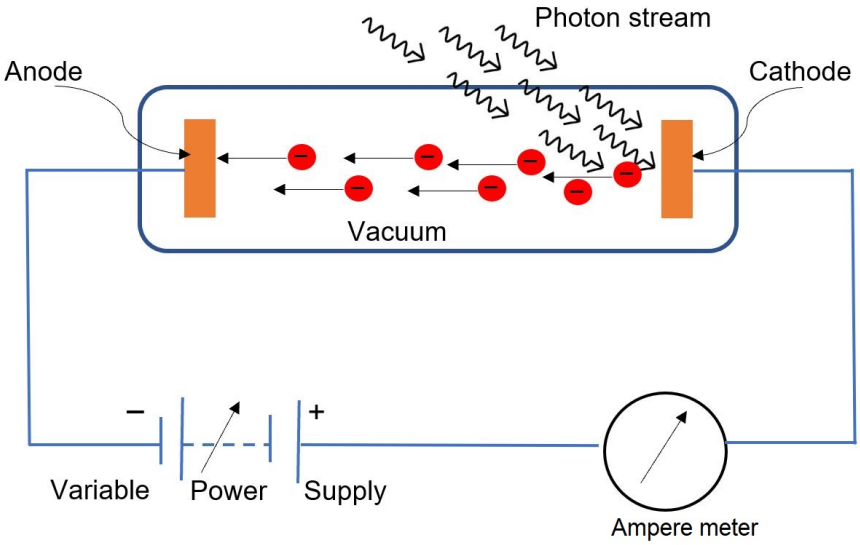

Figure 8.1: Schematic representation of the experimental setup for the measurement of the stopping potential.

The stopping potential, denoted by V_s, is connected to the highest kinetic energy of the emitted photoelectrons (E_k). The fastest photoelectron reaches the anode just before the photocurrent drops to zero. The voltage required for this is called the "stopping voltage". It's represented as V_s and defined as [247],

$$E_k = eV_s \tag{8.1}$$

Equation 8.1 can also be written as,

$$E_k = \frac{1}{2}mv_{\max}^2 = eV_s \tag{8.2}$$

From Einstein's photoelectric equation we know [247],

$$h\nu = W + \frac{1}{2}mv_{\max}^2 \tag{8.3}$$

Where $h\nu$ represents the photon of energy and W represents the material's Work function.

Substituting the kinetic energy, then equation 8.3 can be written as,

$$h\nu = W + eV_s \tag{8.4}$$

$$V_s = \left(\frac{h}{e}\right) \cdot \nu - \frac{W}{e} \tag{8.5}$$

So, if we conduct an experiment where we change the frequency of the light shining on the metal plate and measure the resulting stopping potential, we can show our findings on a graph, as seen in Fig. 8.2. Extending the graph will let us find the point where it crosses the Y-axis. This negative intercept will tell us the metal's work function. The gradient of the graph gives us the Planck constant.

The graph presented in Fig. 8.2 is for metals; however, the stopping potential vs. frequency (V_s-ν) curve for a semiconductor material can be more complex than for a simple metal because semiconductors have a more complex band structure with a bandgap between the valence band and the conduction band. In a semiconductor material, photoelectrons can be excited from the valence band to the conduction band by absorbing photons with energy equal to or greater than the bandgap energy. As the frequency of the incident photons increases, they can excite electrons across the bandgap with increasing efficiency due to their higher energy. However, the actual V_s-ν curve for a semiconductor material can be more complex, even non-linear, due to the influence of the band structure. The exact shape of the V_s-ν curve for a semiconductor can be influenced by various factors, including the density of states in the valence band and conduction band, electron-electron interactions, electron-phonon scattering, defects in the lattice structure, and the specific band structure of the material. These factors can lead to deviations from the simple linear relationship described by the photoelectric effect in metals. In the following section, the stopping potential vs. frequency of the grown cathodes, such as KCsSb,KSb,

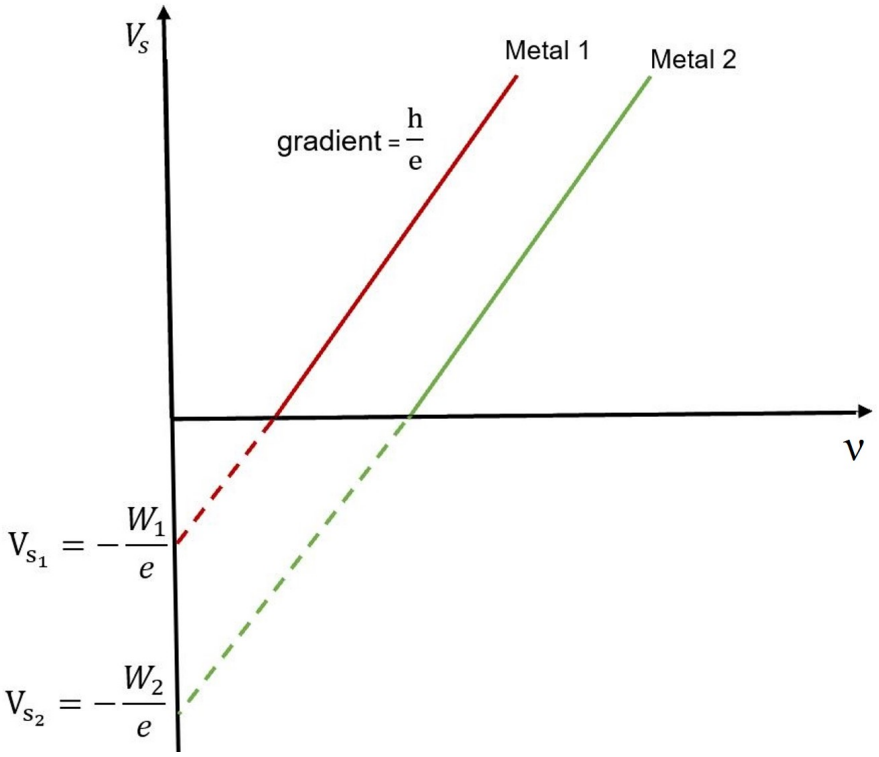

Figure 8.2: Stopping potential (V_s) vs. frequency of light (ν).

and NaKSb cathodes, is described.

A.1 KCsSb Cathode

Initially, we examined the voltage-current characteristics of the KCsSb cathode (KCsSb-8). During this investigation, we quantified both the saturation current and the stopping potential of the KCsSb-8 cathode. Our experimental setup closely resembled the configuration depicted in Figure 8.1. Figure 8.3 illustrates the voltage-current characteristics measured at 543 nm wavelength for the KCsSb-8 cathode.

As it can be seen in Fig. 8.3, there is a gradual increase in the photocurrent (interpreted as a gradual rise in the number of electrons reaching the collector or anode) with respect to the change in applied positive voltages. Saturation of the photocurrent occurred upon applying a voltage of more than 200V. Additionally, we observed a detectable photocurrent even at 0V, suggesting the presence of an upper limit to the kinetic energy of emitted

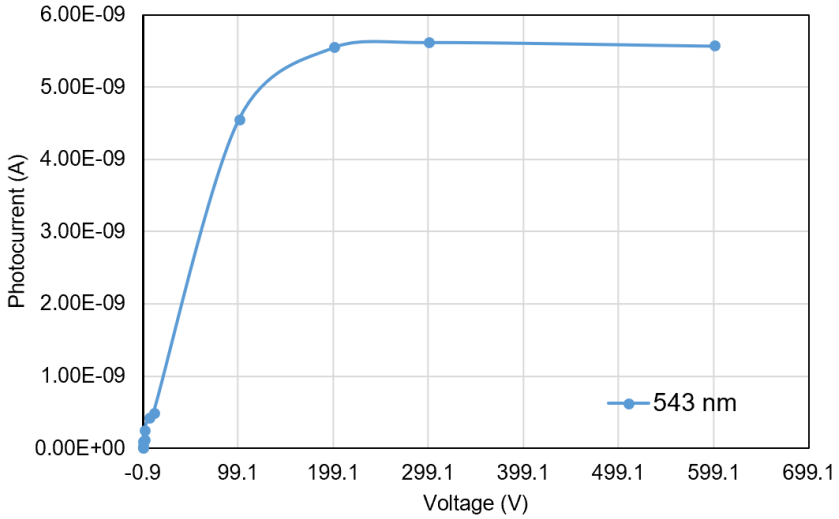

Figure 8.3: V-I characteristics of the KCsSb-8 cathode, measured at a wavelength of 543 nm.

electrons. At -0.85V, the net photocurrent measured was 0, signifying the stopping potential or stopping voltage.

Then, we conducted measurements of the stopping voltage using different light wavelengths. Fig. 8.4 illustrates the plot presenting the correlation between stopping voltage and photon energy (which is equivalent to V_s-ν), as recorded for the KCsSb-8 cathode. To ensure the accuracy of these measurements, they were repeatedly performed, and the values were found to be reproducible.

As depicted in Fig. 8.4, the pattern of the stopping potential curve in relation to the photon energy is non-linear. As described in the previous section, this characteristic is attributed to the intricate band structure of the semiconductor material. To understand the behaviour of this stopping potential curve, we need to examine it alongside the cathode's spectral response and reflectivity data. The spectral response and reflectivity plot for the KCsSb-8 cathode is shown in Fig. 8.5.

The references [157, 248] provide an illustration of the interpretation of spectral response connected to the band structure, using the example of the Cs_2Te photocathode. In our study, we're using the same model from that reference to analyse the spectral response of our photocathodes. The objective is to gain an understanding of how the spectral re-

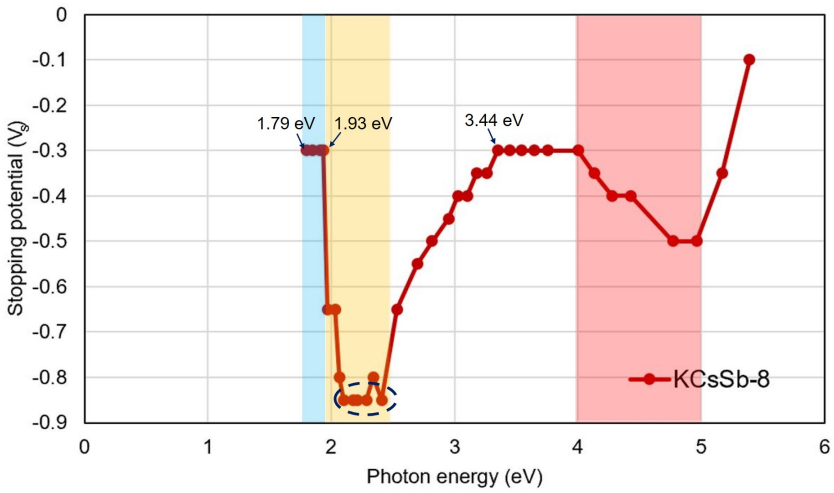

Figure 8.4: V_s-ν distribution for the KCsSb-8 cathode.

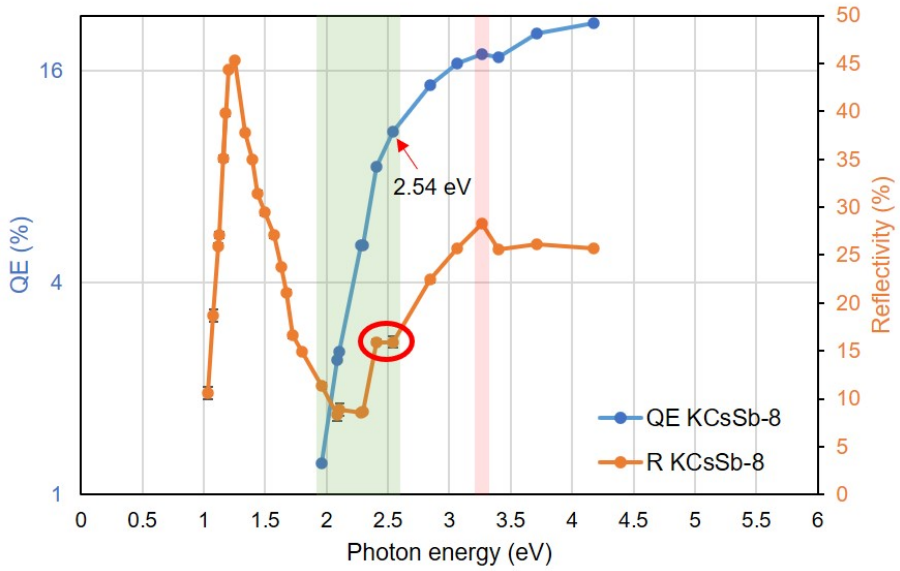

Figure 8.5: Spectral response and spectral reflectivity for the KCsSb-8 cathode.

sponse behaviour is influenced by the electronic structure of the material.

As it described in the references [157, 248], the slope of the rising quantum yield above the threshold in the spectral response is influenced primarily by two key elements: the threshold escape function and the finite width of the valence band (VB). As depicted in Figure 8.5, a pronounced rise (with an $\sim$ 8-fold rise in QE from 1.9 eV to 2.54 eV)

is evident in the spectral response curve, extending by more than half of an electron volt from the threshold value (i.e., 1.9 eV) to 2.54 eV (indicated within the green box). The presence of such a pronounced threshold is the indication of a narrow valence band, suggesting that the cathode possesses a direct band gap. This can be supported by referencing the DFT band structure plot (Fig. 5.4c) of the K_2CsSb compound, as discussed in Chapter 5 (page - 182), where the width of the valence band is observed to be approximately 1.25 eV. Above 2.54 eV in Figure 8.5, the yield keeps increasing, with a rise of around 66%, until it reaches a peak at 3.26 eV (highlighted by the red coloured box). Afterwards, it starts to decrease. To verify the consistency of this peak, we compared the spectral response patterns of all our produced cathodes, presented in Fig. 8.6. The presence of such a peak in the spectral response within the range of 3.06-3.54 eV from cathode to cathode is evident and is highlighted by the red-colored box in Fig. 8.6. Such minor variations in the peak position among cathodes are expected due to differences in growth conditions, such as substrate temperature and deposition rate, as discussed in Chapter 4. These differences can introduce minor changes in the electronic structure of each cathode, leading to the observed variations in peak position. Furthermore, such peak in the spectral response of KCsSb cathodes around $\sim$3 eV was also observed in other studies [145]. Moreover, it is noteworthy to observe in Fig. 8.6 that after reaching this peak (3.06-3.54 eV), the QE consistently decreases across all the cathodes.

Following the decrease in spectral response in Fig. 8.6, a subsequent rise in quantum efficiency can be observed. This phenomenon can effectively be explained through a simple model presented in Figure 8.7 and also discussed in References [157, 248].

As discussed in Chapter 2 (Section 2.3.1), if the electron energy is sufficiently high (due to photon absorption), the primary energy-loss mechanism for photoelectrons during their transport to the surface is inelastic electron-electron scattering. This process can have a significant impact on the photoemission data. In semiconductors, a primary electron can only lose energy through electron-electron scattering, which corresponds to the band gap energy (E_g). Therefore, electron-electron scattering cannot occur for photon energies below $2E_g$ [157]. Consequently, the escape depth may be several hundred Å, limited only by electron-phonon scattering. As a result, within this energy range

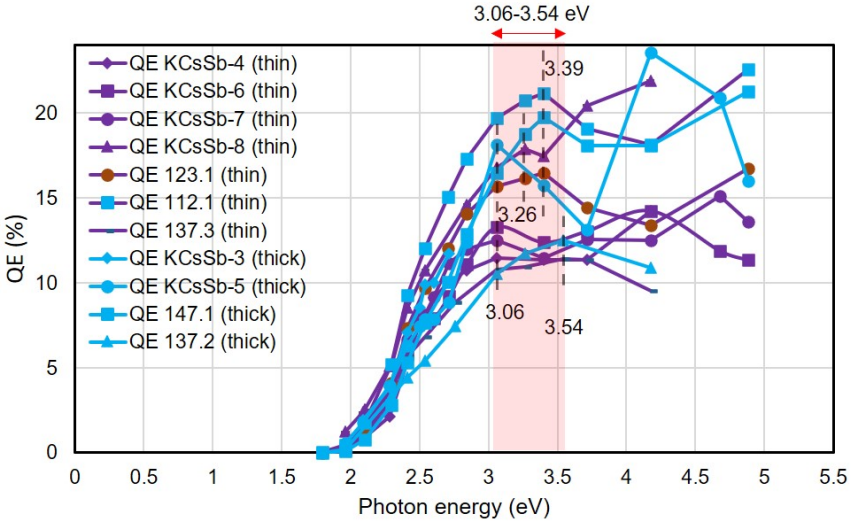

Figure 8.6: Spectral response of K-Cs-Sb cathodes produced in both the "R&D" and "Production" systems. The spectral response of thin and thick cathodes is highlighted in violet (with different symbols and colors) and light sky (with different symbols) color lines, respectively. For more effective visualization of the peaks and falls in the curve, the y-axis of the plot is taken on a linear scale.

(from the threshold to the onset of electron-electron scattering), the model anticipates a significant quantum yield. Given the narrow valence band (VB) in the K_2CsSb compound, it would be reasonable to anticipate a substantial yield prior to the reduction of escape depth caused by the initiation of electron-electron scattering. Since the band gap of K_2CsSb is around 1.2 eV [79], the threshold for electron-electron scattering is expected near $h\nu \approx 2.4$ eV (i.e.,$2E_g$). However, due to the increasing number of potential scattering events, the likelihood of electron-electron scattering rises gradually as the final-state energy increases, usually becoming significant only several electronvolts higher than the electron-electron scattering threshold [157]. Considering this, the decrease in QE beyond the local maximum ($h\nu \sim$ 3.06-3.54 eV, Fig. 8.6) is attributed to the effect of the electron-electron scattering. The local maximum observed around 3.06-3.54 eV (before the drop) indicates that the initiation of electron-electron scattering happens at a somewhat lower photon energy, which is in agreement with the band-gap value. The decline beyond the local maximum in the spectral response (Fig. 8.6) signifies a corresponding reduction in

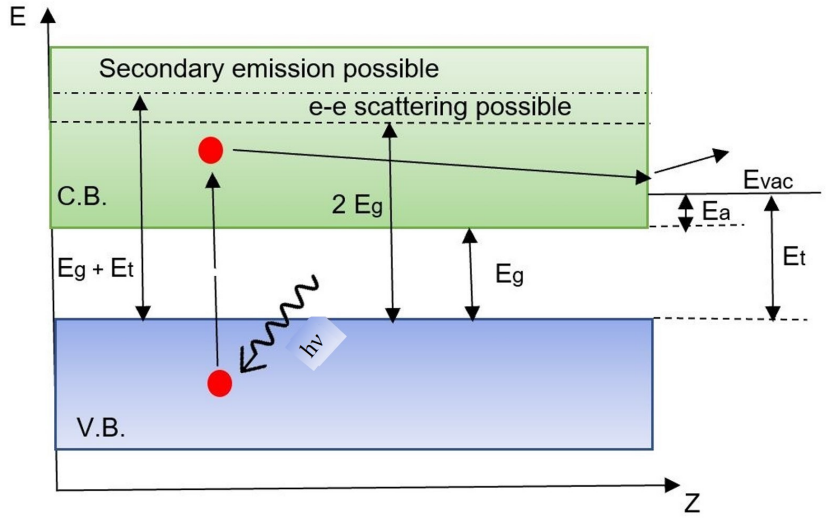

Figure 8.7: Schematic energy-level diagram of a semiconductor photoemitter. The diagram indicates the minimum threshold energies for electron-electron scattering ($2E_g$) and secondary electron emission (E_g+ E_t). The band diagram is inspired by the reference [157].

the mean free path of electrons due to electron-electron scattering. At first, the scattered electrons fall below the escape threshold, leading to a notable drop in the yield. However, as the photon energy rises, a threshold is crossed for $h\nu \geq E_g+E_t = 2E_g+E_a$, where the scattered primary or secondary electrons attain sufficient energy to escape. Hence, in our case, following the decrease in spectral response in Fig. 8.6, a subsequent rise in quantum efficiency is observed, attributed to a certain number of electrons becoming energetic enough to escape. This contributes to the observed subsequent rise in QE.

Comparing this model with Fig. 8.4, it appears that the decline in the stopping potential (or electron kinetic energy) above 4 eV (highlighted by red coloured box) is likely attributed to the described electron-electron scattering phenomenon. However, if we compare it with the spectral response curve (Fig. 8.5), there is some difference in the onset of the decrease: in the spectral response curve (Fig. 8.5), the decrease started above the local maximum at around 3.2 eV, while in the V_s-ν plot (Fig. 8.4), it starts above 4 eV. This discrepancy can be attributed to various factors, including the comparison of the different parameters and experimental limitations. The two plots may also capture different

aspects of the cathode's behavior. The spectral response plot emphasizes quantum efficiency, which quantifies emitted electrons per incident photon, highlighting the quantity of emitted electrons. This might not accurately display the information related to the kinetic energy of the electrons. On the other hand, the stopping potential plot reflects the kinetic energy of the emitted electrons. This discrepancy between spectral response and V_s-ν plots is further examined and discussed in the case of KSb film in the subsequent section.

As depicted in Fig. 8.4, the stopping potential remained constant between 1.79 eV and 1.93 eV (highlighted by blue coloured box). Subsequently, there was a decrease in the stopping potential (highlighted in the yellow-coloured box), followed by another period of stagnation between 2.10 eV and 2.40 eV (highlighted by blue dashed circle). Beyond this range, the stopping potential rises again until 3.44 eV. As we know, while photoelectrons travel to the surface, they encounter two primary energy-loss mechanisms: 1) electron-phonon scattering and 2) electron-electron scattering. As discussed above, electron-electron scattering is not feasible for photon energies $h\nu < 2E_g$. Therefore, the decline observed after 1.93 eV cannot be attributed to electron-electron scattering but rather may be attributed to inelastic electron-phonon scattering. Such phenomenon of electron-phonon scattering possibilities at lower photon energies in the case of the Cs_2Te photocathode has already been discussed in reference [157]. Therefore, it is plausible that as the photoexcited electrons experience successive scattering events with phonons within the conduction band (CB), they can progressively dissipate energy and achieve thermal equilibrium, aligning with the minimum of the conduction band density of states around 2.1- 2.4 eV. This becomes clear by looking at the spectral reflectivity plot in Fig. 8.5. It is evident that a small peak appears in the spectral reflectivity at 2.41 eV (highlighted by the red circle). Furthermore, we observed that this particular peak (peak B' in Fig. 6.8a & b) is reproducible across all produced KCsSb cathodes, as can be seen in Fig. 6.8a & b. As discussed in Section 5.5.1.2 (page - 185), this particular peak B is attributed to the excitation of electrons from the valence band to the vicinity of the lowest level of the conduction band [230]. Therefore, this observation lends support to the above-mentioned hypothesis. With increasing photon energy beyond 2.4 eV, the electron gains enough energy to surpass electron-phonon scattering effects, leading to an observed rise in the

stopping potential. Furthermore, this hypothesis can be further tested by measuring the stopping potential at a lower temperature. Since we understand that lower temperatures generally result in reduced energy loss per electron-phonon scattering event, it's reasonable to anticipate a lower rate of decline or no decline under such conditions. However, there is a need for further research before a complete understanding of these phenomena can be achieved. Obtaining more stopping potential readings from different cathodes is necessary to attain a comprehensive understanding.

A.2 KSb Cathodes

A.2.1 KSb-1

Similar to the KCsSb-8 cathode, we also analyzed the stopping potential for the KSb-1 and KSb-2 cathodes in a similar manner. The preparation details of these cathodes have already been described in the Section (4.3.1.1.3) (page 76). But here, we again want to highlight that the key difference between the KSb-1 and KSb-2 cathodes is that the cathodes are prepared at two different deposition rates (i.e., K is deposited at a deposition rate of 0.6–1 nm/min for KSb-1 and 0.2–0.4 nm/min for KSb-2). As a consequence, we observed a higher QE value for KSb-2 compared to KSb-1 (see Fig. 4.12b). Fig. 8.8 illustrates the plot presenting the V_s-ν diagram recorded for the KSb-1 cathode.

Similar to our approach with the KCsSb-8 cathode, to understand the trends observed in Fig. 8.8, we need to establish a correlation with the spectral response and spectral reflectivity plots of the KSb-1 cathode. Figure 8.9 depicts the spectral response and spectral reflectivity curves corresponding to the KSb-1.

In Figure 8.9, a pronounced rise is evident in the spectral response curve, extending by nearly one electron volt from the threshold value (i.e., 2.08 eV) to 2.75 eV (highlighted by green-colored box). The presence of such a pronounced threshold indicates the presence of a narrow valence band, suggesting that the cathode possesses a direct band gap. This is supported by the DFT band structure of the K_3Sb compound, as shown in Fig. 5.12c and discussed in Chapter 5. Where the width of the valence band is observed at approximately 1.3 eV. Above 2.75 eV in Fig. 8.9, the yield keeps increasing until it reaches a peak

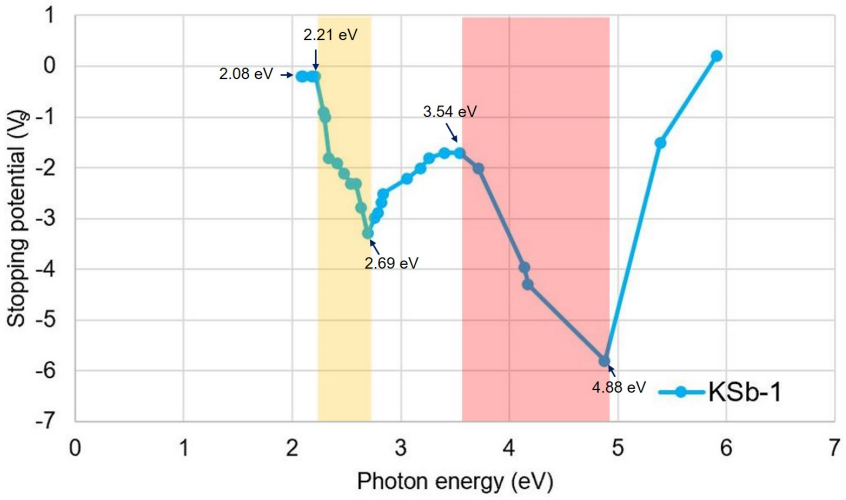

Figure 8.8: V_s-ν distribution, as recorded for the KSb-1 cathode.

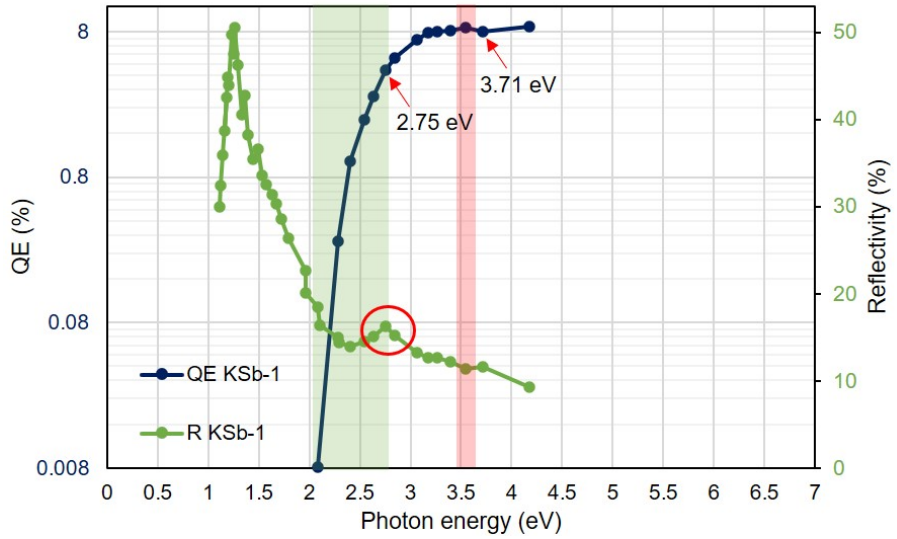

Figure 8.9: Spectral response and spectral reflectivity for the KSb-1 cathode.

or local maximum at 3.54 eV (highlighted by red colored box). Afterward, it starts to decrease. This decrease is also observed in Fig. 4.12b (Chapter 4). Similar to KCsSb cathodes, to verify the reproducibility of such peak or local maximum around 3.5 eV, we examined the spectral response patterns of all our produced KSb films, as depicted in Fig. 8.10. The presence of such a peak in the spectral response within the range of 3.06-

3.54 eV from cathode to cathode is evident and is highlighted by the red-colored box in Fig. 8.10. As previously mentioned for KCsSb cathodes, minor variations in the peak position among cathodes are anticipated due to differences in growth conditions, such as substrate temperature and deposition rate, as discussed in Chapter 4. Interestingly, when comparing this observation with KCsSb cathodes (Fig. 8.6), we can notice that the local maximum in the spectral response at around similar energy rage. This similarity may be attributed to the similarity in the bandgap values of the two films (i.e., E_g of KSb = 1.1 eV to 1.4 eV [75, 158], E_g of KCsSb = 1.2 eV [79]).

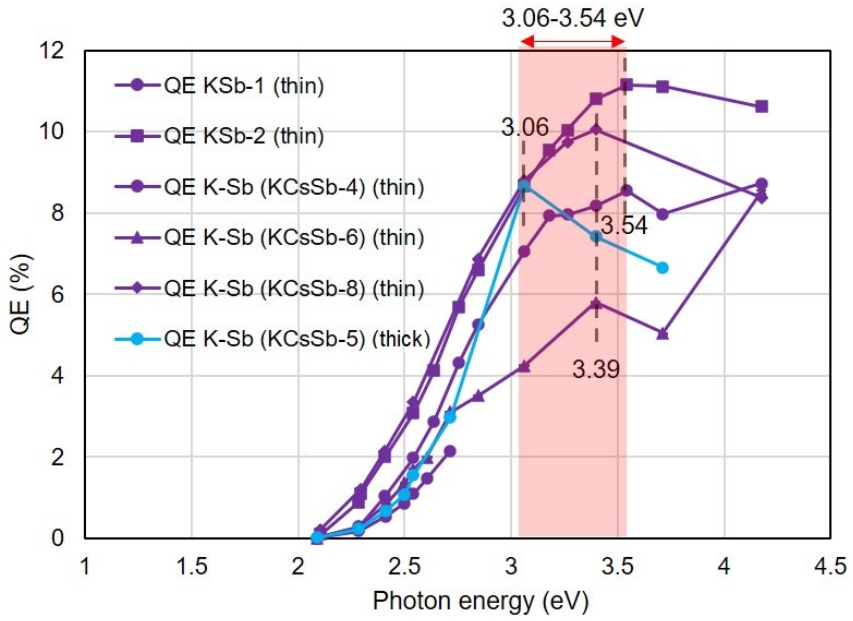

Figure 8.10: Spectral response of K-Sb cathodes produced in both the "R&D" and "Production" systems. The spectral response of thin and thick cathodes is highlighted in violet (with different symbols and colors) and light sky color lines, respectively. For more effective visualization of the peaks and falls in the curve, the y-axis of the plot is taken on a linear scale.

As discussed earlier in the section, the threshold for electron-electron scattering is expected to occur near $h\nu \approx$ 2.2-2.8 eV for K_3Sb compounds (i.e., $2E_g$, where the bandgap energy (E_g) of K_3Sb is considered to be 1.1 to 1.4 eV [75, 158]). However, as previously explained, the likelihood of electron-electron scattering increases gradually with the final-state energy due to more potential scattering events, usually becoming significant only

several eV higher than the electron-electron scattering threshold [157]. Considering this, the decrease in QE beyond the local maximum ($h\nu \sim$ 3.06-3.54 eV, Fig. 8.10) is attributed to stem from the electron-electron scattering phenomenon.

By comparing the spectral response plot (Fig. 8.9) with Figure 8.8, it becomes evident that a similar decrease in the stopping potential occurs above 3.54 eV in Fig. 8.8 (highlighted by the red colored box). The similarities in behaviour of both distributions (Figure 8.8 and Figure 8.9) suggest that e-e scattering might be responsible for the observed drop above 3.54 eV in both cases. However, after the dip in the stopping potential beyond 3.54 eV (Fig. 8.8), there is a subsequent increase observed after a local minimum at 4.88 eV. In the spectral response (Fig. 8.9), the subsequent increase in QE after the dip beyond 3.54 eV occurs after a local minimum at 3.71 eV. This disparity between the two plots may be attributed to the factors mentioned earlier, including the comparison of the two different parameters and experimental limitations.

In Fig. 8.8, it is evident that a drop in the stopping potential occurs after 2.21 eV and continues up to 2.69 eV (highlighted by the yellow-colored box). As previously discussed, this decrease could be associated with photoexcited electrons undergoing successive scattering events with phonons within the conduction band. This results in gradual energy dissipation and achievement of thermal equilibrium, aligning with the minimum of the conduction band density of states around 2.7 eV. This would be clearer by looking at the spectral reflectivity distribution in Fig. 8.9. It is evident that a peak appears in the spectral reflectivity at 2.75 eV (highlighted by the red circle). Additionally, the reproducibility of the peak at this point in the spectral reflectivity across all produced KSb-thin films can be observed in Fig. 6.2 (peak C'). As discussed in section 6.1.1.1 (Chapter 6, page 222), this particular peak at 2.75 eV (peak C') is attributed to the excitation of electrons from the valence band to the lowest level of the conduction band. Therefore, this observation lends support to the above-mentioned hypothesis. Beyond the point (i.e., 2.69 eV) in Fig. 8.8, a subsequent rise in the stopping potential is noticed. With increasing photon energy beyond 2.69 eV (Fig. 8.8), the electron gains enough energy to surpass electron-phonon scattering effects, leading to an observed rise in the stopping potential.

A.2.2 KSb-2

We analyzed the stopping potential for the KSb-2 cathode in a manner similar to that used for the KSb-1 cathode. Figure 8.11 illustrates the distribution, presenting the V_s-ν curve for both cathodes, KSb-2 and KSb-1. The data for KSb-1 is included for comparison purposes. The preparation details of the KSb-2 cathode have already been covered in Section 4.3.1.1.3 (page 76) and also discussed in the previous section (page 259).

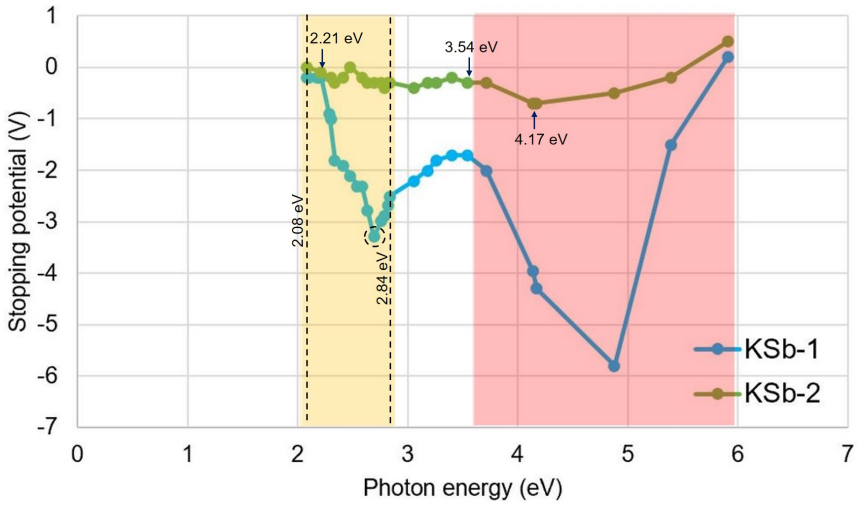

Figure 8.11: V_s-ν distribution, as recorded for the KSb-1 and KSb-2 cathodes. The data for KSb-1 is included in the plot for comparison purposes.

Similar to our approach with the KSb-1 cathode, in order to understand the trends observed in Fig. 8.11, we need to establish a correlation with the spectral response and spectral reflectivity plots of the KSb-2 cathode. Figure 8.12 depicts the spectral response and spectral reflectivity curves corresponding to the KSb-2 cathode.

As previously discussed, the spectral response and spectral reflectivity of both the KSb-1 and KSb-2 cathodes have been found to be similar; see Fig. 4.12b (Chapter 4). Furthermore, as detailed in Section 4.3.1.1.3 (page 76), the similarity in the spectral behavior between the two films strongly suggests the potential creation of a similar compound (potentially with similar crystal orientation) in both cases. However, when looking at Fig. 8.11, in the energy range from 2.08 eV to 2.84 eV (highlighted by the yellow box), a discrepancy in the behaviour of the stopping potential curve between the

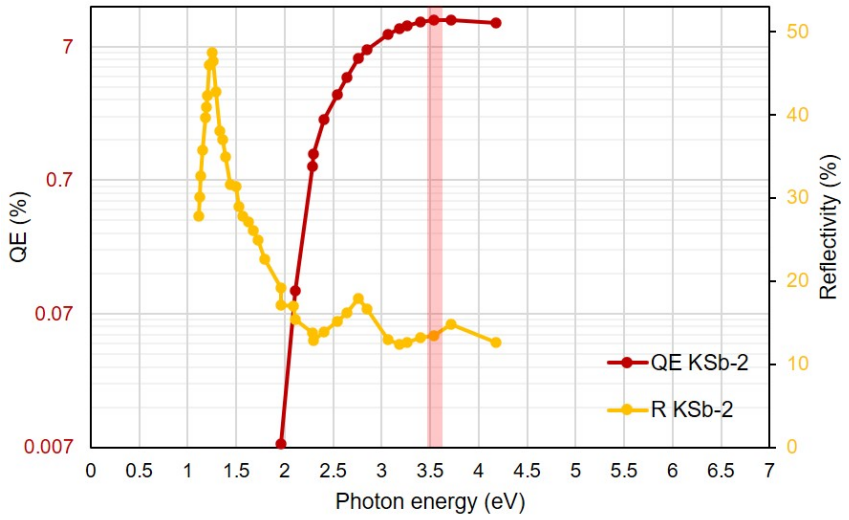

Figure 8.12: Spectral response and spectral reflectivity plot for the KSb-2 cathode.

two cathodes becomes apparent. As can be observed in Figure 8.11, there is a drop in the stopping potential curve above 2.21 eV, reaching a local minimum at 2.69 eV (highlighted by black dashed circle), followed by an increase above 2.69 eV for the KSb-1 cathode (yellow-coloured box). For the KSb-2 cathode, there is a marginal change in the stopping potential within this frequency range. As previously mentioned (for KSb-1 and KCsSb-8 cathodes), the observed reduction in the stopping potential curve within the mentioned energy range is primarily attributed to electron-phonon scattering. Furthermore, as discussed in Section 4.3.1.1.3 (page 76), the higher QE observed in the KSb-2 case can be attributed to the lower deposition/flux rate during K deposition, resulting in improved crystallinity in the material. This explanation aligns with the observed stopping potential behaviour of KSb-2 in Fig. 8.11. As mentioned above, there's minimal change in the stopping potential behaviour between 2.08 eV and 2.84 eV for KSb-2 (highlighted by the yellow box). The disparity in V_s-ν behavior observed within the above-mentioned energy range for the two cathodes (KSb-1 and KSb-2) suggests a potential variation in their crystal arrangements. Due to the lower deposition rate in the case of KSb-2, it gives more time to arrange the K-Sb crystals in a preferred order; potentially, this leads to a reduction in the defect density in the material. In general, the kinetic energy of a pho-

toexcited electron in a semiconductor material depends on various factors, such as the energy of the photon, the band structure of the semiconductor, the substrate temperature, and the defect density. In this case, all the factors are presumably constant for both cathodes except for the defect density. Defects provide extra scattering points for electrons, increasing the likelihood of electron-phonon interactions, which might explain the behaviour seen in the stopping potential distribution for KSb-1 within the highlighted range (yellow coloured box in Fig. 8.11). Whereas a minimal change in the stopping potential within the highlighted range for KSb-2 might suggest improved crystalline quality and fewer imperfections in the material.

In Fig. 8.11, it can be observed that above 3.54 eV, there is a drop in the stopping potential curve, followed by an increase after reaching a local minimum at 4.17 eV (highlighted by the red-coloured box). If we compare the two cathodes, the patterns are very similar. Furthermore, when comparing it with the spectral response of KSb-2 (Fig. 8.12), there is a decrease in the QE above the local maximum at around 3.54 eV (highlighted by red color box). All of these observations suggest that the drop in the stopping potential curve after 3.54 eV (highlighted in the red box in Fig. 8.11) is likely a result of the electron-electron (e-e) scattering phenomenon. For a more comprehensive understanding, it is crucial to investigate the stopping potential behavior in KSb cathodes with varying deposition rates across a broader range of cathodes in the future.

A.3 NaKSb Cathode

Similar to the above, we also analyzed the stopping potential distribution for the NaKSb-1 cathode. Fig. 8.13 illustrates the measured V_s-ν distribution for the NaKSb-1 cathode. Since the NaKSb-1 cathode is fabricated on the KSb-2 film (Section 4.3.3), we include the stopping potential information for KSb-2 on the same graph (Fig. 8.13). The preparation details of the NaKSb-1 cathode have already been covered in Section 4.3.3. Fig. 8.14 illustrates the spectral response and spectral reflectivity curves relevant to the NaKSb-1 cathode.

In Fig. 8.13, it is evident that the stopping potential for the NaKSb-1 cathode rises from above 2.29 eV to 3.39 eV (highlighted in the yellow box). When comparing this

behavior with the KSb-2 cathode, there is a noticeable difference. It suggests that adding Na to the KSb-2 cathode might change the electronic band structure of the compound. Moreover, when we examine the spectral reflectivity of the NaKSb-1 compound (Fig. 8.14), we notice a change in the pattern between 2.29 eV and 3.39 eV (highlighted by a blue dashed circle) in comparison to the spectral reflectivity of the KSb-2 compound (Fig. 8.12). This observation can also be seen in Fig. 4.30. These findings indicate that the addition of Na to the KSb-2 compound has indeed modified its electronic structure. Furthermore, our DFT study reveals a difference in the band structure between these two compounds (Figures 5.12c, 5.20b). Sodium atoms have a different mass and size compared to the atoms in the original K-Sb compound. Therefore, introducing Na could potentially influence the vibrations of the lattice or phonons in the compound. The changes in phonon behaviour could then impact how electrons interact with the lattice, leading to the observed increase in stopping potential in Fig. 8.13 (highlighted in yellow-colored box). However, to validate this hypothesis and gain a more comprehensive understanding, additional experimental data or further investigation is required.

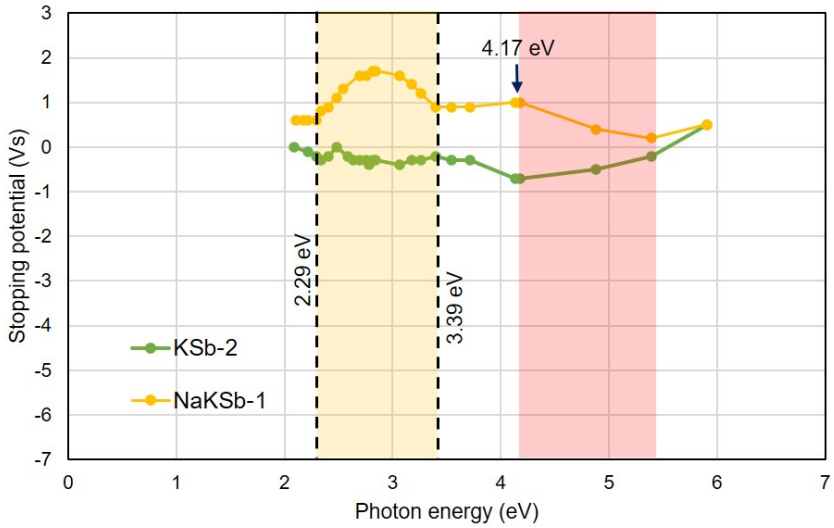

Figure 8.13: V_s-ν distribution, as recorded for the NaKSb-1, and KSb-2 cathodes. The data for KSb-2 is included in the plot for comparison purposes.

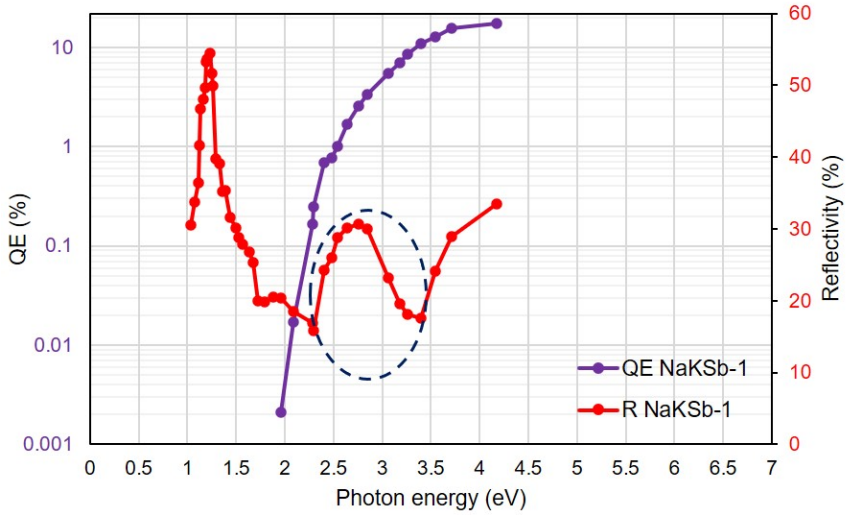

Figure 8.14: Spectral response and spectral reflectivity plot for the NaKSb-1 cathode.

Above 4.17 eV in Fig. 8.13, a drop in the distribution is noticed for NaKSb-1 cathode (highlighted by red colored box). As explained above, such a drop could be due to the e-e scattering phenomenon.

A.4 Summary & Discussion

Stopping potential studies were carried out on the KSb, KCsSb, and NaKSb cathodes produced in the "R&D" preparation system. Additionally, utilizing an established model in the reference [157, 248] aids in further interpreting the spectral response of the aforementioned cathode materials. Upon comparing both the stopping potential and spectral response data, it appears to be a viable approach for characterizing and comprehending the electronic structure of the photoemissive material. The method offers valuable insights into the band structure of the grown material. Nevertheless, as explained, conducting additional stopping potential studies involving different cathodes is essential to achieve a more comprehensive understanding and pave the way forward.

B Fabrication Recipes for Yo-Yo Deposition of Cs and Sb on NaKSb(Cs)-1 Cathode

As mentioned in Chapter 4 (Section 4.3.2.1), given the relatively low QE of NaKSb(Cs)-1, we opted for a yo-yo deposition of Sb and Cs on the pre-existing NaKSb(Cs)-1 compound. Since the Cs deposition was conducted at a higher temperature and led to a decrease in the QE for NaKSb(Cs)-1 at the end, we decided to implement a consecutive deposition process for Sb and Cs, known as yo-yo deposition, to enhance the overall QE of the compound. Figure 8.15 illustrates the QE and temperature profiles during this yo-yo deposition. The yo-yo deposition process significantly raised the QE from 0.29% to 0.6% at 543 nm. However, it was observed that when a thin layer of Na was subsequently grown on the cathode, it caused the QE to decline, ultimately stabilizing at 0.43%, as depicted in the Figure 8.15.

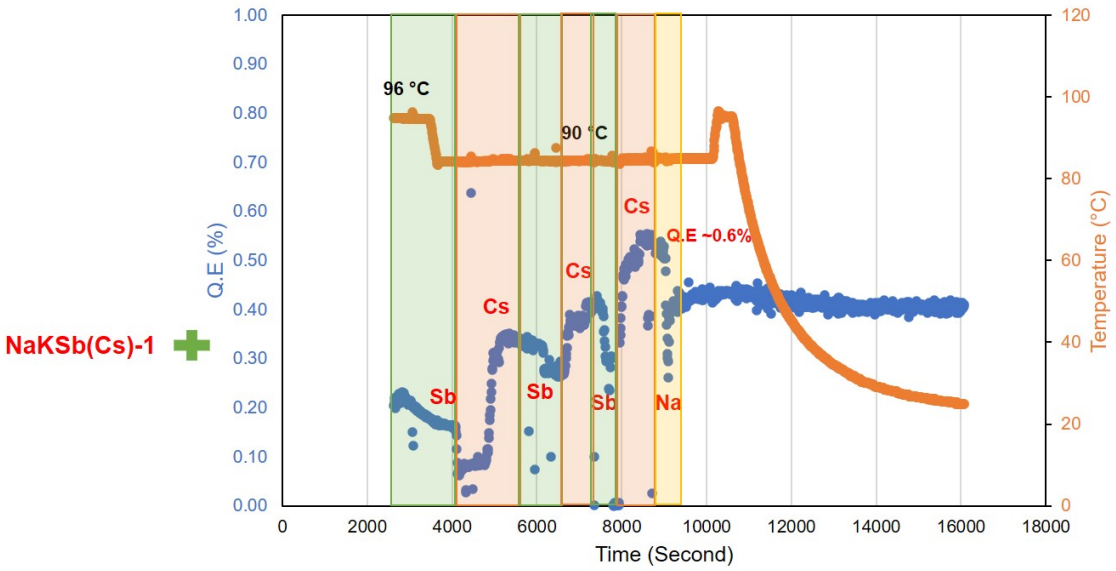

Figure 8.15: illustrates QE (blue) (at 543 nm) and temperature (orange) history during yo-yo type deposition of NaKSb(Cs)-1 cathode.

C Real-time Analysis of Spectral Response and Reflectivity during Sb and K Deposition of Cathode 137.1.

Fig. 8.16 illustrates the real-time QE at 540 nm (central plot) during the deposition of Sb and K of cathode 137.1. The figure also displays real-time spectral response plots (surrounding the central plot) at different thicknesses of Sb and K deposition. The central plot serves as a focal point for understanding the overall trend and behavior at 540 nm during the deposition process of Sb and K. By incorporating the spectral response plots; one can correlate variations in the spectral response with the evolution of QE at 540 nm. This correlation aids in tracking the formation of different compounds that occur throughout the deposition process. The spectral response plots are generated by reconstructing data Fig. 4.45a.

Between spectral response, plot 1 (at 10 nm Sb) and plot 2 (Sb + 10 nm K), a clear decline after 3.39 eV (highlighted by a black circle) is evident in plot 2 (see Fig. 8.16). As explained in Section 4.4.5.1 (Cathode 137.1, page 129) and also in Appendix A.2.1 (page 254-257), this decline likely results from electron-electron scattering and indicates the initial formation of the KSb compound. Between spectral response plots 2 (Sb + 10 nm K) and 3 (Sb + 20 nm K), an increase in the photoemission threshold (Eg + Ea) is observed, rising from 1.79 eV in plot 2 to 1.96 eV in plot 3, as highlighted by the red circle. This increase in the photoemission threshold clearly indicates the transition from Sb to KSb compound (for KSb compound, E_g+E_a $\sim$ 2.08 eV). Between spectral response plot 4 (Sb + 40 nm K) and 5 (Sb + 60 nm K), there is a tenfold increase in the QE response at the threshold value (1.96 eV) in plot 5 (highlighted by a green circle). This signifies that the material becomes significantly more efficient at emitting electrons at that energy level. Between spectral response plots 5 (Sb + 60 nm K) and 6 (Sb + 90 nm K), the decline after 3.39 eV (highlighted by the orange circle) in Plot 6 is less pronounced compared to Plot 5. This change could be attributed to some modification in the electronic structure of the compound.

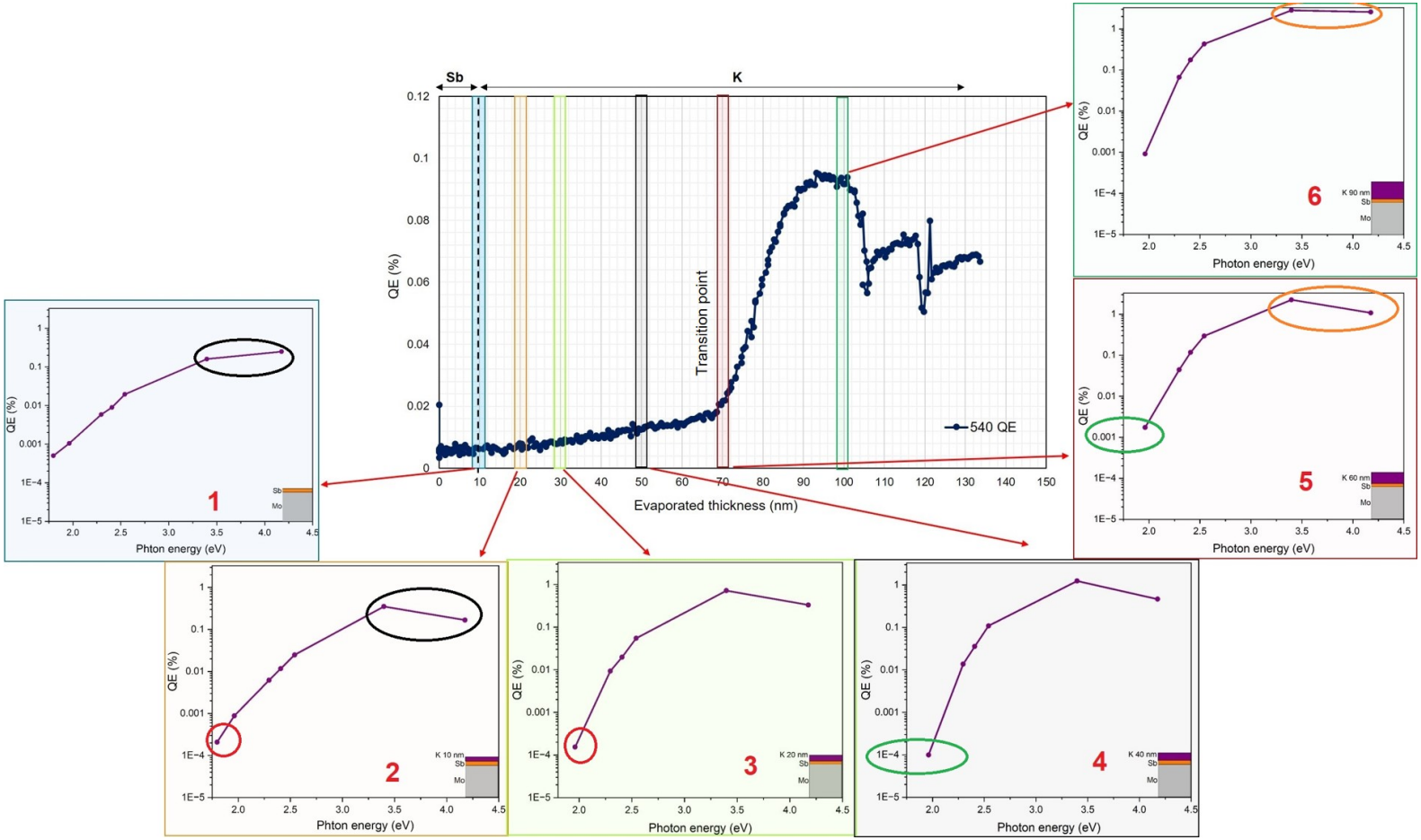

Figure 8.16: Real-time QE at 540 nm (central plot) during the Sb and K deposition of cathode 137.1 as a function of the evaporated thicknesses of Sb and K, with a dashed line separating them. The real-time spectral responses (as a function of the wavelength) during the different phases of Sb and K deposition are presented around the central plot. These spectral response plots are highlighted by differently colored boxes (1-6), corresponding to the colored boxes in the central plot (1-6). The various colored circles within the spectral response plots highlight the observed variations in the spectral response patterns during the deposition.

Fig. 8.17 depicts the real-time reflectivity at 540 nm (central plot) during the deposition of Sb and K on cathode 137.1, mirroring the format of Fig. 8.16. The figure also displays the real-time spectral reflectivity (around the central plot) at different thicknesses of Sb and K deposition. The spectral reflectivity plots are generated by reconstructing data from Fig. 4.45b.

Between spectral reflectivity plot 1 (at 10 nm Sb) and plot 2 (Sb + 10 nm K), a clear difference in the spectral reflectivity (highlighted by the red circle) is evident in plot 2 (see Fig. 8.17), indicating the beginning of the formation of the KSb compound. Then, in plot 4 (Sb + 40 nm K), the reflectivity from 1.79 eV to 2.54 eV (highlighted by the black circle) has decreased compared to plot 2 and 3. Between spectral response plot 5 (Sb + 60 nm K) and plot 6 (Sb + 95 nm K), a noticeable difference in the pattern of spectral reflectivity can be observed. As explained in Section 4.4.5.1 (Cathode 137.1, page 129), after the transition point (i.e., after 70 nm total evaporated thickness in the central plot of Fig. 8.17), there is a difference in the behavior of reflectivity between the two sets of wavelengths (Fig. 4.45b). This difference is attributed to the complex crystallization of the KSb compound, and therefore, we observed changes in the spectral reflectivity as shown in plot 6 in Fig. 8.17.

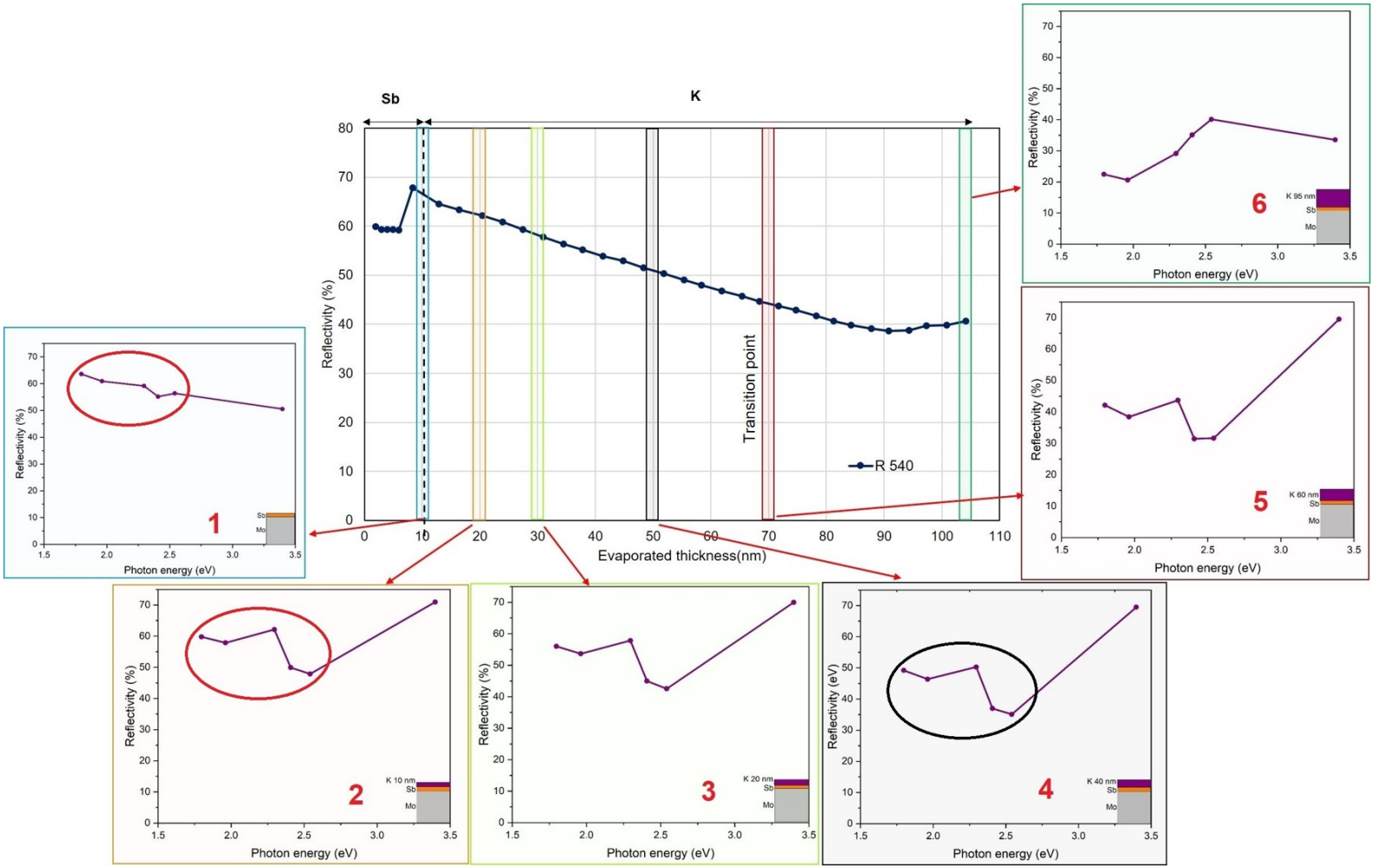

Figure 8.17: Real-time reflectivity at 540 nm (central plot) during the Sb and K deposition of cathode 137.1 as a function of the evaporated thicknesses of Sb and K, with a dashed line separating them. The real-time spectral reflectivity (as a function of the wavelength) during the different phases of Sb and K deposition are presented around the central plot. These spectral reflectivity plots are highlighted by differently colored boxes (1-6), corresponding to the colored boxes in the central plot (1-6). The various colored circles within the spectral reflectivity plots highlight the observed variations in the spectral reflectivity patterns during the deposition.

D Real-time Analysis of Spectral Response and Reflectivity during Sb, K, and Cs Deposition of Cathode 137.2.

D.1 Real-time Analysis of Spectral Response and Reflectivity during Sb and K Deposition of Cathode 137.2.

Fig. 8.18 illustrates the real-time QE at 540 nm (central plot) during the deposition of Sb and K of cathode 137.2. The figure also presents the real-time spectral response (shown around the central plot) during the deposition process. The spectral response plots are generated by reconstructing data from Fig. 4.48a.

Between spectral response plots 1 (at 10 nm Sb) and 2 (Sb + 20 nm K) in Fig. 8.18, an increase in the photoemission threshold ($E_g + E_a$) from 1.79 eV to 1.96 eV is observed in plot 2, as highlighted by the red circle. This change indicates the reaction of K with Sb. Moving on to the transition between spectral response plot 2 (Sb + 20 nm K) and 3 (Sb + 40 nm K), we can observe a shift in the spectral response pattern, particularly in the range between 3.39 eV and 4.17 eV (highlighted by the black circle). In plot 4 (Sb + 60 nm K), a clear decline is evident above 3.39 eV (highlighted by a black circle). This decline is attributed to electron-electron scattering and is a sign of the formation of the KSb compound. Notably, in the case of cathode 137.1, this decline occurred at the initial stage of K deposition (Fig. 8.16). For cathode 137.2, this behavior occurs a bit later in the K deposition process, suggesting a potentially slower reaction rate between Sb and K, possibly due to a relatively lower substrate temperature.

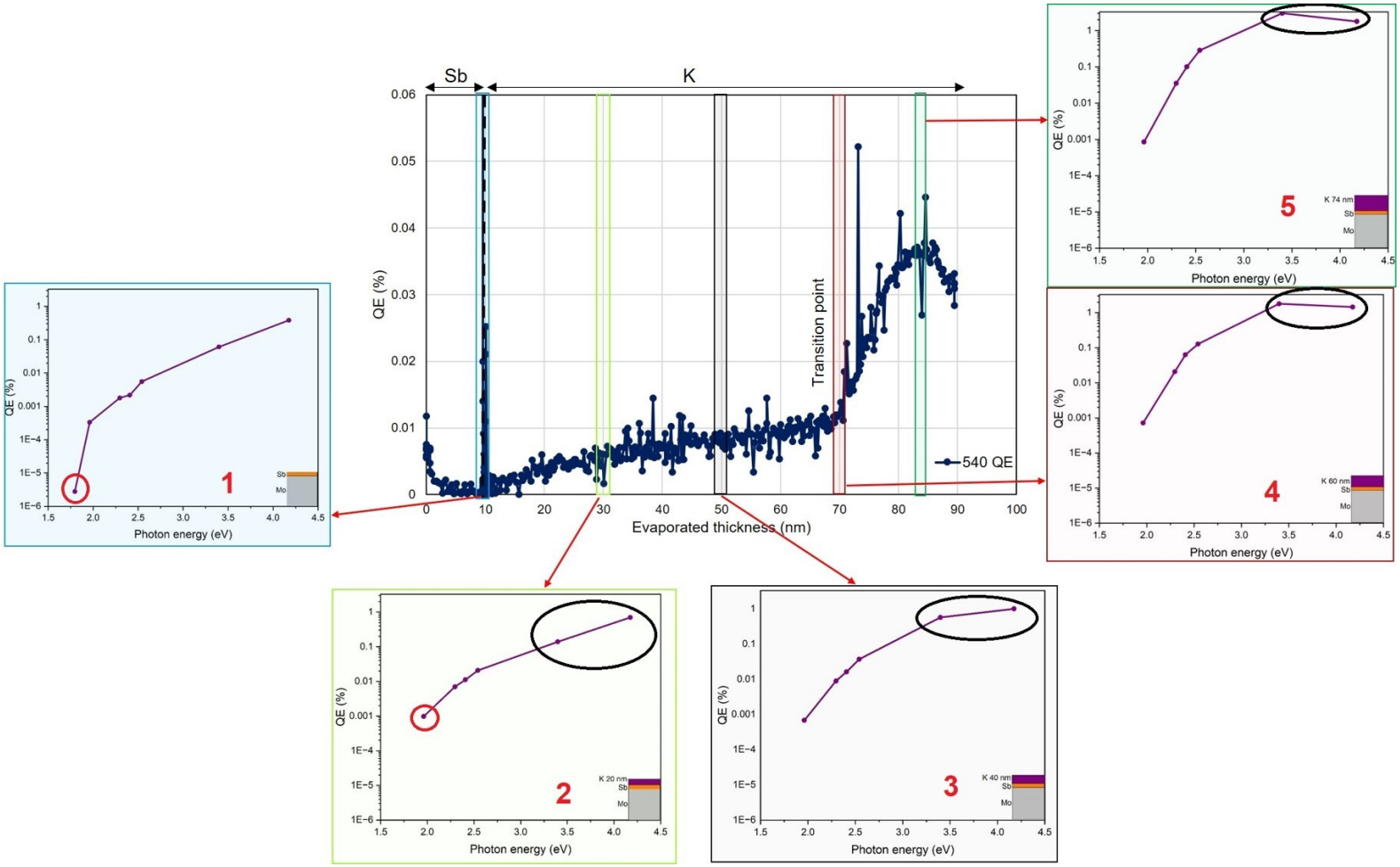

Figure 8.18: Real-time QE at 540 nm (central plot) during the Sb and K deposition of cathode 137.2 as a function of the evaporated thicknesses of Sb and K, with a dashed line separating them. The real-time spectral responses (as a function of wavelength) during the different phases of Sb and K deposition are presented around the central plot. These spectral response plots are highlighted by differently colored boxes (1-5), corresponding to the colored boxes in the central plot (1-5). The various colored circles within the spectral response plots highlight the observed variations in the spectral response patterns during the deposition.

Fig. 8.19 depicts the real-time reflectivity at 540 nm (central plot) during the deposition of Sb and K of cathode 137.2, mirroring the format of Fig. 8.18. The figure also displays the real-time spectral reflectivity (located around the central plot) at different thicknesses of Sb and K deposition. The spectral reflectivity plots are generated by reconstructing data from Fig. 4.48b.

By examining spectral reflectivity plots 1 (at 10 nm Sb), 2 (Sb + 10 nm K), and 3 (Sb + 20 nm K) (in Fig. 8.19), an observable trend emerges: the reflectivity consistently decreases across all six wavelengths as K deposition progresses. In plot 4 (Sb + 40 nm K), there is a slight change in the spectral reflectivity patterns. In plot 5 (Sb + 60 nm K), there is a small curve formed between 2.29 eV and 2.54 eV (highlighted by the black circle). In plot 6 (Sb + 78 nm K), the spectral reflectivity pattern undergoes a noticeable change. When compared to Fig. 8.17 (plot 6), a similar spectral reflectivity pattern can be observed, indicating the reproducibility of spectral reflectivity. For a clearer view of the evolution of spectral reflectivity during Sb and K deposition (Fig. 8.19), please refer to the .gif image in the cited reference [249, 250].

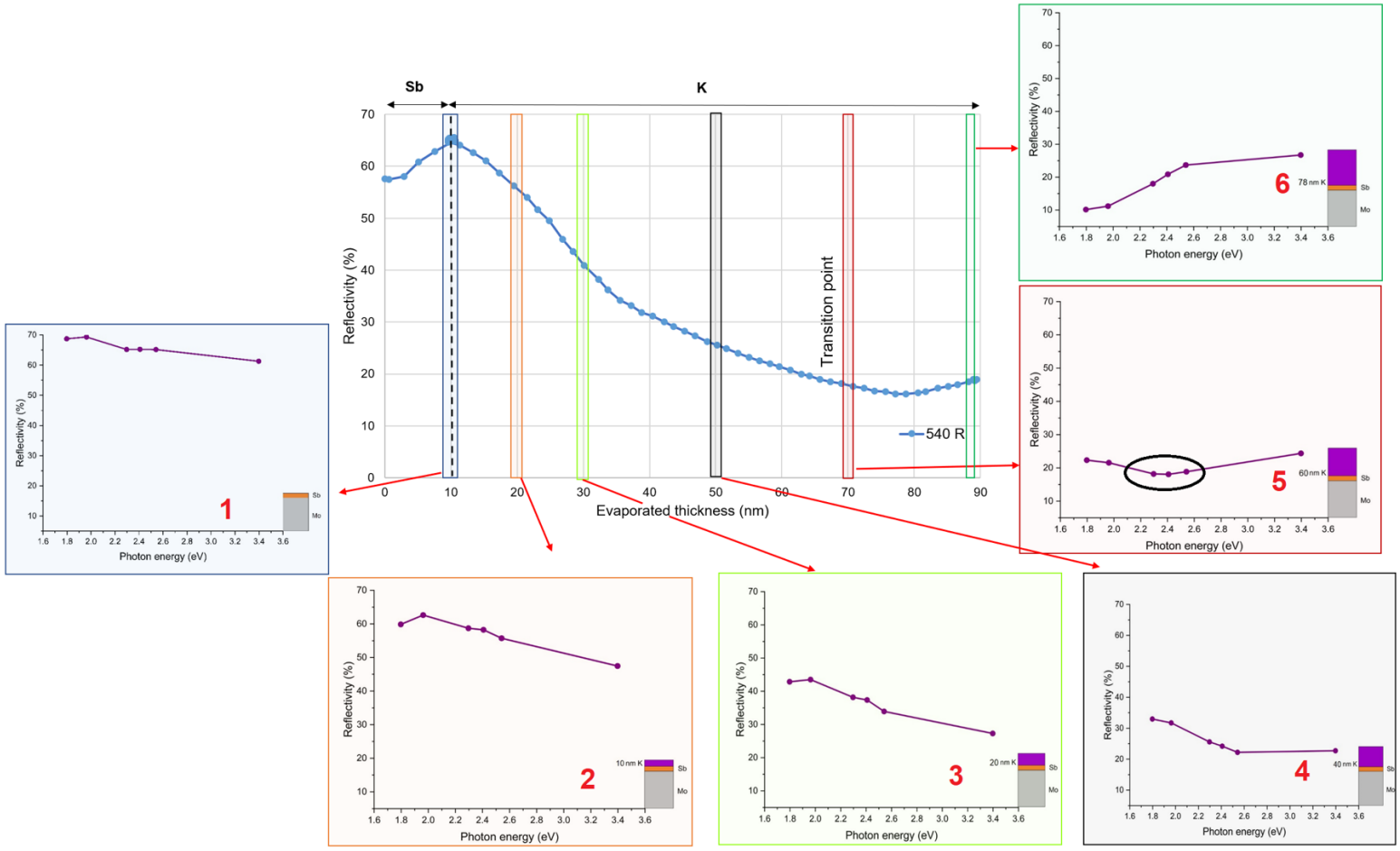

Figure 8.19: Real-time reflectivity at 540 nm (central plot) during the Sb and K deposition of cathode 137.2 as a function of the evaporated thicknesses of Sb and K, with a dashed line separating them. The real-time spectral reflectivity (as a function of wavelength) during the different phases of Sb and K deposition are presented around the central plot. These spectral reflectivity plots are highlighted by differently colored boxes (1-6), corresponding to the colored boxes in the central plot (1-6). The colored circles within the spectral reflectivity plots highlight the observed variations in the spectral reflectivity patterns during the deposition.

D.2 Real-time Analysis of Spectral Response and Reflectivity during Cs Deposition of Cathode 137.2.

As for Sb, K deposition, we have also measured the real-time QE and reflectivity during Cs deposition. Fig. 8.20 illustrates the real-time QE at 540 nm (central plot) during the deposition of Cs of cathode 137.2. The figure also presents the real-time spectral response (around the central plot) during various thicknesses of Cs deposition. The spectral response plots are generated by reconstructing data from Fig. 4.49a.

Between spectral response, plot 1 (KSb + 10 nm Cs) and plot 2 (KSb + 30 nm Cs), a decrease in the photoemission threshold (E_g+E_a) from 1.96 eV to 1.79 eV is observed in plot 2 (highlighted by the red circle). This indicates that Cs has reacted with the bulk, forming the KCsSb compound. Moving on to the comparison between plot 3 (KSb + 70 nm Cs) and plot 4 (KSb + 150 nm Cs), the QE at all wavelengths has increased in plot 4. This demonstrates that continuous Cs diffusion has led to an increase in QE. After 181 nm of Cs evaporation (highlighted by the green-colored box in the central plot), the previously mentioned (Section 4.4.5.2.2, page 136-137) QE jump can be observed in the central plot. As shown in Fig. 4.49a, this QE jump is evident across all wavelengths. Therefore, between plot 4 (KSb + 150 nm Cs) and plot 5 (KSb + 181 nm Cs) in Fig. 8.20, the QE across all wavelengths has increased in plot 5. Subsequently, a decrease in the QE at 540 nm becomes evident, as highlighted by the orange-colored box in the central plot. As shown in Fig. 4.49a, at this specific point, the QE increased at UV wavelengths (297 nm and 365 nm), while it decreased at visible wavelengths (488 nm, 515 nm, 540 nm, 632 nm, and 690 nm). Therefore, in plot 6 (KSb + 203 nm Cs) in Fig. 8.20, the QE at visible wavelengths (highlighted by the red-colored box) has decreased compared to plot 5, while the QE at UV wavelengths (297 nm and 365 nm) has increased.

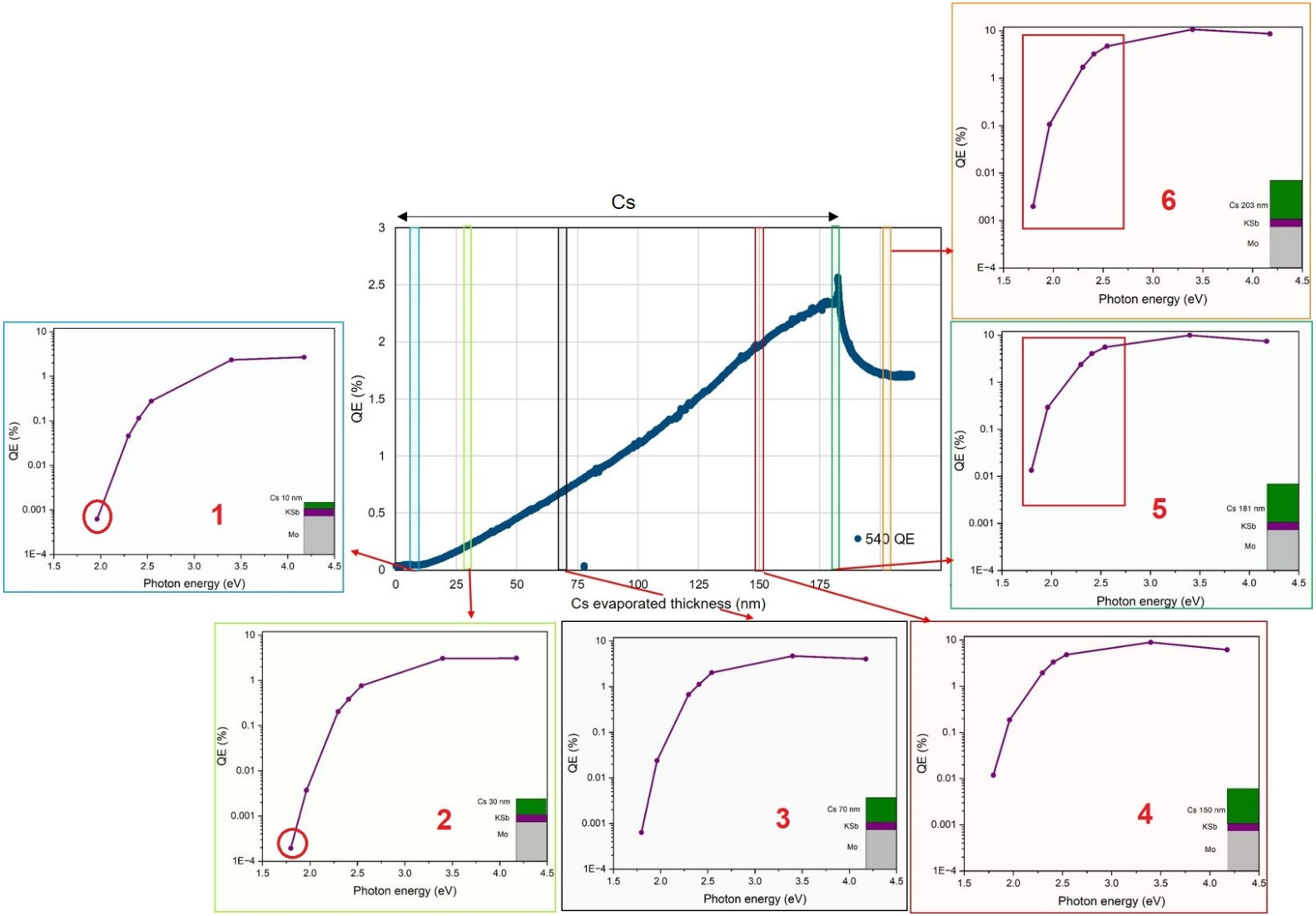

Figure 8.20: Real-time QE at 540 nm (central plot) during the Cs deposition of cathode 137.2 as a function of the evaporated thicknesses of Cs. The real-time spectral responses (as a function of wavelength) during the different phases of Cs deposition are presented around the central plot. These spectral response plots are highlighted by differently colored boxes (1-6), corresponding to the colored boxes in the central plot (1-6). The various colored circles and rectangular boxes within the spectral response plots highlight the observed variations in the spectral response patterns during the deposition.

Fig. 8.21 depicts the real-time reflectivity at 540 nm (central plot) during the deposition of Cs of cathode 137.2. The figure also displays the real-time spectral reflectivity (located around the central plot) at different thicknesses of Cs deposition.

Upon analyzing reflectivity plots 2 (KSb+ 31 nm Cs) and 3 (KSb + 70 nm Cs) in Fig. 8.21, it becomes evident that the reflectivity at 515 nm (2.40 eV) has increased in plot 3 compared to plot 2 (highlighted by a black-colored box). This same trend is also observable in Fig. 4.49b, where an increase in reflectivity at 515 nm becomes noticeable after 30 nm of Cs evaporation. Subsequently, as Cs deposition progressed in plot 4 (KSb+ 150 nm Cs) in Fig. 8.21, the reflectivity at 515 nm (2.40 eV) and 540 nm (2.29 eV) further increases, culminating in a peak at 515 nm (highlighted by a red-colored circle). In plots 5 and 6, the spectral reflectivity pattern continues without significant modifications, resembling what was observed in plot 4. For a clearer view of the evolution of spectral reflectivity during Cs deposition that is shown in Fig. 8.21, please refer the .gif image provided in the reference [249].

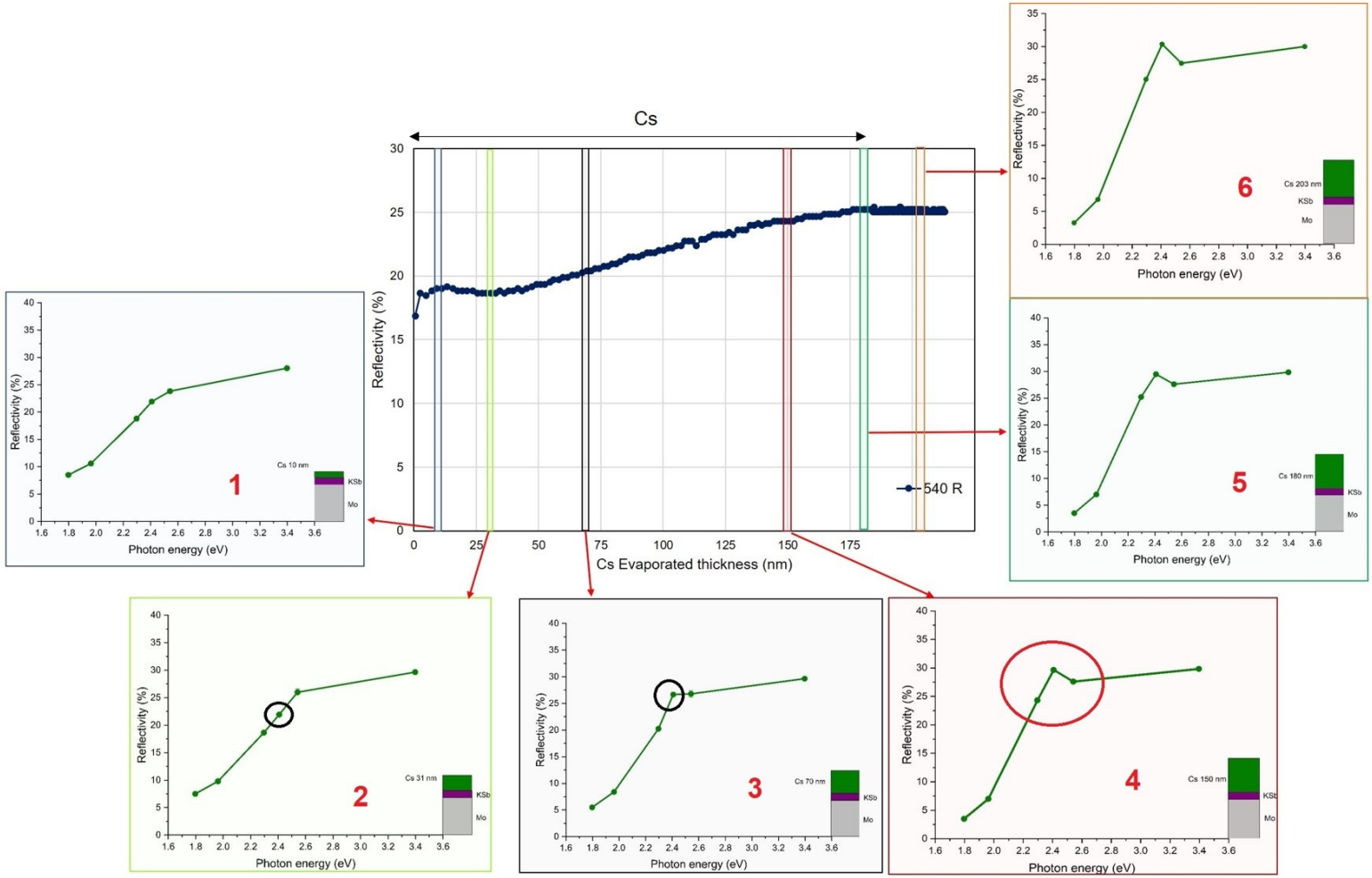

Figure 8.21: Real-time reflectivity at 540 nm (center plot) during the Cs deposition of cathode 137.2 as a function of the evaporated thicknesses of Cs. The real-time spectral reflectivity (as a function of wavelength) during the different phases of Cs deposition is presented around the central plot. These spectral reflectivity plots are highlighted by differently colored boxes (1-6), corresponding to the colored boxes in the central plot (1-6). The colored circles within the spectral reflectivity plots highlight the observed variations in the spectral reflectivity patterns during the deposition.

E Real-time Analysis of Spectral Response and Reflectivity during Sb, K, and Cs Deposition of Cathode 137.3.

E.1 Real-time Analysis of Spectral Response and Reflectivity during Sb and K Deposition of Cathode 137.3.

Fig. 8.22 illustrates the real-time QE at 515 nm (central plot) during the deposition of Sb and K of cathode 137.3. The figure also shows the real-time spectral response plots (around the central plot) during various thicknesses of Sb and K deposition. The spectral response plots are generated by reconstructing data from Fig. 4.52a.

Between spectral response plots 2 (Sb + 10 nm K) and 3 (Sb + 20 nm K) in Fig. 8.22, we observe an increase in the photoemission threshold (E_g+E_a), rising from 1.79 eV to 1.96 eV (highlighted by a red circle) in plot 3. This shift indicates the reaction of Sb with K, leading to the formation of the KSb compound. Moving on to the transition between spectral response plots 4 (Sb + 30 nm K) and 5 (Sb + 36 nm K), there is a noticeable change in the spectral response pattern, especially in the energy range between 3.39 eV and 4.17 eV (highlighted by a black circle). In plot 6 (Sb + 43 nm K), a clear decline is evident above 3.39 eV (highlighted by a black circle). This decline is attributed to electron-electron scattering, indicating the formation of the crystalline KSb compound. Comparing the evolution of real-time spectral response in Fig. 8.22 with the cathode 137.2 (as shown in Fig. 8.18), we notice similar patterns, suggesting that both compounds formed under similar substrate temperature conditions.

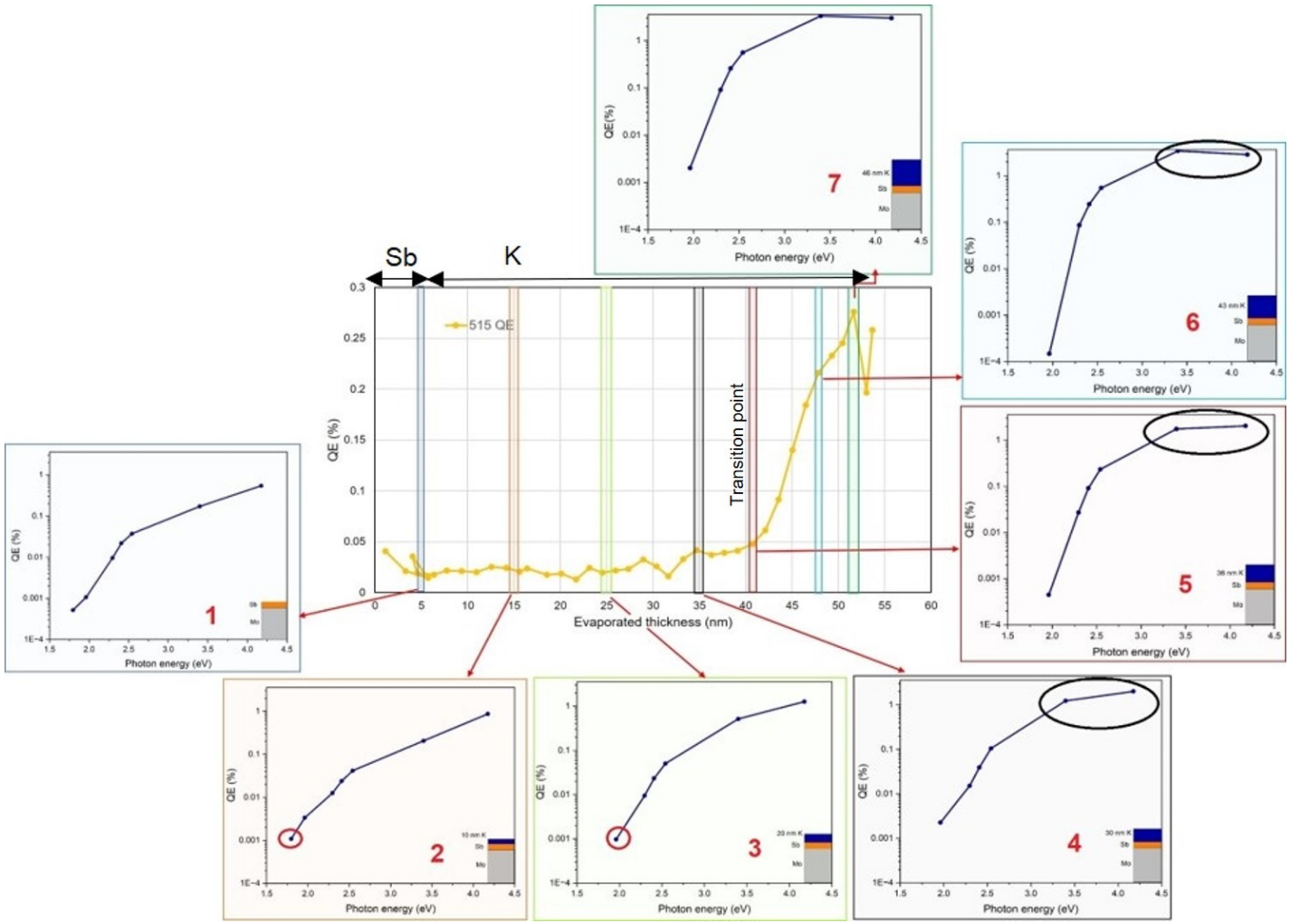

Figure 8.22: Real-time QE at 515 nm (central plot) during the Sb and K deposition of cathode 137.3 as a function of the evaporated thicknesses of Sb and K. The real-time spectral responses (as a function of wavelength) during the different phases of Sb and K deposition are presented around the central plot. These spectral response plots are highlighted by differently colored boxes (1-7), corresponding to the colored boxes in the central plot (1-7). The various colored circles within the spectral response plots highlight the observed variations in the spectral response patterns during the deposition.

Fig. 8.23 depicts the real-time reflectivity at 515 nm (central plot) during the deposition of Sb and K of cathode 137.3. The figure also displays the real-time spectral reflectivity (located around the central plot) at different thicknesses of Sb and K deposition.

In Fig. 8.23, a noticeable trend emerges as K is progressively added to Sb in spectral reflectivity plots 1 (Sb 5 nm), 2 (Sb + 10 nm K), and 3 (Sb + 20 nm K) – a consistent decrease in reflectivity across the six wavelengths. Subsequently, with further K addition, a small curve emerges between 1.96 eV to 2.54 eV (highlighted by the black circle) in plots 5 (Sb + 36 nm), 6 (Sb + 43 nm), and 7 (Sb + 46 nm). Comparing these spectral reflectivity evolutions with the cathode 137.2 reveals interesting insights. When we compare Fig. 8.19 and 8.23, we notice striking similarities in the spectral reflectivity patterns up to the transition point. For example, spectral reflectivity plots from 1 to 5 closely resemble each other in both figures. However, beyond this transition point (after 41 nm total evaporated thickness in the central plot of Fig. 8.23 and after 68 nm total evaporated thickness in the central plot of Fig. 8.19), a noticeable difference in the spectral reflectivity patterns occurs between the two cathodes (as observed in plot 6 in Fig. 8.19 and plot 7 in Fig. 8.23). As previously discussed, these changes after the transition point likely indicate the transformation of the amorphous K-Sb compound into a crystalline phase. Therefore, the differences in spectral reflectivity between these two cathodes after the transition point suggest potential variations in crystal modifications that occurred during the KSb crystallization process. For a clearer view of the evolution of spectral reflectivity during Sb and K deposition (Fig. 8.23), please refer to the .gif image in the cited reference [249, 250].

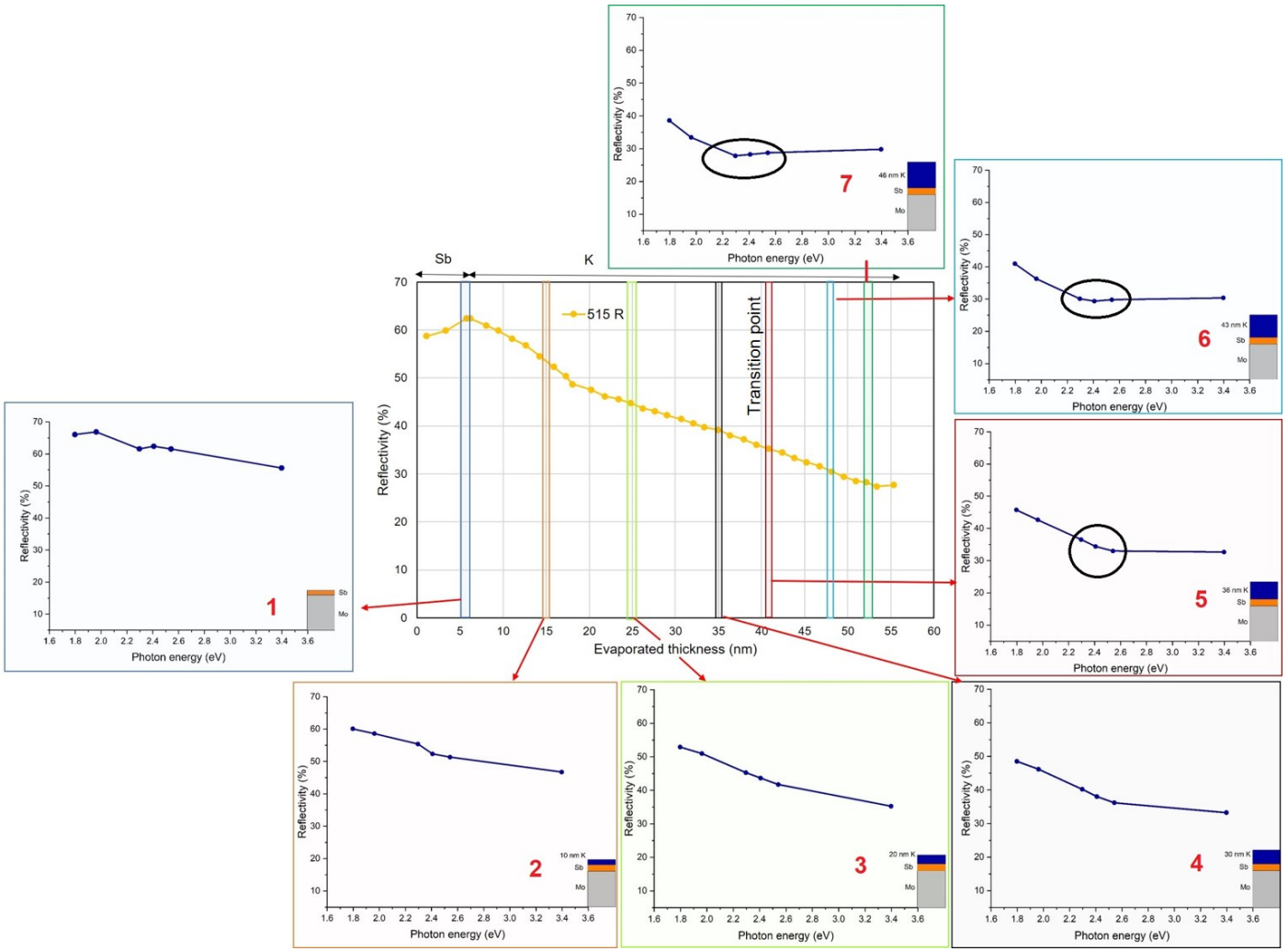

Figure 8.23: Real-time reflectivity at 515 nm (central plot) during the Sb and K deposition of cathode 137.3 as a function of the evaporated thicknesses of Sb and K. The real-time spectral reflectivity (as a function of wavelength) during the different phases of Sb and K deposition are presented around the central plot. These spectral reflectivity plots are highlighted by differently colored boxes (1-7), corresponding to the colored boxes in the central plot (1-7). The colored circles within the spectral reflectivity plots highlight the observed variations in the spectral reflectivity patterns during the deposition.

E.2 Real-time Analysis of Spectral Response and Reflectivity during Cs Deposition of Cathode 137.3.

Fig. 8.24 illustrates the real-time QE at 540 nm (central plot) during the deposition of Cs of cathode 137.3. The figure also shows the real-time spectral response plots (around the central plot) during various thicknesses of Cs deposition. The spectral response plots are generated by reconstructing data from Fig. 4.53a.

Between spectral response plot 2 (KSb + 30 nm Cs) and plot 3 (KSb + 40 nm Cs) in Fig. 8.24, there is a decrease in the photoemission threshold (E_g+E_a) from 1.96 eV to 1.79 eV (highlighted by the red circle) in plot 3. This indicates that Cs has reacted with the bulk, forming the KCsSb compound. Continuing with the comparison between 5 (KSb + 80 nm Cs) and 6 (KSb + 86 nm Cs), the QE at all wavelengths has increased from plots 5 to 6. This demonstrates that continuous Cs diffusion has led to an increase in QE. After 86 nm of Cs evaporation (highlighted by the red-colored box in the central plot), the previously mentioned QE jump can be observed in the central plot. Following the jump, subsequently, there is a noticeable decrease in the QE (at 540 nm) in the central plot (highlighted by the violet-colored box in the central plot). A similar corresponding drop (visible wavelengths) in the spectral response can be observed in plot 7 (highlighted by red colored box).

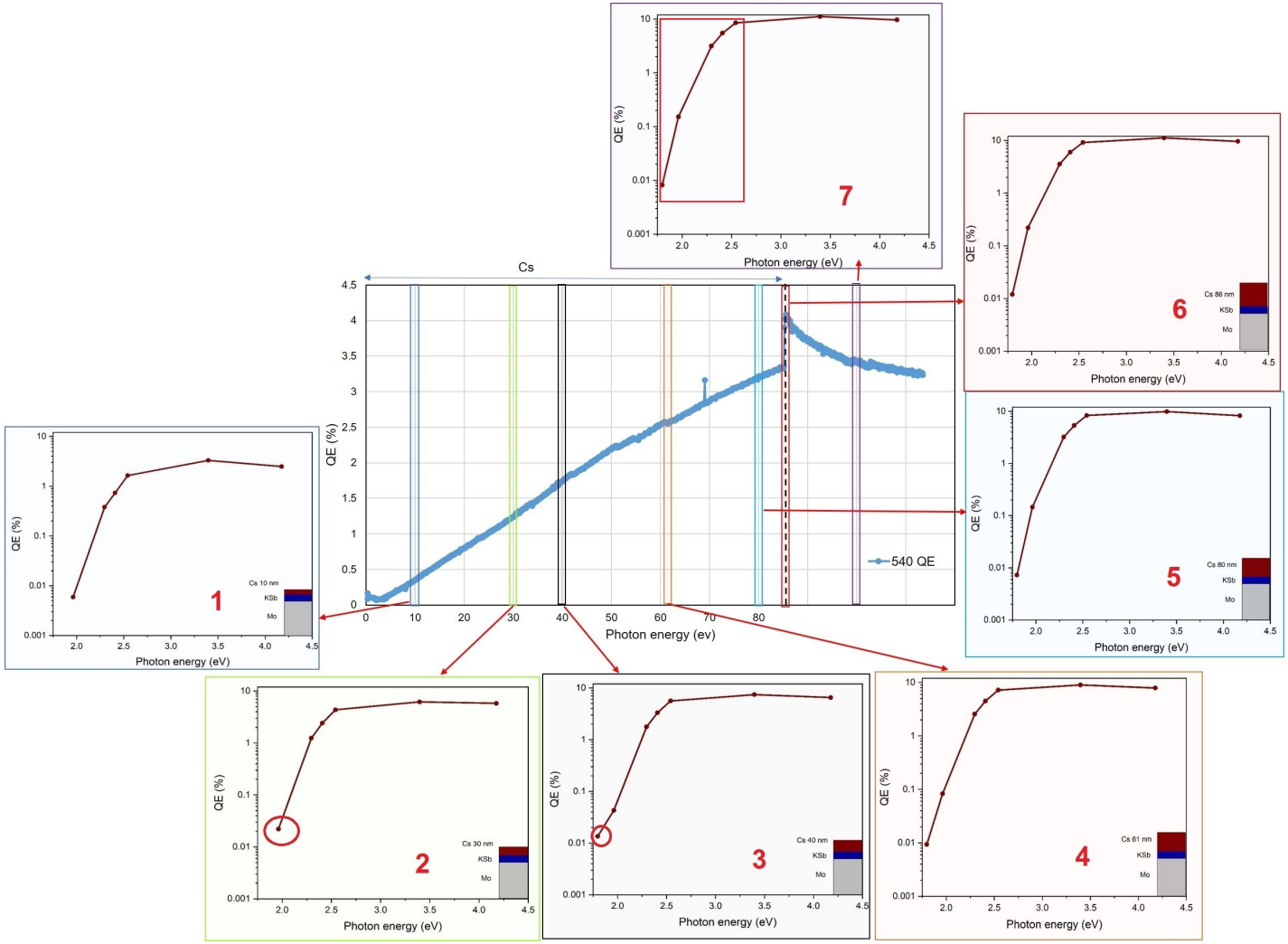

Figure 8.24: Real-time QE at 540 nm (central plot) during the Cs deposition of cathode 137.3 as a function of the evaporated thicknesses of Cs. The real-time spectral responses (as a function of wavelength) during the different phases of Cs deposition are presented around the central plot. These spectral response plots are highlighted by differently colored boxes (1-7), corresponding to the colored boxes in the central plot (1-7). The various colored circles and rectangular boxes within the spectral response plots highlight the observed variations in the spectral response patterns during the deposition.

Fig. 8.25 depicts the real-time reflectivity at 540 nm (central plot) along with the real-time spectral reflectivity (located around the central plot) at different thicknesses of Cs deposition. As previously discussed, towards the end of K deposition, a small curve emerges between 1.96 eV and 2.54 eV (highlighted by the black circle) in the spectral reflectivity plot in Fig. 8.23 (plots 6 and 7). Comparing these observations with plot 1 (KSb + 10 nm Cs) in Fig. 8.25, it becomes apparent that this "curve" still exists after the deposition of 10 nm of Cs (highlighted by black colored circle). Subsequently, a noticeable trend becomes apparent: the shape of this curve becomes more conical with the further addition of Cs onto the KSb structure in plots 2 (KSb + 30 nm Cs), 3 (KSb + 40 nm Cs), 4 (KSb + 61 nm Cs), 5 (KSb + 80 nm Cs), and 6 (KSb + 86 nm Cs). Moreover, it is interesting to note that when comparing the spectral reflectivity shape at the end of the Cs deposition between cathodes 137.2 (thick) and 137.3 (thin) (plot 6 in Fig. 8.21 and plot 6 in Fig. 8.25), we can observe that the shape of the spectral reflectivity is completely different for these two cathodes. This difference in behavior potentially indicates changes in the crystal structure formation between these two cathodes. However, other effects related to thickness could also be potential reasons for the different behavior. Therefore, these reflectivity results are compared with the theoretical model and comprehensively discussed in Chapters 5 and 6. For better visualization of the evolution of the spectral reflectivity during Cs addition presented in Fig. 8.25, please check the .gif image provided in the reference [249, 250].

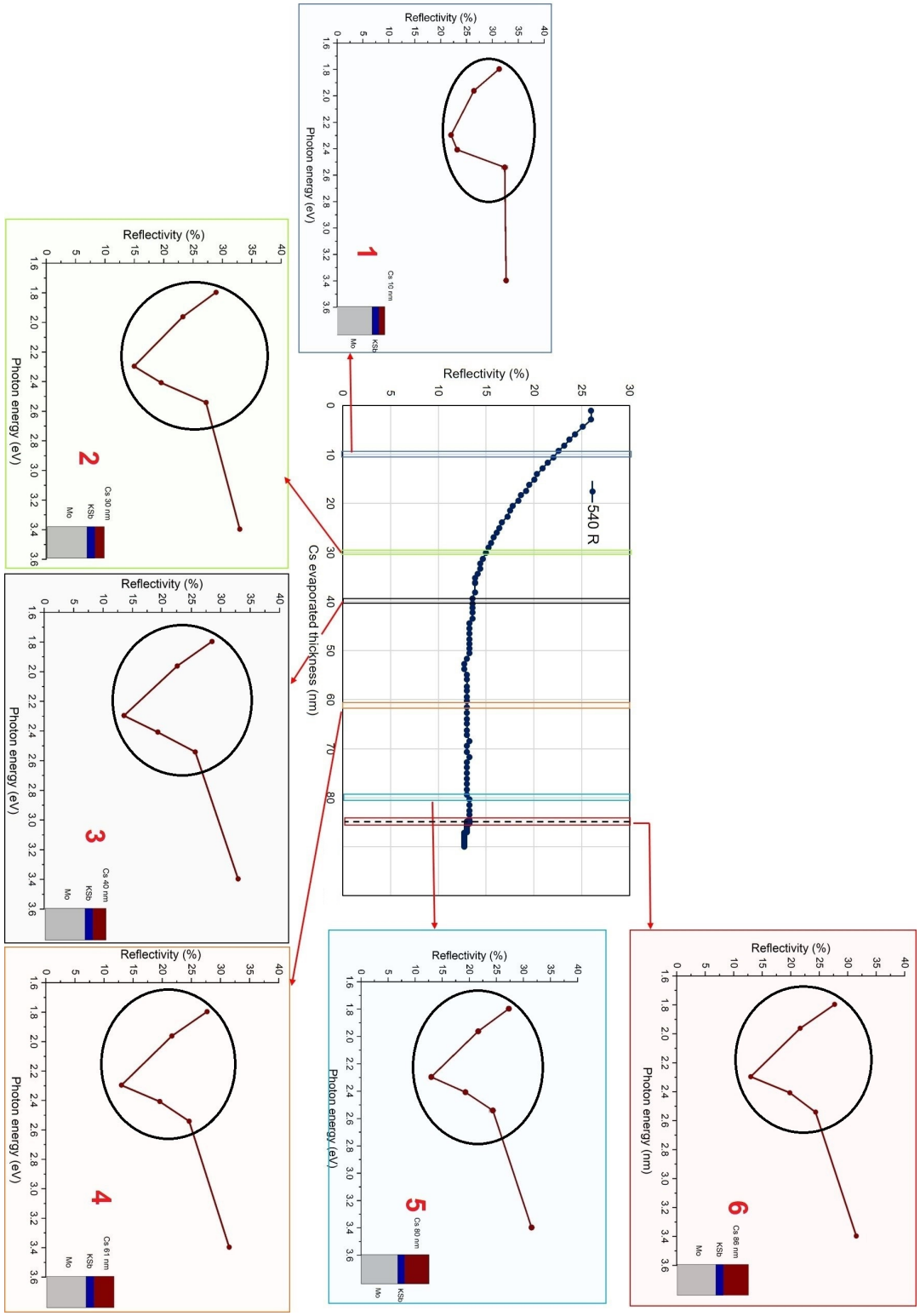

Figure 8.25: Real-time reflectivity at 540 nm (central plot) during the Cs deposition of cathode 137.3 as a function of the evaporated thicknesses of Cs. The real-time spectral reflectivity (as a function of wavelength) during the different phases of Cs deposition is presented around the central plot. These spectral reflectivity plots are highlighted by differently colored boxes (1-6), corresponding to the colored boxes in the central plot (1-6). The colored circles within the spectral reflectivity plots highlight the observed variations in the spectral reflectivity patterns during the deposition.

F Transmittance Curve of K_3Sb Cubic and Hexagonal Compounds: Experimental Data by Ebina and Takahashi et al. and A. H. Sommer.

F.1 Transmittance Curve of K_3Sb Cubic

The transmittance curve of the K_3Sb cubic compound, obtained through experimental measurements by Ebina and Takahashi et al. and A. H. Sommer [233]), is depicted in Figure 8.26. It is well-established that the transmittance and the imaginary part of the dielectric function values are interconnected [208, 251]. Therefore, it is expected that the peaks observed in the transmittance plot (Figure 8.26) would exhibit similarities to the peaks observed in plot 6.1a (Section 6.1.1.1) of the imaginary part of the dielectric function. The transmitted curve (Fig. 8.26) exhibits distinct peaks at energy values of 1.36 eV, 2.44 eV, 2.74 eV, 3.34 eV, 3.69 eV, 3.95 eV, 4.43 eV, and 5.10 eV, which are labeled as A', B', C', E', F', G', H', and I', respectively. The peaks observed in the transmittance curve show a strong agreement with the peaks obtained from our DFT calculations for the imaginary part of the dielectric function, as depicted in Figure 6.1b (Section 6.1.1.1).

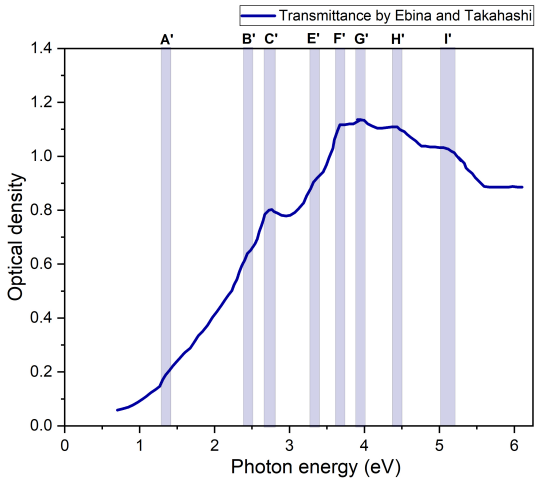

Figure 8.26: Transmittance curve of the K_3Sb cubic compound, as documented in reference [233]. The plot presented in this work has been generated with permission using data from reference [233].

F.2 Transmittance Curve of K_3Sb Hexagonal

The transmittance curve of the K_3Sb hexagonal compound, obtained through experimental measurements by Ebina and Takahashi et al. and A. H. Sommer [233], is depicted in Figure 8.27. As discussed earlier in this section, it is well-established that the transmittance value and the imaginary part of the dielectric function are interconnected. Therefore, it is expected that the peaks observed in the transmittance plot (Figure 8.27) would exhibit similarities to the peaks observed in plot 6.4a of the imaginary part of the dielectric function. The transmitted curve (Fig. 8.27) exhibits distinct peaks at energy values of 1.05 eV, 1.67 eV, 2.24 eV, 2.45 eV, 3.49 eV, 4.13 eV, 5.15 eV which are labelled as A', B', C', D', F', I', and K', respectively. The peaks observed in the transmittance curve show a strong agreement with the peaks obtained from our DFT calculations for the imaginary part of the dielectric function, as depicted in Figure 6.4b.

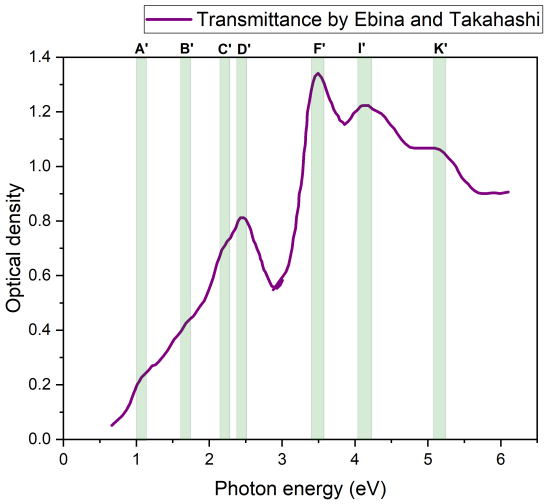

Figure 8.27: Transmittance curve of the K_3Sb hexagonal compound, as documented in reference [233]. The plot presented in this work has been generated with permission using data from reference [233].

F.3 Comparison of Transmittance Curves between K_3Sb Cubic and K_3Sb Hexagonal Compounds

To identify the major differences in the excitonic peaks between cubic and hexagonal K_3Sb, we compared the transmittance data as reported by Ebina and Takahashi et al. [233] of both compounds, shown in Figure 8.28. As discussed in Section 6.1, in Fig. 8.28, both the K_3Sb cubic and hexagonal compounds exhibit three major peaks that can be distinguished: the first peak A1 for K_3Sb hexagonal and A2 for K_3Sb cubic (corresponding to fundamental absorption), the second peak D1 for K_3Sb hexagonal and D2 for K_3Sb cubic, and the third peak F1 for K_3Sb hexagonal and F2 for K_3Sb cubic. As depicted in Figure 8.28, a noticeable shift in the peaks can be observed between the two plots. In the case of K_3Sb cubic, these three peaks are shifted towards higher photon energy.

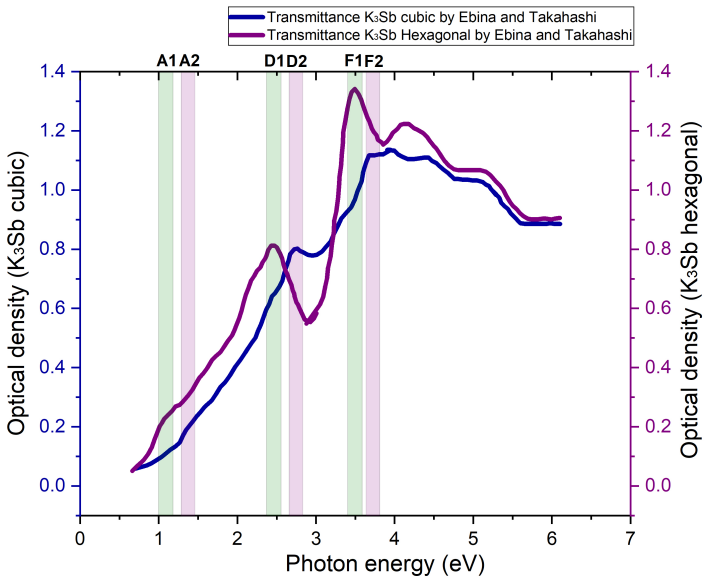

Figure 8.28: Comparison of the transmittance data obtained from the K_3Sb-cubic and hexagonal material as reported by Ebina and Takahashi et al. [233]. The similarities of peaks between the two graphs are highlighted using letters A, D, and F. Furthermore, these similar peaks are visually marked with different colored boxes, where violet-colored boxes represent the peaks in the K_3Sb cubic compound, and green-colored boxes represent the peaks in the K_3Sb hexagonal compound.

G Comparison of Reflectivity data: Experimental (literature) vs. DFT Simulations for K_3Sb (Hexagonal) Compound

Similar to the comparison of dielectric function data, we also conducted a comparison of reflectivity data between experimental (literature) and DFT simulated datasets for the K_3Sb (hexagonal) compound. Figure 8.29a displays the experimental reflectivity measurements of a K_3Sb (hexagonal) film, as conducted by Ebina and Takahashi et al. [236]. The reflectivity plot (Fig. 8.29a) reveals distinct peaks at 1.69 eV (a shoulder), 2.17 eV, 2.42 eV, 3.52 eV, 4.47 eV, and 5.40 eV (a shoulder), which correspond to the B', C', D', F', J', and K' peaks, respectively. In Figure 8.29b, the DFT calculated reflectivity of K_3Sb (hexagonal) compound is presented. As already reported in the DFT results section (Section 5.5.3.1.2, page 209), several peaks are observed at specific energy values in the simulated reflectivity plot: 1.00 eV, 1.51 eV, 2.16 eV, 2.45 eV, 2.85 eV, 3.36, 3.56 eV, 3.90 eV, 4.18 eV, 4.47 eV, and 5.27-5.45 eV (highlighted by violet-coloured boxes), corresponding to the A, B, C, D, E, F, G, H, I, J and K peaks, respectively. Figure 8.29c illustrates the comparison between the experimental (literature [236]) and simulated reflectivity plot of the K_3Sb (hexagonal) compound. The peaks in both curves show a noticeable similarity, as depicted by the light blue-coloured boxes highlighting the corresponding peaks. The consistency observed between the two plots not only verifies the precision of the simulation but also provides confirmation of the existence of distinct electronic transitions or excitations within the material at the energy levels in question. It is important to acknowledge that the peak labelled B in the simulated plot does not precisely align with the corresponding peak in the experimental data. This slight deviation may stem from a range of factors, including measurement uncertainties, limitations inherent to the simulation method employed, or other unaccounted variables. Furthermore, it is worth noting that the experimental reflectivity plot (Fig. 8.29a) does not cover the full range of photon energies, as it begins from 1.48 eV. Consequently, it does not capture the onset peak labeled as A, as observed in the simulated plot (Fig. 8.29b). Moreover, the

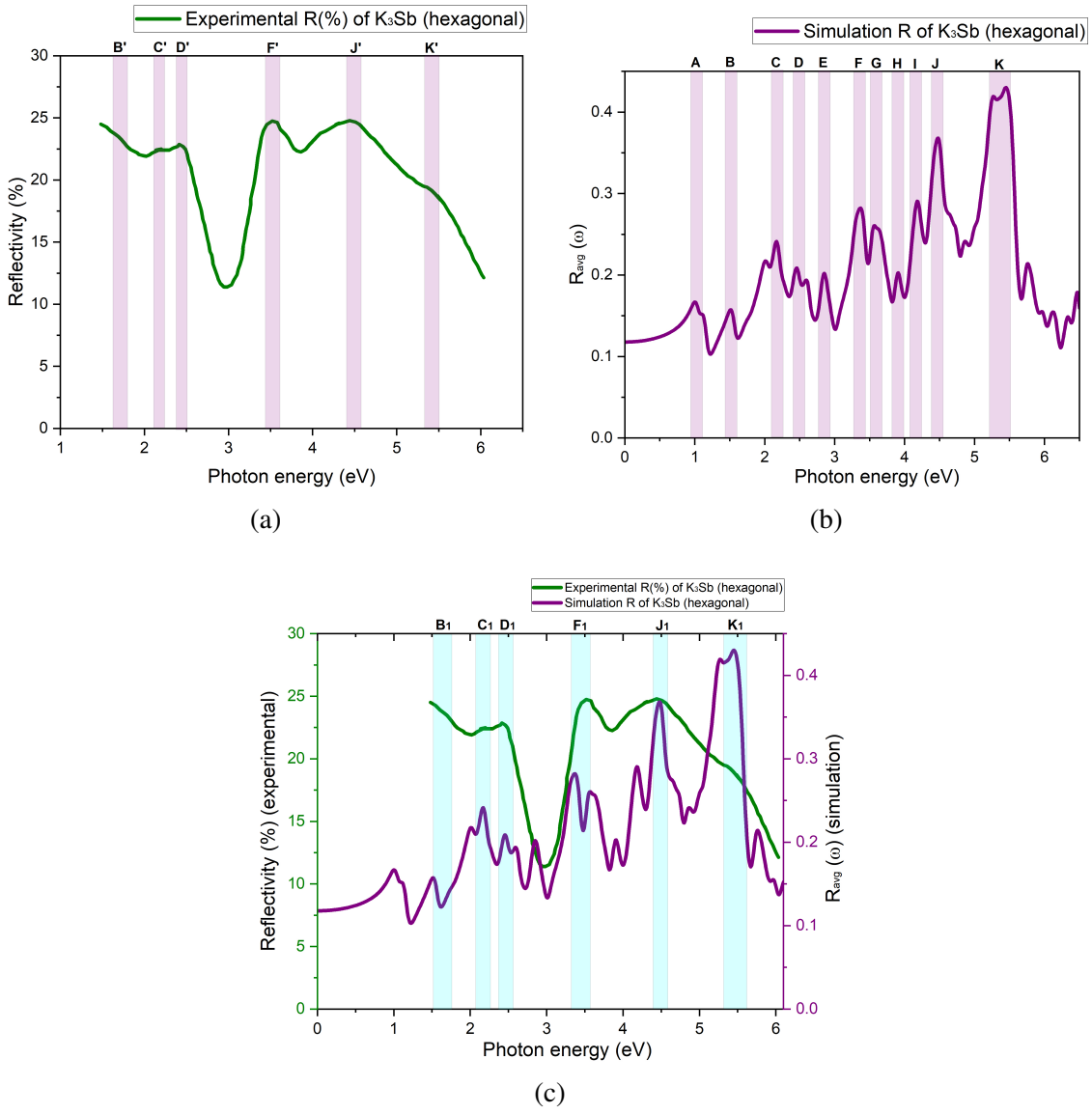

Figure 8.29: (a) Reflectivity curve of the K_3Sb hexagonal compound, as documented in reference [236]. The plot presented in this work has been generated with permission using data from reference [236]. (b) simulated reflectivity of K_3Sb (hexagonal) obtained from density functional theory (DFT) calculations (c) depicts a comparison between the reflectivity obtained experimentally (by A. Ebina et.al. [236]) and through simulation.

peaks E, G, H, and I, which are clearly observed in the simulated plot, are not prominently present in the experimental plot. This discrepancy could be attributed to certain limitations in the measurement process, such as sensitivity or resolution issues. However,

it is noteworthy that two major dips in the reflectivity plot, occurring near 3 eV and 3.8 eV, exhibit consistency between both the experimental and simulated plots.

H Published Papers

1. **Mohanty, S.K.**; Krasilnikov, M.; Oppelt, A.; Stephan, F.; Sertore, D.; Monaco, L.; Pagani, C.; Hillert, W. Development and Characterization of Multi-Alkali Antimonide Photocathodes for High-Brightness RF Photoinjectors. Micromachines 2023, 14, 1182. doi:10.3390/mi14061182.

2. L. Monaco; D. Sertore; M. Krasilnikov; **S. Mohanty**; A. Oppelt; F. Stephan, "Photocathode activities at INFN LASA," in *Proc. IPAC'23*, Venice, Italy, May 2023, pp. 1370–1373. doi:10.18429/JACoW-IPAC2023-TUPA008.

3. **S. Mohanty**; H. Qian; Z. Aboulbanine; G. D. Adhikari; N. Aftab; et al., "Development and Test Results of Multi-Alkali Antimonide Photocathodes in the High Gradient RF Gun at PITZ," in *Proc. FEL2022*, Trieste. doi:10.18429/jacow-fel2022-tup04.

4. D. Sertore; M. Bertucci; G. Guerini Rocco; **S.K. Mohanty**; L. Monaco; H.J. Qian; F. Stephan, "R&D on High QE Photocathodes at INFN LASA," in *Proc. IPAC'22*, Bangkok, Thailand, Jun. 2022, pp. 2633–2636. doi:10.18429/JACoW-IPAC2022-THPOPT027.

5. **S.K. Mohanty**; M. Krasilnikov; A. Oppelt; H. Qian; F. Stephan; et al., "Development of Multi-Alkali Antimonides Photocathodes for High-Brightness RF Photoinjectors," in *Proc. IPAC'21*, Campinas, SP, Brazil, May 2021, pp. 1416–1419. doi:10.18429/JACoW-IPAC2021-TUPAB034.

6. **S.K. Mohanty**, G. Guerini Rocco, P. Michelato, L. Monaco, C. Pagani, and D. Sertore, "Development of a Multialkali Antimonide Photocathode at INFN LASA", in Proc. FEL'19, Hamburg, Germany, Aug. 2019, pp. 448-451. doi:10.18429/JACoW-FEL2019-WEP053.

7. D. Sertore, G. Guerini Rocco, P. Michelato, **S.K. Mohanty**, L. Monaco, and C. Pagani, "Photocathode Activities at INFN LASA", in Proc. IPAC'19, Melbourne, Australia, May 2019, pp. 2203-2206. doi:10.18429/JACoW-IPAC2019-TUPTS117.

References

[1] E. Jaeschke, S. Khan, J. R. Schneider, and J. B. Hastings, Eds., *Synchrotron Light Sources and Free-Electron Lasers: Accelerator Physics, Instrumentation and Science Applications*. Springer, 2016. [Online]. Available: https://doi.org/10.1007/978-3-319-14394-1

[2] "Europe turns on bright x-ray source," *Nature Photonics*, vol. 11, no. 10, pp. 609–609, Sep. 2017. [Online]. Available: https://doi.org/10.1038/s41566-017-0025-z

[3] T. Rao and D. H. Dowell, "An engineering guide to photoinjectors," 2014.

[4] C. M. R. Greaves, "Metal Photocathodes for Free Electron Laser Applications," Ph.D. dissertation, University of California, Berkeley, Jan. 2012.

[5] L. Guo, M. Kuriki, A. Yokota, M. Urano, and K. Negishi, "Substrate dependence of CsK_2Sb photo-cathode performance," *Progress of Theoretical and Experimental Physics*, vol. 2017, no. 3, Mar. 2017. [Online]. Available: https://doi.org/10.1093/ptep/ptx030

[6] F. S. *et al.*, "Detailed characterization of electron sources yielding first demonstration of european x-ray free-electron laser beam quality," *Physical Review Special Topics - Accelerators and Beams*, vol. 13, no. 2, Feb. 2010. [Online]. Available: https://doi.org/10.1103/physrevstab.13.020704

[7] P. Michelato, C. Pagani, A. di Bona, and S. Valeri, "R&D activity on high QE alkali photocathodes for RF guns," *Conf. Proc. C*, vol. 950501, pp. 1049–1051, 1996.

[8] L. Cultrera, J. Maxson, I. Bazarov, S. Belomestnykh, J. Dobbins, B. Dunham, S. Karkare, R. Kaplan, V. Kostroun, Y. Li, X. Liu, F. Löhl, K. Smolenski, Z. Zhao, D. Rice, P. Quigley, M. Tigner, V. Veshcherevich, K. Finkelstein, D. Dale, and B. Pichler, "Photocathode behavior during high current running in the cornell energy recovery linac photoinjector," *Physical Review Special Topics - Accelerators and Beams*, vol. 14, no. 12, Dec. 2011. [Online]. Available: https://doi.org/10.1103/physrevstab.14.120101

[9] H. Qian, J. Feng, D. Filippetto, R. Li, J. Nasiatka, H. Padmore, F. Sannibale, J. Schmerge, and F. Zhou, "Alkali cathode testing for LCLS-II at APEX," *Proceedings of the 37th International Free Electron Laser Conference*, vol. FEL2015, p. Republic of Korea, 2015. [Online]. Available: http://accelconf.web.cern.ch/AccelConf/DOI/FEL2015/JACoW-FEL2015-MOD03.html

[10] P. Michelato, Jun 1996. [Online]. Available: https://accelconf.web.cern.ch/e96/PAPERS/THPL/THP068L.PDF

[11] A. L. Smith and R. Breitwieser, "Richardson-Dushman Equation Monograph," *Journal of Applied Physics*, vol. 41, no. 1, pp. 436–437, 01 1970. [Online]. Available: https://doi.org/10.1063/1.1658371

[12] D. M. Goebel and I. Katz, *"Fundamentals of electric propulsion"*, ser. JPL Space Science and Technology Series. Nashville, TN: John Wiley & Sons, Dec. 2008.

[13] M. Bakr, R. Kinjo, Y. Choi, M. Omer, K. Yoshida, K. Ishida, N. Kimura, T. Komai, M. Shibata, K. Shimahashi, H. Imon, T. Sonobe, H. Zen, M. Kawai, T. Kii, K. Masuda, and H. Ohgaki, "Assessment of thermionic emission properties and back bombardment effects for LaB6 and CeB6," *FEL 2011 - 33rd International Free Electron Laser Conference*, pp. 557–560, 01 2011.

[14] M. Borland, "A high-brightness thermionic microwave electron gun," Tech. Rep., Feb. 1991. [Online]. Available: https://doi.org/10.2172/10164508

[15] V. Zworykin and E. Ramberg, *"Photoelectricity and Its Application"*. New York, 1949. [Online]. Available: https://books.google.de/books?id=QSndxwEACAAJ

[16] A. H. Sommer, *"Photoemissive materials"*. John Wiley & Sons, Jan. 1968.

[17] J. Elster and H. Geitel, "Ueber die Entladung negativ electrischer Körper durch das Sonnen- und Tageslicht," *Annalen der Physik*, vol. 274, no. 12, pp. 497–514, 1889. [Online]. Available: https://onlinelibrary.wiley.com/doi/abs/10.1002/andp.18892741202

[18] B. R. Wheaton, "Philipp Lenard and the Photoelectric Effect, 1889-1911," *Historical Studies in the Physical Sciences*, vol. 9, pp. 299–322, 01 1978. [Online]. Available: https://doi.org/10.2307/27757381

[19] P. Lenard, "Ueber die lichtelektrische wirkung," Sep. 2018. [Online]. Available: https://doi.org/10.1002/andp.19023130510

[20] A. Pais, "Einstein and the quantum theory," *Rev. Mod. Phys.*, vol. 51, pp. 863–914, Oct 1979. [Online]. Available: https://link.aps.org/doi/10.1103/RevModPhys.51.863

[21] "The Nobel Prize in Physics 1921," NobelPrize.org, 1921, accessed: 2024-04-22. [Online]. Available: https://www.nobelprize.org/prizes/physics/1921/summary/

[22] D. Dowell, S. Lidia, and J. Schmerge, "Lecture 2: Electron emission and cathode, uspas course on high brightness electron injectors for 4th generationlight sources," Santa Rosa, CA, January 2008.

[23] L. Cultrera, "Advances in photocathodes for accelerators," *Proceedings of the 5th Int. Particle Accelerator Conf.*, vol. IPAC2014, p. Germany, 2014. [Online]. Available: http://jacow.org/ipac2014/doi/JACoW-IPAC2014-MOZB02.html

[24] Wikipedia, "Reflectance — Wikipedia," http://en.wikipedia.org/w/index.php?title=Reflectance&oldid=1188640736, 2024, [Online; accessed 29-January-2024].

[25] D. Edwards and M. Syphers, "An introduction to the physics of high energy accelerators." Wiley-VCH Verlag GmbH, Jan. 2008.

[26] E. Chiadroni, "Electron sources and injection system: Proceedings of the CAS-CERN accelerator school on free electron lasers and energy recovery linacs," pp. 401–402, 2018. [Online]. Available: https://e-publishing.cern.ch/index.php/CYRSP/issue/view/47

[27] J. Yang, *"Femtosecond Electron Diffraction Using Relativistic Electron Pulses"*. IntechOpen, Jun. 2020. [Online]. Available: http://dx.doi.org/10.5772/intechopen.88511

[28] D. Dowell, "Sources of emittance in rf photocathode injectors," SLAC National Accelerator Laboratory, Menlo Park, CA, Tech. Rep. SLAC-PUB-16895, 2016, available online: https://arxiv.org/abs/1610.01242v3.

[29] D. H. Dowell and J. F. Schmerge, "Quantum efficiency and thermal emittance of metal photocathodes," *Physical Review Special Topics - Accelerators and Beams*, vol. 12, no. 7, Jul. 2009. [Online]. Available: https://doi.org/10.1103/physrevstab.12.074201

[30] L. Cultrera, I. Bazarov, A. Bartnik, B. Dunham, S. Karkare, R. Merluzzi, and M. Nichols, "Thermal emittance and response time of a cesium antimonide photocathode," *Applied Physics Letters*, vol. 99, no. 15, 10 2011, 152110. [Online]. Available: https://doi.org/10.1063/1.3652758

[31] J. L. M. *et.al.*, "Performance study of K_2CsSb photocathode inside a DC high voltage gun," *Proceedings of 2011 Particle Accelerator Conference*, vol. PAC2011, pp. NY,USA, 2011. [Online]. Available: https://accelconf.web.cern.ch/pac2011/papers/wep284.pdf

[32] C. Shonaka, H. Higaki, K. Ito, D. Kubo, M. Kuriki, H. Okamoto, T. Konomi, T. Nakanishi, S. Okumi, and M. Yamamoto, "A Study of Lifetime of GaAs Photo-

cathode for High Brightness Electron Source," in *Particle Accelerator Conference (PAC 09)*, 2010, p. MO6RFP069.

[33] J. H. Han, M. Krasilnikov, and K. Flöttmann, "Secondary electron emission in a photocathode rf gun," *Phys. Rev. ST Accel. Beams*, vol. 8, p. 033501, Mar 2005. [Online]. Available: https://link.aps.org/doi/10.1103/PhysRevSTAB.8.033501

[34] H. Chen, Y. Du, W. Gai, A. Grudiev, J. Hua, W. Huang, J. Power, E. E. Wisniewski, W. Wuensch, C. Tang, L. Yan, and Y. You, "Photocathode emission studies: Dark current and Schottky-enabled photo-electrons in a high-field RF gun," *AIP Conference Proceedings*, vol. 1507, no. 1, pp. 435–439, 12 2012. [Online]. Available: https://doi.org/10.1063/1.4773736

[35] S. L. *et.al*., "Investigations on the increased lifetime of photocathodes at FLASH and PITZ," *Proceedings of PAC09*, pp. Vancouver, CANADA, 2009. [Online]. Available: https://accelconf.web.cern.ch/pac2009/papers/mo6rfp055.pdf

[36] D. Sertore, S. Schreiber, K. Floettmann, F. Stephan, K. Zapfe, and P. Michelato, "First operation of cesium telluride photocathodes in the TTF injector RF gun," *Nuclear Instruments and Methods in Physics Research Section A: Accelerators, Spectrometers, Detectors and Associated Equipment*, vol. 445, no. 1, pp. 422–426, 2000. [Online]. Available: https://www.sciencedirect.com/science/article/pii/S0168900200000954

[37] C. Suzuki, T. Nakanishi, S. Okumi, T. Gotou, K. Togawa, F. Furuta, K. Wada, T. Nishitani, M. Yamamoto, J. Watanabe, S. Kurahashi, K. Asano, H. Matsumoto, M. Yoshioka, and H. Kobayakawa, "Fabrication of ultra-clean copper surface to minimize field emission dark currents," *Nuclear Instruments and Methods in Physics Research Section A: Accelerators, Spectrometers, Detectors and Associated Equipment*, vol. 462, no. 3, pp. 337–348, 2001. [Online]. Available: https://www.sciencedirect.com/science/article/pii/S0168900200011232

[38] H. Rosenberg, *"The Solid State: An Introduction to the Physics of Crystals for Students of Physics, Materials Science, and Engineering"*, ser.

Oxford physics series. Oxford University Press, 1988. [Online]. Available: https://books.google.de/books?id=BRimQgAACAAJ

[39] C. Kittel and P. McEuen, *"Introduction to Solid State Physics"*. John Wiley & Sons, 2018.

[40] S. A. Holgate, *"Understanding Solid State Physics"*. CRC Press, Apr. 2021. [Online]. Available: https://doi.org/10.1201/9780429288234

[41] W. E. Spicer and A. Herrera-Gomez, "Modern theory and applications of photocathodes," in *SPIE Proceedings*, K. J. Kaufmann, Ed. SPIE, Oct. 1993. [Online]. Available: https://doi.org/10.1117/12.158575

[42] D. Dowell, I. Bazarov, B. Dunham, K. Harkay, C. Hernandez-Garcia, R. Legg, H. Padmore, T. Rao, J. Smedley, and W. Wan, "Cathode R&D for future light sources," *Nuclear Instruments and Methods in Physics Research Section A: Accelerators, Spectrometers, Detectors and Associated Equipment*, vol. 622, no. 3, pp. 685–697, 2010. [Online]. Available: https://www.sciencedirect.com/science/article/pii/S0168900210006868

[43] S. Kong, J. Kinross-Wright, D. Nguyen, and R. Sheffield, "Photocathodes for free electron lasers," *Nuclear Instruments and Methods in Physics Research Section A: Accelerators, Spectrometers, Detectors and Associated Equipment*, vol. 358, no. 1-3, pp. 272–275, Apr. 1995. [Online]. Available: https://doi.org/10.1016/0168-9002(94)01425-6

[44] C. Benjamin, G. Bell, H. Churn, L. Jones, T. Noakes, and T. Rehaag, "Photocathode Performance Characterisation of Ultra-Thin MgO Films on Polycrystalline Copper," *Proceedings of the 13th International Particle Accelerator Conference*, vol. IPAC2022, p. Thailand, 2022. [Online]. Available: https://jacow.org/ipac2022/doi/JACoW-IPAC2022-MOPOMS025.html

[45] J. T. *et al.*,, "Report on photocathodes," Tech. Rep., JULY 2004. [Online]. Available: https://cds.cern.ch/record/941432/files/care-report-05-028.pdf

[46] A. di Bona, F. Sabary, S. Joly, P. Michelato, D. Sertore, C. Pagani, and S. Valeri, "Development, operation and analysis of bialkali antimonide photocathodes for high-brightness photo-injectors," *Nuclear Instruments and Methods in Physics Research Section A: Accelerators, Spectrometers, Detectors and Associated Equipment*, vol. 385, no. 3, pp. 385–390, 1997. [Online]. Available: https://www.sciencedirect.com/science/article/pii/S0168900296008091

[47] Y. Honda, S. Matsuba, X. Jin, T. Miyajima, M. Yamamoto, T. Uchiyama, M. Kuwahara, and Y. Takeda, "Temporal response measurements of GaAs-based photocathodes," *Japanese Journal of Applied Physics*, vol. 52, no. 8R, p. 086401, Jul. 2013. [Online]. Available: https://doi.org/10.7567/jjap.52.086401

[48] D. Sertore, S. Schreiber, K. Floettmann, F. Stephan, K. Zapfe, and P. Michelato, "First operation of cesium telluride photocathodes in the TTF injector RF gun," *Nuclear Instruments and Methods in Physics Research Section A: Accelerators, Spectrometers, Detectors and Associated Equipment*, vol. 445, no. 1-3, pp. 422–426, May 2000. [Online]. Available: https://doi.org/10.1016/s0168-9002(00)00095-4

[49] P. Michelato, "Photocathodes for RF photoinjectors," *Nuclear Instruments and Methods in Physics Research Section A: Accelerators, Spectrometers, Detectors and Associated Equipment*, vol. 393, no. 1-3, pp. 455–459, Jul. 1997. [Online]. Available: https://doi.org/10.1016/s0168-9002(97)00545-7

[50] S. Lederer and S. Schreiber, "Cs_2Te Photocathode Lifetime at Flash and European XFEL," in *Proc. 9th International Particle Accelerator Conference (IPAC'18), Vancouver, BC, Canada, April 29-May 4, 2018*, ser. International Particle Accelerator Conference, no. 9. Geneva, Switzerland: JACoW Publishing, June 2018, paper WEPMF056, pp. 2496–2498. [Online]. Available: http://jacow.org/ipac2018/papers/wepmf056.pdf

[51] S. Lederer, F. Brinker, L. Monaco, S. Schreiber, and D. Sertore, "Update on the Photocathode Lifetime at FLASH and European XFEL," in *Proc. FEL'19*,

ser. Free Electron Laser Conference, no. 39. JACoW Publishing, Geneva, Switzerland, nov 2019, paper WEP047, pp. 427–429. [Online]. Available: http://jacow.org/fel2019/papers/wep047.pdf

[52] G. Loisch, Y. Chen, C. Koschitzki, H. Qian, M. Gross, A. Hannah, A. Hoffmann, D. Kalantaryan, M. Krasilnikov, S. Lederer, X. Li, O. Lishilin, D. Melkumyan, L. Monaco, R. Niemczyk, A. Oppelt, D. Sertore, F. Stephan, R. Valizadeh, G. Vashchenko, and T. Weilbach, "Direct measurement of photocathode time response in a high-brightness photoinjector," *Applied Physics Letters*, vol. 120, no. 10, 03 2022, 104102. [Online]. Available: https://doi.org/10.1063/5.0078927

[53] S. K. Mohanty, M. Krasilnikov, A. Oppelt, F. Stephan, D. Sertore, L. Monaco, C. Pagani, and W. Hillert, "Development and Characterization of Multi-Alkali Antimonide Photocathodes for High-Brightness RF Photoinjectors," *Micromachines*, vol. 14, no. 6, 2023. [Online]. Available: https://www.mdpi.com/2072-666X/14/6/1182

[54] E. Chevallay, J. Durand, S. Hutchins, G. Suberlucq, and H. Trautner, "Photo-cathodes for the CERN CLIC Test Facility," 1998. [Online]. Available: https://cds.cern.ch/record/364521

[55] E. Chevallay, J. Durand, S. Hutchins, G. Suberlucq, and M. Wurgel, "Photocathodes tested in the dc gun of the CERN photoemission laboratory," *Nuclear Instruments and Methods in Physics Research Section A: Accelerators, Spectrometers, Detectors and Associated Equipment*, vol. 340, no. 1, pp. 146–156, 1994. [Online]. Available: https://www.sciencedirect.com/science/article/pii/0168900294912939

[56] T. Vecchione, I. Ben-Zvi, D. H. Dowell, J. Feng, T. Rao, J. Smedley, W. Wan, and H. A. Padmore, "A low emittance and high efficiency visible light photocathode for high brightness accelerator-based X-ray light sources," *Applied Physics Letters*, vol. 99, no. 3, 07 2011, 034103. [Online]. Available: https://doi.org/10.1063/1.3612916

[57] S. Mohanty, H. Qian, Z. Aboulbanine, G. Adhikari, N. Aftab, P. Boonpornprasert, J. Good, M. Gross, A. Hoffmann, M. Krasilnikov, A. Lueangaramwong, R. Niemczyk, A. Oppelt, F. Stephan, T. Weilbach, D. Sertore, L. Monaco, G. G. Rocco, C. Pagani, W.Hillert, and G. Loisch, "Development and test results of multi-alkali antimonides photocathodes in the high gradient RF gun at PITZ," in *Proc. FEL'22*, ser. Free Electron Laser Conference. JACoW Publishing, Geneva, Switzerland, Aug 2022.

[58] I. Martini, "Characterization of Cs-Sb cathodes for high charge RF photoinjectors," 2016, presented 19 Feb 2016. [Online]. Available: https://cds.cern.ch/record/2228514

[59] P. Saha, O. Chubenko, G. S. Gevorkyan, A. Kachwala, C. J. Knill, C. Sarabia-Cardenas, E. Montgomery, S. Poddar, J. T. Paul, R. G. Hennig, H. A. Padmore, and S. Karkare, "Physically and chemically smooth cesium-antimonide photocathodes on single crystal strontium titanate substrates," *Applied Physics Letters*, vol. 120, no. 19, 05 2022, 194102. [Online]. Available: https://doi.org/10.1063/5.0088306

[60] A. Galdi, W. J. I. DeBenedetti, J. Balajka, L. Cultrera, I. V. Bazarov, J. M. Maxson, and M. A. Hines, "The effects of oxygen-induced phase segregation on the interfacial electronic structure and quantum efficiency of Cs_3Sb photocathodes," *The Journal of Chemical Physics*, vol. 153, no. 14, 10 2020, 144705. [Online]. Available: https://doi.org/10.1063/5.0024020

[61] A. H. Sommer, "New Photoemissive Cathodes of High Sensitivity," *Review of Scientific Instruments*, vol. 26, no. 7, pp. 725–726, 12 2004. [Online]. Available: https://doi.org/10.1063/1.1715296

[62] P. Dolizy, "Growth of alkali-antimonide films for photocathodes. ," 1982. [Online]. Available: https://www.pearl-hifi.com/06_Lit_Archive/02_PEARL_Arch/Vol_16/Sec_53/Philips_Tech_Review/PTechReview-40-1982-019.pdf

[63] L. Cultrera, S. Karkare, B. Lillard, A. Bartnik, I. Bazarov, B. Dunham, W. Schaff, and K. Smolenski, "Growth and characterization of rugged sodium

potassium antimonide photocathodes for high brilliance photoinjector," *Applied Physics Letters*, vol. 103, no. 10, 09 2013, 103504. [Online]. Available: https://doi.org/10.1063/1.4820132

[64] S. Mohanty, G. Guerini Rocco, W. Hillert, M. Krasilnikov, P. Michelato, L. Monaco, A. Oppelt, C. Pagani, H. Qian, D. Sertore, and F. Stephan, "Development of Multi-Alkali Antimonides Photocathodes for High-Brightness RF Photoinjectors," in *Proceedings of the 12th International Particle Accelerator Conference, IPAC2021, Campinas, SP, Brazil*. 12th International Particle Accelerator Conference, Campinas (Brazil), 24 May 2021 - 28 May 2021, May 2021, pp. 1416–1419. [Online]. Available: https://bib-pubdb1.desy.de/record/472757

[65] C. Pennington, "Testing alkali antimonide photocathodes in high gradient injectors," 2021. [Online]. Available: https://conf.slac.stanford.edu/photocathode-physics-photoinjectors-2021/agenda

[66] A. H. Sommer, "A NEW ALKALI ANTIMONIDE PHOTOEMITTER WITH HIGH SENSITIVITY TO VISIBLE LIGHT," *Applied Physics Letters*, vol. 3, no. 4, pp. 62–63, 11 2004. [Online]. Available: https://doi.org/10.1063/1.1753869

[67] S. Schubert, J. Wong, J. Feng, S. Karkare, H. Padmore, M. Ruiz-Osés, J. Smedley, E. Muller, Z. Ding, M. Gaowei, K. Attenkofer, X. Liang, J. Xie, and J. Kühn, "Bi-alkali antimonide photocathode growth: An X-ray diffraction study," *Journal of Applied Physics*, vol. 120, no. 3, 07 2016, 035303. [Online]. Available: https://doi.org/10.1063/1.4959218

[68] S. Mohanty, G. G. Rocco, P. Michelato, L. Monaco, C. Pagani, and D. Sertore, "Development of a Multialkali Antimonide Photocathode at INFN LASA," in *Proc. FEL'19*, ser. Free Electron Laser Conference, no. 39. JACoW Publishing, Geneva, Switzerland, nov 2019, paper WEP053, pp. 448–451, https://doi.org/10.18429/JACoW-FEL2019-WEP053. [Online]. Available: http://jacow.org/fel2019/papers/wep053.pdf

[69] Z. Ding, M. Gaowei, J. Sinsheimer, J. Xie, S. Schubert, H. Padmore, E. Muller, and J. Smedley, "In-situ synchrotron x-ray characterization of K_2CsSb photocathode grown by ternary co-evaporation," *Journal of Applied Physics*, vol. 121, no. 5, 02 2017, 055305. [Online]. Available: https://doi.org/10.1063/1.4975113

[70] M. A. H. Schmeißer, S. Mistry, H. Kirschner, S. Schubert, A. Jankowiak, T. Kamps, and J. Kühn, "Towards the operation of Cs-K-Sb photocathodes in superconducting rf photoinjectors," *Phys. Rev. Accel. Beams*, vol. 21, p. 113401, Nov 2018. [Online]. Available: https://link.aps.org/doi/10.1103/PhysRevAccelBeams.21.113401

[71] P. Michelato, A. Di Bona, C. Pagani, D. Sertore, and S. Valeri, "R&D activity on high qe alkali photocathodes for rf guns," in *Proceedings Particle Accelerator Conference*, vol. 2, 1995, pp. 1049–1051 vol.2.

[72] E. Wang, V. N. Litvinenko, I. Pinayev, M. Gaowei, J. Skaritka, S. Belomestnykh, I. Ben-Zvi, J. C. Brutus, Y. Jing, J. Biswas, J. Ma, G. Narayan, I. Petrushina, O. Rahman, T. Xin, T. Rao, F. Severino, K. Shih, K. Smith, G. Wang, and Y. Wu, "Long lifetime of bialkali photocathodes operating in high gradient superconducting radio frequency gun," *Scientific Reports*, vol. 11, no. 1, Feb. 2021. [Online]. Available: https://doi.org/10.1038/s41598-021-83997-1

[73] L. Monaco, G. Guerini Rocco, P. Michelato, C. Pagani, and D. Sertore, "Growing and Characterization of Cs_2Te Photocatodes with Different Thicknesses at INFN LASA," *Proceedings of the 39th Free Electron Laser Conference*, vol. FEL2019, p. Germany, 2019. [Online]. Available: http://jacow.org/fel2019/doi/JACoW-FEL2019-WEA04.html

[74] D. Anderson, S. Kwan, and V. Peskov, "CsI photocathode QE and a simple production technique," *Nuclear Instruments and Methods in Physics Research Section A: Accelerators, Spectrometers, Detectors and Associated Equipment*, vol. 326, no. 3, pp. 611–612, 1993. [Online]. Available: https://www.sciencedirect.com/science/article/pii/016890029390866G

[75] W. E. Spicer, "Photoemissive, Photoconductive, and Optical Absorption Studies of Alkali-Antimony Compounds," *Phys. Rev.*, vol. 112, pp. 114–122, Oct 1958. [Online]. Available: https://link.aps.org/doi/10.1103/PhysRev.112.114

[76] S. Mistry, J. Dube, T. Kamps, J. Kühn, and C. Wang, "EVALUATION OF THE IN-SITU PHOTOCATHODE HANDLING FOR SRF PHOTOINJECTOR OF SEALab," 09 2023. [Online]. Available: https://accelconf.web.cern.ch/ipac2023/doi/jacow-ipac2023-thpa141/

[77] W. H. McCarroll, R. J. Paff, and A. H. Sommer, "Role of Cs in the (Cs)Na_2KSb (S-20) Multialkali Photocathode," *Journal of Applied Physics*, vol. 42, no. 2, pp. 569–572, 12 2003. [Online]. Available: https://doi.org/10.1063/1.1660065

[78] S. Mohanty, G. G. Rocco, W. Hillert, M. Krasilnikov, P. Michelato, L. Monaco, A. Oppelt, C. Pagani, H. Qian, D. Sertore, and F. Stephan, "Development of Multi-Alkali Antimonides Photocathodes for High-Brightness RF Photoinjectors," in *Proc. IPAC'21*, ser. International Particle Accelerator Conference, no. 12. JACoW Publishing, Geneva, Switzerland, 08 2021, pp. 1416–1419, https://doi.org/10.18429/JACoW-IPAC2021-TUPAB034. [Online]. Available: https://jacow.org/ipac2021/papers/tupab034.pdf

[79] C. Ghosh and B. P. Varma, "Preparation and study of properties of a few alkali antimonide photocathodes," *Journal of Applied Physics*, vol. 49, no. 8, pp. 4549–4553, 08 2008. [Online]. Available: https://doi.org/10.1063/1.325465

[80] S. Mohanty, et al., "Development and Test Results of Multi-Alkali Antimonide Photocathodes in the High Gradient RF Gun at PITZ," in *Proc. FEL2022*, ser. International Free Electron Laser Conference, no. 40. JACoW Publishing, Geneva, Switzerland, 08 2022, paper TUP04, pp. 163–167. [Online]. Available: https://indico.jacow.org/event/44/contributions/471

[81] M. Herbert, J. Enders, M. Poelker, and C. Hernandez-Garcia, "Lifetime Measurements of GaAs photocathodes at the Upgraded Injector Test Facility at

Jefferson Lab," 09 2020, p. 042. [Online]. Available: https://doi.org/10.22323/1.379.0042

[82] J. K. Bae, M. Andorf, A. Bartnik, A. Galdi, L. Cultrera, J. Maxson, and I. Bazarov, "Operation of Cs–Sb–O activated GaAs in a high voltage DC electron gun at high average current," *AIP Advances*, vol. 12, no. 9, p. 095017, 09 2022. [Online]. Available: https://doi.org/10.1063/5.0100794

[83] J. Biswas, E. Wang, M. Gaowei, W. Liu, O. Rahman, and J. T. Sadowski, "High quantum efficiency GaAs photocathodes activated with Cs, O_2, and Te," *AIP Advances*, vol. 11, no. 2, Feb. 2021. [Online]. Available: https://doi.org/10.1063/5.0026839

[84] Y. Chen, M. Krasilnikov, and F. Stephan, "The cooling effect of beam self-fields on the photocathode surface in high gradient RF injectors," *Journal of Physics: Conference Series*, vol. 1350, no. 1, p. 012121, Nov. 2019. [Online]. Available: https://doi.org/10.1088/1742-6596/1350/1/012121

[85] G. Shu, Y. Chen, S. Lal, H. Qian, S. H. Shaker, and F. Stephan, "Multiphysics Analysis of a CW VHF Gun for European XFEL," *Proceedings of the 39th Free Electron Laser Conference*, vol. FEL2019, p. Germany, 2019. [Online]. Available: http://jacow.org/fel2019/doi/JACoW-FEL2019-WEP055.html

[86] G. Loisch, G. Asova, P. Boonpornprasert, R. Brinkmann, Y. Chen, J. Engel, J. Good, M. Gross, F. Grüner, H. Huck, D. Kalantaryan, M. Krasilnikov, O. Lishilin, A. M. de la Ossa, T. J. Mehrling, D. Melkumyan, A. Oppelt, J. Osterhoff, H. Qian, Y. Renier, F. Stephan, C. Tenholt, V. Wohlfarth, and Q. Zhao, "Observation of High Transformer Ratio Plasma Wakefield Acceleration," *Phys. Rev. Lett.*, vol. 121, p. 064801, Aug 2018. [Online]. Available: https://link.aps.org/doi/10.1103/PhysRevLett.121.064801

[87] M. Gross, R. Brinkmann, J. Good, F. Grüner, M. Khojoyan, A. Martinez de la Ossa, J. Osterhoff, G. Pathak, C. Schroeder, and F. Stephan, "Preparations for a plasma wakefield acceleration (PWA) experiment at PITZ," *Nuclear Instruments and*

Methods in Physics Research Section A: Accelerators, Spectrometers, Detectors and Associated Equipment, vol. 740, pp. 74–80, 2014, proceedings of the first European Advanced Accelerator Concepts Workshop 2013. [Online]. Available: https://www.sciencedirect.com/science/article/pii/S0168900213015817

[88] H. Qian, M. Groß, M. Krasilnikov, A. Oppelt, and F. Stephan, "Investigation of High Repetition Rate Femtosecond Electron Diffraction at PITZ," in *Proc. of International Particle Accelerator Conference (IPAC'17), Copenhagen, Denmark, 14-19 May, 2017*, ser. International Particle Accelerator Conference, no. 8. Geneva, Switzerland: JACoW, May 2017, paper THPAB017, pp. 3727–3729. [Online]. Available: http://jacow.org/ipac2017/papers/thpab017.pdf

[89] P. Boonpornprasert, "Investigations on the Capabilities of THz Production at the PITZ Facility," Dissertation, Universität Hamburg, 2020, dissertation, Universität Hamburg, 2020. [Online]. Available: https://bib-pubdb1.desy.de/record/435127

[90] M. Krasilnikov, Z. Aboulbanine, G. Adhikari, N. Aftab, A. Asoyan, P. Boonpornprasert, H. Davtyan, G. Georgiev, J. Good, A. Grebinyk, M. Gross, W. Hillert, A. Hoffmann, E. Kongmon, X.-K. Li, A. Lueangaramwong, D. Melkumyan, S. Mohanty, R. Niemczyk, A. Oppelt, H. Qian, C. Richard, J. Rossbach, E. Schneidmiller, F. Stephan, G. Vashchenko, T. Weilbach, and M. Yurkov, "THz SASE FEL at PITZ: lasing at a wavelength of 100 μm," *Journal of Physics: Conference Series*, vol. 2687, no. 3, p. 032016, Jan. 2024. [Online]. Available: http://dx.doi.org/10.1088/1742-6596/2687/3/032016

[91] Frank Stephan, Matthias Gross, Anna Grebinyk, Zakaria Aboulbanine, Zohrab Amirkhanyan, Volker Budach, Vincent Henrique Ehrhardt, Angeles Faus-Golfe, Marcus Frohme, Jean-Francois Germond, James David Good, et al., "FLASHlab@PITZ: New R&D platform with unique capabilities for electron FLASH and VHEE radiation therapy and radiation biology under preparation at PITZ," *Physica Medica*, vol. 104, pp. 174–187, 2022. [Online]. Available: https://www.sciencedirect.com/science/article/pii/S1120179722020877

[92] T. Weilbach, P. Boonpornprasert, G. Georgiev, G. Koss, M. Krasilnikov, X. Li, A. Lueangaramwong, F. Mueller, A. Oppelt, S. Philipp, H. Shaker, F. Stephan, and L. Vu, "Beam Line Design and Instrumentation for THz@PITZ - the Proof-of-Principle Experiment on a THz SASE FEL at the PITZ Facility," *Proceedings of the 12th International Particle Accelerator Conference*, vol. IPAC2021, p. Brazil, 2021. [Online]. Available: https://jacow.org/ipac2021/doi/JACoW-IPAC2021-TUPAB071.html

[93] I. Will, G. Koss, and I. Templin, "The upgraded photocathode laser of the TESLA Test Facility," *Nuclear Instruments and Methods in Physics Research Section A: Accelerators, Spectrometers, Detectors and Associated Equipment*, vol. 541, no. 3, pp. 467–477, 2005. [Online]. Available: https://www.sciencedirect.com/science/article/pii/S0168900205000082

[94] M. Hanel, "Experimental investigations on the influence of the photocathode laser pulse parameters on the electron bunch quality in an RF-photoelectron source," 2010. [Online]. Available: http://www-library.desy.de/preparch/desy/thesis/desy-thesis-10-027.pdf

[95] I. Will and G. Klemz, "Generation of flat-top picosecond pulses by coherent pulse stacking in a multicrystal birefringent filter," *Opt. Express*, vol. 16, no. 19, pp. 14 922–14 937, Sep 2008. [Online]. Available: https://opg.optica.org/oe/abstract.cfm?URI=oe-16-19-14922

[96] J. Bahr, et al., "Upgrades of the laser beam-line at PITZ," *Proceedings of the 27th International Free Electron Laser Conference*, vol. FEL2005, pp. Stanford, California, USA, 2005. [Online]. Available: https://accelconf.web.cern.ch/f05/PAPERS/MOPP034.PDF

[97] M Gross and H J Qian and P Boonpornprasert and Y Chen and J D Good and H Huck and I Isaev, C Koschitzki, M Krasilnikov, S Lal, X Li, O Lishilin, G Loisch, D Melkumyan, S K Mohanty, R Niemczyk, et al., "Emittance reduction of rf photoinjector generated electron beams by transverse laser beam shaping,"

Journal of Physics: Conference Series, vol. 1350, no. 1, p. 012046, nov 2019. [Online]. Available: https://dx.doi.org/10.1088/1742-6596/1350/1/012046

[98] Light conversion. [Online]. Available: https://lightcon.com/product/pharos-femtosecond-lasers/

[99] S. Y. Mironov, A. K. Potemkin, E. I. Gacheva, A. V. Andrianov, V. V. Zelenogorskii, M. Krasilnikov, F. Stephan, and E. A. Khazanov, "Shaping of cylindrical and 3D ellipsoidal beams for electron photoinjector laser drivers," *Appl. Opt.*, vol. 55, no. 7, pp. 1630–1635, Mar 2016. [Online]. Available: https://opg.optica.org/ao/abstract.cfm?URI=ao-55-7-1630

[100] B. Carlsten, "New photoelectric injector design for the los alamos national laboratory XUV FEL accelerator," *Nuclear Instruments and Methods in Physics Research Section A: Accelerators, Spectrometers, Detectors and Associated Equipment*, vol. 285, no. 1, pp. 313–319, 1989. [Online]. Available: https://www.sciencedirect.com/science/article/pii/0168900289904725

[101] I. Isaev, "Stability and Performance Studies of the PITZ Photoelectron Gun," Ph.D. dissertation, 2018. [Online]. Available: http://bib-pubdb1.desy.de/record/400083

[102] G. Loisch, "Demonstrating High Transformer Ratio Beam-Driven Plasma Wakefield Acceleration," Ph.D. dissertation, 2019. [Online]. Available: http://bib-pubdb1.desy.de/record/426401

[103] V. Paramonov, S. Philipp, I. Rybakov, A. Skassyrskaya, and F. Stephan, "Design of an L-band normally conducting RF gun cavity for high peak and average RF power," *Nuclear Instruments and Methods in Physics Research Section A: Accelerators, Spectrometers, Detectors and Associated Equipment*, vol. 854, pp. 113–126, 2017. [Online]. Available: https://www.sciencedirect.com/science/article/pii/S0168900217302541

[104] M. Krasilnikov, Z. Aboulbanine, G. Adhikari, N. Aftab, P. Boonpornprasert, M. Bousonville, F. Brinker, M. E. Castro Carballo, G. Georgiev, J. Good, M. Groß,

A. Hoffmann, M. Hoffmann, L. Knebel, C. Koschitzki, D. Kostin, S. Lederer, X. Li, L. Lilje, A. Lueangaramwong, D. Melkumyan, R. Niemczyk, A. Oppelt, B. Petrosyan, S. Pfeiffer, S. Philipp, M. Pohl, H. Qian, C. Richard, R. Ritter, S. Schreiber, J. Schultze, G. Shu, F. Stephan, G. Vashchenko, T. Weilbach, H. Weise, M. Wenskat, and J. Ziegler, "RF Performance of a Next-Generation L-Band RF Gun at PITZ," *Proceedings of the 31st International Linear Accelerator Conference*, vol. LINAC2022, p. UK, 2022. [Online]. Available: https://jacow.org/linac2022/doi/JACoW-LINAC2022-THPOJO03.html

[105] Li, Xiangkun, Bousonville, Michael, Schlarb, Holger, Aftab, Namra, Boonpornprasert, Prach, Knebel, Lennart, Lueangaramwong, Anusorn, Schreiber, Siegfried, Jachmann, Lutz, Niemczyk, Raffael, Oppelt, Anne, Schultze, Joerg, Philipp, Sebastian, Melkumyan, David, Stephan, Frank, Hoffmann, Andreas, Castro-Carballo, Maria-Elena, Weilbach, Tobias, Lederer, Sven, Vashchenko, Grygorii, Adhikari, Gowri, Richard, Christopher, Pfeiffer, Sven, Pohl, Mario, Shu, Guan, Wenskat, Marc, Ritter, Rene, Good, James, Aboulbanine, Zakaria, Kostin, Denis, Krasilnikov, Mikhail, Hoffmann, Matthias, Lilje, Lutz, Brinker, Frank, Qian, Houjun, Koschitzki, Christian, Weise, Hans, Georgiev, Georgi, Ziegler, Joerg, Koehler, Winfried, Petrosyan, Bagrat, and Gross, Matthias, "RF Performance of a Next-Generation L-Band RF Gun at PITZ," 2023. [Online]. Available: https://jacow.org/fel2022/doi/jacow-fel2022-tup03

[106] B. Instrumentation, *Bergoz Instrumentation*, http://www.bergoz.com/.

[107] B. Walasek-Höhne, P. Forck, K. Hoehne, R. Ischebeck, and G. Kube, "Screens for High Precision Measurements," in *Proc. IBIC'19*, ser. International Beam Instrumentation Conferenc, no. 8. JACoW Publishing, Geneva, Switzerland, nov 2019, paper TUBO01, pp. 242–248, https://doi.org/10.18429/JACoW-IBIC2019-TUBO01. [Online]. Available: http://jacow.org/ibic2019/papers/tubo01.pdf

[108] R. Niemczyk *et al.*, "Comparison of YAG Screens and LYSO Screens at PITZ," in *Proc. 7th International Beam Instrumentation Conference (IBIC'18), Shanghai, China, 09-13 September 2018*, ser. International Beam Instrumentation

Conference, no. 7. Geneva, Switzerland: JACoW Publishing, Jan. 2019, paper WEPB04, pp. 438–440. [Online]. Available: http://jacow.org/ibic2018/papers/wepb04.pdf

[109] Allied vision technologies gmbh. [Online]. Available: https://www.alliedvision.com/en/products/cameras.html

[110] G. Vashchenko, "Transverse phase space studies with the new CDS booster cavity at PITZ," Ph.D. dissertation, University of Hamburg, Hamburg, 2013, iSSN 1435-8085; University of Hamburg, Diss., 2013. [Online]. Available: https://bib-pubdb1.desy.de/record/154547

[111] R. Niemczyk, "Subpicosecond-Resolved Emittance Measurements of High-Brightness Electron Beams with Space Charge Effects at PITZ," Dissertation, University of Hamburg, 2021, dissertation, University of Hamburg, 2021. [Online]. Available: https://bib-pubdb1.desy.de/record/472174

[112] S. Rimjaem, F. Stephan, M. Krasilnikov, W. Ackermann, G. Asova, J. Bähr, E. Gjonaj, H.J. Grabosch, L. Hakobyan, M. Hänel, Y. Ivanisenko, M. Khojoyan, G. Klemz, et al., "Optimizations of transverse projected emittance at the photo-injector test facility at DESY, location Zeuthen," *Nuclear Instruments and Methods in Physics Research Section A: Accelerators, Spectrometers, Detectors and Associated Equipment*, vol. 671, pp. 62–75, 2012. [Online]. Available: https://www.sciencedirect.com/science/article/pii/S0168900211023540

[113] Krasilnikov, M., Stephan, F., Asova, G., Grabosch, H.-J., Groß, M., Hakobyan, L., Isaev, I. and Ivanisenko, Y. and Jachmann, L. and Khojoyan, M. and Klemz, G., Köhler, W. and Mahgoub, et al., "Experimentally minimized beam emittance from an *L*-band photoinjector," *Phys. Rev. ST Accel. Beams*, vol. 15, p. 100701, Oct 2012. [Online]. Available: https://link.aps.org/doi/10.1103/PhysRevSTAB.15.100701

[114] D. Sertore, et al., "Review of the production process of TTF and PITZ photocathodes," *Proceedings of 2005 Particle Accelerator Conference*, vol.

PAC2005, pp. Knoxville, Tennessee, 2005. [Online]. Available: https://accelconf.web.cern.ch/p05/PAPERS/MOPB009.PDF

[115] P. Michelato, P. Gallina, and C. Pagani, "Alkali photocathode development for superconducting rf guns," *Nuclear Instruments and Methods in Physics Research Section A: Accelerators, Spectrometers, Detectors and Associated Equipment*, vol. 340, no. 1, pp. 176–181, 1994. [Online]. Available: https://www.sciencedirect.com/science/article/pii/0168900294912963

[116] SAES Getters SpA. [Online]. Available: https://www.saesgetters.com/

[117] A. G. Mathewson, "Making it work," 1992. [Online]. Available: https://cds.cern.ch/record/245418

[118] D. Sertore, D. Favia, P. Michelato, L. Monaco, and P. Pierini, "Cesium Telluride and Metals Photoelectron Thermal Emittance Measurements Using a Time-of-flight Spectrometer," 2004. [Online]. Available: https://cds.cern.ch/record/822628

[119] "Product Catalogue, UHV Vacuum Components, VACGEN," pp. 185–191. [Online]. Available: https://b2b.partcommunity.com/community/public/document/d0/10/0f/82c48d12a6295a48acdeea3b88d0e9bd.pdf

[120] D. Sertore, M. Bertucci, G. G. Rocco, S. Mohanty, L. Monaco, H. Qian, and F. Stephan, "R&D on High QE Photocathodes at INFN LASA," in *Proc. IPAC'22*, ser. International Particle Accelerator Conference, no. 13. JACoW Publishing, Geneva, Switzerland, 07 2022, pp. 2633–2636. [Online]. Available: https://jacow.org/ipac2022/papers/thpopt027.pdf

[121] P. Michelato, C. Gesmundo, and D. Sertore, "High quantum efficiency photocathode preparation system for TTF injector II," Tech. Rep. DESY-TESLA-FEL-99-07I, 1999, in Hamburg 1999, Free electron lasers II-97-98. [Online]. Available: https://bib-pubdb1.desy.de/record/584166

[122] "SAES High Vacuum solutions [online]," https://www.saesgetters.com/highvacuum/solutions/, [Accessed 25-02-2024].

[123] P. Michelato, C. Gesmundo, and D. Sertore, "High quantum efficiency photocathode preparation system for TTF injector II," in *21st International Conference on Free Electron Laser and 6th FEL Applications Workshop (FEL 99)*, 12 1999, pp. 97–98.

[124] P. Michelato, L. Monaco, P. Pierini, and D. Sertore, "REPORT ON STUDIES ON PHOTOCATHODE PERFORMANCES," jan 2005. [Online]. Available: https://www.researchgate.net/publication/264874053_REPORT_ON_STUDIES_ON_PHOTOCATHODE_PERFORMANCES

[125] E. D. PALIK, "Chapter 1 - Introductory Remarks," in *Handbook of Optical Constants of Solids*, E. D. PALIK, Ed. Boston: Academic Press, 1985, pp. 3–9. [Online]. Available: https://www.sciencedirect.com/science/article/pii/B978008054721350006X

[126] L. Monaco, "Photocathode activities at INFN LASA," in *Proc. IPAC'23*, ser. IPAC'23 - 14th International Particle Accelerator Conference, no. 14. JACoW Publishing, Geneva, Switzerland, 05 2023, paper TUPA008, pp. 1352–1355. [Online]. Available: https://indico.jacow.org/event/41/contributions/1397

[127] SAES Getters, "Getters & dispensers - industrial solutions," 2023, accessed: 2023-04-10. [Online]. Available: https://www.saesgetters.com/industrial/solutions/getters-dispensers/

[128] D. Sertore, P. Michelato, L. Monaco, and C. Pagani, "R&D Activity on Alkali-Antimonied Photocathodes at INFN-LASA," *Proceedings of the 9th Int. Particle Accelerator Conf.*, vol. IPAC2018, p. Canada, 2018. [Online]. Available: http://jacow.org/ipac2018/doi/JACoW-IPAC2018-THPMF088.html

[129] S. Mohanty, G. Guerini Rocco, P. Michelato, L. Monaco, C. Pagani, and D. Sertore, "Development of a Multialkali Antimonide Photocathode at INFN LASA," *Proceedings of the 39th Free Electron Laser Conference*, vol. FEL2019, p. Germany, 2019. [Online]. Available: http://jacow.org/fel2019/doi/JACoW-FEL2019-WEP053.html

[130] D. Sertore, G. Guerini Rocco, P. Michelato, S. Mohanty, L. Monaco, and C. Pagani, "Photocathode Activities at INFN LASA," *Proceedings of the 10th Int. Particle Accelerator Conf.*, vol. IPAC2019, p. Australia, 2019. [Online]. Available: http://jacow.org/ipac2019/doi/JACoW-IPAC2019-TUPTS117.html

[131] Junqi Xie, Marcel Demarteau, Robert Wagner, Susanne Schubert, Mengjia Gaowei, Klaus Attenkofer, John Walsh, John Smedley, Jared Wong, Jun Feng, Howard Padmore, Miguel Ruiz-Oses, et al., "Synchrotron x-ray study of a low roughness and high efficiency K_2CsSb photocathode during film growth," *Journal of Physics D: Applied Physics*, vol. 50, no. 20, p. 205303, apr 2017. [Online]. Available: https://dx.doi.org/10.1088/1361-6463/aa6882

[132] J. O. Porteus, "Relation between the Height Distribution of a Rough Surface and the Reflectance at Normal Incidence," *J. Opt. Soc. Am.*, vol. 53, no. 12, pp. 1394–1402, Dec 1963. [Online]. Available: https://opg.optica.org/abstract.cfm?URI=josa-53-12-1394

[133] P. Michelato, L. Monaco, D. Sertore, and S. Bettoni, "Optical Properties of Cesium Telluride," 06 2002. [Online]. Available: https://accelconf.web.cern.ch/e02/PAPERS/TUPRI080.pdf

[134] A. Sommer and L. Marton, *"Photoemissive Materials"*, 1980.

[135] M. Ruiz-Osés, S. Schubert, K. Attenkofer, I. Ben-Zvi, X. Liang, E. Muller, H. Padmore, T. Rao, T. Vecchione, J. Wong, J. Xie, and J. Smedley, "Direct observation of bi-alkali antimonide photocathodes growth via in operando x-ray diffraction studies," *APL Materials*, vol. 2, no. 12, p. 121101, 12 2014. [Online]. Available: https://doi.org/10.1063/1.4902544

[136] A. Sharma, P. Kumar, and S. Ghosh, "Anistropic growth and high performance organic thin film transistor," *AIP Conference Proceedings*, vol. 1447, no. 1, pp. 30–33, 06 2012. [Online]. Available: https://doi.org/10.1063/1.4709871

[137] A. Sommer and L. Marton, *"Photoemissive Materials: Preparation, Properties, and Uses"*. Wiley: New York, NY, USA, 1968.

[138] W. M. Haynes, Ed., *"CRC Handbook of Chemistry and Physics"*. CRC Press, Jun. 2014. [Online]. Available: https://doi.org/10.1201/b17118

[139] E. Montgomery, "Characterization of quantum efficiency and robustness of Cesium based photocathodes." Ph.D. dissertation. [Online]. Available: https://psec.uchicago.edu/library/photocathodes/Dissertation1.pdf(accessedon15May2023)

[140] E. J. Montgomery, D. W. Feldman, P. G. O'Shea, Z. Pan, N. A. Moody, and K. L. Jensen, "Fabrication and measurement of efficient, robust cesiated dispenser photocathodes," in *2007 IEEE Particle Accelerator Conference (PAC)*, 2007, pp. 1206–1208.

[141] R. R. Mammei, R. Suleiman, J. Feingold, P. A. Adderley, J. Clark, S. Covert, J. Grames, J. Hansknecht, D. Machie, M. Poelker, T. Rao, J. Smedley, J. Walsh, J. L. McCarter, and M. Ruiz-Osés, "Charge lifetime measurements at high average current using a K_2CsSb photocathode inside a dc high voltage photogun," *Phys. Rev. ST Accel. Beams*, vol. 16, p. 033401, Mar 2013. [Online]. Available: https://link.aps.org/doi/10.1103/PhysRevSTAB.16.033401

[142] M. A. Mamun, C. Hernandez-Garcia, M. Poelker, and A. A. Elmustafa, "Correlation of CsK_2Sb photocathode lifetime with antimony thickness," *APL Materials*, vol. 3, no. 6, p. 066103, 06 2015. [Online]. Available: https://doi.org/10.1063/1.4922319

[143] A. Natarajan, A. T. Kalghatgi, B. M. Bhat, and M. Satyam, "Role of the cesium antimonide layer in the Na_2KSb/Cs_3Sb photocathode," *Journal of Applied Physics*, vol. 90, no. 12, pp. 6434–6439, Dec. 2001. [Online]. Available: https://doi.org/10.1063/1.1413943

[144] L. S. L. Soriano and L. G. L. Galán, "Interaction of Cesium-Potassium Antimonide Photocathode Materials with Oxygen: an X-Ray Photoelectron Spectroscopy

Study," *Japanese Journal of Applied Physics*, vol. 32, no. 10R, p. 4737, oct 1993. [Online]. Available: https://dx.doi.org/10.1143/JJAP.32.4737

[145] Z. Ding, S. Karkare, J. Feng, D. Filippetto, M. Johnson, S. Virostek, F. Sannibale, J. Nasiatka, M. Gaowei, J. Sinsheimer, E. Muller, J. Smedley, and H. Padmore, "Temperature-dependent quantum efficiency degradation of K-Cs-Sb bialkali antimonide photocathodes grown by a triple-element co-deposition method," *Phys. Rev. Accel. Beams*, vol. 20, p. 113401, Nov 2017. [Online]. Available: https://link.aps.org/doi/10.1103/PhysRevAccelBeams.20.113401

[146] P. Michelato, C. Pagani, and D. Sertore, "Multialkali Thin Photocathodes for High Brightness guns," in *EPAC 1994*, 1994, [Accessed 03-02-2024].

[147] Peng-Wei Huang, Houjun Qian, Ye Chen, Filippetto, Daniele, Matthias Gross, Igor Isaev, Christian Koschitzki, Mikhail Krasilnikov, Shankar Lal, Xiangkun Li, Osip Lishilin, David Melkumyan, Raffael Niemczyk, Anne Oppelt, et al., "Single shot cathode transverse momentum imaging in high brightness photoinjectors," *Phys. Rev. Accel. Beams*, vol. 23, p. 043401, Apr 2020. [Online]. Available: https://link.aps.org/doi/10.1103/PhysRevAccelBeams.23.043401

[148] H. Qian, M. Krasilnikov, Z. Aboulbanine, G. Adhikari, N. Aftab, P. Boonpornpras, G. Georgiev, J. Good, M. Gross, C. Koschitzki, X. Li, O. Lishilin, A. Lueangaramwong, R. Niemczyk, A. Oppelt, G. Shu, F. Stephan, G. Vashchenko, and T. Weilbach, "Analysis of photoinjector transverse phase space in action and phase coordinates," *Phys. Rev. Accel. Beams*, vol. 25, p. 103401, Oct 2022. [Online]. Available: https://link.aps.org/doi/10.1103/PhysRevAccelBeams.25.103401

[149] B. E. Carlsten, "Space-charge-induced emittance compensation in high-brightness photoinjectors*," 2009. [Online]. Available: https://api.semanticscholar.org/CorpusID:212615287

[150] F. Stephan, C.H. Boulware, M. Krasilnikov, J. Bähr, G. Asova, A. Donat, U. Gensch, H. J. Grabosch, M. Hänel, L. Hakobyan, H. Henschel, Y. Ivanisenko,

L. Jachmann, et al., “Detailed characterization of electron sources yielding first demonstration of European X-ray Free-Electron Laser beam quality,” *Phys. Rev. ST Accel. Beams*, vol. 13, p. 020704, Feb 2010. [Online]. Available: https://link.aps.org/doi/10.1103/PhysRevSTAB.13.020704

[151] G. Shu, H. Qian, N. Aftab, P. Boonpornprasert, G. Georgiev, J. Good, M. Gross, C. Koschitzki, M. Krasilnikov, A. Lueangaramwong, O. Lishilin, X. Li, S. Mohanty, R. Niemczyk, et al., “Dark current studies of an L-band normal conducting RF gun,” *Nuclear Instruments and Methods in Physics Research Section A: Accelerators, Spectrometers, Detectors and Associated Equipment*, vol. 1010, p. 165546, 2021. [Online]. Available: https://www.sciencedirect.com/science/article/pii/S0168900221005313

[152] R. Xiang, A. Arnold, T. Kamps, P. Lu, P. Michel, P. Murcek, H. Vennekate, G. Staats, and J. Teichert, “Experimental studies of dark current in a superconducting rf photoinjector,” *Phys. Rev. ST Accel. Beams*, vol. 17, p. 043401, Apr 2014. [Online]. Available: https://link.aps.org/doi/10.1103/PhysRevSTAB.17.043401

[153] R. Huang, D. Filippetto, C. F. Papadopoulos, H. Qian, F. Sannibale, and M. Zolotorev, “Dark current studies on a normal-conducting high-brightness very-high-frequency electron gun operating in continuous wave mode,” *Phys. Rev. ST Accel. Beams*, vol. 18, p. 013401, Jan 2015. [Online]. Available: https://link.aps.org/doi/10.1103/PhysRevSTAB.18.013401

[154] B. Van Zeghbroeck and M. Silver, *“Principles of semiconductor devices and heterojunctions"*. Upper Saddle River, NJ: Pearson, Dec. 2013.

[155] J. W. Wang and G. A. Loew, “Field emission and rf breakdown in high-gradient room temperature linac structures,” 10 1997. [Online]. Available: https://www.osti.gov/biblio/663321

[156] P. Michelato, D. Maschinenphysik, L. Monaco, C. Pagani, D. Sertore, F. Stephan, S. Lederer, and S. Schreiber, “Cs_2Te Photocathode Robustness Studies,” 06 2008.

[157] R. A. Powell, W. E. Spicer, G. B. Fisher, and P. Gregory, "Photoemission Studies of Cesium Telluride," *Physical Review B*, vol. 8, no. 8, pp. 3987–3995, Oct. 1973. [Online]. Available: https://doi.org/10.1103/physrevb.8.3987

[158] A. H. Sommer and W. H. McCarroll, "A New Modification of the Semiconducting Compound K_3Sb," *Journal of Applied Physics*, vol. 37, no. 1, pp. 174–179, 06 2004. [Online]. Available: https://doi.org/10.1063/1.1707801

[159] B. Ofuonye, J. Lee, M. Yan, C. Sun, J.-M. Zuo, and I. Adesida, "Electrical and microstructural properties of thermally annealed Ni/Au and Ni/Pt/Au Schottky contacts on AlGaN/GaN heterostructures," *Semiconductor Science and Technology*, vol. 29, p. 095005, 07 2014.

[160] R. M. Martin, *"Electronic Structure: Basic Theory and Practical Methods"*. Cambridge University Press, 2004.

[161] J. Chen, "Sparse Representation of Wannier Functions from L_1 Regularized Optimization," Ph.D. dissertation, 2018, [Accessed 26-10-2023]. [Online]. Available: https://escholarship.org/uc/item/6jc5k8j2

[162] M. Born and R. Oppenheimer, "Zur quantentheorie der molekeln," *Annalen der Physik*, vol. 389, no. 20, pp. 457–484, 1927. [Online]. Available: https://onlinelibrary.wiley.com/doi/abs/10.1002/andp.19273892002

[163] E. Merzbacher, *"Quantum Mechanics: Theory and Applications"*, 2nd ed. Wiley, 1970.

[164] P. Hohenberg and W. Kohn, "Inhomogeneous electron gas," *Phys. Rev.*, vol. 136, pp. B864–B871, Nov 1964. [Online]. Available: https://link.aps.org/doi/10.1103/PhysRev.136.B864

[165] W. Kohn and L. J. Sham, "Self-consistent equations including exchange and correlation effects," *Phys. Rev.*, vol. 140, pp. A1133–A1138, Nov 1965. [Online]. Available: https://link.aps.org/doi/10.1103/PhysRev.140.A1133

[166] M. S. Hybertsen and S. G. Louie, "Electron correlation in semiconductors and insulators: Band gaps and quasiparticle energies," *Phys. Rev. B*, vol. 34, pp. 5390–5413, Oct 1986. [Online]. Available: https://link.aps.org/doi/10.1103/PhysRevB.34.5390

[167] L. H. Thomas, "The calculation of atomic fields," *Mathematical Proceedings of the Cambridge Philosophical Society*, vol. 23, no. 5, p. 542–548, 1927.

[168] E. Fermi, "Un Metodo Statistico per la Determinazione di alcune Priorieta' dell'Atomo." *Accademia Nazionale dei Lincei*, vol. 6, p. 602–607, 1927.

[169] J. P. Perdew and A. Zunger, "Self-interaction correction to density-functional approximations for many-electron systems," *Phys. Rev. B*, vol. 23, pp. 5048–5079, May 1981. [Online]. Available: https://link.aps.org/doi/10.1103/PhysRevB.23.5048

[170] D. C. Langreth and M. J. Mehl, "Beyond the local-density approximation in calculations of ground-state electronic properties," *Phys. Rev. B*, vol. 28, pp. 1809–1834, Aug 1983. [Online]. Available: https://link.aps.org/doi/10.1103/PhysRevB.28.1809

[171] C. Filippi, C. J. Umrigar, and M. Taut, "Comparison of exact and approximate density functionals for an exactly soluble model," *The Journal of Chemical Physics*, vol. 100, no. 2, pp. 1290–1296, 01 1994. [Online]. Available: https://doi.org/10.1063/1.466658

[172] J. P. Perdew, K. Burke, and M. Ernzerhof, "Generalized gradient approximation made simple," *Phys. Rev. Lett.*, vol. 77, pp. 3865–3868, Oct 1996. [Online]. Available: https://link.aps.org/doi/10.1103/PhysRevLett.77.3865

[173] G. Ortiz and P. Ballone, "Pseudopotentials for non-local-density functionals," *Phys. Rev. B*, vol. 43, pp. 6376–6387, Mar 1991. [Online]. Available: https://link.aps.org/doi/10.1103/PhysRevB.43.6376

[174] G. Ortiz, "Gradient-corrected pseudopotential calculations in semiconductors," *Phys. Rev. B*, vol. 45, pp. 11 328–11 331, May 1992. [Online]. Available: https://link.aps.org/doi/10.1103/PhysRevB.45.11328

[175] A. García, C. Elsässer, J. Zhu, S. G. Louie, and M. L. Cohen, "Use of gradient-corrected functionals in total-energy calculations for solids," *Phys. Rev. B*, vol. 46, pp. 9829–9832, Oct 1992. [Online]. Available: https://link.aps.org/doi/10.1103/PhysRevB.46.9829

[176] C. Filippi, D. J. Singh, and C. J. Umrigar, "All-electron local-density and generalized-gradient calculations of the structural properties of semiconductors," *Phys. Rev. B*, vol. 50, pp. 14 947–14 951, Nov 1994. [Online]. Available: https://link.aps.org/doi/10.1103/PhysRevB.50.14947

[177] C. Lee, D. Vanderbilt, K. Laasonen, R. Car, and M. Parrinello, "Ab initio studies on high pressure phases of ice," *Phys. Rev. Lett.*, vol. 69, pp. 462–465, Jul 1992. [Online]. Available: https://link.aps.org/doi/10.1103/PhysRevLett.69.462

[178] F. Sim, A. St. Amant, I. Papai, and D. R. Salahub, "Gaussian density functional calculations on hydrogen-bonded systems," *Journal of the American Chemical Society*, vol. 114, no. 11, pp. 4391–4400, 1992. [Online]. Available: https://doi.org/10.1021/ja00037a055

[179] K. Laasonen, M. Sprik, M. Parrinello, and R. Car, "Ab-initio liquid water," *The Journal of Chemical Physics*, vol. 99, no. 11, pp. 9080–9089, 12 1993. [Online]. Available: https://doi.org/10.1063/1.465574

[180] A. Dal Corso and R. Resta, "Density-functional theory of macroscopic stress: Gradient-corrected calculations for crystalline se," *Phys. Rev. B*, vol. 50, pp. 4327–4331, Aug 1994. [Online]. Available: https://link.aps.org/doi/10.1103/PhysRevB.50.4327

[181] A. Dal Corso, S. Baroni, and R. Resta, "Density-functional theory of the dielectric constant: Gradient-corrected calculation for silicon," *Phys.*

Rev. B, vol. 49, pp. 5323–5328, Feb 1994. [Online]. Available: https://link.aps.org/doi/10.1103/PhysRevB.49.5323

[182] J. P. Perdew, "Unified theory of exchange and correlation beyond the local density approximation," in *Electronic Structure of Solids '91*, ser. Physical Research, P. Ziesche and H. Eschrig, Eds., vol. 17. Berlin: Akademie Verlag, 1991, pp. 11–20.

[183] A. Dal Corso, A. Pasquarello, A. Baldereschi, and R. Car, "Generalized-gradient approximations to density-functional theory: A comparative study for atoms and solids," *Phys. Rev. B*, vol. 53, pp. 1180–1185, Jan 1996. [Online]. Available: https://link.aps.org/doi/10.1103/PhysRevB.53.1180

[184] A. D. Becke, "Density-functional thermochemistry. IV. A new dynamical correlation functional and implications for exact-exchange mixing," *The Journal of Chemical Physics*, vol. 104, no. 3, pp. 1040–1046, 01 1996. [Online]. Available: https://doi.org/10.1063/1.470829

[185] A. Gonis, N. Kioussis, and M. Ciftan, Eds., *"Electron Correlations and Materials Properties"*. Springer US, 1999. [Online]. Available: https://doi.org/10.1007/978-1-4615-4715-0

[186] J. Tao, J. P. Perdew, V. N. Staroverov, and G. E. Scuseria, "Climbing the Density Functional Ladder: Nonempirical Meta–Generalized Gradient Approximation Designed for Molecules and Solids," *Phys. Rev. Lett.*, vol. 91, p. 146401, Sep 2003. [Online]. Available: https://link.aps.org/doi/10.1103/PhysRevLett.91.146401

[187] T. Van Voorhis and G. E. Scuseria, "A novel form for the exchange-correlation energy functional," *The Journal of Chemical Physics*, vol. 109, no. 2, pp. 400–410, 07 1998. [Online]. Available: https://doi.org/10.1063/1.476577

[188] J. Heyd, G. E. Scuseria, and M. Ernzerhof, "Hybrid functionals based on a screened Coulomb potential," *The Journal of Chemical Physics*, vol. 118, no. 18, pp. 8207–8215, 04 2003. [Online]. Available: https://doi.org/10.1063/1.1564060

[189] A. D. Becke, "Density-functional exchange-energy approximation with correct asymptotic behavior," *Phys. Rev. A*, vol. 38, pp. 3098–3100, Sep 1988. [Online]. Available: https://link.aps.org/doi/10.1103/PhysRevA.38.3098

[190] F. A. Hamprecht, A. J. Cohen, D. J. Tozer, and N. C. Handy, "Development and assessment of new exchange-correlation functionals," *The Journal of Chemical Physics*, vol. 109, no. 15, pp. 6264–6271, 10 1998. [Online]. Available: https://doi.org/10.1063/1.477267

[191] H. L. Schmider and A. D. Becke, "Optimized density functionals from the extended G2 test set," *The Journal of Chemical Physics*, vol. 108, no. 23, pp. 9624–9631, 06 1998. [Online]. Available: https://doi.org/10.1063/1.476438

[192] C. Lee, W. Yang, and R. G. Parr, "Development of the Colle-Salvetti correlation-energy formula into a functional of the electron density," *Phys. Rev. B*, vol. 37, pp. 785–789, Jan 1988. [Online]. Available: https://link.aps.org/doi/10.1103/PhysRevB.37.785

[193] C. Adamo and V. Barone, "Exchange functionals with improved long-range behavior and adiabatic connection methods without adjustable parameters: The mPW and mPW1PW models," *The Journal of Chemical Physics*, vol. 108, no. 2, pp. 664–675, 01 1998. [Online]. Available: https://doi.org/10.1063/1.475428

[194] G. H. Wannier, "The structure of electronic excitation levels in insulating crystals," *Phys. Rev.*, vol. 52, pp. 191–197, Aug 1937. [Online]. Available: https://link.aps.org/doi/10.1103/PhysRev.52.191

[195] N. Marzari, A. A. Mostofi, J. R. Yates, I. Souza, and D. Vanderbilt, "Maximally localized wannier functions: Theory and applications," *Rev. Mod. Phys.*, vol. 84, pp. 1419–1475, Oct 2012. [Online]. Available: https://link.aps.org/doi/10.1103/RevModPhys.84.1419

[196] N. Marzari and D. Vanderbilt, "Maximally localized generalized wannier functions

for composite energy bands," *Phys. Rev. B*, vol. 56, pp. 12 847–12 865, Nov 1997. [Online]. Available: https://link.aps.org/doi/10.1103/PhysRevB.56.12847

[197] I. Souza, N. Marzari, and D. Vanderbilt, "Maximally localized wannier functions for entangled energy bands," *Phys. Rev. B*, vol. 65, p. 035109, Dec 2001. [Online]. Available: https://link.aps.org/doi/10.1103/PhysRevB.65.035109

[198] J. M. Foster and S. F. Boys, "Canonical configurational interaction procedure," *Rev. Mod. Phys.*, vol. 32, pp. 300–302, Apr 1960. [Online]. Available: https://link.aps.org/doi/10.1103/RevModPhys.32.300

[199] S. Boys, *"Localized orbitals and localized adjustment functions"*. Quantum Theory Atoms, Mol. Solid State, 1966, vol. 253.

[200] E. I. Blount, "Formalisms of band theory," *Journal of Physics C: Solid State Physics*, vol. 13, pp. 305–373, 1962.

[201] A. A. Mostofi, J. R. Yates, Y.-S. Lee, I. Souza, D. Vanderbilt, and N. Marzari, "wannier90: A tool for obtaining maximally-localised Wannier functions," *Computer Physics Communications*, vol. 178, no. 9, pp. 685–699, 2008. [Online]. Available: https://www.sciencedirect.com/science/article/pii/S0010465507004936

[202] Paolo Giannozzi, Stefano Baroni, Nicola Bonini, Matteo Calandra, Roberto Car, Carlo Cavazzoni, Davide Ceresoli, Guido L Chiarotti, Matteo Cococcioni, Ismaila Dabo, Andrea Dal Corso, Stefano de Gironcoli, Stefano Fabris, et al., "QUANTUM ESPRESSO: a modular and open-source software project for quantum simulations of materials," *Journal of Physics: Condensed Matter*, vol. 21, no. 39, p. 395502, sep 2009. [Online]. Available: https://dx.doi.org/10.1088/0953-8984/21/39/395502

[203] P. Giannozzi, O. Andreussi, T. Brumme, O. Bunau, M. Buongiorno Nardelli, M. Calandra, R. Car, C. Cavazzoni, D. Ceresoli, M. Cococcioni, N. Colonna, I. Carnimeo, A. Dal Corso, at al., "Advanced capabilities

for materials modelling with Quantum ESPRESSO," *Journal of Physics: Condensed Matter*, vol. 29, no. 46, p. 465901, oct 2017. [Online]. Available: https://dx.doi.org/10.1088/1361-648X/aa8f79

[204] [Online]. Available: https://gitlab.com/QEF/q-e/-/tree/master/PP/examples/W90_open_grid_example

[205] "QE tutorial 2022 - Hands-on: Maximally localized Wannier functions using Wannier90 - Marrazzo Qiao — youtube.com," https://www.youtube.com/watch?v=FhYAEDFYzlk&t=2078s, [Accessed 28-07-2023].

[206] N. E. Brener, "Random-phase-approximation dielectric function for diamond, with local field effects included," *Phys. Rev. B*, vol. 12, pp. 1487–1492, Aug 1975. [Online]. Available: https://link.aps.org/doi/10.1103/PhysRevB.12.1487

[207] A. Benassi, A. Ferretti, and C. Cavazzoni, "Pwscf.'s epsilon.x user's manual." [Online]. Available: www.quantum-espresso.org/Doc/pp_user_guide.pdf

[208] F. Wooten, *Optical Properties of Solids*. Academic Press, 1972. [Online]. Available: https://books.google.com/books/about/Optical_Properties_of_Solids.html?id=A_dHNRXFq28C

[209] P. Rani, G. S. Dubey, and V. Jindal, "DFT study of optical properties of pure and doped graphene," *Physica E: Low-dimensional Systems and Nanostructures*, vol. 62, pp. 28–35, 2014. [Online]. Available: https://www.sciencedirect.com/science/article/pii/S1386947714001374

[210] R. O. Jones, "Density functional theory: Its origins, rise to prominence, and future," *Rev. Mod. Phys.*, vol. 87, pp. 897–923, Aug 2015. [Online]. Available: https://link.aps.org/doi/10.1103/RevModPhys.87.897

[211] A. Jain, Y. Shin, and K. A. Persson, "Computational predictions of energy materials using density functional theory," *Nature Reviews Materials*, vol. 1, no. 1, Jan. 2016. [Online]. Available: http://dx.doi.org/10.1038/natrevmats.2015.4

[212] M. Gajdoš, K. Hummer, G. Kresse, J. Furthmüller, and F. Bechstedt, "Linear optical properties in the projector-augmented wave methodology," *Phys. Rev. B*, vol. 73, p. 045112, Jan 2006. [Online]. Available: https://link.aps.org/doi/10.1103/PhysRevB.73.045112

[213] C. Ambrosch-Draxl and J. O. Sofo, "Linear optical properties of solids within the full-potential linearized augmented planewave method," *Computer Physics Communications*, vol. 175, no. 1, pp. 1–14, 2006. [Online]. Available: https://www.sciencedirect.com/science/article/pii/S0010465506001299

[214] F. Kootstra, P. L. de Boeij, and J. G. Snijders, "Application of time-dependent density-functional theory to the dielectric function of various nonmetallic crystals," *Phys. Rev. B*, vol. 62, pp. 7071–7083, Sep 2000. [Online]. Available: https://link.aps.org/doi/10.1103/PhysRevB.62.7071

[215] S. Botti, F. Sottile, N. Vast, V. Olevano, L. Reining, H.-C. Weissker, A. Rubio, G. Onida, R. Del Sole, and R. W. Godby, "Long-range contribution to the exchange-correlation kernel of time-dependent density functional theory," *Phys. Rev. B*, vol. 69, p. 155112, Apr 2004. [Online]. Available: https://link.aps.org/doi/10.1103/PhysRevB.69.155112

[216] J. Paier, M. Marsman, and G. Kresse, "Dielectric properties and excitons for extended systems from hybrid functionals," *Phys. Rev. B*, vol. 78, p. 121201, Sep 2008. [Online]. Available: https://link.aps.org/doi/10.1103/PhysRevB.78.121201

[217] M. Nishiwaki and H. Fujiwara, "Highly accurate prediction of material optical properties based on density functional theory," *Computational Materials Science*, vol. 172, p. 109315, 2020. [Online]. Available: https://www.sciencedirect.com/science/article/pii/S0927025619306147

[218] F. Birch, "Finite elastic strain of cubic crystals," *Phys. Rev.*, vol. 71, pp. 809–824, Jun 1947. [Online]. Available: https://link.aps.org/doi/10.1103/PhysRev.71.809

[219] F. D. Murnaghan, "The compressibility of media under extreme pressures," *Proceedings of the National Academy of Sciences*, vol. 30, no. 9, pp. 244–247, 1944. [Online]. Available: https://www.pnas.org/doi/abs/10.1073/pnas.30.9.244

[220] W. McCarroll, "Chemical and structural characteristics of the potassium-cesium-antimony photocathode," *Journal of Physics and Chemistry of Solids*, vol. 26, no. 1, pp. 191–195, 1965. [Online]. Available: https://www.sciencedirect.com/science/article/pii/0022369765900879

[221] L. Kalarasse, B. Bennecer, and F. Kalarasse, "Optical properties of the alkali antimonide semiconductors Cs_3Sb, Cs_2KSb, CsK_2Sb and K_3Sb," *Journal of Physics and Chemistry of Solids*, vol. 71, no. 3, pp. 314–322, 2010. [Online]. Available: https://www.sciencedirect.com/science/article/pii/S0022369709004363

[222] G. MURTAZA, M. ULLAH, N. ULLAH, M. RANI, M. MUZAMMIL, R. KHENATA, S. M. RAMAY, and U. KHAN, "Structural, elastic, electronic and optical properties of bi-alkali antimonides," *Bulletin of Materials Science*, vol. 39, no. 6, pp. 1581–1591, Sep. 2016. [Online]. Available: https://doi.org/10.1007/s12034-016-1300-1

[223] C. Cocchi, S. Mistry, M. Schmeißer, R. Amador, J. Kühn, and T. Kamps, "Electronic structure and core electron fingerprints of caesium-based multi-alkali antimonides for ultra-bright electron sources," *Scientific Reports*, vol. 9, no. 1, Dec. 2019. [Online]. Available: https://doi.org/10.1038/s41598-019-54419-0

[224] D. R. Hamann, "Optimized norm-conserving Vanderbilt pseudopotentials," *Phys. Rev. B*, vol. 88, p. 085117, Aug 2013. [Online]. Available: https://link.aps.org/doi/10.1103/PhysRevB.88.085117

[225] H.-D. Saßnick and C. Cocchi, "Electronic structure of cesium-based photocathode materials from density functional theory: performance of PBE, SCAN, and HSE06 functionals," *Electronic Structure*, vol. 3, no. 2, p. 027001, May 2021. [Online]. Available: https://doi.org/10.1088/2516-1075/abfb08

[226] F. Tran and P. Blaha, "Accurate band gaps of semiconductors and insulators with a semilocal exchange-correlation potential," *Phys. Rev. Lett.*, vol. 102, p. 226401, Jun 2009. [Online]. Available: https://link.aps.org/doi/10.1103/PhysRevLett.102.226401

[227] J. P. Perdew, W. Yang, K. Burke, Z. Yang, E. K. U. Gross, M. Scheffler, G. E. Scuseria, T. M. Henderson, I. Y. Zhang, A. Ruzsinszky, H. Peng, J. Sun, E. Trushin, and A. Görling, "Understanding band gaps of solids in generalized Kohn–Sham theory," *Proceedings of the National Academy of Sciences*, vol. 114, no. 11, pp. 2801–2806, Mar. 2017. [Online]. Available: https://doi.org/10.1073/pnas.1621352114

[228] E. R. Antoniuk, P. Schindler, W. A. Schroeder, B. Dunham, P. Pianetta, T. Vecchione, and E. J. Reed, "Novel Ultrabright and Air-Stable Photocathodes Discovered from Machine Learning and Density Functional Theory Driven Screening," *Advanced Materials*, vol. 33, no. 44, p. 2104081, 2021. [Online]. Available: https://onlinelibrary.wiley.com/doi/abs/10.1002/adma.202104081

[229] A. Ettema and R. de Groot, "Electronic structure of Cs_2KSb and K_2CsSb," *Phys. Rev. B*, vol. 66, p. 115102, Sep 2002. [Online]. Available: https://link.aps.org/doi/10.1103/PhysRevB.66.115102

[230] C. Cocchi, S. Mistry, M. Schmeißer, J. Kühn, and T. Kamps, "First-principles many-body study of the electronic and optical properties of CsK_2Sb, a semiconducting material for ultra-bright electron sources," *Journal of Physics: Condensed Matter*, vol. 31, no. 1, p. 014002, nov 2018. [Online]. Available: https://dx.doi.org/10.1088/1361-648X/aaedee

[231] M. Moorhead and N. Tanner, "Optical properties of an EMI K_2CsSb bialkali photocathode," *Nuclear Instruments and Methods in Physics Research Section A: Accelerators, Spectrometers, Detectors and Associated Equipment*, vol. 378, no. 1, pp. 162–170, 1996. [Online]. Available: https://www.sciencedirect.com/science/article/pii/0168900296004470

[232] M. Gaowei, Z. Ding, S. Schubert, H. B. Bhandari, J. Sinsheimer, J. Kuehn, V. V. Nagarkar, M. S. J. Marshall, J. Walsh, E. M. Muller, K. Attenkofer, H. J. Frisch, H. Padmore, and J. Smedley, "Synthesis and x-ray characterization of sputtered bi-alkali antimonide photocathodes," *APL Materials*, vol. 5, no. 11, p. 116104, 11 2017. [Online]. Available: https://doi.org/10.1063/1.5010950

[233] A. Ebina and T. Takahashi, "Transmittance Spectra and Optical Constants of Alkali-Antimony Compounds K_3Sb, Na_3Sb, and Na_2KSb," *Phys. Rev. B*, vol. 7, pp. 4712–4719, May 1973. [Online]. Available: https://link.aps.org/doi/10.1103/PhysRevB.7.4712

[234] W. McCarroll, "Phases in the photoelectric sodium-potassium-antimony system," *Journal of Physics and Chemistry of Solids*, vol. 16, no. 1, pp. 30–36, 1960. [Online]. Available: https://www.sciencedirect.com/science/article/pii/0022369760900664

[235] R. Amador, H.-D. Saßnick, and C. Cocchi, "Electronic structure and optical properties of Na_2KSb and NaK_2Sb from first-principles many-body theory," *Journal of Physics: Condensed Matter*, vol. 33, no. 36, p. 365502, Jul. 2021. [Online]. Available: https://doi.org/10.1088/1361-648x/ac0e70

[236] Atsuko Ebina and Tadashi Takahashi, "Optical Constants of K_3Sb," *J. Opt. Soc. Am.*, vol. 62, no. 5, pp. 639–644, May 1972. [Online]. Available: https://opg.optica.org/abstract.cfm?URI=josa-62-5-639

[237] X. Lin, C. Li, H. Hao, G. Zhao, and H. Liu, "Accelerated search for ABO3-type the electronic contribution of polycrystalline dielectric constants by machine learning," *Computational Materials Science*, vol. 193, p. 110404, 2021. [Online]. Available: https://www.sciencedirect.com/science/article/pii/S0927025621001294

[238] J. Bean, "Modelling polycrystalline materials and interfaces," August 2017. [Online]. Available: https://etheses.whiterose.ac.uk/19008/

[239] S. Schubert, K. Attenkofer, T. Kamps, E. Muller, H. Padmore, M. Ruiz-Osés, M. Schmeißer, J. Smedley, J. Wong, and J. Xie, "Influence of Growth Method on K_3Sb Photocathode Structure and Performance," *Proceedings of the 5th Int. Particle Accelerator Conf.*, vol. IPAC2014, p. Germany, 2014. [Online]. Available: http://jacow.org/IPAC2014/doi/JACoW-IPAC2014-MOPRI018.html

[240] A. H. Sommer, "n-Type and p-Type Conduction in Alkali-Antimonide Photoemitters," *Journal of Applied Physics*, vol. 29, no. 11, pp. 1568–1569, 06 2004. [Online]. Available: https://doi.org/10.1063/1.1722994

[241] M. S. Dresselhaus, "Optical properties of solids," [Accessed 13-03-2024]. [Online]. Available: https://web.mit.edu/6.732/www/6.732-pt2.pdf

[242] online, "Interband absorption," https://dsl.nju.edu.cn/lectures/Chapter3.ppt, [Accessed 13-03-2024].

[243] V. Pavlenko, "Automated growth of photocathode films: from the basics of process control towards artificial intelligence," 2021, [Accessed 15-03-2024]. [Online]. Available: https://conferences.slac.stanford.edu/sites/default/files/2023-05/SessionF_Pavlenko_Presentation_v2.pdf

[244] J. K. Bae, L. Cultrera, P. DiGiacomo, and I. Bazarov, "Rugged spin-polarized electron sources based on negative electron affinity GaAs photocathode with robust Cs_2Te coating," *Applied Physics Letters*, vol. 112, no. 15, Apr. 2018. [Online]. Available: https://doi.org/10.1063/1.5026701

[245] H. Sugiyama, K. Ogawa, J. Azuma, K. Takahashi, M. Kamada, T. Nishitani, M. Tabuchi, T. Motoki, K. Takashima, A. Era, and Y. Takeda, "A study of an electron affinity of cesium telluride thin film," *Journal of Physics: Conference Series*, vol. 298, p. 012014, May 2011. [Online]. Available: https://doi.org/10.1088/1742-6596/298/1/012014

[246] L. Piccirillo, *Introduction to the Maths and Physics of Quantum Me-*

chanics. CRC Press, 2023. [Online]. Available: https://www.amazon.com/Introduction-Maths-Physics-Quantum-Mechanics-ebook/dp/B0CD7VZM8X

[247] Wikipedia, "Photoelectric effect — Wikipedia," http://en.wikipedia.org/w/index.php?title=Photoelectric%20effect&oldid=1173513294, 2023, [Online; accessed 10-September-2023].

[248] G. B. Fisher, W. E. Spicer, P. C. McKernan, V. F. Pereskok, and S. J. Wanner, "A Standard for Ultraviolet Radiation," *Appl. Opt.*, vol. 12, no. 4, pp. 799–804, Apr 1973. [Online]. Available: https://opg.optica.org/ao/abstract.cfm?URI=ao-12-4-799

[249] S. Mohanty, "Development of multialkali antimonides photocathodes for high-brightness photoinjectors," P3 Photocathode Workshopnbsp; Physics for Photoinjectors, Oct 2023. [Online]. Available: https://indico.bnl.gov/event/19730/

[250] S. Mohanty, "Development of multialkali antimonides photocathodes for high-brightness photoinjectors," FLS2023, Luzern, Switzerland. [Online]. Available: http://fls2023.vrws.de/talks/we3a5_talk.pdf

[251] M. Born, E. Wolf, A. B. Bhatia, P. C. Clemmow, D. Gabor, A. R. Stokes, A. M. Taylor, P. A. Wayman, and W. L. Wilcock, *"Principles of Optics: Electromagnetic Theory of Propagation, Interference and Diffraction of Light"*, 7th ed. Cambridge University Press, 1999.

Acknowledgement

I would like to express my sincere gratitude to all the people who have supported me along this long road.

First of all, I want to thank my supervisor, Anne Oppelt, for her supervision, invaluable guidance, patience, and support throughout this research journey.

I extend my gratitude to Daniele Sertore, Laura Monaco, and Paolo Michelato at INFN LASA for their invaluable assistance and for granting access to the resources and facilities crucial for carrying out this research at LASA. Their expertise and encouragement have been fundamental in navigating the complexities of this project.

I am grateful to my professor, Prof. Wolfgang Hillert, for his guidance and valuable feedback, which have been instrumental in keeping the project on track and feasible.

I extend my heartfelt thanks to my group leader at PITZ, Frank Stephan, for his trust, guidance, and encouragement throughout the course of this thesis.

I am thankful to Houjun Qian, Mikhail Krasilnikov, Xiangkun Li, Andreas Hoffmann, and Matthias Gross for the numerous insightful discussions at PITZ.

I also extend my thanks to all the members of the PITZ and INFN LASA groups for providing the best possible conditions for the experiment.

Lastly, I want to express my deepest appreciation to my family and friends for their unwavering love, understanding, and support. Despite the physical distance, their emotional closeness has been a constant source of strength for me.

Declaration on oath

I hereby declare and affirm that this doctoral dissertation is my own work and that I have not used any aids and sources other than those indicated.

If electronic resources based on generative artificial intelligence (gAI) were used in the course of writing this dissertation, I confirm that my own work was the main and value-adding contribution and that complete documentation of all resources used is available in accordance with good scientific practice. I am responsible for any erroneous or distorted content, incorrect references, violations of data protection and copyright law or plagiarism that may have been generated by the gAI.

18.10.2024	*Sandeep Kumar Mohanty*
Date:	Signature: